

Geological Storage of Carbon Dioxide

Principal Investigators

Jerry Harris, Professor of Geophysics; Anthony R. Kovscek, Associate Professor of Energy Resources Engineering; Franklin M. Orr Jr, Professor of Energy Engineering; and Mark D. Zoback, Professor of Geophysics

Investigators

Paul Hagin, Youli Quan, Research Associates, Geophysics; Laura Chiramonte, L. Gerst, Jolene Robin-McCaskill, Evan S. Um, John P. Vermeylen Tiejuan Zhu Graduate Research Assistants, Geophysics; Abhishek Dutta, Taku Ide, Wenjuan Lin, Graduate Research Assistants, Energy Resources Engineering.

Collaborators

Marco Bonhoff, Helmholtz-Centre Potsdam, Neeraj Gupta, Battelle Memorial Institute, David Pollard, Professor, Geological and Environmental Sciences, Reginald Mitchell, Professor, Mechanical Engineering

Executive Summary

We report our progress in a fundamental, interdisciplinary study of carbon dioxide (CO₂) transport, adsorption, and sequestration in geological porous media. Experiments, modeling, field observations, and theory development are combined. Our focus is unmineable coal seams. Ancillary studies in gas shale and oil and gas settings that are relevant to coalbeds are also reported. We put much focus upon the beneficial use of CO₂ during sequestration to achieve, for instance, enhanced gas recovery or the control of underground coal fires. Our work is generally divided into site assessment, prediction, and monitoring activities. Summary of the various activities follow.

Using the lessons learned from studies on enhanced coalbed methane (ECBM) as a starting point, we have begun laboratory experiments, reservoir modeling, fluid flow simulation, risk analysis, and economic assessment to assess the feasibility of the sequestration and enhanced recovery concept using the Barnett shale in Texas as a case study. Laboratory work will investigate both adsorption and mechanical properties of shale samples to use as inputs for fluid flow simulation. Adsorption and mechanical properties of shale samples will be simultaneously measured using a triaxial press under realistic reservoir conditions with varying gas saturations. Fluid flow simulation will be conducted using the reservoir simulator GEM that has successfully modeled enhanced recovery in coal. Stochastic reservoir models will be generated to test the full range of likely reservoir properties. The results of the flow simulation will be used to answer questions related to CO₂ sequestration capacity, CO₂ leakage risk, and CO₂ sequestration economics in the Barnett shale. If enhanced recovery and CO₂ sequestration is feasible in gas shales, it will have a major impact on production strategies as well as regional and national plans for carbon sequestration due to the thickness and areal extent of these types of reservoirs.

Also, in the area of site assessment, a 3D reservoir model and fluid flow simulation of the Tensleep Formation was conducted using geomechanical constraints in advance of a

proposed CO₂-EOR and sequestration pilot at Teapot Dome Oil Field, WY. The objective of this work is to model the migration of the injected CO₂ as well as to obtain limits on the rates and volumes of CO₂ that can be injected, without compromising seal integrity. We combine our previous geomechanical analysis, geostatistical reservoir modeling, and fluid flow simulations to investigate critical questions regarding the feasibility of the CO₂-EOR and sequestration project in the Tensleep Fm. The analysis takes in consideration the initial trapping and sealing mechanisms of the reservoir, the consequences of past and present oil production on the system, and the potential effect of the CO₂ injection on the reservoir and the seal. Finally, we also assess the storage capacity of the Tensleep Fm. in this particular trap. The results of the simulations indicate that the injected CO₂ will rapidly rise to the top layers, above the main producing interval, and will accumulate in the fractures (almost none will get into the matrix). A well control strategy, consisting of shutting in and re opening wells, will be necessary to improve oil recovery without circulating CO₂. Incremental oil production is predicted to be less than 10% and this value could go up to almost 30% if double the amount of CO₂ is injected in twice the amount of time. The results suggest that the present trap could eventually hold 2 wells injecting 1 MMcf/d each, during 15 years. This will sequester $\sim 5 \times 10^5$ tonnes of CO₂ corresponding to a small power plant of $\sim 37,800$ tonnes per year.

Understanding gas adsorption and desorption behavior of gas on coal is important to predict gas transport and for enhanced coalbed methane recovery estimation. Adsorption/desorption processes need to be taken into account when estimating the amount of coalbed methane resources in place and the storage capacity of coal beds for CO₂ storage, determining the bottomhole pressure for CBM primary recovery, and designing enhanced coalbed methane recovery by gas (CO₂, N₂, or a mixture of the two) injection. Adsorption is usually quantified using adsorption isotherms. Adsorption isotherms in the literature were reviewed and summarized. Several algorithms for calculating multi-component adsorption based on the isotherms were investigated. Experiments were designed to measure the necessary parameters for multi-component adsorption calculations.

The time scale for diffusive transport of CO₂ from cleats to the matrix of coal is also of interest. A numerical model is also developed for multicomponent (ternary) gas diffusion and adsorption in coal beds, focusing on CO₂, N₂-CH₄ counter diffusion and simultaneous adsorption associated with CO₂ sequestration enhanced coal bed methane (CO₂-ECBM) recovery. We present, for the first time, consistent models to incorporate adsorption along with diffusion of multicomponent (ternary) gas mixtures. The diffusion model uses a Fickian formulation, integrated with Maxwell-Stefan (MS) diffusion theory. The Maxwell-Stefan (MS) diffusion formulation deals rigorously with the interactions between multicomponent gas molecules. The Extended Langmuir and Ideal Adsorbate Solution (IAS) models are used to model the adsorption phenomenon in ternary gas mixtures. We use the IAS model and compare the predicted behavior against the Extended Langmuir model. The comparative study suggests that the multicomponent sorption equilibria described using IAS and Extended Langmuir model are quite different. IAS prediction however is strongly dependent upon the choice of pure gas isotherm equation. The results also show a significant effect of composition on diffusivities. Thus, concentration dependent diffusivities need to be taken into account

when considering gas transport from the coal matrix to fractures, particularly for a multicomponent domain.

Results of field observations and modeling of an active, uncontrolled, underground coalbed fire are also reported. Surface measurements include surface subsidence, systematic surface fissures, temperature measurements of gases vented from the surface fissures and delineation of surface thermal anomalies using IR cameras and melted snow regions after a snow storm. The surface measurements were combined in various ways to better characterize the coalbed fire in Durango, CO. We also began using numerical simulation models to investigate the processes involved in this coalbed fire. Modeling of subsidence that occurs when coal is consumed by combustion indicates there is a relationship between the location and magnitude of subsidence caused by the fire and the opening of fissures. The fissures are believed to open when subsurface subsidence gives rise to tensile stresses around pre-existing joints. Possible combustion simulation models are suggested in this report, which will be pursued in 2009 to investigate the rate of coal consumption in the subsurface at the coalbed fire near Durango, CO. The combination of field observations and modeling suggests a conceptual picture for the way a coalbed fire is sustained: collapse of overburden in burned zones opens pre-existing fractures in a way that provides exit pathways for hot gases and inlets for the air required to support combustion.

In the area of monitoring, a pilot carbon dioxide (CO₂) sequestration experiment was carried out in the Michigan Basin in which ~10,000 tonnes of supercritical CO₂ was injected into the Bass Island Dolomite (BILD) at 1050 m depth. A Passive Seismic Monitoring (PSM) network was operated before, during and after the ~17 day injection period. The seismic monitoring network consisting of two arrays of eight, three-component sensors was deployed in two monitoring wells at distances of only a few hundred meters from the injection point. 225 microseismic events were detected by the network. Of these, only one event was clearly an injection-induced microearthquake. It occurred during injection, approximately 100 m above the BILD formation. No events, down to the magnitude -3 detection limit, occurred within the BILD formation during the injection. The observed seismic waveforms associated with the other 224 events were quite unusual in that they appear to contain dominantly compressional (P) but no or extremely weak shear (S) waves, indicating that they are not primarily associated with a shear slip source process. They were unusual in two other ways. First, almost all of the events occurred prior to the start of injection into the BILD formation. Second, hypocenters of the 94 locatable events cluster around the wells where the sensor arrays were deployed, not the injection well. While the temporal evolution of these events show no correlation with the BILD injection, they do correlate with EOR-related CO₂ injection into the 1670 m deep Coral Reef formation that had been going on for ~2.5 years prior to the injection experiment into the BILD formation began. We conclude that the unusual microseismic events detected near the two monitoring arrays are leakage along the well casings during the EOR-related CO₂ injection into the Coral Reef formation. These events, therefore, represent the first known seismic detection of CO₂ leakage along pre-existing wellbores. Our conclusion is also supported by the observation that, as soon as injection into the Coral Reef formation resumed at the conclusion of the BILD demonstration experiment, seismic events (essentially identical to the events associated

with the Coral Reef injection prior to the BILD experiment) again started to occur close to a monitoring array ~600 m above the Coral Reef formation. Taken together, these observations point to potential vertical migration pathways around the casings of the pre-existing wellbores. Our detection of these unusual microseismic events was somewhat fortuitous in that the arrays were deployed exactly at the depth where the CO₂ undergoes a phase change from a critical state to a gas. However, given the large number of pre-existing wellbores that exist in depleted oil and gas reservoirs that might be considered for CO₂ sequestration projects, seismic monitoring systems could be deployed at optimal depths to detect leakage along them.

Additional monitoring activities focused on True 4-D seismic subsurface monitoring for CO₂ storage in Coal is examined. Our GCEP project is divided into two tasks: (1) Innovative scenarios for continuous seismic monitoring, and (2) development of a laboratory measurement for the signature of CO₂ in coal. Under task #1, we have carried out a comprehensive simulation study that involved reservoir simulation, seismic simulation, and simulated depth imaging. The goal was to test and demonstrate the efficacy of True 4-D subsurface monitoring. The approach we take may be succinctly described as trading off spatial resolution for higher temporal resolution. The fourth-dimension in True 4-D monitoring is the dense sampling of slow time. With the help of this slow time axis we have developed a methodology for early detection of leaks or small changes in a reservoir due to CO₂. We propose to use permanently embedded data acquisition hardware, and dynamic imaging. Dynamic imaging is implemented through either iterative inversion of continuously streaming data or evolution of sparse datasets. We also summarize the development of a finite element method for simulating transient electromagnetics for subsurface monitoring, especially for a relatively shallow target like coal. The algorithm is especially well suited for complex geology and surface tomography. The True 4-D monitoring task is complemented by a laboratory activity on the acoustic signature of CO₂ in coals. In particular, this task seeks to add pressure control to DARS I and measure the acoustic compressibility and attenuation of saturated coal at approximately 1000 Hz.

Introduction

Projections of worldwide energy use predict that fossil fuels continue to play a significant role through, at least, the first half of the twenty-first century. The growth of energy efficiency, renewable energy, and other energy alternatives does not diminish the need to develop technologies that enable the use of fossil fuels while mitigating atmospheric emissions of greenhouse gases. Capture and long-term storage of a portion of the carbon dioxide (CO₂) released as a result of combustion of fossil fuels offers one approach to limiting carbon emissions. Possible settings for geologic sequestration include reservoir rocks that are currently producing oil or gas, deep formations that contain salt water, and deep coal beds that are not candidates to be mined in the future.

This report presents our progress in the area of geological sequestration in target formations such as coalbeds as well as gas shales. We also consider the beneficial use of carbon dioxide for enhanced gas recovery and to modify flow fields within coal so as to

extinguish underground coal fires. The organization follows themes of site assessment and evaluation, carbon dioxide transport coupled to adsorption, and monitoring strategies assessing plume dynamics

As described in our report for 2007-8, three laboratory groups currently conduct experiments on coal samples. We continue to take full advantage of the combined capabilities of our laboratory equipment, and we have tightly integrated our experimental research efforts. To summarize, Mark Zoback is directing an effort to measure the elastic, viscoplastic and flow properties of coal and gas shale, including shrinkage and swelling, as a function of gas adsorption. Tony Kovscek is directing an effort to measure adsorption isotherms, probe adsorption induced permeability changes to coal, and study the flow and transport properties of coal. Jerry Harris is directing an effort to measure the dynamic elastic properties and attenuation of coal. Our experimental plans, efforts, and results are summarized in the sections entitled “Feasibility Assessment of CO₂ Sequestration and Enhanced Recovery in Gas Shale Reservoirs,” “Multicomponent Gas Diffusivity and Sorption in Coal,” “Multicomponent Sorption Modeling During Convective Transport in Coalbeds,” and “Estimating the Attenuation of Porous Rock with Changing Pressure and Saturation using Differential Acoustic Resonance Spectroscopy (DARS).” A similar high level of activity is underway in the area of site assessment and modeling. Mark Zoback and coworkers are investigating site assessment techniques incorporating fluid flow and geomechanical constraints. Tony Kovscek and collaborators are probing numerical description of carbon dioxide transport-adsorption and subsequent swelling of coal matrix. These contributions are found in the sections entitled “Feasibility Assessment of CO₂ Sequestration and Enhanced Recovery in Gas Shale Reservoirs”, “3D Stochastic Reservoir Model and Fluid Flow Simulation of the Tensleep Formation” and “Multicomponent Sorption Modeling During Convective Transport in Coalbeds.

Lynn Orr and coworkers continue their study of reactive processes in coal to characterize, from a subsurface perspective, the progression of events leading to a self-sustaining fire in a coalbed. Coalbed fires account for significant emissions of carbon dioxide to the atmosphere. The study is entitled, “Characterization of a Coalbed Fire near Durango, CO: Fieldwork, numerical simulation modeling, and Analysis.” Geological field observations and coalbed gas composition data are combined with geomechanical modeling for the formation of fissures in coal.

Mark Zoback, Jerry Harris and collaborators are investigating monitoring strategies for CO₂ leakage as well as CO₂ migration within target formations. The work of Mark Zoback and coworkers is described in “Seismic Detection of CO₂ Leakage in Monitoring Wellbores.” Jerry Harris and collaborators are examining quasi-continuous strategies for monitoring the subsurface volume contacted by carbon dioxide. This work includes acquisition strategies as well as the optimal tradeoffs made between temporal and spatial accuracy. These techniques are designed to construct time-lapse subsurface images using relatively low-resolution active seismic imaging in order to reduce the cost of quasicontinuous long-term monitoring. Details are described in the sections “True 4-D Seismic Subsurface Monitoring,” “An Approach to Quasi-continuous Time-lapse Seismic Monitoring using Data Evolution of Sparse Data Recording,” and “A Finite Element

Algorithm for 3D Transient Electromagnetic Modeling”

Background

Three principal settings are being considered for geologic sequestration of carbon dioxide – deep saline aquifers, depleted oil and gas reservoirs, and deep unmineable coal seams. Of these, coal bed storage of CO₂ remains the least well understood. While the potential volumes of storage in coal beds are more variable in comparison to the other geological settings, the appreciable coal deposits in the U.S., China, Russia and India, provide important opportunities to sequester CO₂ if coalbeds are indeed a viable storage setting for greenhouse gases. The work summarized here represents concrete steps related to improved quantitative evaluation of this storage mechanism as well as the potential for cost recovery associated with ECBM.

FEASIBILITY ASSESSMENT OF CO₂ SEQUESTRATION AND ENHANCED RECOVERY IN GAS SHALE RESERVOIRS

INTRODUCTION

Near to medium-term CO₂ storage in oil and gas fields, unminable coal seams, and deep saline aquifers does not seem to be limited by total storage capacity. An IPCC report from 2005 found that worldwide geologic sequestration capacity is 675 to 900 GtCO₂ for oil and gas fields, 3 to 200 GtCO₂ for unminable coal seams, and >1000 GtCO₂ for deep saline aquifers (IPCC, 2005). Given the expense of capturing CO₂ at a point source, cost is the largest limiting factor in the near-term. Thus, it is most likely that large-scale CO₂ storage will be implemented in combined enhanced hydrocarbon recovery and sequestration projects in order to offset the capture and storage costs.

Oil reservoirs have been enhanced by CO₂ injection since the 1970's. Natural gas reservoirs, however, are not typical candidates for enhanced recovery because the free gas phase flows easily in a conventional reservoir. In some "unconventional" gas reservoirs, such as deep unminable coal seams and organic-rich black shales, methane (CH₄) is found both free within the pore and fracture space as well as adsorbed onto internal solid surfaces. These unconventional reservoirs are candidates for enhanced recovery with carbon sequestration because in some cases CO₂ is preferentially adsorbed over CH₄, allowing for increased production with secure carbon storage as the CO₂ displaces the CH₄. The conceptual model for gas production in both coal beds and gas shale reservoirs is shown in Figure 1.

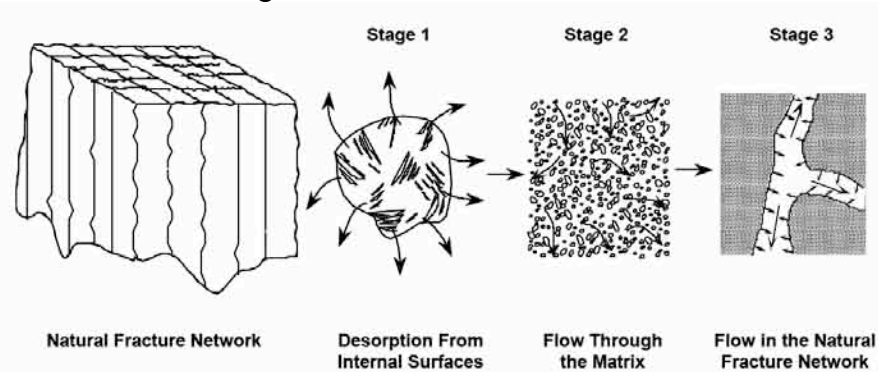


Figure 1: Conceptual model of gas production in shale and coal. From Zuber et al. 2002.

Enhanced recovery with CO₂ sequestration has been tested in the field for coal, but it has not yet been tested for gas shale reservoirs. Since gas shales and coals share similar properties, it is important to investigate if gas shales could also benefit from enhanced recovery with CO₂. While shales by their nature do not have the porosity and permeability of typical petroleum reservoirs or saline aquifers, they may still be attractive targets for CO₂ sequestration. They are extensive in area and thickness (Figure 2), which is helpful in matching them with point sources of CO₂.

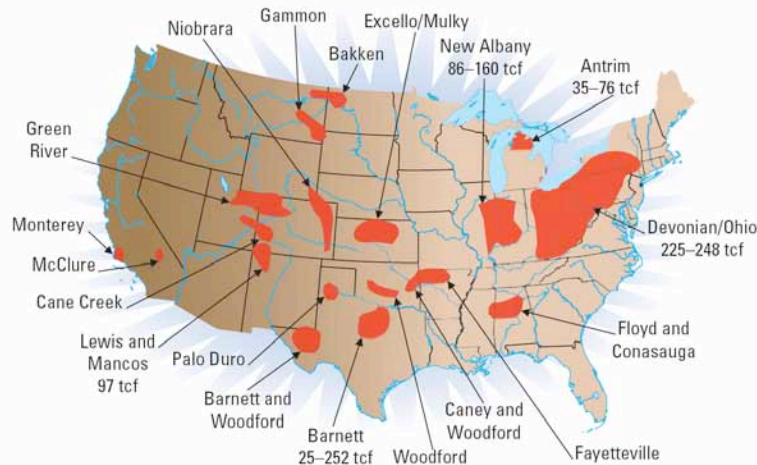


Figure 2: Map of extensive gas shale resources in U.S. From Schlumberger, 2007.

Our work will test the feasibility of enhanced recovery and CO₂ sequestration in gas shale reservoirs using the Barnett shale in Texas as a case study. Using the lessons learned from studies on ECBM as a starting point, we will do an initial test of the concept by integrating laboratory experimentation, reservoir modeling, fluid flow simulation, risk analysis, and economic assessment. These studies will provide a greater physical understanding of gas shale reservoirs as well as guide future investigations in enhanced recovery and CO₂ sequestration. Additional background on gas shales and details of our research plans can be found below.

BACKGROUND

The Barnett lies at a depth of 6500 to 8500 feet, which is associated with formation pressures of 3000 to 4000 psi (Curtis, 2002). Net thickness of organic-rich shale layers is 50 to 200 feet, thickening towards the deeper eastern part of the formation (Curtis, 2002). Typical composition of the producing facies of the Barnett are 45% quartz, 27% illite, 8% carbonate, 7% feldspar, 5% organic matter, 5% pyrite, and 3% siderite (Montgomery, 2004). Porosity is on average 4-5%, while permeability of the intact matrix is measured in the tens to hundreds of nanodarcies (Curtis, 2002).

Like coals, Barnett shale samples exhibit adsorption of CH₄. A set of Langmuir isotherms for Barnett shales is shown below in Figure 3. This database did not reveal the composition for each sample, thus it is not possible to correlate the range of adsorption capacities with a property such as TOC. In general, adsorption in gas shales is believed to be a combination of adsorption in microporous organic material, typically kerogen, and adsorption on layered clays, such as illite. A linear relation between TOC and CH₄ adsorption capacity has been previously found for Appalachian and Antrim shales (Nuttall et al, 2005).

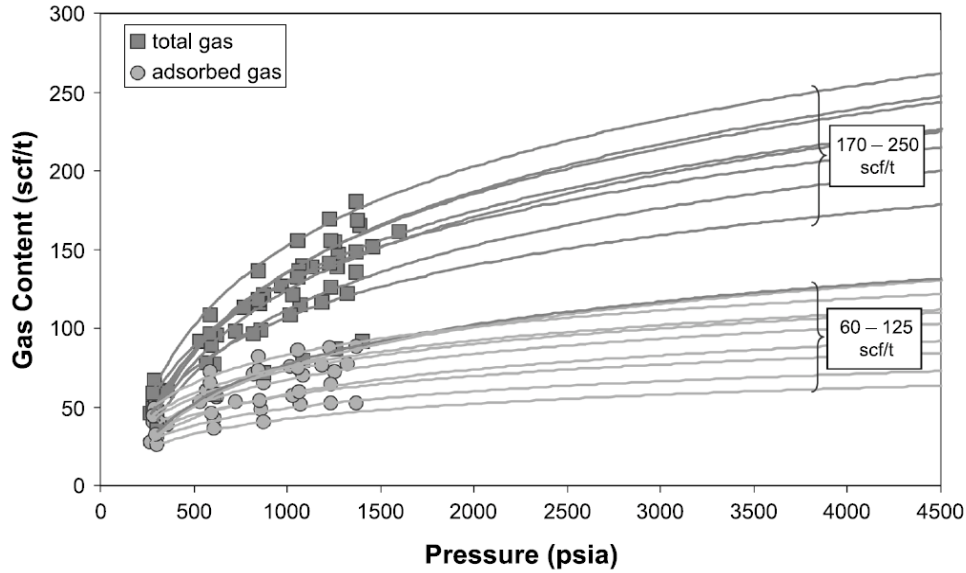


Figure 3: Methane adsorption isotherms for Barnett shale core samples. From Montgomery, 2004.

Nuttall et al. (2005) is the only study that has tested the adsorption of CO₂ on gas shale samples. They report that CO₂ is preferentially adsorbed at over five times the volume of CH₄ on average in organic-rich shales (Figure 4). They also find a linear correlation between TOC and CO₂ adsorption capacity (Figure 5). While adsorption studies of CH₄ have been conducted for Barnett shale reservoirs, no adsorption studies for carbon dioxide exist. Thus, it will be necessary to study the adsorption of CO₂ and CH₄ on Barnett shale samples in order to verify that a similar relation exists as was found for Devonian shale samples.

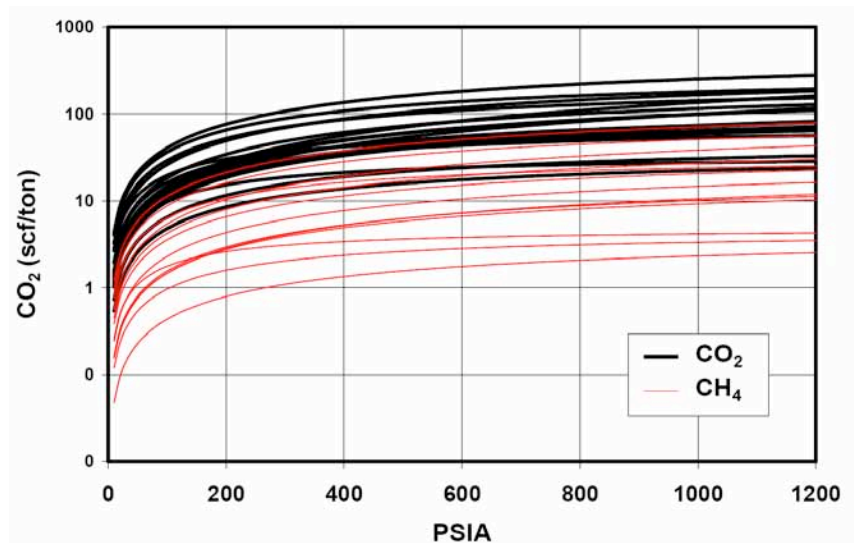


Figure 4: Preferential adsorption of CO₂ over CH₄ in Devonian shale samples. From Nuttall et al., 2005.

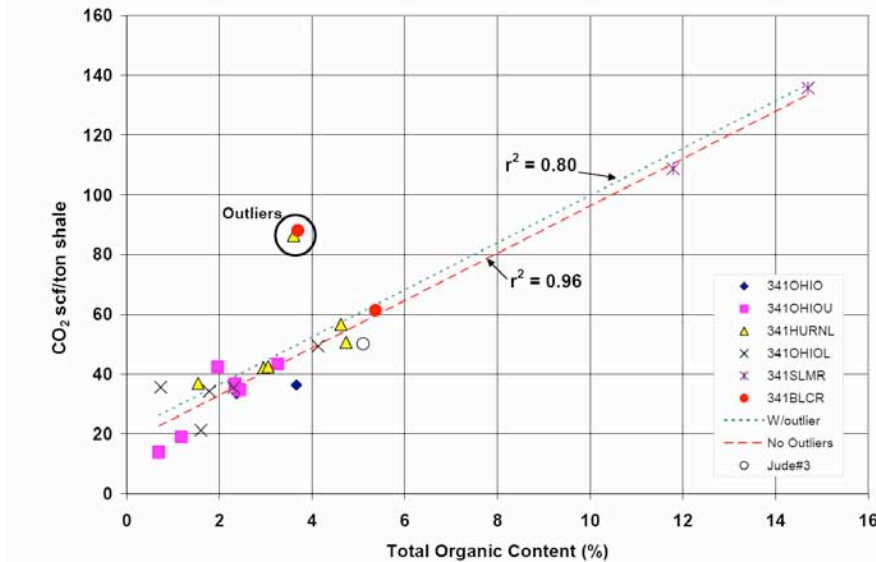


Figure 5: Relationship between Total Organic Carbon and CO₂ adsorption at 400 psi in Devonian shale samples. Linear trend of CO₂ adsorption capacity vs. TOC is consistent with linear trend found for methane. From Nuttall et al., 2005.

In addition to adsorption properties, knowledge of the mechanical state of a gas shale reservoir is critical for optimal design of an enhanced recovery and CO₂ sequestration project. The in situ stress of the Barnett shale is in a normal faulting environment, with an overburden (S_v) gradient of 1 psi/ft but relatively isotropic horizontal stresses of about 0.7 psi/ft (Palmer et al., 2007). The development of hydraulic fracturing techniques has made the Barnett an economically viable natural gas reservoir. However, the geomechanical aspects of hydraulic fracture stimulation in the Barnett are not well understood. Thus, mechanical studies on Barnett shale rocks as well as further research on the stimulation process in the Barnett will be crucial to understanding the potential for CO₂ sequestration and enhanced recovery.

FUTURE PLANS

We are currently negotiating with several oil and gas companies for access to samples and data from gas shale reservoirs. Once the samples and data arrive in early summer 2008, we will begin a comprehensive study to test the feasibility of carbon sequestration and enhanced recovery using laboratory studies, fluid flow simulations, and integrated assessment techniques.

Laboratory Studies

In order to model the process of carbon sequestration and enhanced recovery in gas shale reservoirs, a collection of material properties must be used as inputs for fluid flow simulation. Because so little is known about the physical properties of gas shales, this study will investigate both adsorption and mechanical properties of shale samples to use as inputs for simulation.

To measure the mechanical and adsorption properties of gas shale samples, a triaxial press apparatus will be used. With this setup, we will measure adsorption properties at varying pressures and temperatures, as well as static and dynamic mechanical properties

like Young's modulus, compressibility, and Poisson's ratio. In addition, we will measure permeability on the intact shale matrix using pressure pulse transient testing. As coals are known to exhibit change in physical properties as a function of the gas adsorbed to the matrix, He, CH₄, and CO₂ will be varied within the sample to test for property changes.

Specific research questions to be addressed by these experiments include:

- Do Barnett shale samples show preferential adsorption of CO₂ over CH₄?
- Does adsorption in shales exhibit hysteresis, as has been seen in coals?
- Do the mechanical properties of the Barnett shale depend on gas composition?
- Do shales exhibit shrinkage or swelling with adsorption that might affect permeability, as has been seen in coals?
- What is the permeability of the intact matrix?
- Can a composition-based metric be determined for adsorption parameters?

Field-Scale Simulation

The goal of this portion of the project is to test whether CO₂ sequestration and enhanced recovery are feasible in a producing gas shale field. Using the data acquired from experimental efforts, along with geological, geophysical, and production data from a real-world reservoir, three-dimensional fluid flow simulations will be conducted on a set of probable reservoir models. These simulations will test if the volume of CH₄ that can be produced and the volume of CO₂ that can be sequestered in a gas shale reservoir is promising. The study will also test the importance of different reservoir properties for enhanced recovery and sequestration.

The basic workflow of this study will follow that used in previous studies on coalbed methane (Ross, 2007). The workflow is comprised primarily of two steps, stochastic reservoir modeling and fluid flow simulation. The stochastic modeling will employ geostatistical techniques to populate a 3D grid with reservoir properties by using spatial correlations that are conditional to the sampled data. All available data (e.g. well logs, laboratory measurements, seismic, etc.) will be used to populate a gridded structural model filled with petrophysical properties.

For fluid flow simulations, we will use the Computer Modeling Group's simulator GEM. GEM is a compositional reservoir simulator with the ability to simulate dual porosity, multiple gas components, mixed gas diffusion, mixed gas adsorption, and stress dependent porosity and permeability. GEM has been used with success in studies of CO₂ sequestration in coal beds, and thus it is expected to be successful in simulating gas shale reservoirs because of the similarity in physical properties.

- Overall, the simulation study will directly address the following questions:
- What is a reasonable estimate of enhanced recovery potential in the Barnett shale?
- What is a reasonable estimate of CO₂ sequestration potential in the Barnett shale?
- What is a reasonable estimate of CO₂ injectivity in the Barnett shale?
- What well configuration will co-optimize enhanced recovery and sequestration?

- How should the complex fracture network in the Barnett shale be modeled?
- What effect do the following geologic properties, geomechanical properties, and engineering practices have on enhanced recovery and sequestration?
 - Fracture spacing and orientation
 - Fracture permeability and porosity
 - Shale matrix permeability and porosity
 - Shale thickness, dip and depth
 - Reservoir pressure and temperature
 - Adsorption isotherms
 - Shale composition
 - Diffusion coefficients
 - Rock compressibility in the matrix and fractures
 - Seal capacity

Integrated Assessment

We will use the results of the flow simulation to answer questions related to CO₂ sequestration capacity, CO₂ leakage risk, and CO₂ sequestration economics in gas shale reservoirs.

Capacity Assessment

Nuttall et al. (2005) reported a sequestration capacity of 25 GtCO₂ in the Devonian shales of Kentucky. This large estimate is based on an average adsorption capacity for Kentucky black shales multiplied with an estimate of black shale volume in the state. This methodology gives an absolute upper bound for sequestration capacity under ideal conditions. Given the low permeability of gas shale reservoirs, it is likely that effective sequestration capacity will be much lower than this upper bound. In addition, injectivity may be quite low, thus limiting the rate at which CO₂ can be sequestered. The flow simulations will give an estimate of effective storage capacity for a shale gas sequestration project. This value will then be extrapolated to estimate the total sequestration capacity in the Barnett shale. It will also give a first-order estimate of sequestration capacity in other shale gas reservoirs based on a ratio of gas-in-place to carbon sequestration potential. The estimate of total capacity can then be used to gauge the potential of shale gas reservoirs as sequestration targets and guide the priorities of future research.

Risk Assessment

The risk of CO₂ leakage from a gas shale sequestration project is as of yet unknown. In the traditional model of sequestration, shale layers are considered the seal for injection, rather than the reservoir. Thus, there may be unique challenges and risks that are not well captured by the existing models for leakage. A particular focus will be on the extent of vertical migration of CO₂ within the reservoir and how effective the adsorption of CO₂ is within the reservoir. Specific flow simulations may address slow leakage through the overlying units to estimate the scale of the problem. In addition, geomechanical constraints will be applied to minimize risk of fracturing out of the Barnett shale into

overlying formations. Simple estimates of leakage risk will be used as a cost input for economic analysis.

Economic Assessment

Using the results of the flow simulations, along with information on the costs associated with drilling and production, the economic feasibility of a gas shale injection project will be calculated. This analysis will use the techniques to measure the net present value (NPV) of a sequestration project as has been done for previous ECBM studies (Reeves, 2005).

REFERENCES

- Curtis, 2002, "Fractured shale-gas systems", AAPG Bulletin, v. 86, no. 11, p. 1921-1938.
- IPCC, 2005, Carbon Capture and Storage, Cambridge University Press, UK.
- Montgomery, 2004, "Barnett Shale: A new gas play in the Fort Worth basin", Petroleum Frontiers, vol. 20, no. 1.
- Nuttall et al., 2005, "Analysis of Devonian black shales in Kentucky for potential carbon dioxide sequestration and enhanced natural gas production", Kentucky Geological Survey.
- Palmer et al. 2007, "Modeling shear failure and stimulation of the Barnett Shale after hydraulic fracturing", SPE Paper 106113
- Reeves, 2005, "The Allison Unit CO₂-ECBM Pilot – A Reservoir and Economic Analysis", 2005 International Coalbed Methane Symposium.
- Ross, H.E., 2007, CO₂ sequestration and enhanced coalbed methane recovery in unmineable coalbeds of the Powder River Basin, Wyoming, Ph.D. Thesis, Stanford University.
- Schlumberger, 2007, Shale Gas White Paper,
http://www.slb.com/media/services/solutions/reservoir/shale_gas.pdf
- Zuber et al., 2002, "A comprehensive reservoir evaluation of a shale reservoir – The New Albany Shale", Society of Petroleum Engineers Paper 77469.

3D Stochastic Reservoir Model and Fluid Flow Simulation of the Tensleep Formation

Introduction

In previous stages of this project, the Tensleep Formation has been analytically evaluated as the target horizon for a pilot CO₂-EOR and carbon storage experiment in a three-way closure trap against a bounding fault, termed the S1 fault. From the comprehensive geomechanical analysis, we estimated the geomechanical constraints we use in the fluid flow simulation described in this chapter.

It was found that the S1 fault does not appear to be at risk of reactivation and it was estimated that caprock integrity is not a risk by the buoyancy pressure of the maximum CO₂ column height that the formation can hold. Besides, we established the presence of critically stressed minor faults and fractures in the reservoir and caprock. If these minor faults are reactivated, they could enhance the permeability of the reservoir, creating permeability anisotropy inside it.

In this chapter, we develop a stochastic 3D reservoir model of the Tensleep Formation, as input of a fluid flow simulation, using these geomechanical constraints. Our objective is to model the migration of the injected CO₂, as well as to obtain limits on the rates and volumes of CO₂ that can be injected, without compromising seal integrity.

4D Stochastic Reservoir Model

In the lifetime of an oil field, models play a fundamental role in understanding and predicting the main geological, geophysical, and engineering reservoir components. Reservoir modeling is never a goal on its own. It takes the geological model as an input and delivers a product that will then be the input for a flow simulation. Good model building requires focus on the end goal, whether it is the estimation of the original oil in place (OOIP), the optimal placement of a well, the design of secondary recovery methods, the prediction of water breakthrough, or the optimization of a CO₂-EOR and Sequestration project, etc. (Caers, 2005).

The objective of 3D modeling is to provide one or several alternative numerical models intended to represent those geological, geophysical and reservoir engineering aspects of the subsurface that matter for the particular goal of the study. These numerical models are used to estimate key reservoir parameters, predict production performance, and provide uncertainty statements when needed. The uncertainty statements of these reservoir parameters are as important as providing estimates of the parameters themselves (Caers, 2005). A stochastic simulation will provide different equiprobable numerical reservoir models (different realizations) that when processed by the flow simulator will yield a distribution of reservoir forecasts. This allows the transfer of uncertainty from the geological/petrophysical model to the final forecast (Journel, 1994).

Gringarten (2005) summarized the main parts involved in stochastic 3D modeling, which consist of a series of hierarchical steps starting with the visualization and analysis of the data, followed by building the structural model, creating a velocity model to perform the time-depth conversion, and gridding the structural model. Once the reservoir is gridded, geostatistics is used to populate the grid with the petrophysical reservoir

properties. A common applied technique in this step is Sequential Gaussian Simulation (SGS), which is a simple method for simulating continuous properties (porosity, permeability) requiring only knowledge of a variogram and histogram (Caers, 2005). In this simulation process, numerous equally probable realizations are created to quantify the uncertainty of the model. The final step once the grid is populated is to upscale it to the chosen flow simulation grid. In the present study, this process was carried out with a commercial software application: Earth Decision Suite 2.1.6 – Gocad.

Reservoir Characterization in Section 10 (S1 fault area)

The Tensleep Fm. consists of an intercalation of eolian-dune sandstones and inter-dune deposits. The dune sandstones are permeable and porous intervals with different levels of cementation that affects their porosity, permeability, and fracture intensity. The inter-dune deposits consist of thin sabkha carbonates, minor evaporates (mostly anhydrite), and thin but widespread extensive beds of very low-permeability dolomiticrites (Zhang et al., 2005). The caprock for the Tensleep Fm. consists of two intervals of the Goose Egg Fm., the Opeche Shale member and the Minnekhata member. The depth of these intervals ranges from ~1600 to ~1750 m below the surface. Figure 1 shows the schematic stratigraphic column of the reservoir and caprock, following Yin (2005), that we use to construct the reservoir model.

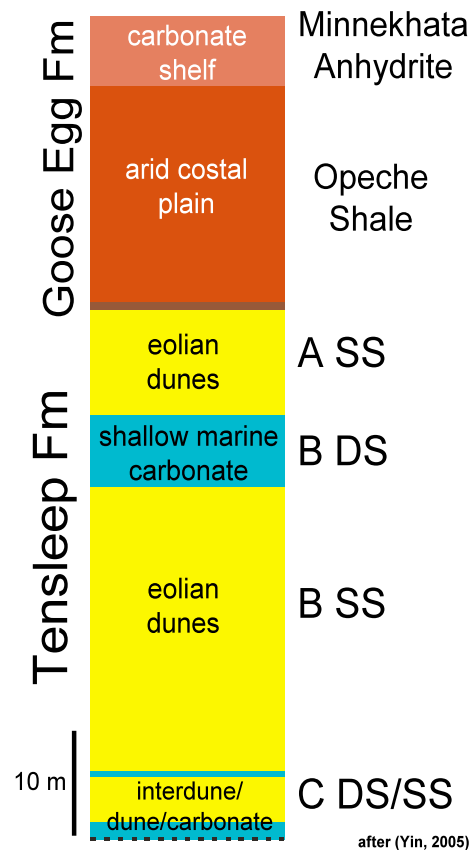


Figure 1: Schematic stratigraphic column of reservoir (Tensleep Fm.) and caprock (Goose Egg Fm.). SS = sandstone, DS = dolostone (after Yin, 2005).

The geometry of this model is based on time structure maps from the 3D seismic volume at the top of the Tensleep Fm. (A-Sandstone) and at the top of the main producing interval (B-Sandstone) interpreted by McCutcheon (2003). We converted the time-structure maps to depth using a linear velocity model obtained from the Dip-moveout (DMO) velocity analysis performed during the 3D seismic processing. This velocity model was adjusted with the corresponding well-log tops from ~36 wells along the anticline (Figure 4, left). We then segmented these surfaces at the intersection with the reservoir-bounding fault, S1, to construct a detailed model focusing in the Section 10 area (Figure 2 right).

To build the detailed model we also used well log tops of the Minekhata Member, Opeche Shale Member, A-Sandstone, B-Dolostone, B-Sandstone, C1-Dolostone, and C1-Sandstones from ~26 wells in the Section 10 area (Figure 2 right). Furthermore, we divided the B-Sandstone in two intervals, where the upper one is more porous and permeable than the lower one. The subdivision was based on detailed correlations of density, neutron and porosity logs of the mentioned wells in the area. The lowest and water filled C2-Sandstone interval was incorporated as an explicit aquifer layer beneath the reservoir.

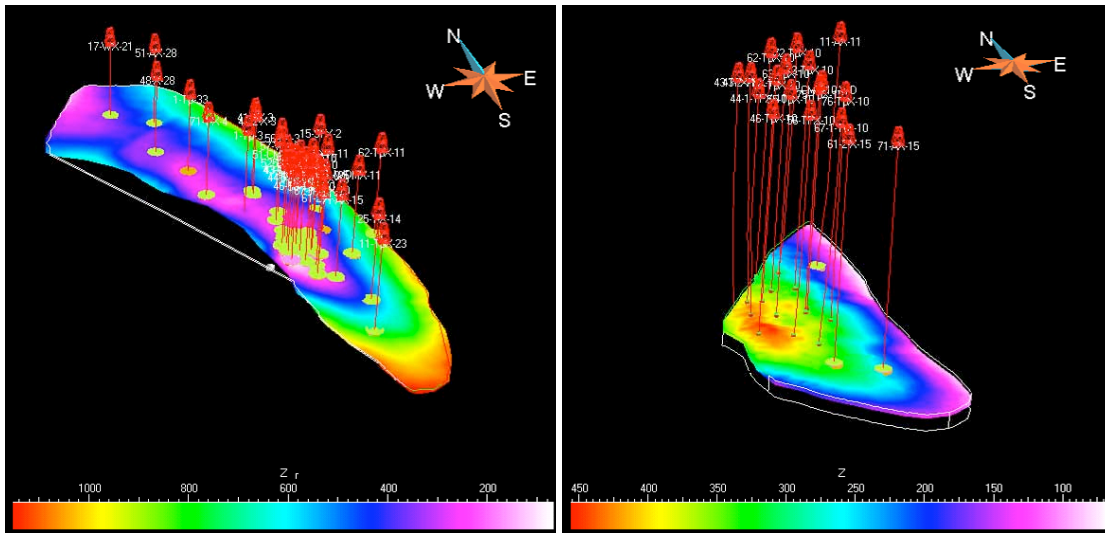


Figure 2: Depth-structure map of the Tensleep Fm. displaying the 36 wells used to adjust the time-depth conversion.

The 11 grid-layers correspond to the 9 stratigraphic units shown in Figure 1. The Upper and Lower B-Sandstones are represented in the grid by two layers each, allowing for more detailed characterization in the main producing intervals. In order to account for the permeability anisotropy caused by fractures, described in Chapter 3, we oriented the grid blocks in a direction approximately parallel to the S_{Hmax} direction, 116° Az. This scenario would correspond to a normal faulting (NF) environment.

We built a $\sim 1.5 \times 3 \times 0.15$ km, 11-layer grid, where each cell is ~ 10 by 10 m and their heights vary from ~ 1 to 50 m, depending on the thickness of the corresponding horizon. This grid contains 515,361 cells ($161 \times 291 \times 11$).

After populating the original grid with porosity and permeability distributions, which will be described in the following section, we upscaled it to a coarser grid to optimize running time in the fluid flow simulator, trying to minimize loss of detail. The upscaled grid has cell dimensions of ~ 50 by 100 m, but maintaining their original height. This corresponds to a total of 8,976 ($17 \times 48 \times 11$) grid cells (Figure 3). For the upscaling process, we used a geometric mapping method and an arithmetic average algorithm for continuous properties, built in Gocad.

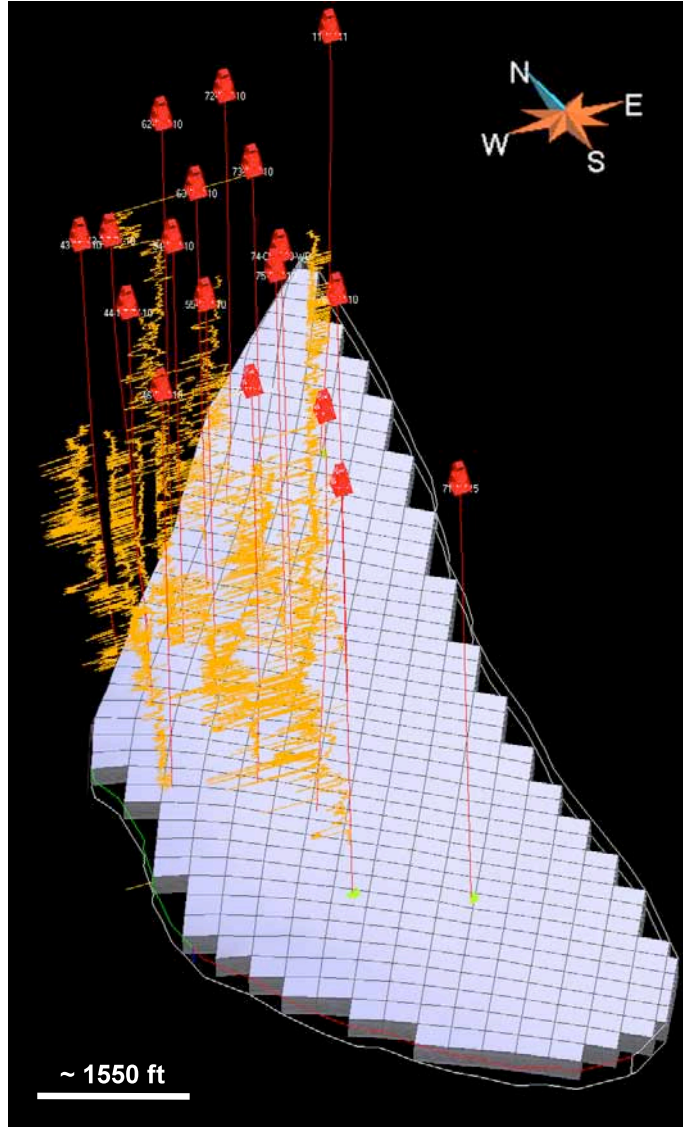


Figure 3: 3D Upscaled grid aligned parallel to S_{Hmax} Az = 116° , showing wells in the area and their porosity logs.

Using Geostatistics to populate the 3D model with porosity and permeability distributions

One of the biggest challenges in building a 3D geological model is that hard data is limited and the few available pieces of information come from different sources at different scales and with various degrees of reliability. The major contribution of geostatistics is, therefore, data integration. It combines different types of data, taking in consideration their uncertainty, and transferring such uncertainty to the final forecast (Journal, 1994).

In the present study, we use the sequential Gaussian simulation (SGS) method (Isaaks, 1990) to produce equally probable realizations of porosity and permeability that reflect the data variability and spatial statistics. Hard data from wells was incorporated in

the interval where it existed, such as porosity data from density, neutron, and sonic logs as well as from cores from four different wells. Soft data was incorporated as well, including porosity-permeability correlations from core measurements, and porosity and permeability distribution from the reservoir lithofacies defined by Yin (2005b) for the Teapot Dome Tensleep Sandstones. Table 1 summarizes the values used in the base case simulations (see example in Figure 4).

Poro [%]			K [mD]			Corr.Coeff.		
Interval	MEAN	Min	Max	Interval	MEAN	Min	Max	K - Poro
MNKT	0	0	0	MNKT	0	0	0	0
OPCH	0	0	0	OPCH	0	0	0	0
ASand	6.13	1.30	10.30	ASand	2.82	0.02	30.00	0.33
Bdolo*	3.03	0.20	8.20	Bdolo*	0.21	0.01	1.78	0.74
Upper BSand	15.38	7.80	24.00	Upper BSand	62.58	0.02	240.00	0.75
Lower BSand	5.01	0.70	12.70	Lower BSand	0.17	0.02	1.10	0.37
Cdolo*	4.35	0.70	10.10	Cdolo*	1.06	0.02	15.00	0.74
C1Sand	4.38	0.70	12.70	C1Sand	0.23	0.02	1.10	0.26
C2Sand	<i>Idem than C1Sand</i>			C2Sand	<i>Idem than C1Sand</i>			<i>Idem than C1Sand</i>

*from core values

Table 1: Porosity and Permeability values from Yin’s lithofacies analysis (2005b).

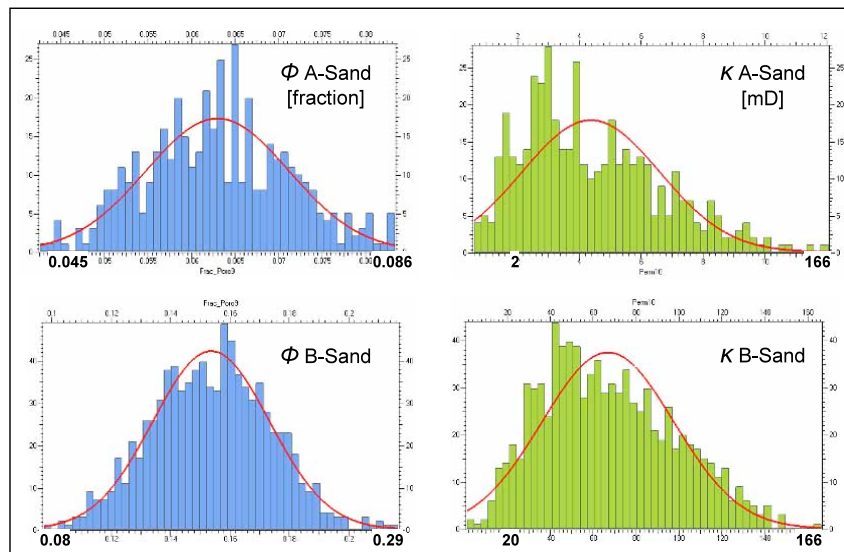


Figure 4: Example of porosity (blue) and permeability (green) geostatistical distribution for A-Sand and upper B-Sand intervals.

We also populated the grid with porosity and permeability distributions from existing cores in 8 wells in the area. Table 2 summarizes the values that will be used in simulations during the sensitivity analysis stage. The mentioned wells are 11-AX-11, 43-TPX-10, 44-1-TPX-10, 54-TPX-10, 55-TPX-10, 56-TPX-10, 62-TPX-10, and 71-AX-15.

Porosity [%]			K [mD]				Corr. Coeff.	
Interval	MEAN	Min	Max	Interval	MEAN	Min	Max	K - Poro
MNKT	0	0	0	MNKT	0	0	0	0
OPCH	0	0	0	OPCH	0	0	0	0
ASand	4.74	0.20	14.60	ASand	3.69	0.01	186.00	0.33
BDolo	3.03	0.20	8.20	BDolo	0.21	0.01	1.78	0.74
Upper BSand	10.54	0.56	28.80	Upper BSand	29.31	0.01	570.00	0.75
Lower BSand	6.95	3.60	9.95	Lower BSand	3.45	0.04	9.98	0.37
CDolo	4.35	0.70	10.10	CDolo	1.06	0.02	15.00	0.74
C1Sand**	4.38	0.70	12.70	C1Sand	0.23	0.02	1.10	0.26
C2Sand	<i>Idem than C1Sand</i>			C2Sand	<i>Idem than C1Sand</i>			<i>Idem than C1Sand</i>

**from Yin facies

Table 2: Porosity and Permeability values from core plugs from 8 wells in Section 10.

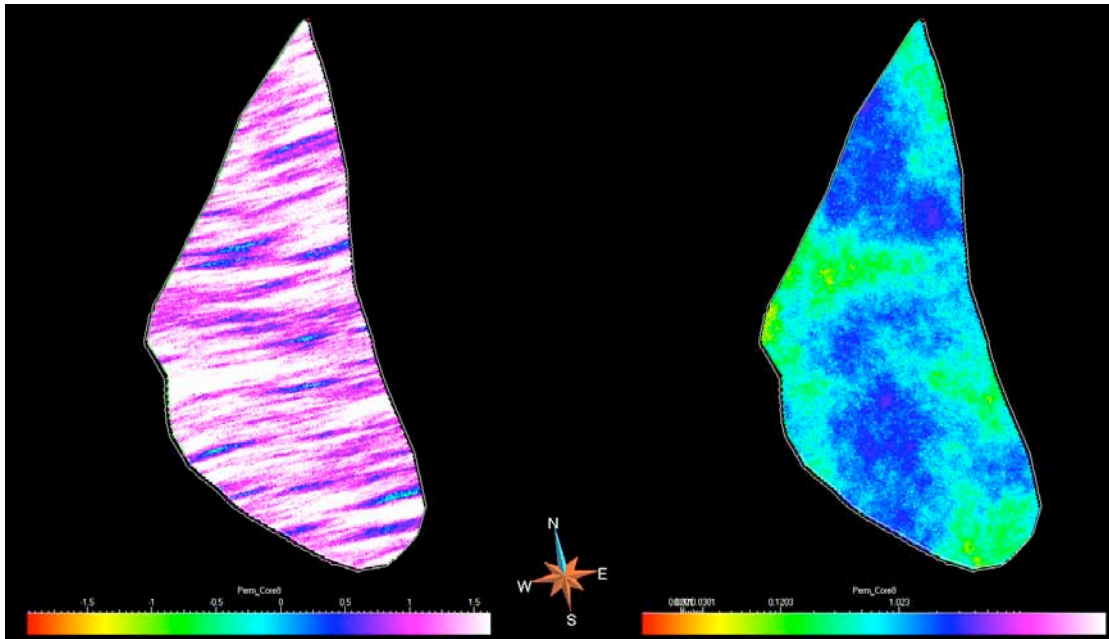


Figure 5: Map showing one of the permeability realizations at the B-Sandstone level (left) and at the B-Dolostone level (right).

The spatial variability of the properties was incorporated into the SGS algorithm using two different types of semivariograms. One was modeled so as to consider the porosity and permeability heterogeneity due to the dune configuration, and the second one represents a more homogeneous pattern corresponding to inter-dune deposits. Milliken and Koepsell (2002), from the analysis of FMI logs in well 67-1-X-14, interpreted a paleo-wind direction ~N-S. Therefore, if we assume that dune propagation was indeed perpendicular to the wind direction, this will correspond to porosity and permeability anisotropy in the E-W direction. For the sandstone intervals, we chose a spherical variogram with a 0.5 nugget effect, 15.71 sill and an anisotropic range of 1749 and 233 ft, with 85° Az for the principal axis. For the dolostones we chose a spherical variogram with a 0.5 nugget effect, 5.39 sill and an isotropic range of 1160.3 ft. Due to the lack of data, the choice of these variograms is highly subjective; however, it represents reasonable values of dune sizes found in the literature and the more

homogeneous spatial correlation expected in the interdune deposits. In total, we created 20 porosity and permeability distributions. Figure 5 shows one of the permeability realizations at the B-Sandstone level (left) and at the B-Dolostone level (right).

As mentioned before, once we populated the grid with porosity and permeability distributions the final step was to upscale it to a coarser grid more suitable for the fluid flow simulation. Figure 6 shows a SSW-NNE cross-section of the upscaled 3D reservoir model color-coded with one of the porosity realizations. Figure 7 displays a map of the upscaled grid showing one of the permeability realizations at the B-Sandstone level (left) and at the B-Dolostone level (right).

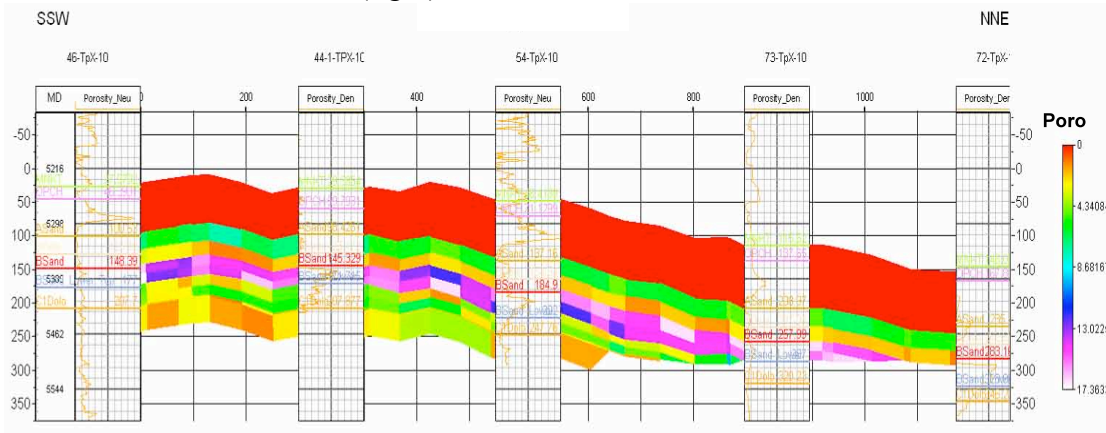


Figure 6: SSW – NNE Cross section of upscaled grid, showing one of the porosity realizations, and the porosity logs and well tops of five of the used wells.

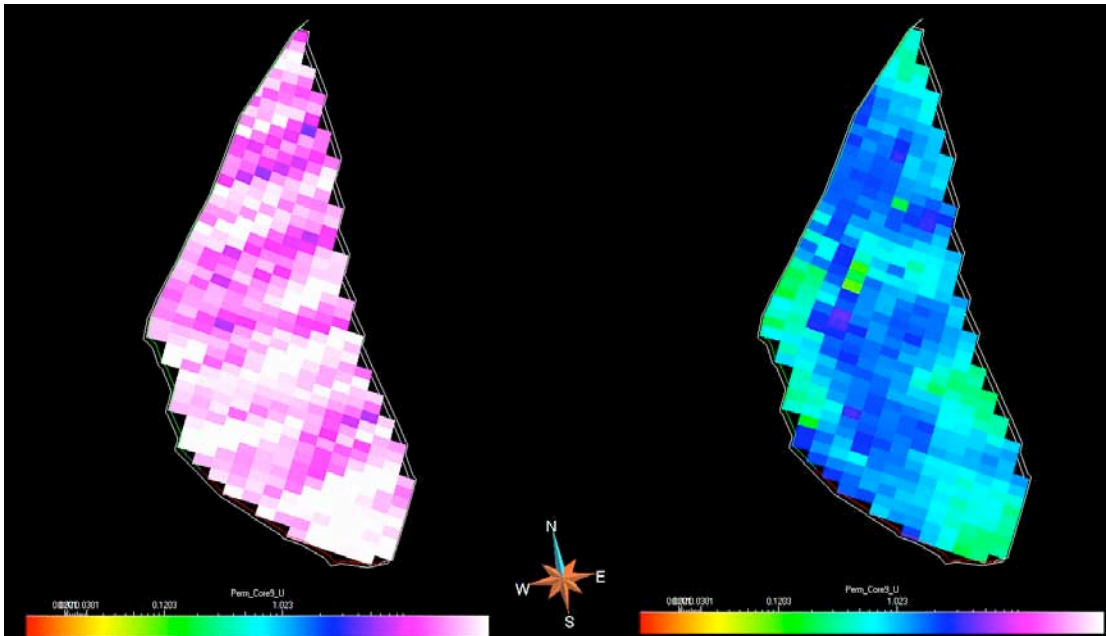


Figure 7: Map of the upscaled grid showing one of the permeability realizations at the B-Sandstone level (left) and at the B-Dolostone level (right).

Even if some detail is lost, it is still possible to notice the ~E-W permeability anisotropy in the sandstone interval (right).

Modeling CO₂-EOR Processes in a Fractured Reservoir

CO₂ injection has been used as a commercial process for enhanced oil recovery (EOR) since the 1970s and is the second-most applied EOR process in the world (Jarrell et al., 2002). As a result, in the oil industry there is considerable experience regarding the execution of this type of projects. Traditionally, the goal has been to recover the higher amount of oil from the reservoir injecting the minimum amount of gas, because the cost of CO₂ affects the profitability of the project. However, when the objective is to combine EOR and CO₂ sequestration, different CO₂ flooding designs will have to be implemented in order to increase the amount of CO₂ left behind when production stops (Kovscek, 2005).

The behavior of the CO₂ in the reservoir, although different from the oil behavior, has enough similarities to allow us to use analogous techniques to better understand, predict, and manage a CO₂-EOR project. The most common technique in practice in the oil industry is the use of Fluid Flow Simulation, where the concept is to apply the conservation of mass over each block of a gridded reservoir; flow rate is computed for each of these blocks by a discrete form of Darcy's Law (Aziz and Settari, 1979). It considers a set of initial boundary conditions and solves second order non-linear partial differential equations using finite difference and/or matrix algebra (Melzer, 2007).

Some of the most commonly used simulators are based on a 3 phase, 3D, fully implicit black oil models, but there is a number of other simulators available that incorporate compositional or thermal effects. For example, in CO₂-EOR applications the modified black-oil simulator and the fully compositional simulator are the two principal types used for predicting CO₂ flood performance. The first one is an approximate technique that accounts for oil displacement by CO₂. The fully compositional one uses an Equation-of-State (EOS) to predict the development of miscibility between CO₂ and oil. According to Jarrell et al. (2002), this approach is more rigorous, but it requires more computation time.

In order to accurately predict a CO₂ flood with this type of simulators, previous production history of the field should be simulated (and validated) to have the correct distribution of oil components at the start of the CO₂ flood to be simulated.

Pruess et al. (2004) studied the capabilities of several numerical simulation codes, including the GEM code of the Computer Modeling Group (CMG), and although pointing out that several improvements needed to be done, they concluded that the current simulation codes were shown capable of modeling the problems related to the CO₂ sequestration in geologic reservoirs.

Previous CO₂-EOR Projects

CO₂ injection has been used for EOR applications since the 1970s. By 2005, 20,000 tons per day of CO₂ were used in oil fields for EOR projects, where approximately 10 bbl of oil were produced for every ton of CO₂ injected. To date, most of the CO₂ utilized is still not anthropogenic, although some of it might be, coming mainly from purification of natural gas (Jensen et al., 2005).

The traditional focus of these type of projects have been on reservoir with light to medium density oils (29° to 48° API) and depths from 760 to 3700 m. In the US, CO₂-EOR operations are mainly in the Permian and Rocky Mountain basins (Texas, New Mexico, and Colorado). (Jensen et al., 2005).

In the Rocky Mountains, in particular in Wyoming, this technology started with Amoco's Lost Soldier and Wertz CO₂ miscible floods in the late 1980s. They are still in operation and they had had a substantial incremental oil production. For example, in the Tensleep reservoir at Lost Soldier the EOR has been estimated in 24 million barrels of oil, which represents 9.9% of the estimated OOIP (EPRI, 1999). The total EOR at Wertz as a percentage of OOIP is approximately the same, although incremental production is less substantial. In Colorado, Chevron-Texaco started the Rangely field, CO₂-based EOR since the mid-1980s with an additional recovery of 10.5% of the estimated OOIP. The project is still in operation.

Previous Fluid Flow Simulations at Teapot Dome:

Wadleigh (2005) performed an in-house simple reservoir simulation for RMOTC during the first planning stages of the CO₂-EOR pilot in the Tensleep. This simulation was done with GEM compositional simulator, which was modeled as a dual-porosity, dual permeability system. The equation of state (EOS) was modeled after laboratory oil-CO₂ tests.

The grid was 14x14x5 (980 blocks) and the layers had constant porosity and permeability values. From this model, 30 to 40% increase in oil recovery was predicted (Friedmann and Stamp, 2006). In the present study, we use the EOS from Wadleigh's work.

Gaviria (2005) compared fully compositional and pseudo-miscible black oil fluid models to test a CO₂-EOR and sequestration project at Teapot Dome. Based on quarter pattern simulations, he concluded that the pseudo-miscible model could not be used to represent the CO₂ injection process in the Tensleep, and that dual porosity models with variable fracture permeability provided a better reproduction of historic oil and water rates; although history matching in fully-compositional field-scale simulations could not be achieved.

CO₂ Process Mechanisms

CO₂ is effective for EOR operations due to its density and viscosity. At super critical conditions, its density approaches liquid density values, but its viscosity remains low.

CO₂ and oil are multiple-contact miscible, i.e. they require many contacts where components of the oil and CO₂ can transfer continuously. At the beginning, CO₂ condenses into the oil making it lighter. Usually, methane is driven out of it. Then, the higher components of the oil vaporize into the CO₂ rich phase, making it denser and more like the oil, therefore increasing its solubility in the oil. This process continues until the oil-enriched CO₂ cannot be distinguished from the CO₂-enriched oil and there is no interface between the CO₂ and the oil (one hydrocarbon phase) (Jarrel et al., 2002). Miscibility is a function of temperature and pressure, but in isothermal reservoirs, only pressure becomes important. The pressure at which miscibility occurs is called the minimum miscibility pressure (MMP).

Options for CO₂ Flood Design

There are five basic injection processes that combine continuous, alternating, and chase fluid injection schemes (Jarrell et al, 2002) (Figure 8):

- Continuous CO₂ injection without any other injected fluid. This is generally used in gravity-drainage reservoirs (CO₂ injected at top of reservoir).
- Continuous CO₂ chased with water, it is similar to the continuous CO₂ flood but with chase water at the end. The immiscible water displaces the mobile and miscible CO₂-oil mix. This design is more effective in reservoirs that are more homogeneous.
- Conventional alternating CO₂ and water, chased with water: Alternating cycles of equal volumes of CO₂ and Water (WAG) at a constant gas/water ratio (WAG ratio). At the end, a chase of continuous water is started. This approach is used in highly stratified heterogeneous reservoirs where the goal is to reduce the amount of CO₂ entering the high-velocity layers.
- Tapered alternating CO₂ and water (sometimes chased with water): CO₂ and water are injected in alternating unequal cycles, where the water cycles are always increasing. The purpose of this design is to reduce the purchase cost of CO₂ but it can also reduce near-term revenues.
- Alternating CO₂ and water chased with gas: This is similar to conventional WAG, but is then chased with a less expensive gas after the total volume of CO₂ is injected. It can also be combined with water chase in between or at the end of the gas chase. This option is good to avoid the use of water on water-sensitive lithologies.

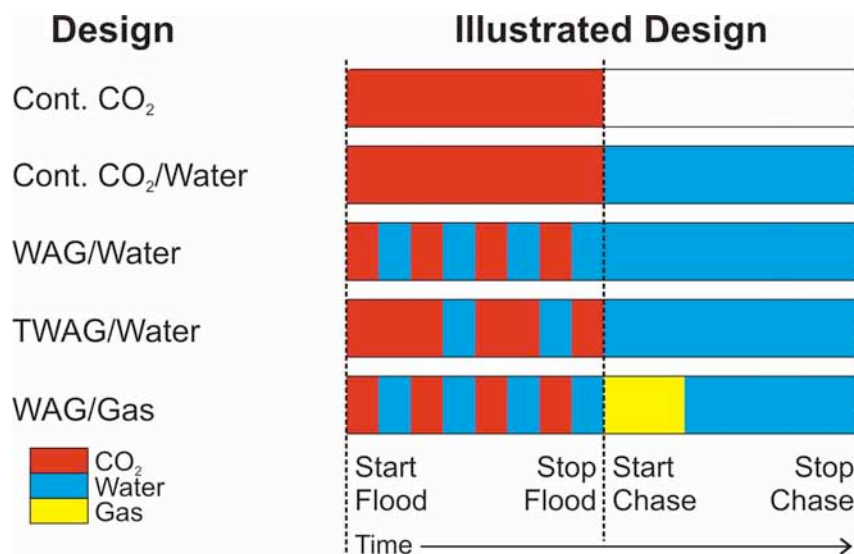


Figure 8: Illustration of typical CO₂ Flood designs. Cont. CO₂ = Continuous CO₂ flood; Cont. CO₂/Water = Continuous CO₂ flood chased with water; WAG/Water = Conventional alternating CO₂ and water chased with water; TWAG/Water = Tapered alternating CO₂ and water chased with water; WAG/Gas = Alternating CO₂ and water chased with gas (Modified from Jarrell et al, 2002).

Since the goal of our study is to co-optimize both oil recovery and CO₂ sequestration, all the options designed to reduce the amount of CO₂ to inject will not serve the objectives of this project.

With respect to the designs that use water to displace the oil-CO₂ mix, or that use it to control mobility of the CO₂, perhaps they would have been quite useful in this project. However, it has been shown that WAG schemes do not contribute to maximizing CO₂ storage, since some of the pore space is filled with water that otherwise could be occupied by CO₂ (Kovscek and Cakici, 2005). Similarly, the injection of water can have a negative effect in a thick highly permeable layer, since the injected CO₂ might flow to the top of the layer, while the water could gravitate to the bottom, seriously influencing mobility ratios. In addition, even if water has little effect on the phase equilibrium of CO₂/oil, CO₂ dissolution in water may prevent some of the CO₂ from contacting the oil and can affect the water formation volume factor and viscosity of water, ultimately reducing the concentration of CO₂ that can contact the oil (Jarrell et al, 2002).

Therefore, we try the well control process approach that shuts in wells with CO₂ breakthroughs and re-opens them after a certain condition is given (i.e. reservoir pressure increases or gas saturations decreases). This has been suggested as the most successful strategy for co-optimization in EOR and sequestrations projects (Kovscek and Cakici, 2005).

Fluid flow simulation

For our fluid flow simulations we use the Generalized Equation-of-State Model Compositional Reservoir Simulator (GEM, version 2007.15). We initially model the projected CO₂-EOR and sequestration pilot in the Tensleep using a continuous CO₂ flood pattern. The parameters of these simulations are described in the following sections.

Reservoir Data

The original oil in place of the Tensleep Fm. has been estimated as 3.8 million bbls (0.6 million m³) of oil and 11 MMscf (0.31 million m³) of natural gas. It is a lower gravity sulfurous oil of 32 °API, of this, more than 1.8 million bbl (0.29 million m³) have been produced together with more than 170 million bbl (27 million m³) of water. Reservoir pressure is 16.2 MPa (2350 psi) and reservoir temperature is 88 °C (190 °F). CO₂ swelling tests suggested that a Tensleep Sandstone CO₂ flood would be miscible or near miscible. These test showed excellent response to CO₂, including oil swelling of more than 20%, interfacial tension reduction of 90%, and five fold viscosity reduction (Friedmann and Stamp, 2006).

Water production rates indicate the influence of a strong aquifer that has maintained almost constant reservoir pressure during the history of the field. Therefore, water drive is considered as the primary producing mechanism in the reservoir (Gaviria, 2005, Friedmann and Stamp, 2006).

Reservoir Property	Value
Formation	Tensleep
Producing area	1.8 km ² (0.7 mi ²)
Average Depth	1670 m (5500 ft)
Gas-oil Contact	No present
Water-oil Contact	~100 m (350 ft) ss
Average Matrix Permeability of Main Producing Interval	~30 mD
Average Matrix Porosity of Main Producing Interval	~10%
Oil Gravity	31 °API
Reservoir Temperature	88 °C (190 °F)
Primary Production Mechanism	Water Drive
Original Reservoir Pressure	~16 MPa (2300 psi)
Bubble Point Pressure	0.3 - 0.5 MPa (40 - 70 psi)
Average Pressure at start of CO ₂ injection	~16 MPa (2300 psi)
Solution GOR at original pressure	4 SCF/BBL
Oil Viscosity at 60 °F and 42 psi	3.5 cp
Minimum Miscibility Pressure (MMP)	9 MPa (1300 psi)

Table 3: Basic reservoir and fluid data (modified from Gaviria, 2005).

Teapot Dome field had its first production well from First Wall Creek sandstone interval in 1908, but the development and exploration program at Teapot Dome started only on 1976. In 1996, a high number of wells were drilled, 27 of them targeted the Tensleep Fm. (Gaviria, 2005). Figure 9 shows the historical oil and water production from the Tensleep.

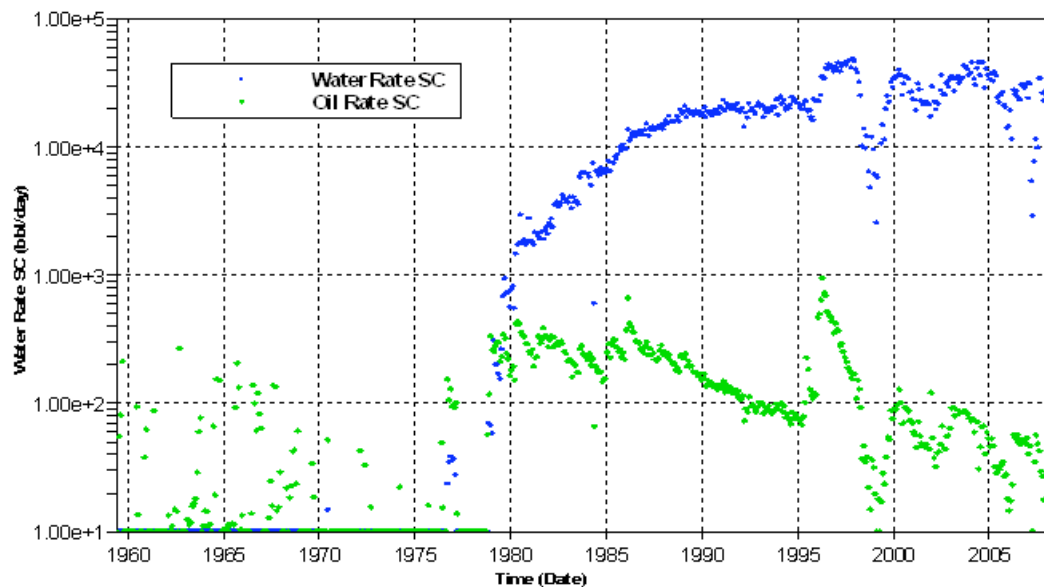


Figure 9: Historic oil and water production from Tensleep Fm. at Teapot Dome, from 1959 – 2008.

Simulation Set Up

MODEL

The chosen model to run in the simulator is the upscaled model from the program Gocad (see Figure 7). It has 8,976 blocks where 3,679 of them are active. Since the caprock is considered impermeable in these simulations, they are set up as Null.

MATRIX POROSITY AND PERMEABILITY

The matrix porosity and permeability distributions for the initial fluid flow simulations are one of the geostatistical realizations from Yin's (2005) facies analysis. In the sensitivity analysis of the final results we consider the variation that takes place due to different geostatistical realizations as well as from using porosity and permeability values measured in core samples in some of Section 10 wells.

FRACTURE POROSITY AND PERMEABILITY

We have very little control on fracture porosity and permeability, since no measurements have been done to get some insight in that respect. We use fracture porosity values from Wadleigh (2005) and tried different fracture permeability values during the history matching process. The final chosen values for the base case scenario (Table 21) are approximately one order of magnitude greater than the matrix permeability, which is a reasonable assumption for sedimentary rocks.

FRACTURE SPACING

We assign fracture spacing values (Table 21) based on the fracture characterization performed by Lorenz and Cooper (2004) in a core sample of well 48-X-28. They found an average of one fracture every foot of core. They defined fracture intensity as cumulative fracture height over core length. The average fracture intensity they found for all cored facies was 20 ft of fracture height per 100 ft of core, which is equivalent to the average fracture count. Therefore, we translated their fracture intensity values to determine the fracture spacing in each of the layers. We used the following values: for high porosity sandstones (such as BSand) 1 fracture every 10 ft.; in dolomitic sandstones (such as A or CSand), 1 fractures every 3 ft; and in heavily cemented intervals (such as the interdune deposits), 1 fracture per ft.

MATRIX RELATIVE PERMEABILITY

We use relative permeability curves determined by Gavira (2005), which were obtained from laboratory tests performed in four Tensleep samples. One sample from well 62-TPX-10 (sample A at 5443') and three samples from well 43-TPX-10 (sample B at 5486', sample C at 5492' and sample D at 5500'). The tests were performed using simulated reservoir brine and mineral oil with a viscosity of 30 cP. All samples showed similar composition, hard rock with fine to very fine grains; however, relative permeability experiments showed important differences in the endpoints. Initial water saturations (S_{wi}) were between 12.5% to 22.1% and residual oil saturations (S_{ro}) were

between 28.7% and 56.3% (Figure 10). The maximum oil relative permeability is 0.65 at connate water saturation ($S_{wc} = 15\%$). At 60% water saturation, the oil relative permeability is almost zero. As water saturation increases in the reservoir, the water relative permeability also increases, reaching a maximum value of 0.04 at 94% water saturation.

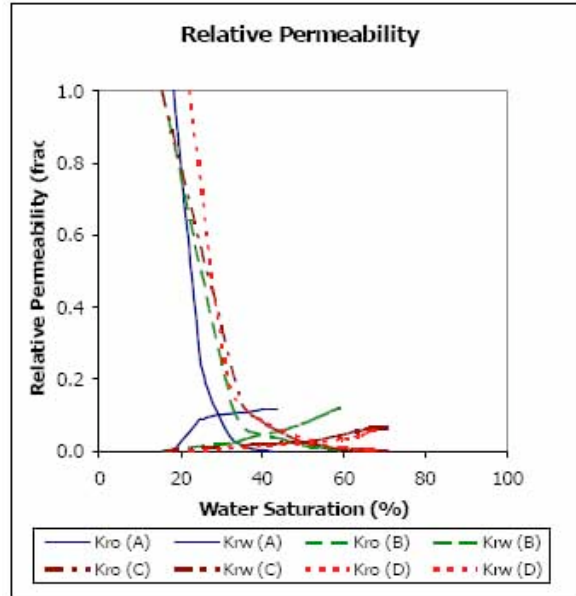


Figure 10: Water-oil relative permeability curves as a function of water saturation measured in four Tensleep samples (Gaviria, 2005).

During the process of history matching, we tried with different matrix relative permeability curves and the one estimated from sample A had the better performance. Figure 11 shows the relative permeability curves issued in our simulations. Hysteresis effect is not considered since this is a water-wet system (Jarrell et al., 2002).

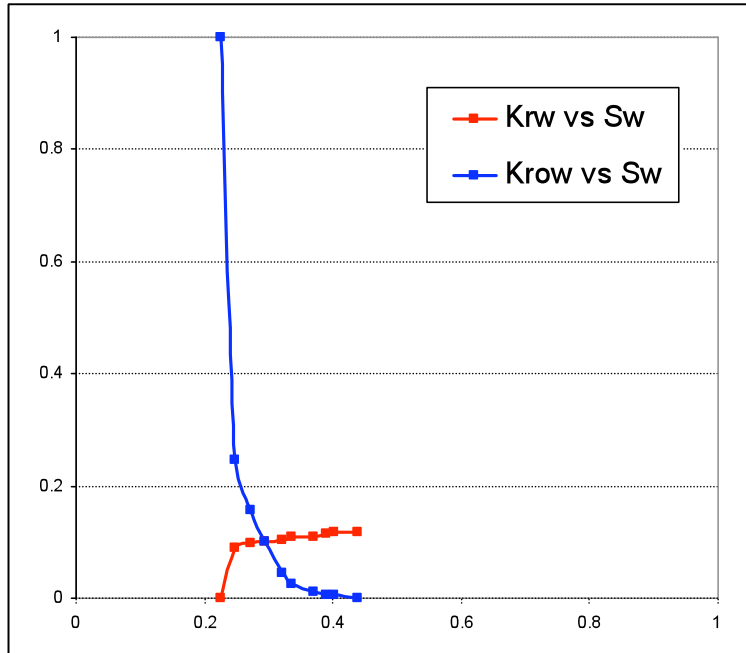


Figure 11a: Water-oil relative permeability curves, from Sample A, used in the base case scenario as a function of water saturation.

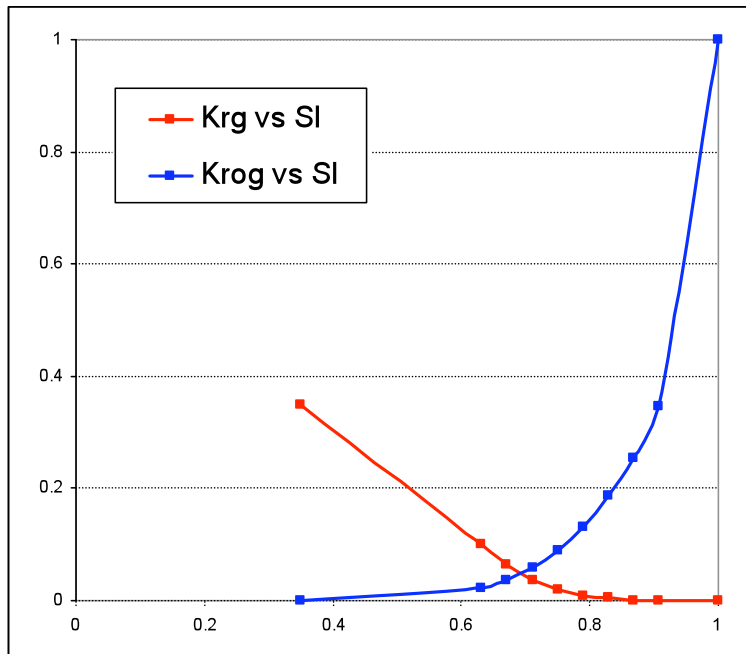


Figure 11b: Gas-oil relative permeability curves, from Sample A, used in the base case scenario as a function of water saturation.

GEM allows the use of Stone's first and second models, as modified by Aziz and Settari (1979), to obtain three phase relative permeability functions from two phase data (GEM 2007.11, Aziz and Settari, 1979). In our simulations, we used Stone's first model.

FRACTURE RELATIVE PERMEABILITY

It is normally assumed that fracture relative permeability curves are straight lines; although these might not be the best representations since fracture aperture changes due to compaction, mineralization, and other factors that affect fluid flow. Similarly, roughness, capillary pressure, and wettability influence fluid flow interference. If very high fracture permeability values are considered, then straight line relative permeability curves might be reasonable assumptions.

Since no data was available for fracture relative permeability curves, during the history matching process we tried several arbitrary curves, close to straight lines configuration. However, it was difficult to match the total produced water without having to use extreme values of fracture permeabilities. Since this is an unconstrained problem, where the only data available for history matching is historic productions of water and oil, we decided to use the same relative permeability curve for both matrix and fracture during the history matching stage. Later, we tested the sensitivity on the results to different fracture permeability curves during the prediction stage.

CO₂ RELATIVE PERMEABILITY

In the case of an immiscible flood (reservoir pressure < MMP) CO₂ will remain in a gas phase which is non-wetting compared to the oil and water. Therefore, usual three phase relative permeability models will apply to the oil, water, and gas relative permeabilities (Jerrell et al., 2002).

In the case of a miscible flood above the MMP the CO₂-rich phase is a solvent that has similar properties to the oil and initially follows the oil relative permeability curve. Here the solvent would be the intermediate wetting phase if the reservoir is oil-wet, and the solvent relative permeability will be affected by the reduction in pore space occupied by oil and water. Or eventually, if the solvent is less wet than water, water blocking could happen (Jerrell et al., 2002).

Since CO₂ is a multiple contact solvent, when injected, it leaves behind a small residual oil saturation that interferes with subsequent flows of solvent and causes the solvent (CO₂-rich phase) relative permeability to be lower than the oil relative permeability (Chopra et al., 1999, Jarrell et al, 2002). This effect was described for oil-wet or mixed-wet reservoirs.

In the case of a strong water-wet reservoir, oil is the intermediate wetting phase and the CO₂-rich phase is the non-wetting phase. Here the solvent relative permeability will be reduced by residual oil.

However, measurements of steady-state relative permeability for solvent, oil, and water for a water-wet dolomite showed that the solvent relative permeability was almost the same as the oil (Dria, et al, 1993, Jerrell et al., 2002).

In a case as the present one, a water-wet reservoir where no measurements of solvent relative permeability are available, we assume that CO₂ relative permeability is equal to oil relative permeability, as recommended by Jerrell et al. (2002).

CAPILLARY PRESSURE

The capillary pressure (Figure 12) we used in our simulation is an average curve obtained from three Tensleep samples (Gaviria, 2005). Two of them were extracted from well 56-TPX-10 (samples E at 5391' and F at 5400') and one from well 44-1-TPX-10 (sample G at 5538'). Capillary pressure curves in these three samples show low displacement pressure (approximately 1 psi), which suggests a good reservoir with very good sorting and big pore throats (Gaviria, 2005).

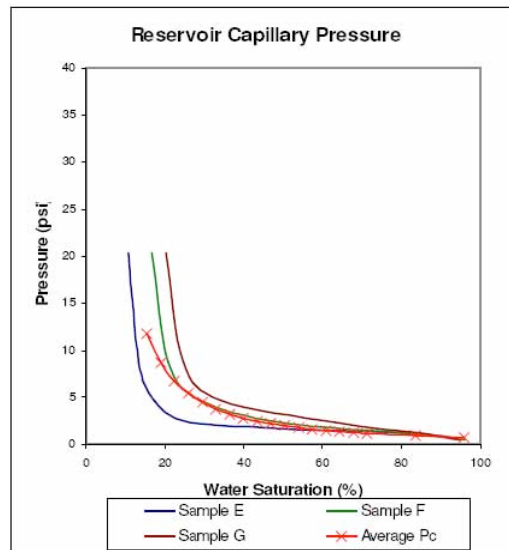


Figure 12: Laboratory and average capillary pressure curves from Gaviria (2005). The average curve (red line) is the one used in our simulations.

WETTABILITY

The wettability was determined by testing a core sample from well 62-TPX-10 (5418') at reservoir temperature (190 °F or 88 °C). Synthetic brine and crude oil were flushed through the sample. The analysis of the test results yielded a water-wet indicator of 0.402 versus oil-wet indicator of 0.033 (Gaviria, 2005). The water-wet indicator is a relationship between volume of oil displaced spontaneously when the oil saturated rock sample is submerged in synthetic brine, and the total oil volume displaced by injecting brine in the sample up to residual oil saturation conditions.

EQUATION OF STATE

Tensleep Formation oil samples were gathered from well 72-TPX-10 and analyzed by Hycal Energy Research Laboratories in 2004. The solvent impact of CO₂ was measured in the laboratory (Figure 13). The results indicate that the oil swells up to 30% as CO₂ contacts dissolves into oil and that the oil viscosity reduces to approximately one-third of its unprocessed reservoir condition, which is very supportive of an EOR application. They describe that the Tensleep oil is very low in light hydrocarbon components (methane and ethane), which could dilute injected CO₂ and detract from the solvent impact of a CO₂ project. Therefore, most CO₂ added to the reservoir is estimated to be dissolved into the oil phase for oil recovery improvement (Hycal, 2004).

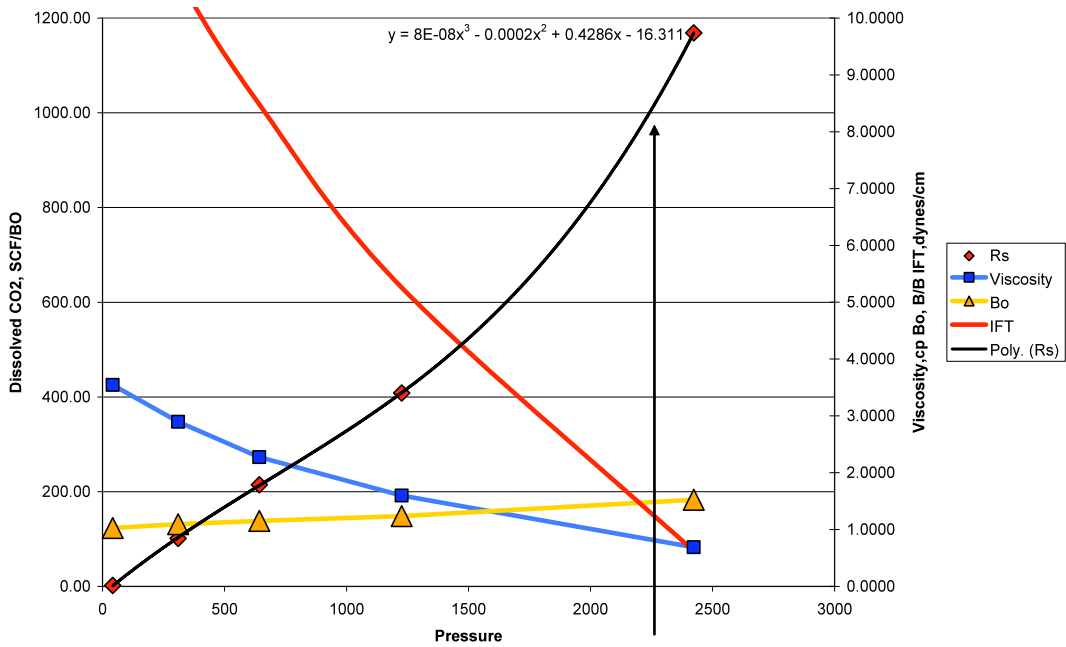


Figure 13: This plot shows laboratory measured increase in oil volume and reduced viscosity as the CO₂ in solution increased beyond the 1000 SCF/BO saturated condition at a reservoir pressure of 2336 psi (190 °F). Estimated IFT values are also plotted to illustrate the near-miscible condition that develops (Hycal, 2004).

Due to the low light-hydrocarbon composition, it was recommended to use a 6-component EOS described in Table 4 (Wadleigh, 2005).

Component	Mw (g/gmole)	Pc (atm)	Tc (°k)	Omega A	Omega B	Accentric Factor
C1 to N2	26.41700	35.146050	134.37819	0.457236	0.0777961	0.035733
CO2	44.01000	52.732012	304.20000	0.457236	0.0777961	0.225000
C2 to IC5	58.66350	31.282130	348.47099	0.457236	0.0777961	0.167679
C6 to C10	114.13127	27.586230	488.61317	0.457236	0.0777961	0.266720
C11 to C14	168.41008	27.276990	780.50523	0.457236	0.0777961	0.783660
C15 to C22	400.95423	12.589630	1018.30460	0.457236	0.0777961	1.012090

Table 4: Six-component EOS definition (Wadleigh, 2005).

AQUIFER

Initially, we used an analytical aquifer to represent the strong water influx in the reservoir. No information is available on the extension and strength of the real aquifer since pressure data have not been collected from the reservoir. Therefore, we used the Carter-Tracy aquifer model (Dake, 1978) connected at the bottom of the simulation grid with the following arbitrary parameters: 3000 ft thickness, 15% porosity, 500 mD permeability, and 30000 ft radius size. However, with only this analytical aquifer, it was extremely hard to match the total produced water during the history of the field.

Since most of the water flows through the fractures, it was necessary to add a fractured aquifer, C2Sand, at the bottom of the simulation grid (K. Aziz, personal communication, 2008). The fracture permeability of the C2Sand in the base case scenario is set to 4000 mD.

Initial Conditions

We ran the simulations in a dual porosity (dual permeability) mode.

The initial conditions were set to: reservoir pressure of 2370 psi at a reference depth of 200 ft sub-sea; reservoir temperature of 190 °F; oil-water contact at 350 ft sub-sea. The initial water saturation from the relative permeability curve was 0.225 and the initial oil saturation within the grid blocks was 0.775.

History Matching

History matching (HM) was performed using historical oil production rates as a constraint and comparing the simulation results to match historical water rates. The few available pressure data in this area consists of pre-production DST from wells 54-TpX-10, 56-TpX-10, and 44-1-TpX-10. Due to the very limited constrain in the system, we did

a HM on the production and water rates at a field scale. Therefore, sensitivity analysis of the simulation results will be essential.

SENSITIVITY ANALYSIS TO HM PARAMETERS:

During the trial and error process of history matching we tried different parameters such as grid size, fracture permeability (kF), fracture porosity (ϕF), fracture spacing (spF), initial oil saturation (S_{io}), capillary pressure (P_c) and relative permeability curves (k_{rel}). Below we present a series of sensitivity analysis that we conducted for these parameters along the process of HM. Each parameter is compared to one of three Scenarios, which were the best cases at the time of performing the sensitivity analysis. All these three scenarios were run with matrix porosity and matrix permeability from Yin’s facies analysis; relative permeability curves from Sample A (Figure 11); $S_w = 0.225$; oil-water contact = 350 ft sub-sea and the parameters shown in Table 5.

Scenario I								
	Fracture k [mD]			ϕ Frac [frac]	spFrac [ft]	Grid Size [ft]	Wells BHP [psi]	No. Layers
	I	J	K					
All Grid	500	100	500				28	11
MNKT	-	-	-	-	-	300x200x21		1
OPCH	-	-	-	-	-	300x200x63		1
ASand	100	50	100	0.5	3	300x200x27		1
BDolo				0.1	5	300x200x20		1
BSand_U				1	10	300x200x20		2
BSand_L				0.5	3	300x200x16		2
C1Dolo				0.1	5	300x200x2		1
C!Sand				0.5	2	300x200x45		1
C2Sand	1000	500	1000	1	2	300x200x168		1

Scenario II
All parameters are the same as in Scenario I except for BHP All Wells BHP [psi] = 500

Scenario III
All parameters are the same as in Scenario II but incorporating P_c

Table 5: Parameters of the three case scenarios used in the history matching sensitivity analysis.

Three tables are presented below with the parameters subjected to sensitivity analysis as well as the percentage comparison of total cumulative water produced with respect to the corresponding scenario.

GRID SIZE

Three cases were tested to see the effect of grid size. The first one divided each original cell size in 3 in the horizontal plane (I and J directions), therefore creating 9 new grid cells while conserving their thickness. Not a significant variation in total amount of water produced was observed there with respect to Scenario I. The other two cases explore the effect of dividing the vertical layers in 2 and 3, and here the impact was significantly more important.

Analyzed Parameter	Description	CW % difference to BC	Running time [hrs]
Grid size	Original grid size split in 3 (I & J directions)	92.99	10.78
	Original layers split in 2 (K direction)	42.64	2.76
	Original layers split in 3 (K direction)	26.86	5.26

Table 6: Sensitivity analysis on some HM parameters compared against Scenario I (see Table 5). Running time of Scenario I is 1.35 hours.

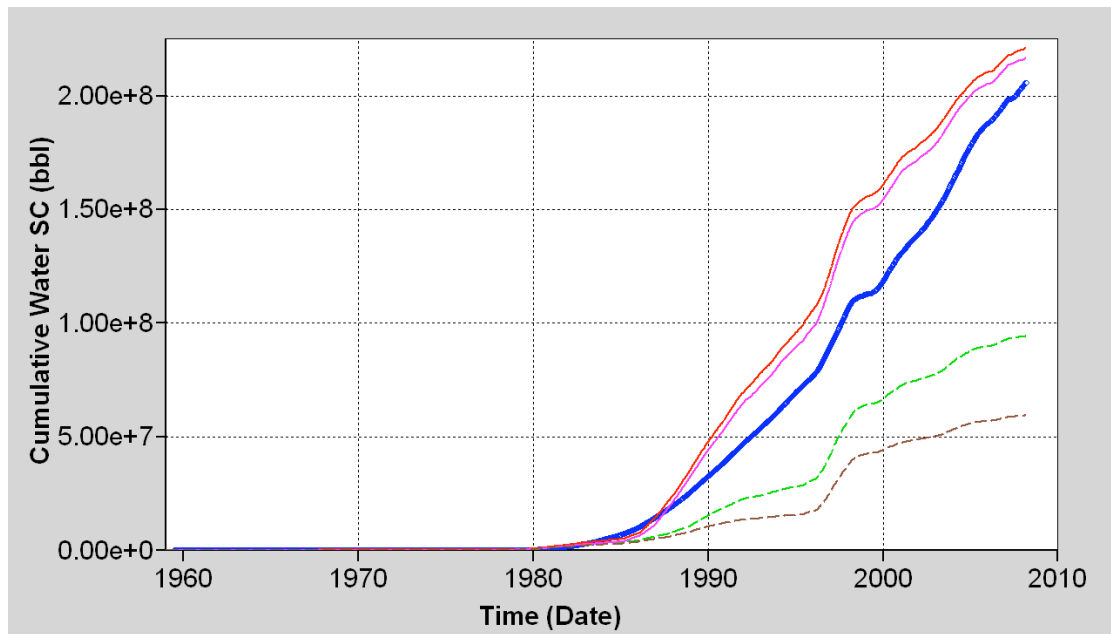


Figure 14: History matching sensitivity to grid size. Curves show cumulative water production [bbl] of Scenario I (red), horizontal refinement case (magenta), vertical refinement by 2 case (green), vertical refinement by 3 case (brown) and field data (blue).

The simulations done using the parameters shown in Table 4.7 are compared to the simulation of Scenario II (Table 5):

Analyzed Parameter	Description	CW % difference to BC	Running time [hrs]
Fracture Permeability (kF)	Double kF	120.17	1.58
	Half kF	65.16	1.25
Fracture Porosity (ϕF)	Double ϕF	62.23	1.04
	Half ϕF	114.55	1.91
Fracture Spacing (spF)	Double spF	99.62	1.31
	Half spF	98.98	1.33
Initial Water Saturation (S_w)	S_{i0} 0.22	86.54	1.34
	S_{i0} 0.23	111.35	1.45
Capillary Pressure (P_c)	including P_c	58.26	2.80

Table 7: Sensitivity analysis on some HM parameters compared against Scenario II (see Table 4.5). Running time of Base Case II is 1.08 hours.

FRACTURE PERMEABILITY & POROSITY

Fracture permeability and porosity are some of the parameters with greater impact in the model, since we are using a dual porosity-permeability simulator. Fracture permeability values can be obtained from the analysis of pressure build-up tests, where the permeabilities are adjusted to match production rates and bottom-hole pressures in the tested wells (Gaviria, 2005). Nevertheless, as mentioned before, there is no available pressure data in the Tensleep, therefore these are some of the most unconstrained parameters that we have to deal with and sensitivity analysis of the final results will be essential.

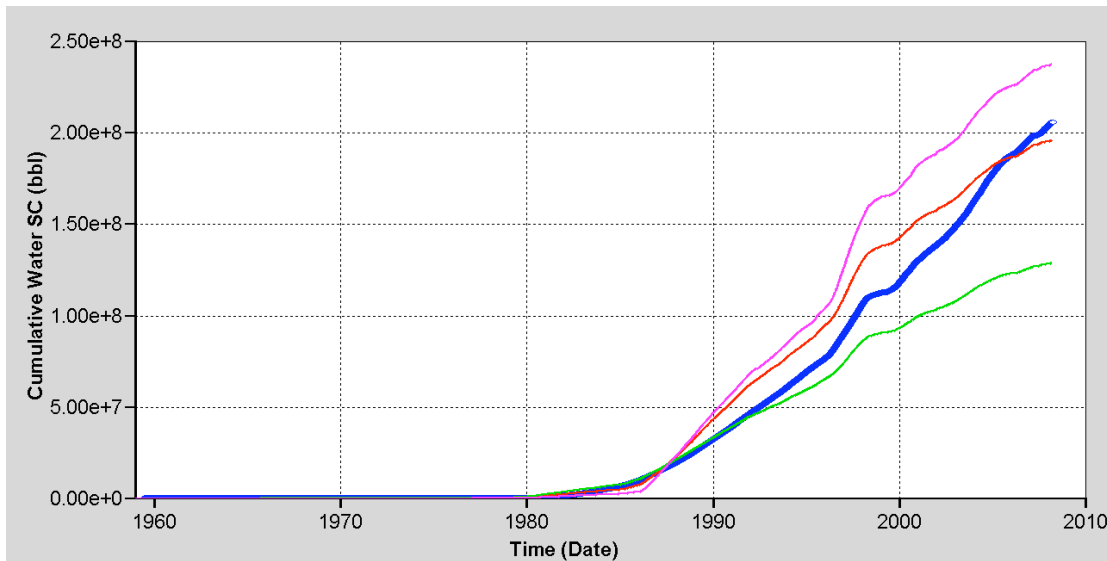


Figure 15: History matching sensitivity to Fracture Permeability. Curves showing cumulative water production [bbl] of Scenario II (red), double- kF case (magenta), half- kF case (green) and field data (blue).

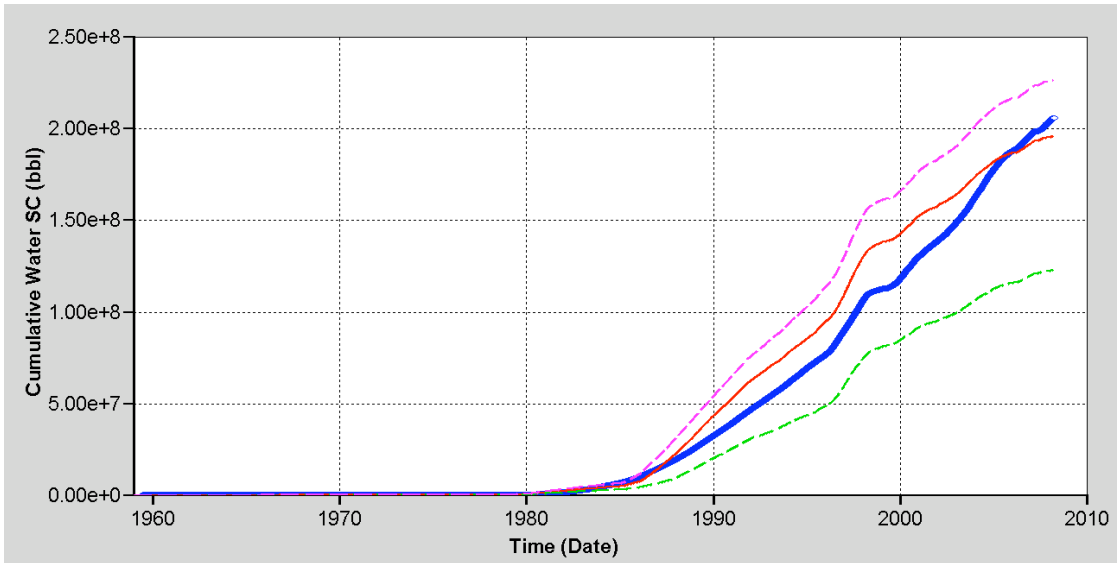


Figure 16: History matching sensitivity to Fracture Porosity. Curves showing cumulative water production [bbl] of Scenario II (red), double- ϕ F case (magenta), half- ϕ F case (green) and field data (blue).

FRACTURE SPACING

Fracture spacing is one of the parameters with less impact in the model.

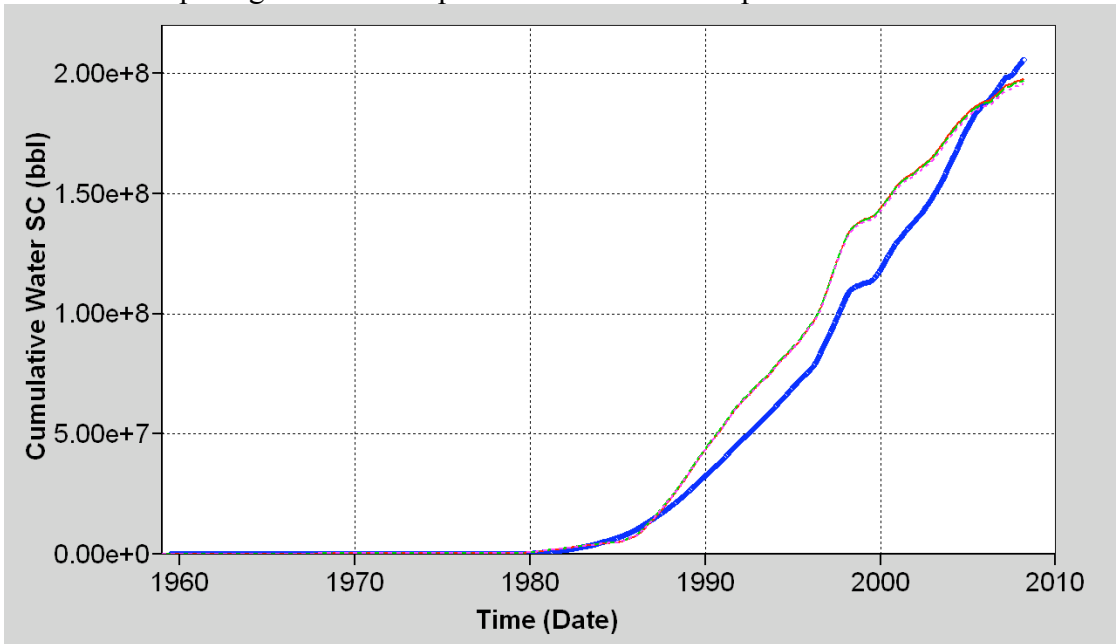


Figure 17: History matching sensitivity to Fracture Spacing. Curves showing cumulative water production [bbl] of Scenario II (red), double-spF case (green), half-spF case (magenta) and field data (blue).

INITIAL FLUID SATURATION

A fluid saturation of 0.225 initially over predicts water production and is also not in agreement with tests performed in five samples of the Tensleep, where water saturations were found in between 0.125 and 0.221.

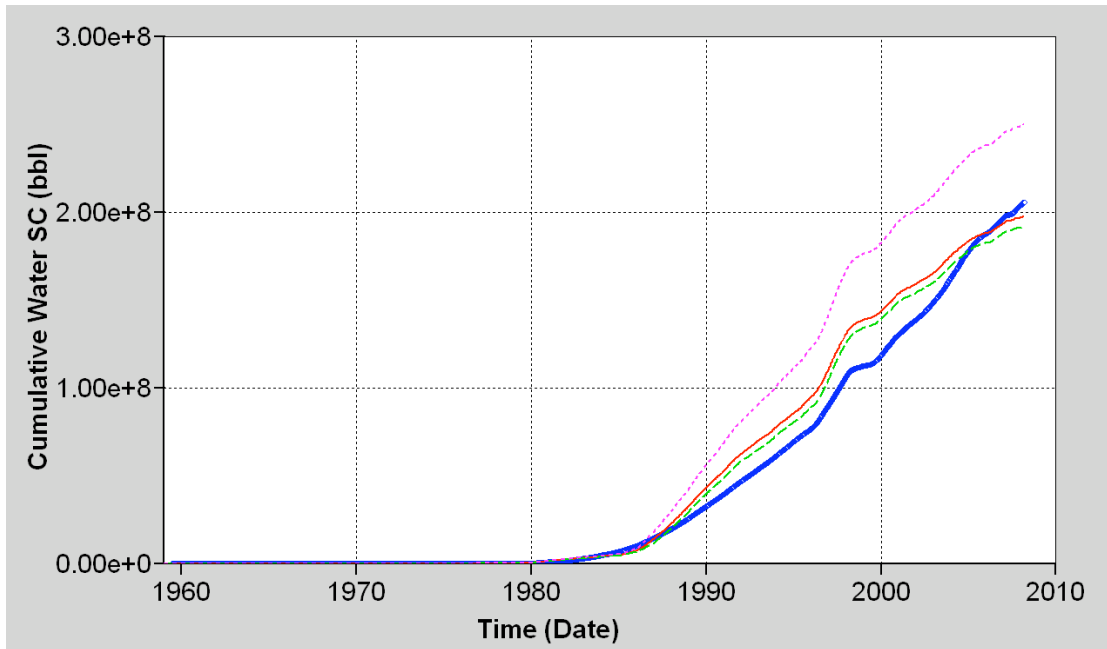


Figure 18: History matching sensitivity to Initial Water Saturation. Curves showing cumulative water production [bbl] of Scenario II where $S_w = 0.225$ case (red), $S_w = 0.23$ case (magenta), $S_w = 0.22$ case (green) and field data (blue)

CAPILLARY PRESSURE

Capillary pressure is an important parameter for low permeability, fractured sandstones, as most of the Tensleep Fm. (A. Kovscek, personal communication, 2008). Therefore, we performed a new history matching after incorporating P_c leading to Scenario III (see Table 5).

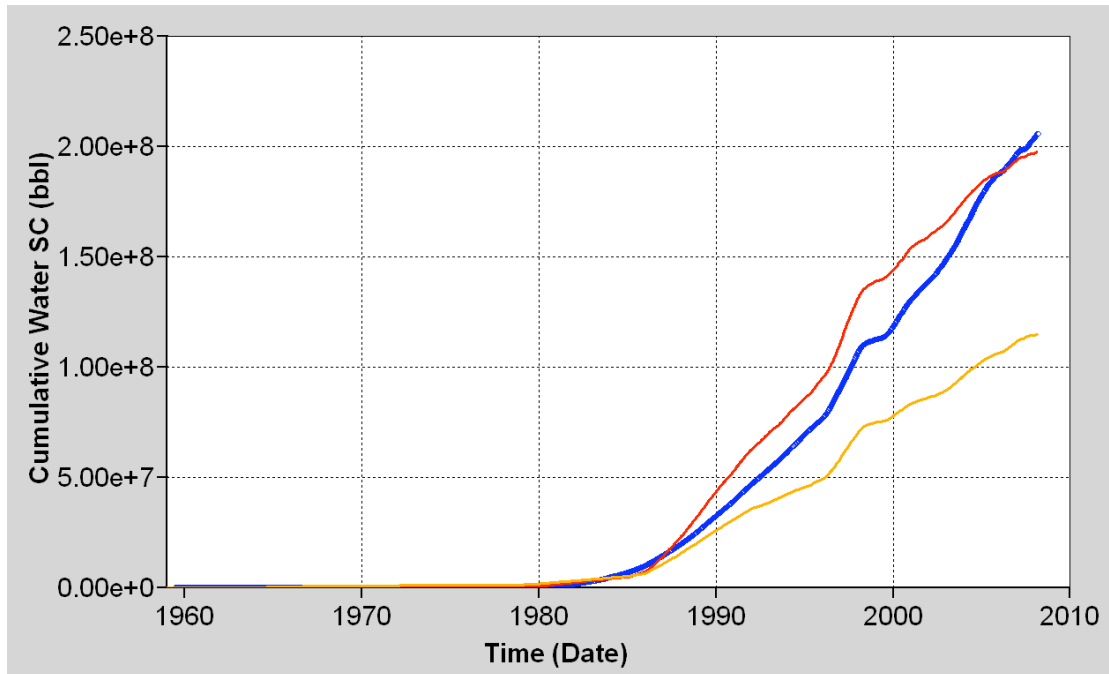


Figure 19: History matching sensitivity to P_c . Cumulative produced water in Scenario II (red); case including P_c (orange) and field data (blue).

RELATIVE PERMEABILITY CURVES

These simulations compare the impact of a different relative permeability curve instead of the one we used in the other two scenarios (Sample A). The new K_{rel} curve (Ave. K_{rel}) is the average of the relative permeability curves of 4 Tensleep samples, including Sample A (Gaviria, 2005). We also tested, the impact of a different initial water saturations $S_w = 0.15$, instead of $S_w = 0.225$ as in all other cases. These simulations were done after incorporating P_c so they are compared with Scenario III (see Table 5).

Analyzed Parameter	Description	CW % difference to BC	Running time [hrs]
K_{rel} Curves	Ave. K_{rel} & $S_w = 0.15$	3.69	2.34
	Ave. K_{rel} & $S_w = 0.225$	4.25	2.35

Table 8: Sensitivity analysis of relative permeability curves (K_{rel}) compared with Scenario III (see Table 5). Running time of Base Case III is 3.01 hours.

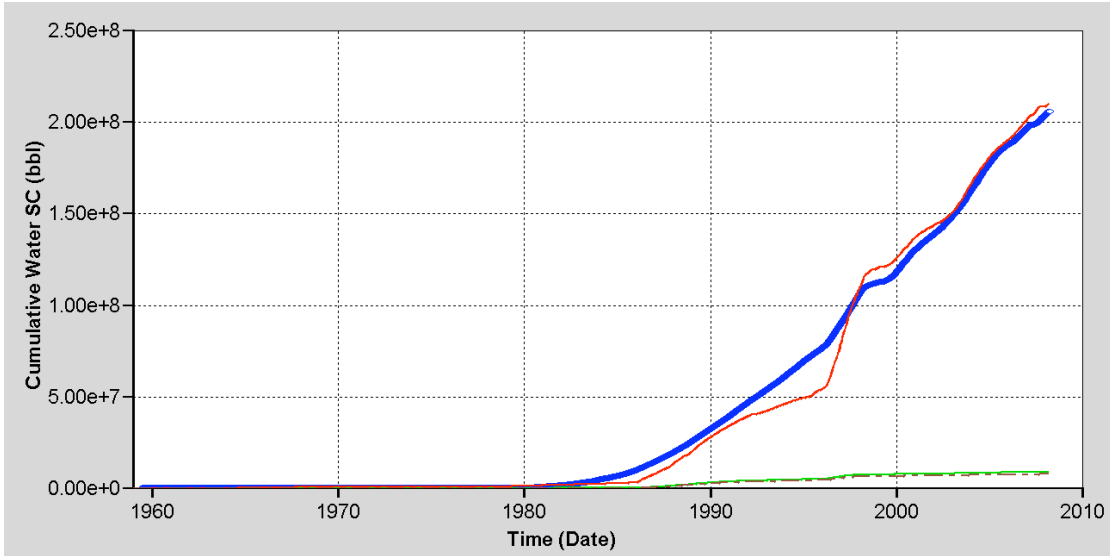


Figure 20: History matching sensitivity to relative permeability curves. Scenario III with K_{rel} from Sample A (red), case with K_{rel} from Gaviria, (2005) and $S_w = 0.225$ (green), case with K_{rel} from Gaviria, (2005) and $S_w = 0.15$ (brown) and field data (blue).

Base case Scenario:

After the HM process, the parameters for the base case scenario (BC) were chosen. The BC was run with matrix porosity and matrix permeability from Yin's facies analysis relative permeability curves from Sample A (Figure 11); $S_w = 0.225$ (even if initially over predicts water production); oil-water contact = 350 ft sub-sea and the parameters shown in Table 9.

	<i>k</i> Frac I [mD]	<i>k</i> Frac J [mD]	<i>k</i> Frac K [mD]	ϕ Frac	<i>sp</i> Frac - [ft]	Grid Size [ft]	No. of Layers
All Grid	800	400	800				11
MNKT	-	-	-	-	-	300x200x21	1
OPCH	-	-	-	-	-	300x200x63	1
ASand	200	100	200	0.5	3	300x200x27	1
BDolo				0.1	5	300x200x20	1
BSand_U				1	10	300x200x20	2
BSand_L				0.5	3	300x200x16	2
C1Dolo				0.1	5	300x200x2	1
C!Sand				0.5	2	300x200x45	1
C2Sand	4000	4000	4000	1	2	300x200x168	1

Table 9: Properties of the Base Case Scenario: Fracture permeability (*k*F) in I, J and K direction, Fracture Porosity (ϕ F), Fracture spacing (*sp*F), grid size of each layer and No. of layers per stratigraphic unit. *sp*F is the same in the I and J direction while it is 0 in the K direction is since there are no horizontal fractures in the model.

The simulation with the base case scenario produces a total of 1.96×10^8 bbl of water at surface conditions, which is 99.23% of the total cumulative water produced in the field. Figure 21 shows the comparison between the base case scenario and the field data, both for water rate (left) and water cut (right) at surface conditions. In Figure 22 cumulative water production is plotted.

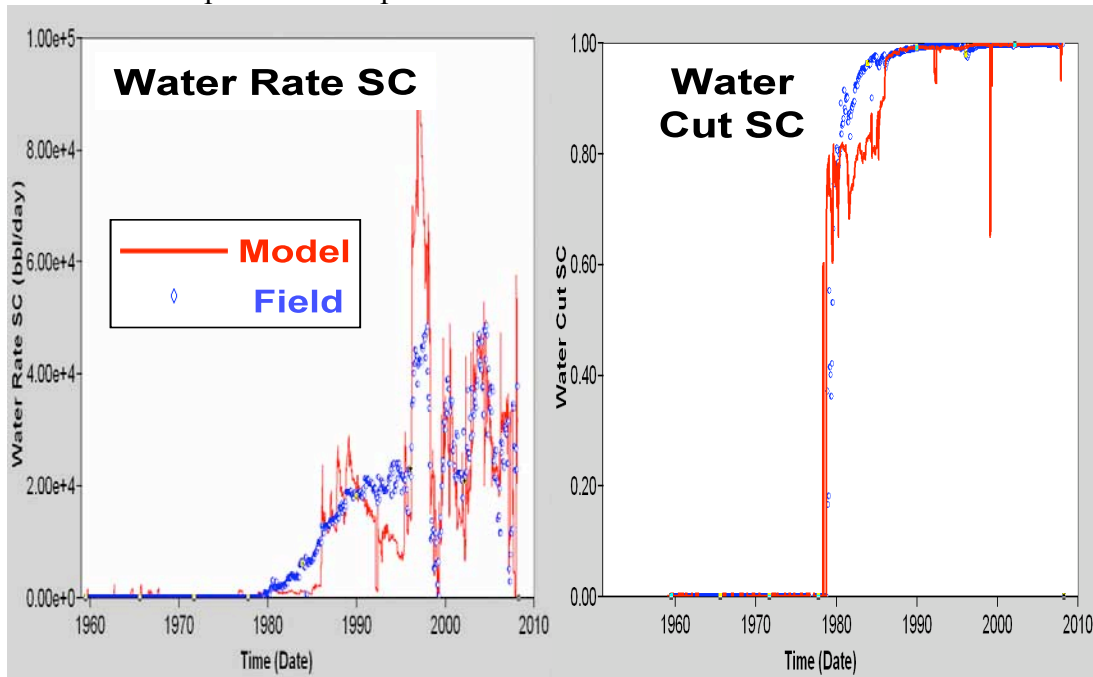


Figure 21: Comparison between the base case scenario (red) and the field data (blue). Left: water rates at surface condition; Right: water cut at surface conditions.

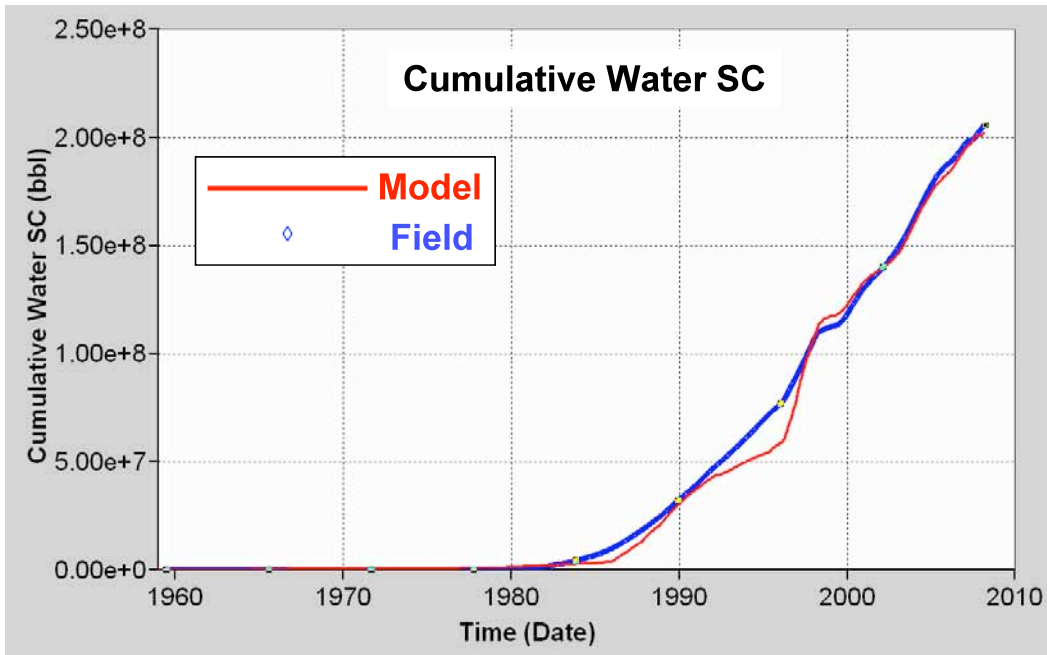


Figure 22: Cumulative water at surface conditions (SC) of base case scenario (red) and field data (blue). Total water produced with the Base Case simulation is 99.23% of total water produced in the field.

Pilot CO₂-EOR Simulations

The projected CO₂-EOR pilot will inject 52 tonnes/day or 1 MMcfd of supercritical CO₂ during six weeks.

The CO₂ will be injected in the crest of the anticline in a gravity stable flood where the objective is for the CO₂ to replace the water in the fractures (high in the structure). It is expected to interact with the oil in the adjacent matrix pores, reducing its viscosity and interfacial tension to be drained into the fracture system for production at wells lower in the structure (Friedmann and Stamp, 2006).

We simulated this scenario as well as three alternative ones and compared these predictions with the simulated primary production in the field, without any CO₂ injection. The simulated scenarios are listed below:

- Base Case: injection of 1 MMcfd during 6 weeks
- Case 2: injection of 1 MMcfd during 12 weeks
- Case 3: injection of 2 MMcfd during 6 weeks
- Case 4 injection of 2 MMcfd during 12 weeks
- Primary Production Case without CO₂ injection

At the time of starting our predictions, there are 10 producing wells, out of the 14 during the history matching process. Five of these wells are in an area of approximately ¼-mile radius around well 44-1-TpX-10, the injector well (Figure 26). These wells are the ones expected to respond during the injection pilot.

CO₂ is injected in the Upper BSand and the upper half of the Lower BSand (Figure 23). The results obtained from these simulations highlight several important factors that will affect the performance of the flood.

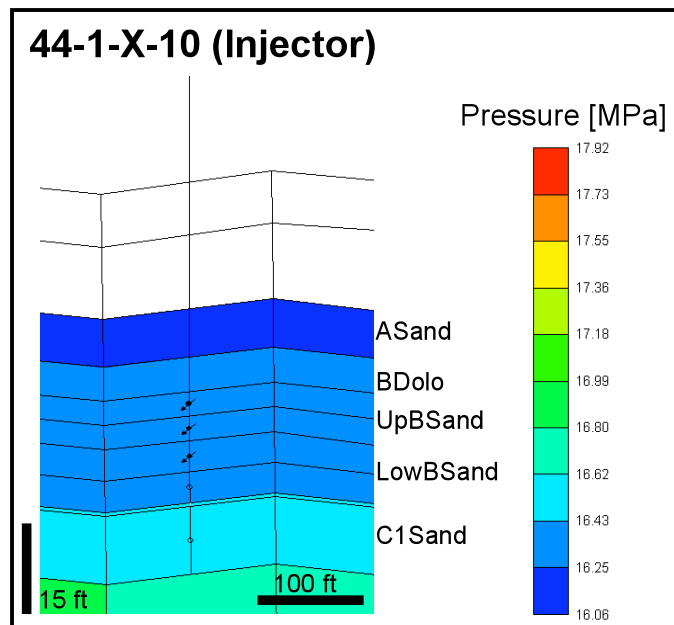


Figure 23: Injector set up. Perforations open in Upper BSand and upper layer of Lower BSand.

First, that CO₂ rapidly rises (2 -3 days) through the highly permeable fracture network (Figure 24, see cross section location on Figure 26) due to buoyancy forces. It accumulates in the fractures at the top layers (ASand and BDolo) almost without penetrating in the matrix pores. Contrary to the expected positive effect of a high permeable fracture network, this rapid buoyancy presents a problem, since the CO₂ migrates away of the main producing interval (BSand) where is being injected, and where it was expected to remain to allow enough time to be dissolved into the oil.

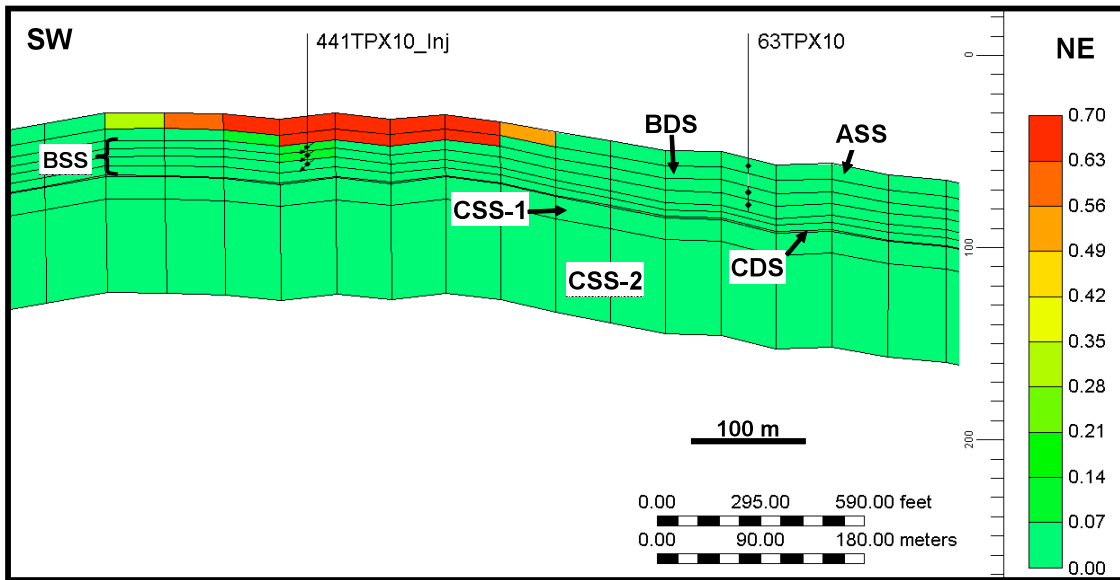


Figure 24: Gas Saturation in the fractures after 6 weeks of injection.

Another problem caused by these high permeability conduits is gas breakthrough times. In the base case simulation (Figure 25) CO₂ breakthrough occurs in well 55-TpX-10 at 16 days after the start of injection. Wells are set up to shut in when the CO₂ rate goes above 5000 cfd, since there are no gas recycling facilities in the field. This brings an important production loss.

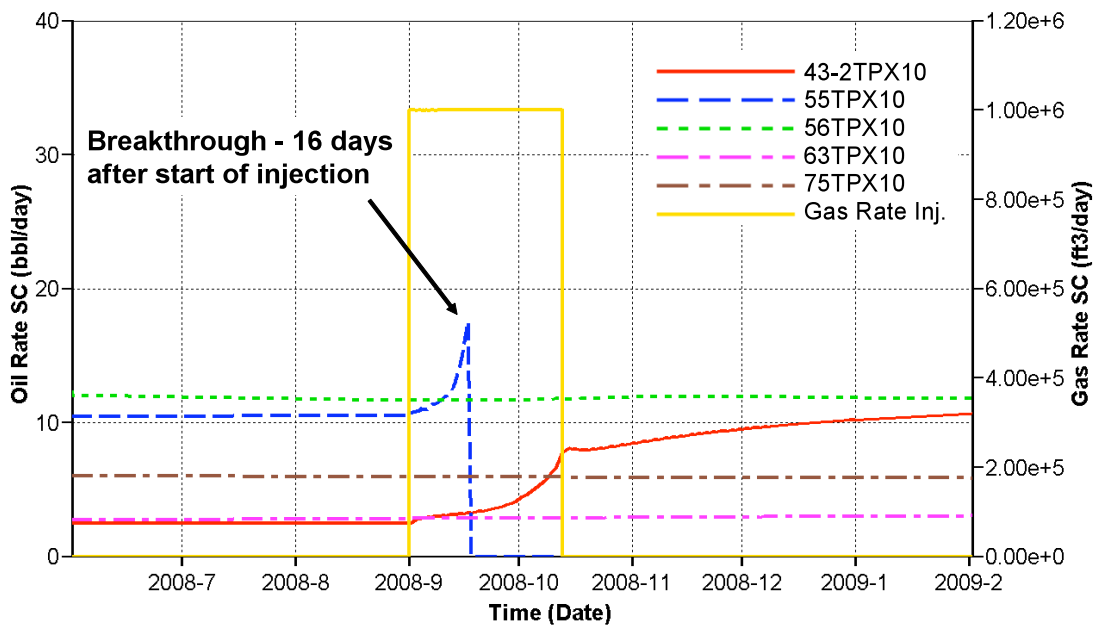


Figure 25: Base Case: Injection of 1 MMcf/d of CO₂ for 6 weeks. Oil rate at surface conditions is plotted for the 5 closest wells to the injector. Injected gas rate is plotted in yellow.

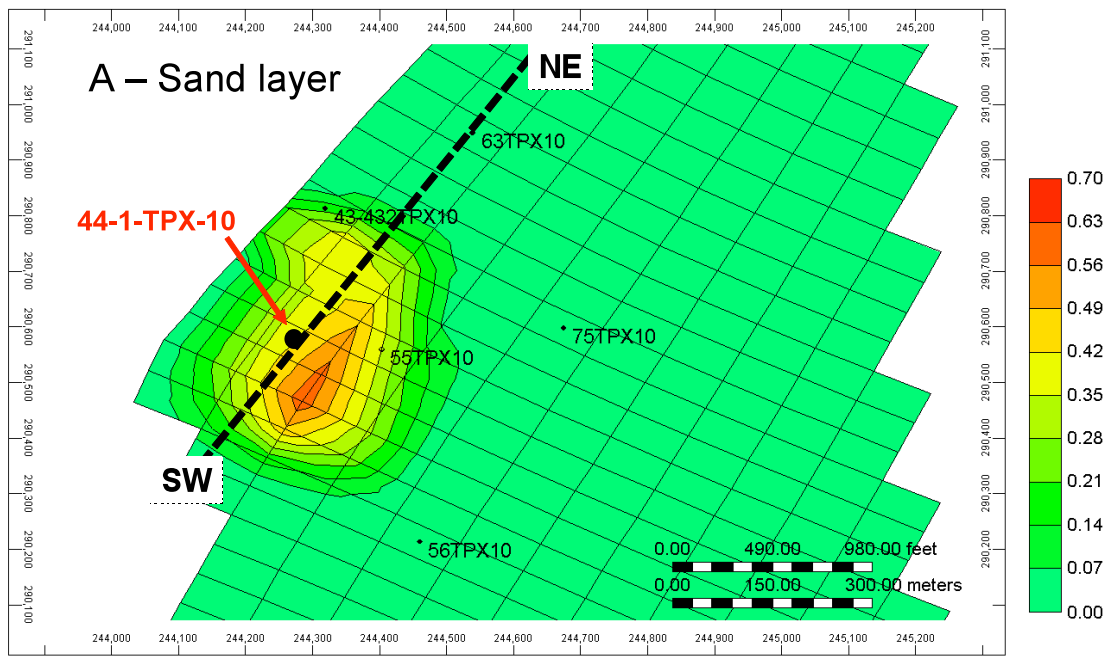


Figure 26: Base Case: Injection of 1 MMcf/d of CO₂ for 6 weeks: Gas Saturation in fractures after 6 weeks of injection in the uppermost layer, ASand.

In all the simulated cases, the gas saturation in the other layers is very small. Besides, in all of them, the pressure change is insignificant, less than 0.20 MPa. At this injection rates there is no risk to either fault stability or seal integrity. The maximum allowable injection pressure is set up to 22.75 MPa (3300 psi), below the estimated lower boundary for S_{hmin} . However, in none of the cases the injection pressure ever rose above 2520 psi.

Table 4 summarizes the incremental oil recovery at 6 weeks, 12 weeks and five years after the start of injection compared to the primary production scenario, without EOR (Figure 27). The reason why most of these cases recover less oil than in the primary production case is due to the closure of wells with high gas oil ratios (GOR). In the first two cases, the main producing well (55-TpX-10) is shut-in at 16 days after start of injection. In the last two cases the same well is shut-in at 9 days after the start of injection. In the last case, wells 56-TpX-10 and 43-2-TpX are also shut-in at 43 and 60 days respectively.

Injection period	Injected CO ₂	% of recovered oil after 6 weeks	% of recovered oil after 12 weeks	% of recovered oil after 5 years
6 weeks	1 MMcfd	90.7	90.1	90.1
12 weeks	1 MMcfd	82.3	97.5	99.4
6 weeks	2 MMcfd	77.3	99.1	99.0
12 weeks	2 MMcfd	72.6	103.5	63.1

Table 10: Percentage of oil recovered in each of the cases compared to primary injection without CO₂.

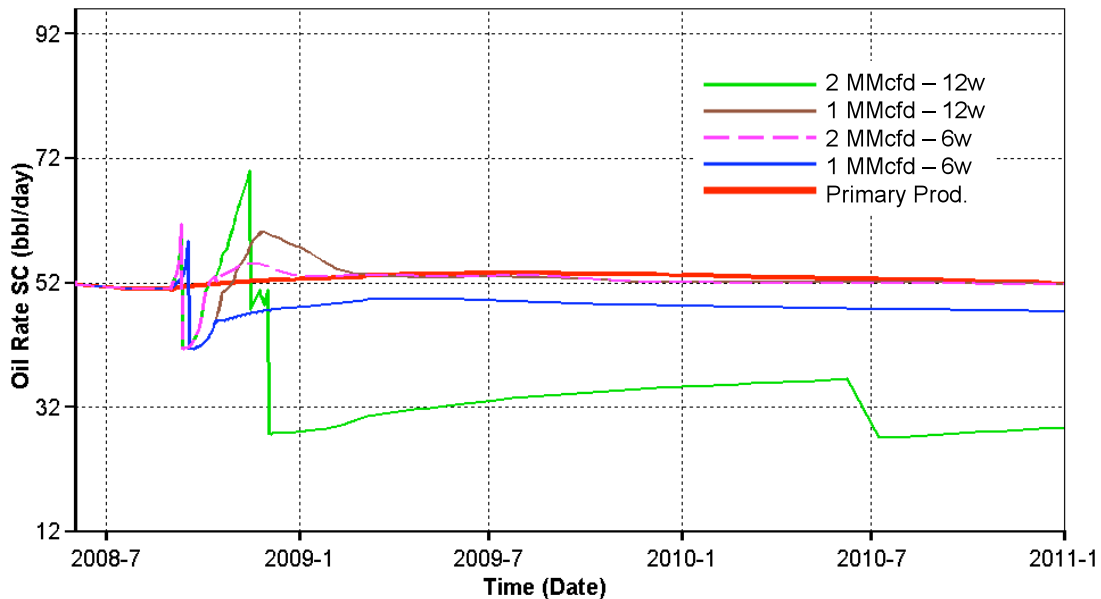


Figure 27: Oil rate in each of the cases as well as primary production without CO₂. Detail over a year and 2.5 years.

To solve the production loss due to well closure, a CO₂ mobility control strategy should be implemented. As mentioned WAG is not recommended for the co-optimization between EOR and storage that we want to achieve. Therefore, a well control strategy of re-opening shut-in wells after certain time (when gas saturation had lower around the well) is tested in the simulation described in the next paragraphs. With these schemes, oil recovery improved noticeably. Table 11 and Figure 28 illustrate these results.

Injection period	Injected CO ₂	% of recovered oil after 6 weeks	% of recovered oil after 12 weeks	% of recovered oil after 5 years
6 weeks	1 MMcfd	91.6	90.6	108.2
12 weeks	1 MMcfd	91.6	97.9	117.6
6 weeks	2 MMcfd	94.4	99.3	117.6
12 weeks	2 MMcfd	94.4	103.7	128.1

Table 11: Percentage of oil recovered in each of the cases with well control strategy compared to primary injection without CO₂.

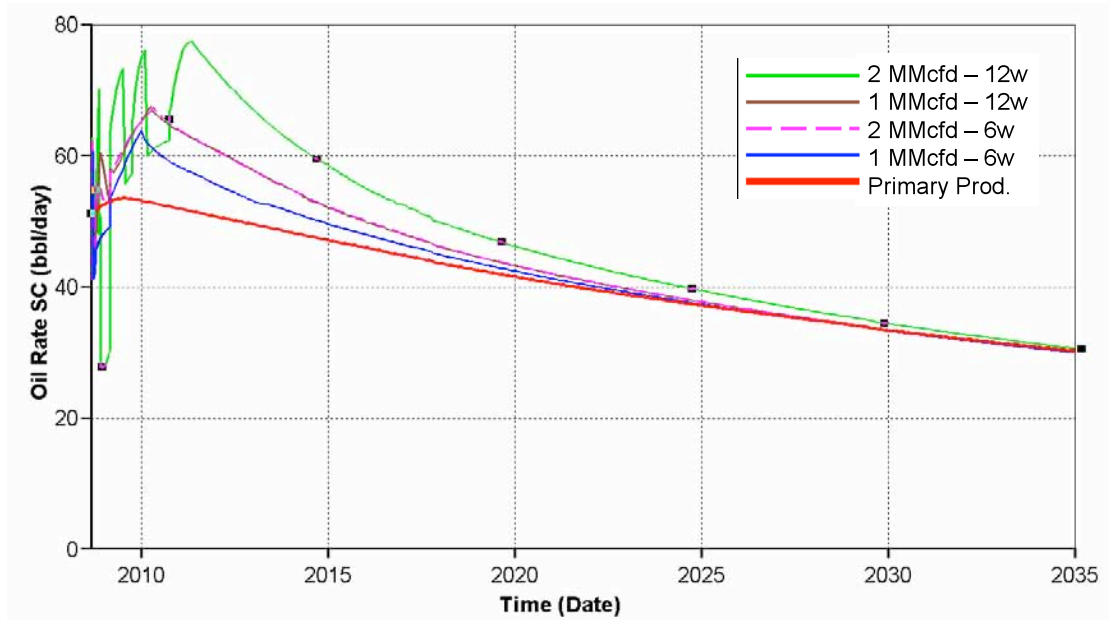


Figure 28: Incremental oil recovery of each of the cases, with a well control strategy. Compared to primary production without CO₂.

Sequestration potential

The pilot CO₂-EOR is an experiment designed to test the short term EOR potential of CO₂ in this formation. However, simulations with larger amounts of injected CO₂ and longer periods of injection time are necessary if we want to understand the storage capacity of the Tensleep, and to make an impact in sequestering CO₂.

To have an idea of how much 52 tonnes a day (1 MMcfd) represent, we can compare it to the total emissions from different power plants. For example the highest emitter US power plant produces 6.30×10^4 tonnes a day (1,217 MMcfd) and Shute Creek, the CO₂ source for this project produces 2.10×10^4 tonnes a day (388 MMcfd). Of course, the Tensleep Fm. in this context has a small trap that does not offer enough reservoir volume to sequester such high amounts of CO₂. But a more reasonable fit for this size of traps, is the 100 highest emitter power plant in the US, which produces 6.30×10^4 tonnes a day (6.3 MMcfd) (Center for Global Development, 2007).

US Power Plants	tonne/yr	tonne/day	MMcfd
Highest emitter: Scherer, GA	2.30×10^7	6.30×10^4	1,216.9
ExxonMobil's Shute Creek	7.33×10^6	2.01×10^4	388
100 highest emitter: Miami Fort, OH	6.86×10^6	1.88×10^4	6.3

Table 12: CO₂ emissions from power plants in the US (Center for Global Development, 2007)

TESTING STORAGE CAPACITY OF RESERVOIR

The capacity of the Tensleep was investigated through a series of simulations summarized in Table 13. The injection rates range from 1 MMcfd to 388 MMcfd.

The first tested example extends the Base Case Scenario (BC) injection (1 MMcfd) during 15 years, and after that, the simulation continued for 227 years (until year 2350). Similarly to the BC, the increase in pressure is also insignificant, no greater than 0.7 MPa. As mentioned before, the CO₂ rises rapidly through the fractures to the top layers, ASand and BDolo, and it takes almost a year for it to start saturating the fractures in the BSand. Gas saturation in the matrix starts being evident in the ASand approximately a year and three months after the start of injection, and it takes two years before it starts saturating the matrix of the BSand. By the end of the simulation, the gas saturations in matrix and fractures are almost equilibrated, although not completely.

We also simulated the injection of 6.3 (Miami Fort power plant scenario), 10, 15, 20, 58 (Shute Creek gas processing plant scenario), and 388 (Scherer power plant scenario) MMcfd for the same period of time. However, in all of these cases the maximum allowable bottom-hole injection pressure was reached much before the planned 15 years. The increase in pressure in all of them is approximately 7.4 MPa. The pressures did not go further up, since by the time these pressure were reached the injector BHP reached the limit, therefore, dramatically lowering the injection rates.

Injected CO ₂ [MMcfd]	Max. Pressure Increase [MPa]	Time of max. BHP reached	Total Injected CO ₂ [tonnes]
1	< 0.7	Not reached (injected 15 yrs)	2.97x10 ⁵
4.2 (in 2 wells)	< 0.7	3y & 5m (well 1) 2y & 5m (well 2)	3.85x10 ⁵
6.3	< 7.4	1 yr, 8 months	2.25x10 ⁵
10	< 7.4	8 months	1.60x10 ⁵
15	< 7.4	5 months	1.54x10 ⁵
20	< 7.4	3 months, 21 days	1.55x10 ⁵
58	< 7	1 month, 4 days	1.12x10 ⁵
388	< 7	4 days	1.37x10 ⁵

Table 13: Summary of simulations to test the Tensleep Fm. storage capacity, y = years, m = months.

In order to test the best scenario for a sequestration only project, we also simulated the injection of 1 MMcfd in 2 and 3 simultaneous injectors as well as 2 MMcfd in 1, 2 and 3 injectors (Figure 29). The best scenario sequesters $\sim 1.19 \times 10^6$ tonnes of CO₂ by injecting 2 MMcfd in only one well. This would correspond to a small power plant of $\sim 40,000$ tonnes per year.

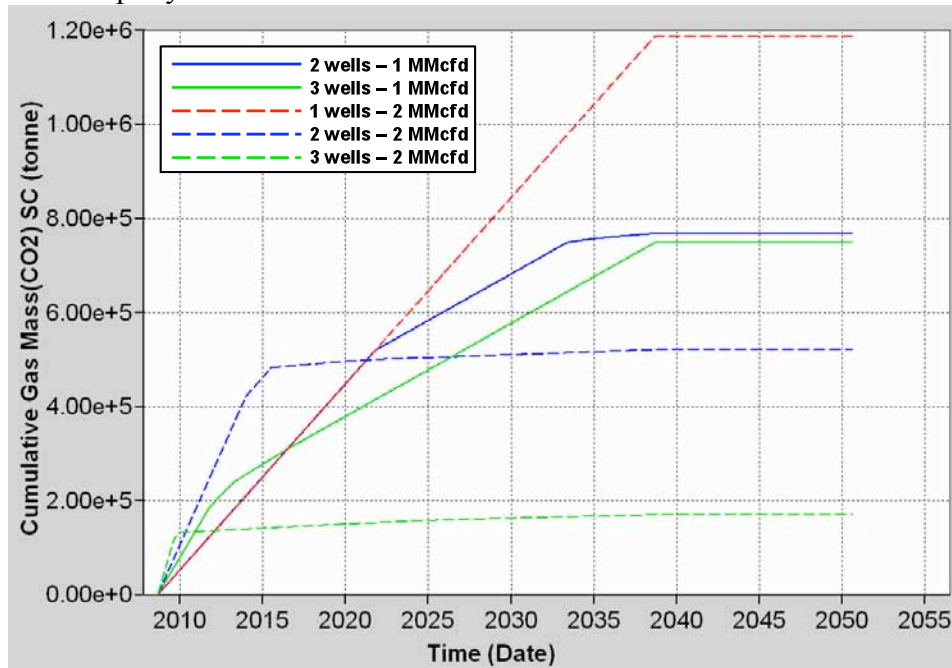


Figure 29: injection of 1 MMcfd in 2 and 3 simultaneous injectors (solid lines) as well as 2 MMcfd in 1, 2 and 3 injector (dashed lines).

Sensitivity Analysis of Pilot CO₂-EOR

The sensitivity analysis was performed with the Base Case scenario (BC) described in the previous section, but keeping the injection time for 5 years in order to be able to observe long term variations.

FRACTURE PERMEABILITY (kF)

Fracture permeability is, as expected, one of the factors that most affects the system. Sensibility cases were ran with 10, 4, 2, 0.5 and 0.25 times the permeability values of the BC scenario. Well control is not applied at this stage.

Although higher permeabilities improve oil recovery considerably in the short term, they also cause earlier gas breakthroughs and therefore, the loss of oil production from the shut-in wells. As a result, there is an overall decrease in oil recovery in the long term. However, if well control is extended beyond the pilot-injection period, these results might change. In the cases of lower permeability scenarios, even if the breakthrough times are delayed lower values of permeability also reduce the amount of recovered oil (Table 14).

kF factor	% Oil recovered after 6 weeks	% Oil recovered after 12 weeks	% Oil recovered after 5 years
10	350.3	265.0	96.0
4	192.3	183.0	100.7
2	131.3	125.3	107.1
0.5	87.7	82.5	72.8
0.25	81.0	69.0	61.7

Table 14: Effect of fracture permeability in oil recovery compared to the BC after 6 and 12 weeks, and 5 years of 1 MMcfd CO₂ injection.

FRACTURE POROSITY (øF)

Fracture porosity has almost zero impact in oil recovery during the first three month and has very little impact in later dates. Five different scenarios were compared with 10, 4, 2, 0.5 and 0.25 times the original fracture porosity used for the BC scenario. However, it does not appear to be a systematic correlation in between fracture porosity and produced oil, or in between fracture porosity and breakthrough times.

FRACTURE SPACING (SPF)

Five different scenarios were produced with 10, 4, 2, 0.5 and 0.25 times the original fracture spacing used for the BC. Table 15 summarizes the percentage oil recovery difference from the BC. The impact is less important than with fracture permeability, and

its effect is not obvious. The loss of production from some of the shut-in wells affects the incremental recovery more than the tested parameter it self.

<i>spF</i> factor	% Oil recovered after 6 weeks	% Oil recovered after 12 weeks	% Oil recovered after 5 years
10	125.1	132.2	102.0
4	106.2	112.3	112.0
2	101.0	103.5	102.8
0.5	100.5	100.0	102.2
0.25	103.1	99.1	96.4

Table 15: Effect of fracture spacing on oil recovered compared to the BC after 6 and 12 weeks, and 5 years of 1 MMcf/d CO₂ injection.

RELATIVE PERMEABILITY CURVES (K_{REL})

Four scenarios were created to test the effect of the relative permeability curves in the model compared to the BC. In the base case scenario we use the same *K_{rel}* for the matrix than the one used in the history matching process while the fracture *K_{rel}* have the same saturations than the matrix, but with the typical X shape of fracture *K_{rel}*. The sensitivity scenarios include:

1. Fracture *K_{rel}* of BC is used for both the matrix and the fracture system.
2. Matrix *K_{rel}* is used for both matrix and fractures, as it was the case during the history matching process (Figure 11).
3. Same matrix *K_{rel}* than in the BC and X shaped fracture *K_{rel}* with 0 initial water saturation.
4. Average *K_{rel}* curves described by Gaviria (2005) (Figure 30).

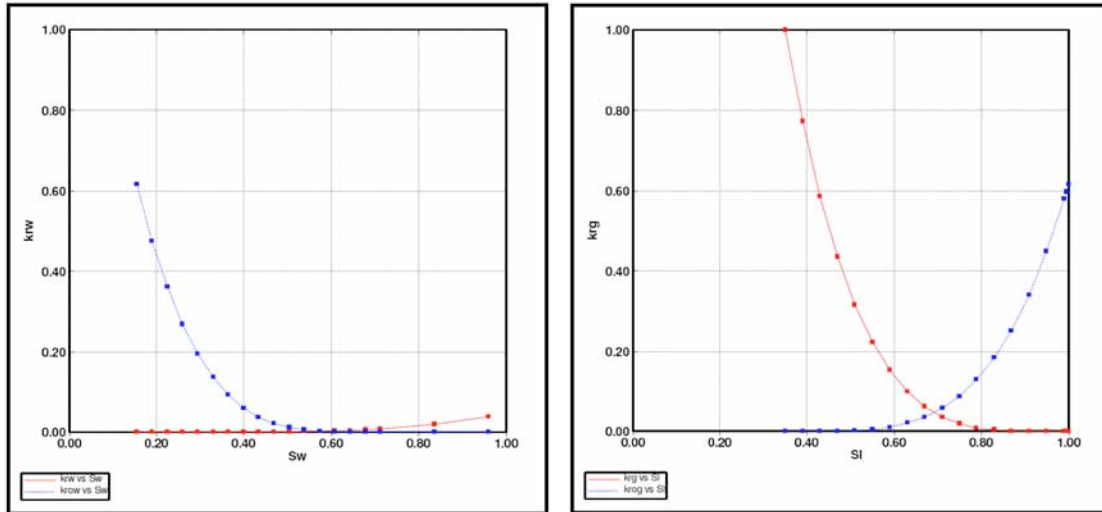


Figure 30: Average *K_{rel}* curves described by Gaviria (2005). Water-oil relative permeability curves (left); Gas-oil relative permeability curves (right).

The difference in oil recovered from all the scenarios is insignificant during the pilot stage, and it becomes slightly noticeable in later dates; but it is still not significant in terms of cumulative oil recovery. Table 4.16 shows the comparison of recovered oil. Scenarios 1, 2, and 3 are almost equal during the first year injection and they are very similar to the BC (red line). The most notorious difference is with the average K_{rel} .

K_{rel}	% Oil recovery after 6 weeks	% Oil recovery after 12 weeks	% Oil recovery after 5 years
Case 1	100	100	97.3
Case 2	100	100	97.3
Case 3	100	100	97.3
Case 4	105.6	111.1	102.5

Table 16: Effect of K_{rel} curves on oil recovered compared to the BC after 6 weeks, 12 weeks, and 5 years of 1 MMcfd CO₂ injection.

MATRIX POROSITY & PERMEABILITY

Several scenarios were tested with different distributions of porosity and permeability. In all of them there was little variation during the initial stages of injection in the amount of oil recovered. Figure 31 shows an example of it, where after the first month the results start varying due to the different timing of gas breakthrough.

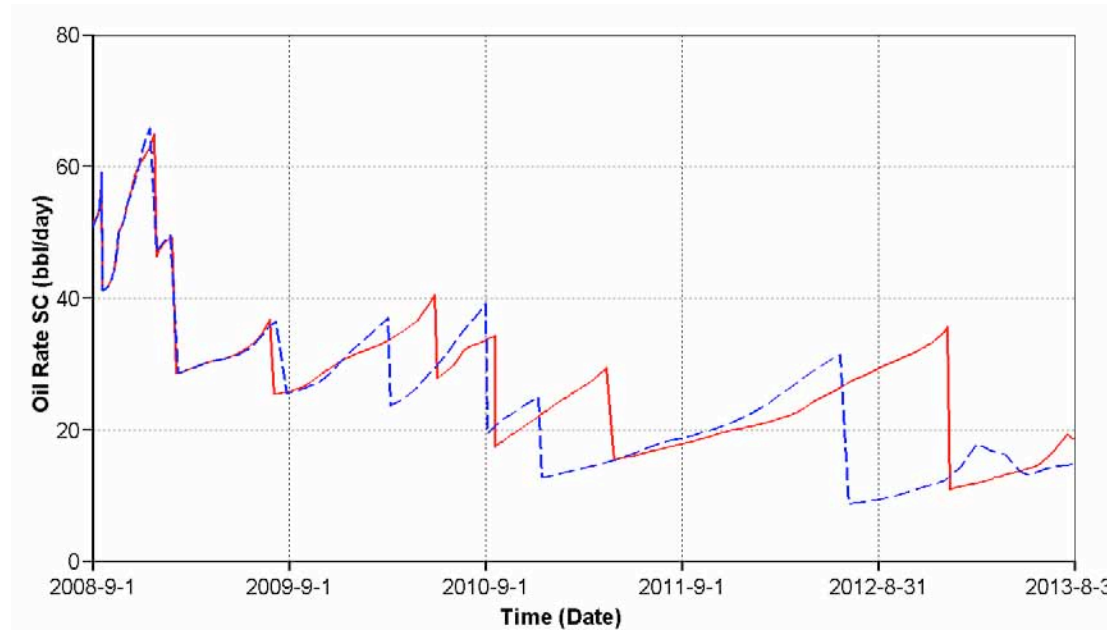


Figure 31: Oil rate comparison between BC (red line) and a case run with a different matrix porosity and permeability distribution.

GRID SIZE

As with the other tested parameters, grid size changes the CO₂ breakthrough times in different wells, complicating the possibility to make any valid quantitative observations on how this refinements influence the system. For example, in the case in which the grid was refined horizontally (I and J directions) by a factor of three, it is possible to observe an increment in oil rates at the beginning of the injection. Cumulative oil after 6 weeks of injection was 167.2% of the BC cumulative oil, while in 12 weeks of injection it was 129.8%. However, breakthrough times diminished, causing the closure of wells sooner than in the BC, and after 5 years of injection the cumulative oil was 80.7% of the BC one.

However, it was clear from the simulations that in order to be able to resolve the CO₂ plume geometry we need a more refined grid both vertically and horizontally.

Sensitivity Analysis of Pilot CO₂-EOR Without Gas Constraints

From the sensitivity analysis described in the previous section, it is extremely difficult to drive any conclusion because the tested parameters greatly affect gas breakthrough times, which also affects the resultant oil production and complicates the direct comparison among scenarios. The imposed constraint in a well is to shut-in when

gas rate is higher than 5000 cfd. Therefore, when the first well shuts-in at different times in each scenario, the distribution of the CO₂ and the conditions of the simulation change.

For these reasons, a different approach for the sensitivity analysis was taken; the wells were allowed to produce without any gas production constraints. This permits to analyze the effect of each tested parameter in the system. Nevertheless, the resultant production is not the real production expected in the field and therefore, this sensitivity analysis does not provide a range of possible outcomes regarding oil production and CO₂ storage.

The sensitivity simulations described in the previous sections were re-run under these new conditions.

Among all the parameters tested, fracture permeability is, as expected, one of the factors that greater affects the system. Where in general, more oil is recovered with higher fracture permeabilities (Figure 32). The other parameter that has a high influence on the results is the relative permeability (Figure 33). On the other hand, fracture spacing and specially fracture porosity are the factors that less influence have on the results (Figures 34 and 35).

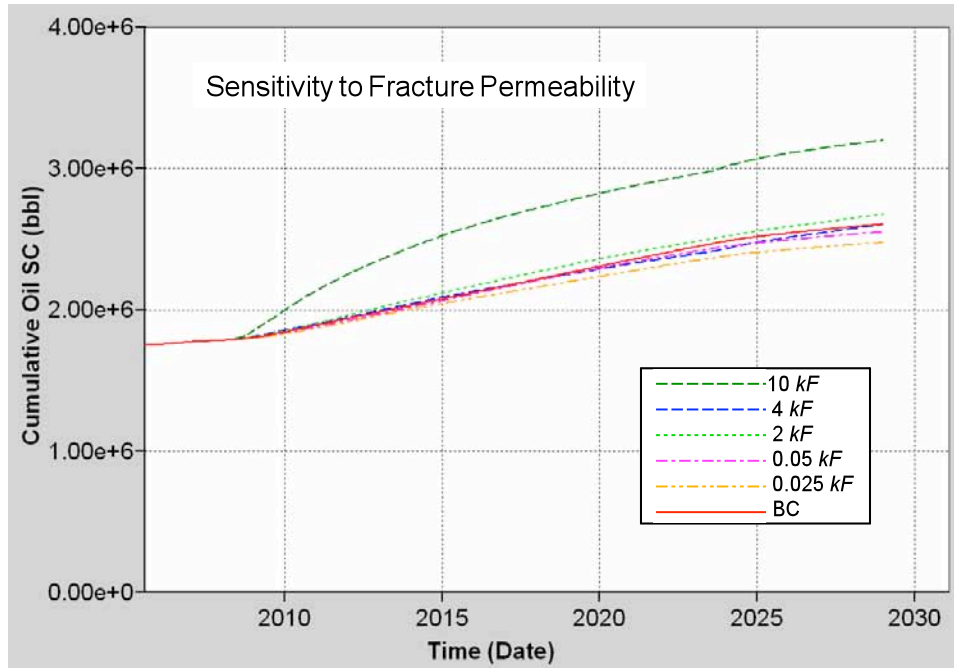


Figure 32: Cumulative Oil comparison between BC (red line) and 10, 4, 2, 0.5, and 0.25 times the original fracture permeability.

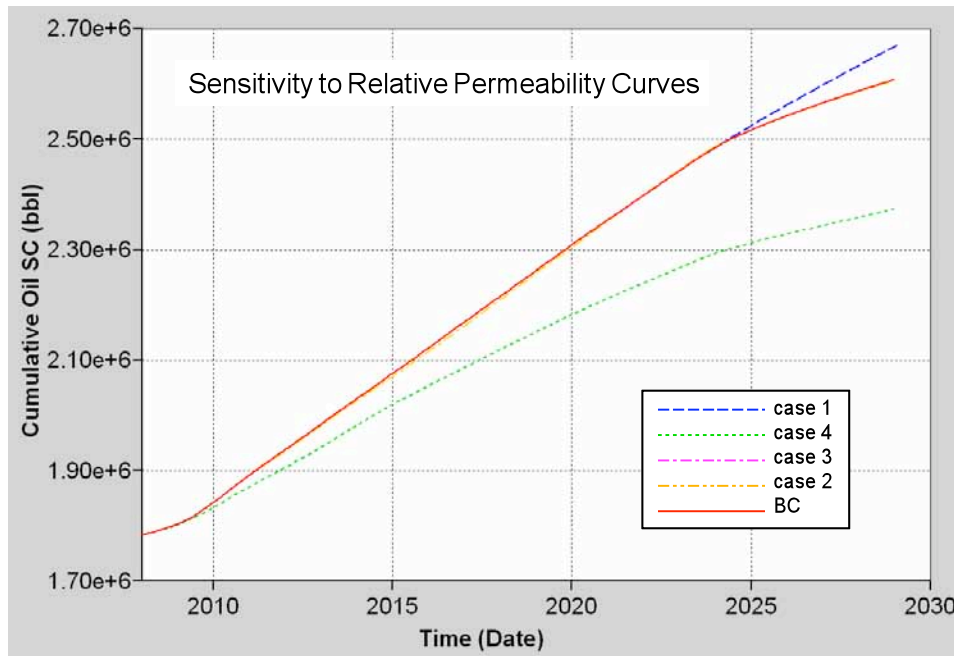


Figure 33: Cumulative Oil comparison between BC (red line) and four different relative permeability curves: case 1 - Fracture Krel of BC is used for both the matrix and the fracture system; case 2 - Matrix Krel is used for both matrix and fractures, as it was the case during the history matching process (Figure 11); case 3 - Same matrix Krel than in the BC and X shaped fracture Krel with 0 initial water saturation; case 4 - Average Krel curves described by Gaviria (2005) (Figure 30).

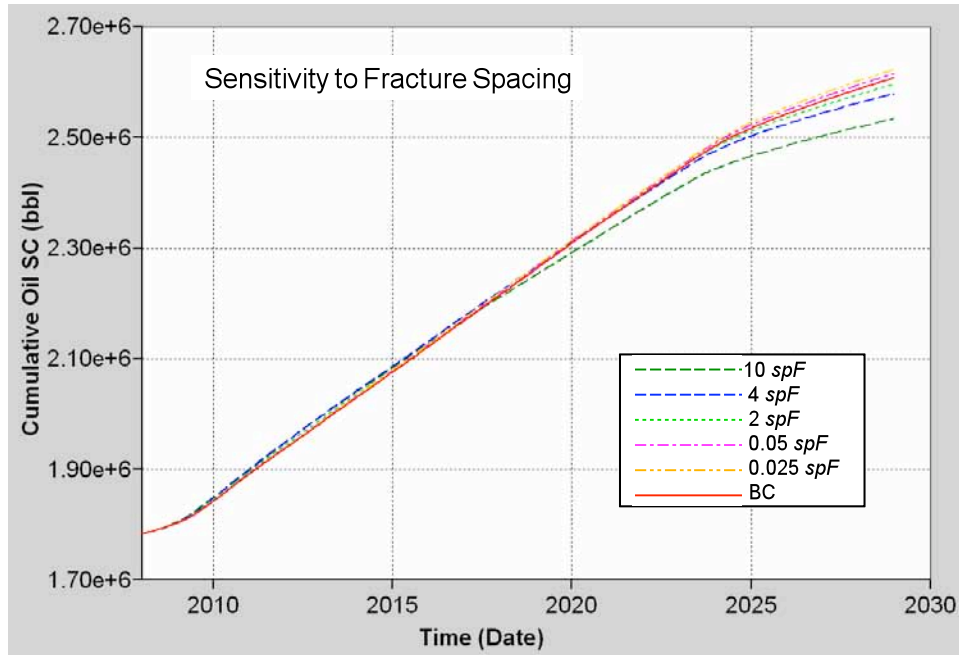


Figure 34: Cumulative Oil comparison between BC (red line) and 10, 4, 2, 0.5, and 0.25 times the original fracture spacing.

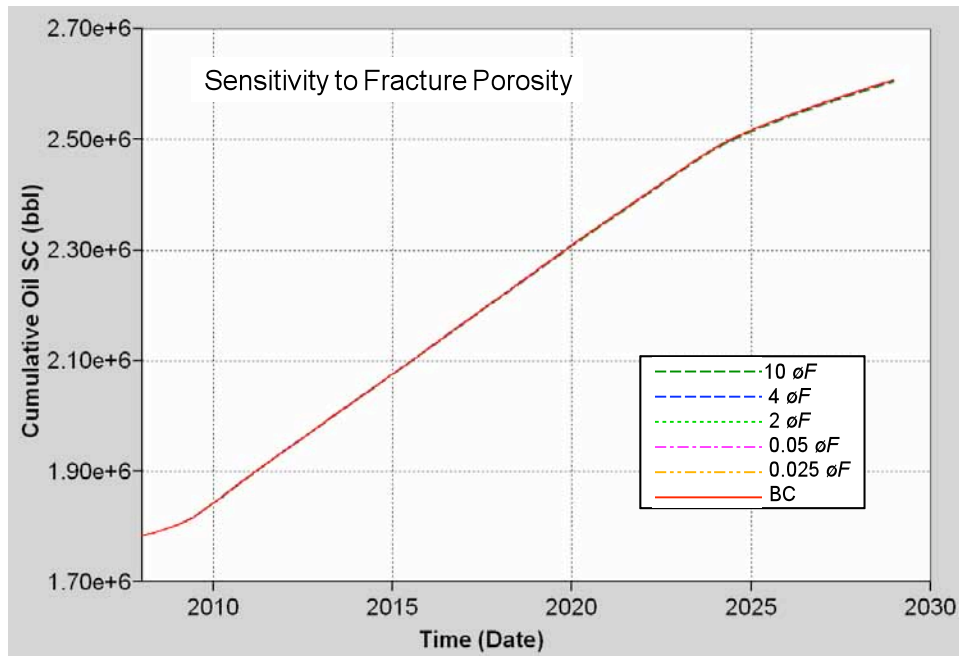


Figure 35: Cumulative Oil comparison between BC (red line) and 10, 4, 2, 0.5, and 0.25 times the original fracture porosity.

We also run the new sensitivity analysis on matrix porosity and permeability. We first tested the values obtained from Yin’s lithofacies analysis keeping the same matrix porosity than in the BC and using 10 different matrix porosity realizations from the geostatistical analysis (Figure 36). Similarly, we tested 10 different matrix porosity realizations keeping the same in matrix permeability used in the BC case (Figure 37). We

repeated this analysis using the matrix porosity and permeability values obtained from core samples (Figures 38 and 39).

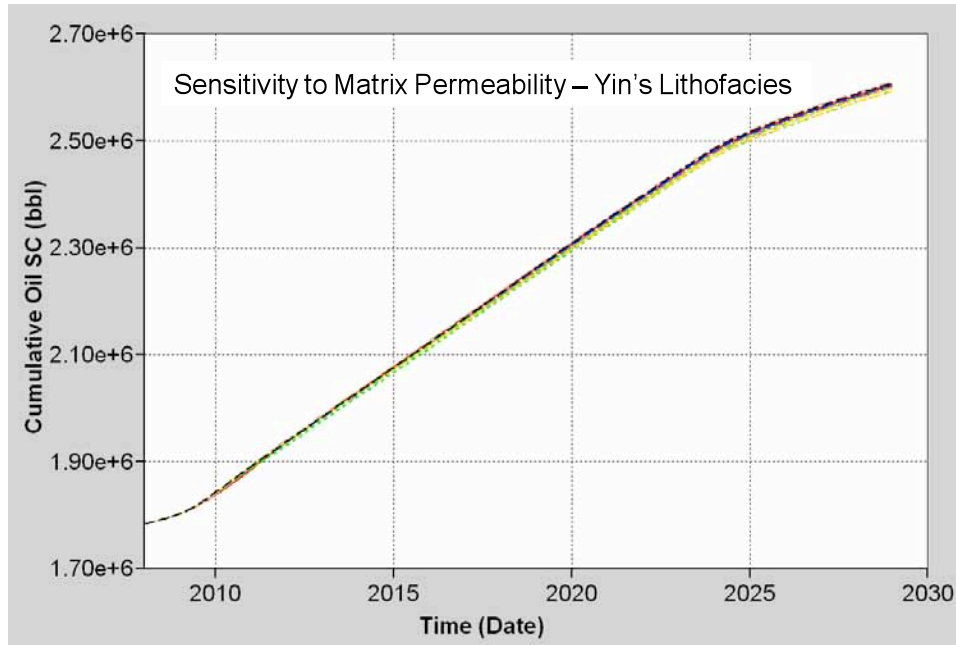


Figure 36: Cumulative Oil comparison between BC (black line) and 10 simulations with different realizations of matrix permeability obtained from the geostatistical analysis using Yin's lithofacies values.

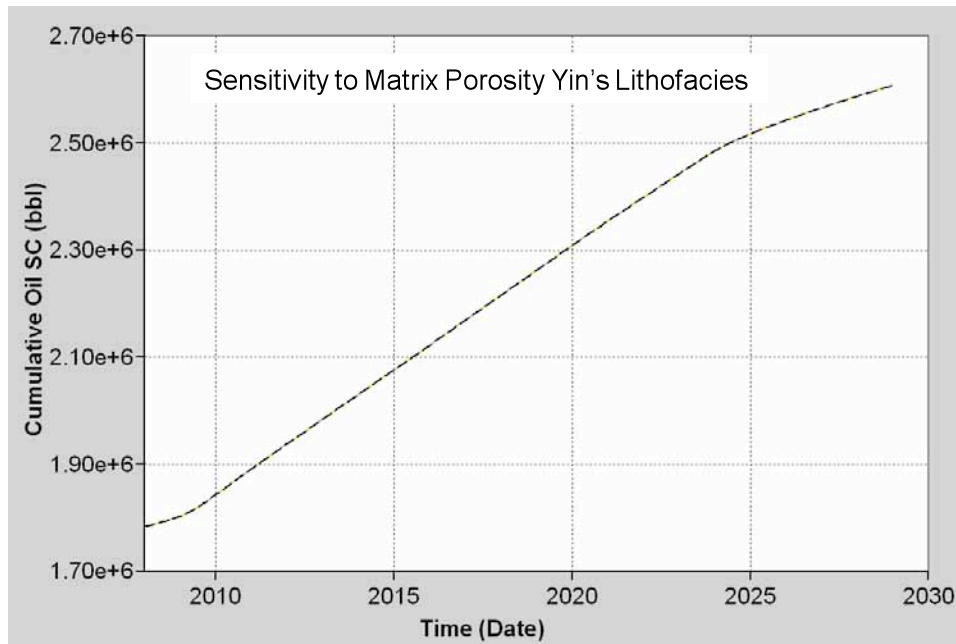


Figure 37: Cumulative Oil comparison between BC (black line) and 10 simulations with different realizations of matrix porosity obtained from the geostatistical analysis using Yin's lithofacies values.

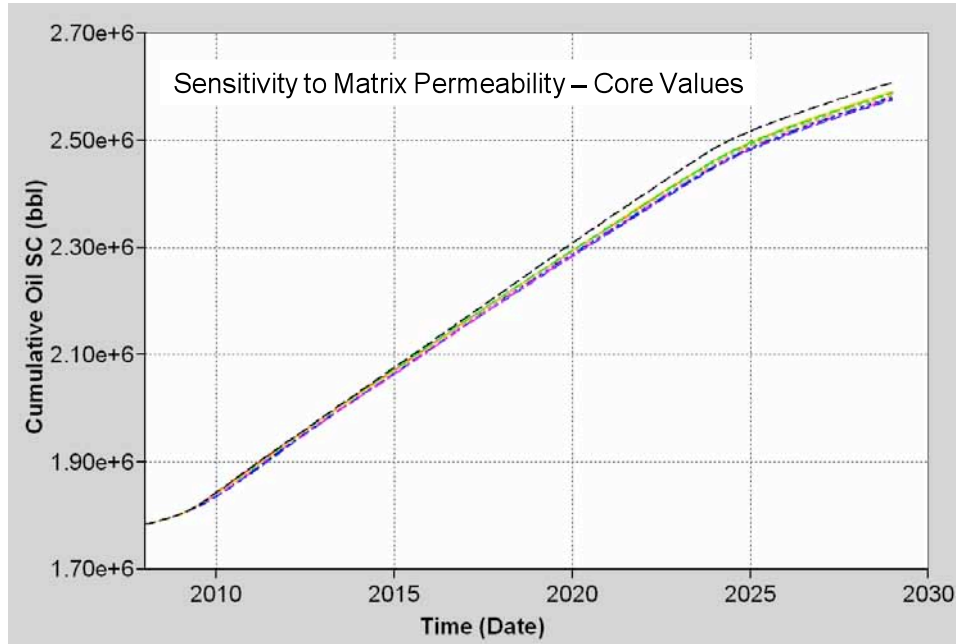


Figure 38: Cumulative Oil comparison between BC (black line) and 10 simulations with different realizations of matrix permeability obtained from the geostatistical analysis using core values

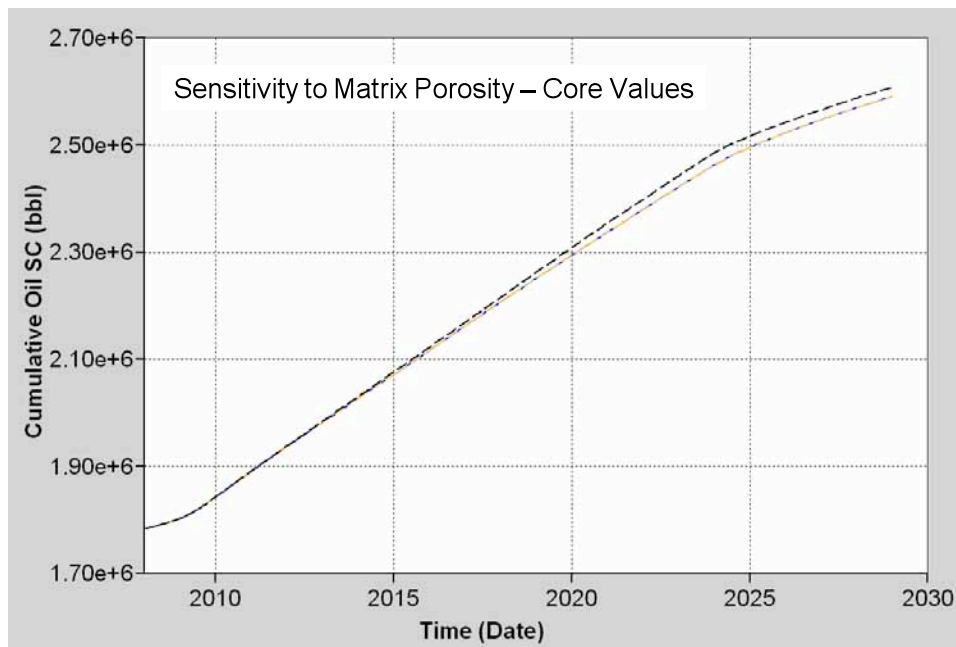


Figure 39: Cumulative Oil comparison between BC (black line) and 10 simulations with different realizations of matrix porosity obtained from the geostatistical analysis using core values (see Section 4.3.2).

In both cases (Yin’s lithofacies and core values), matrix porosity barely modified the results where matrix permeability, although producing slightly more variations, did not produced great differences either. However, running the simulations with matrix porosity and permeability realizations obtained from core values produced more pessimistic outcomes than the ones run with Yin’s lithofacies analysis.

Summary

In order to test the feasibility of the CO₂-EOR pilot project at Teapot Dome, we performed a 3D stochastic reservoir model and fluid flow simulation of the fractured Tensleep Fm. in a three-way trap against the S1 fault. The geological model was based on a structural and stratigraphic seismic interpretation, well logs, and core data. We used geostatistics to populate the model with porosity and permeability distributions. These constraints established the maximum allowable injection rates as well as pressure limits to be avoided at the top of the reservoir and at the fault boundary. Similarly, we also incorporated a fracture permeability anisotropy subparallel to the S_{Hmax} direction. We history matched our model with historic oil and water rates from the field.

The results of the fluid flow simulation showed that the pressure increase is minimal during the pilot project not constituting a risk for fault stability or seal integrity. However, buoyancy and mobility of CO₂ could represent a problem for the EOR performance. CO₂ was injected in the main producing interval (BSand) to dissolve in the oil, but almost immediately rose to the top layers through the high permeability fracture network, taking almost a year to start saturating the fractures in the BSand. The mobility of the gas results in early breakthroughs in the closer wells with their consequent shut-in and loss of production.

Four different scenarios were tested as potential schemes for the projected CO₂-EOR pilot, which consisted on the injection of: 1) 1 MMcfd for 6 weeks, 2) 1 MMcfd for 12 weeks, 3) 2 MMcfd for 6 weeks and 4) 2 MMcfd for 12 weeks. In all of them, oil recovery was less than the predicted from a pure primary production scenario due to the mentioned closure of wells with high GOR. However, when a well control strategy (re-opening wells after a certain period of time) was implemented, incremental oil recovery went up from 8%, in case 1, to 28%, in case 4, of the BC production.

The amount of CO₂ planned to be injected in the initial pilot project is modest in the context of making an impact in sequestering carbon dioxide. The storage potential of the Tensleep was tested injecting higher amounts of CO₂, which are comparable to daily emissions of different size power plants. The results suggest that the present trap could eventually hold an injection scheme of 2 MMcfd in a single well during at least 30 years, sequestering $\sim 1.2 \times 10^6$ tonnes of CO₂ corresponding to a small power plant of $\sim 40,000$ tonnes per year. Due to the small size of the trap, there seems not to be any advantage on injecting in multiple wells at the same time.

During the sensitivity analysis, we studied the impact on the system of several parameters that included fracture permeability, porosity and spacing, relative permeability curves, matrix porosity and permeability, and grid size. The results suggested that several factors would influence the performance of a CO₂ injection. However, it is extremely difficult to drive any conclusion from this sensitivity analysis because these parameters greatly affect gas breakthrough times (the imposed constraint in a well is to shut it in when gas rate is higher than 5000 cfd). Therefore, when the first well shuts-in at different times in each scenario, the distribution of the CO₂ and the conditions of the simulation change, making the quantitative sensitivity analysis meaningless.

A different approach for the sensitivity analysis was also taken, where the wells were allowed to produce without any gas production constraints. This allowed us to analyze

the effect of these parameters in the system. But, since these are not the real production conditions on the field, this approach would not provide a range of possible outcomes regarding oil production and CO₂ storage. Qualitatively, it was observed that fracture permeability is the parameter that most influenced the CO₂ and oil behavior where, K_{rel} curves also have an important impact on the results. Conversely, fracture porosity, fracture spacing, matrix porosity and matrix permeability, seemed to have much less influence.

References

- Aziz, K. and Settari, A., 1979, Petroleum Reservoir Simulation, Applied Science Publishers, New York.
- Caers, J., 2005, Petroleum Geostatistics, SPE Interdisciplinary Primer Series, Society of Petroleum Engineers, Richardson, TX, 96p.
- Chopra, A.K., Stein, M.H., and Dismuke, C.T., 1990, Prediction of Performance of Miscible-Gas Pilots. JPT, December, pp. 1564-1572.
- Dake, L.P., 1978, Fundamentals of Reservoir Engineering, Chapter 9, Elsevier Scientific Publishing Co.
- Dria, D.E., Pope, G.A., and Sepehrnoori, K., 1993. Three-Phase Gas/Oil/Brine Relative Permeabilities Measured Under CO₂ Flooding Conditions, SPERE, May, pp. 143.
- Earth Decision - Gocad 2.1.6 Software
- Friedmann, S.J. and Stamp, V.W., 2006, Teapot Dome: Characterization of a CO₂-enhanced oil recovery and storage site in Eastern Wyoming: Environmental Geosciences, v. 13, no. 3, pp. 181–199
- Gaviria, R., 2005, Reservoir simulation of CO₂ sequestration and enhanced oil recovery in Tensleep Formation, Teapot Dome field: MS Thesis, Texas A&M University, 85p.
- Gray, D. and Todorovic-Marinic, D. 2004, Fracture Detection using 3D Azimuthal AVO, CSEG RECORDER, <http://www.cseg.ca/publications/recorder/2004/12dec/dec04-fracture-detection.pdf>.
- Gringarten, 2005. Practice of 3D Modeling; Talk at Stanford University, PE 246 class (<https://coursework-stanford.edu/coursework/servlet/ShowFile?contentid=300119>)
- Hycal Energy Research Laboratories Ltd., 2004, DOE-RMOTC, Teapot Dome Miscibility study, final report, December 13, 2004, 29 p.
- Isaaks, E. H., 1990, The application of Monte Carlo methods to the analysis of spatially correlated data: Ph.D. thesis, Stanford University, Stanford, California, 213 p.
- Jarrell, P.M., Fox, C.E., Stein, M.H. and Webb, S.L., 2002, Practical Aspects of CO₂ Flooding. Monograph 22, Society of Petroleum Engineers, Richardson, TX, USA.
- Jessen K., Kovscek A.R., Orr Jr F.M., 2005, Increasing CO₂ storage in oil recovery. Energy Convers Manage 46(2): 293–311.
- Journel, A.G., 1994, Geostatistics and reservoir geology, in Computer Applications3: Modeling and Geostatistics, Eds., J.M., Yarus and R.L., Chambers, AAPG, 19-20.
- Kovscek, A.R. and M.D. Cakici, 2005, Geologic storage of carbon dioxide and enhanced oil recovery. II. Cooptimization of storage and recovery. Energy Conversion and Management 46, 1941–1956
- Lorenz, J. C., and S. P. Cooper, 2004, Analysis of fracture characteristics and distribution of 48-X-28 well: Rocky Mountain Oilfield Testing Center Report, 31 p.
- McCutcheon, T., 2003, Time Structure Maps – 3D Seismic Data Interpretation, Teapot Dome Oil Field, Naval Petroleum Reserve No. 3, Natrona County, Wyoming. Rocky Mountain Oilfield Testing Center Report Melzer, S.L., 2007. <http://eori.uwoyo.edu/downloads/Steve%20Melzer%20Oct%2025%20Presentation.pdf>
- Milliken, M.D. and Koepsell, R., 2003, Imaging Technology offers enhanced interpretation of Teapot Dome reservoirs. Wyoming Geological Association Field Guidebook 2002: 41-62
- Pruess, K., Garcia, J., Kovscek, T., Oldenburg, C., Rutqvist, J., Steefel, C., and Xu, T., 2004, Code intercomparison builds confidence in numerical simulation models for Geologic disposal of CO₂. Energy, 29, (9-10), 1431-1444.
- Wadleigh, E.F., 2005, RMOTC in-house reservoir simulation work products.
- Yin, P., 2005, Characterization of Tensleep Sandstone reservoirs: Rocky Mountain Section AAPG Annual Meeting Abstracts and Program, Search and Discovery article 50024:<http://www.searchanddiscovery.com/documents/2005/yin2/images/yin2.pdf>

Yin, P., Nummedal, D. and Shang, Q., 2005b, Reservoir Heterogeneity Caused by Diagenesis in Tensleep Sandstones, Teapot Dome, Wyoming.

<http://www.searchanddiscovery.net/documents/2005/yin/index.htm>

Zhang, Q., Nummedal, D. and Yin, P., 2005, Stratigraphy, sedimentology and petrophysics of the Tensleep Sandstone at Teapot Dome and in outcrop.

<http://www.searchanddiscovery.com/documents/abstracts/2005rocky/RMzha.htm>

Multi-Component Gas Adsorption on Coal

Background

Coalbed methane has been recognized as an important energy resource for over a decade. Once recovered from underground, coalbed methane is used just the same as conventional natural gas. Underground, coalbed methane is different from the conventional natural gas in that gas in coal exists mainly as adsorbed gas on the internal surface areas of the coal; while gas in conventional reservoirs exists mainly as free gas in the pore space. Therefore, in the determination of OGIP (Original Gas In Place) for coalbed methane reservoirs, adsorbed gas must be taken into account. This is one of the reasons that the sorption behavior of gas in coal is studied.

In another aspect, it is essential to learn the sorption behavior of gas on coal to design coalbed methane recovery schemes in the field. First of all, adsorption increases with the increase of pressure, and vice-versa. Depressurization is the most straightforward method to recover coalbed methane. When this is implemented in the field, reservoir pressure is brought down by pumping out a large amount of the formation water. As the decreases of the reservoir pressure, the adsorbed gas on the coal surface would be desorbed and thereafter produced. The reservoir pressure must be brought down to a low enough level for massive desorption to happen. This threshold pressure is determined by the sorption characteristics of gas on coal.

Other than primary recovery, more effective recovery methods, such as enhanced coalbed methane recovery by gas injection are under investigation for field implementation. Nitrogen, carbon dioxide or the mixture of the two gases (such as flue gas) are the gases usually considered for injection. These gases were chosen for different reasons and different mechanisms are employed in enhancing coalbed methane recovery. Nitrogen is used because of its availability in the air and because it is more or less an inert (not reactive) gas. Nitrogen injection enhances coalbed methane recovery by lowering the partial pressure of CH_4 in the free gas phase in the pore spaces to cause desorption. Carbon dioxide is used because it is a greenhouse gas. Injecting CO_2 from anthropogenic source reduces atmospheric emissions of greenhouse gas. Coal has a stronger affinity for CO_2 compared with CH_4 . When CO_2 is present, CH_4 on coal is replaced by CO_2 . The CH_4 is thereafter produced and CO_2 is retained in the coal beds. Therefore, injecting CO_2 into coalbeds, not only enhanced coalbed methane recovery, but also sequestered the greenhouse gas underground. There are no large scale field operation for gas injection ECBM up to date. However, there were several pilot projects of enhancing coalbed methane recovery by CO_2 or flue gas injection. Even though different degree of success gained in those projects due to various operational reasons, conclusions could be drawn that CO_2 was able to be injected into the coal

seams with even very low permeability by creating or opening up existing fractures and gas production could be enhanced given well designed operational schemes [9] [4].

Gas Adsorption Isotherms

Gas adsorption on solid surfaces is usually described by adsorption isotherms. The amount of adsorption for a specific adsorbate on a specific adsorbent at adsorption equilibrium is a function of temperature and pressure [11]:

$$V = f(P, T) \quad (1)$$

At constant temperature, the amount of adsorption is only a function of pressure. More explicitly, adsorption isotherm is the relationship between the amount (volume or moles) of adsorption of a specific adsorbate on a unit (mass) of a specific adsorbent and the pressure at constant temperature. The adsorption isotherms in the literature fall into three categories, as described next.

The Langmuir Approach [11]

The Langmuir approach assumes that adsorption reaches dynamic equilibrium when the rate of adsorption (condensation) equals the rate of desorption (evaporation). It also assumes that each site of adsorption can accommodate only one adsorbate molecule or atom. Therefore, there is a maximum amount of adsorption that will be reached when all the adsorptive sites are occupied by a monolayer of adsorbate molecules or atoms.

The rate of adsorption per unit area of adsorbent is $\alpha v(1 - \theta)$, where α is the sticking probability, v is the collision frequency of adsorbate molecules/atoms striking the adsorbent surface, and θ is the percentage of the available adsorbent surface which has already been occupied by adsorbate molecules/atoms. According to the kinetic theory of gases, the collision frequency of gas molecules striking a solid surface is

$$v = \frac{P}{(2\pi\varpi\kappa T)^{1/2}} \quad (2)$$

where, ϖ is the mass of gas molecules, and κ is the Boltzmann constant.

The rate of desorption is $\beta\theta e^{-E_d/RT}$, where β is the rate constant of desorption, and E_d is the activation energy of desorption.

At adsorption equilibrium, the rate of adsorption equals the rate of desorption:

$$\beta\theta e^{-E_d/RT} = \alpha \frac{P}{(2\pi\varpi\kappa T)^{1/2}} (1 - \theta) \quad (3)$$

which gives us

$$\theta \equiv \frac{V}{V_m} = \frac{BP}{1 + BP} \quad (4)$$

where,

$$B = \frac{\alpha}{\beta (2\pi m \kappa T)^{1/2}} e^{E_d/RT} \quad (5)$$

In Eq. (4), V is the amount (volume) of adsorption on one unit (mass) of adsorbent at pressure P , V_m is the maximum amount of (monolayer) adsorption on one unit (mass) of adsorbent at pressure P , and θ is called the *Fractional Coverage* of adsorption, B and V_m are called the *Langmuir Constants*. Sometimes, the moles of adsorption are used instead of the volume. Then V is replaced by n , and V_m is replaced by m in Eq. (4). Once the Langmuir constants are given, Langmuir-type adsorption is completely specified.

For pure gas adsorption, the amount of adsorption is

$$n = \frac{mBP}{1 + BP} \quad (6)$$

And for gas mixtures:

$$n_t = \frac{m_i B_i P_i}{1 + \sum_{j=1}^{N_C} B_j P_j} \quad (7)$$

where, i and j are component indices, and N_C is the number of components in the adsorbate gas. Equation (6) is called the *Langmuir Equation*, and Eq. (7) is called the *Extended Langmuir Equation*.

The Gibbs Approach [5]

The adsorbate exists in two phases in a system of adsorption: the gaseous phase and the adsorbed phase. The Gibbs approach is based on the concept that the chemical potential of component i in the adsorbed phase equals the chemical potential of component i in the gaseous phase.

$$\mu_i(T, \Pi, x_1 \dots) = \mu_i(T, P, y_1 \dots) \quad (8)$$

Chemical potential is not a variable that has a direct equivalent in the physical world. The following thermodynamic derivation shows how it was used in determining adsorption equilibrium.

The basic thermodynamic equations for the adsorbed phase are in a form analogous to the familiar thermodynamic equations for liquid in vapor-liquid equilibrium (VLE). The only change is that spreading pressure Π is used in place of pressure P , and area A is used instead of volume V . The differential form of the internal energy U and the Gibbs free energy G of the adsorbed phase are written as

$$dU = TdS - \Pi dA + \sum_{i=1}^{N_C} \mu_i dn_i \quad (9)$$

$$dG = -SdT + Ad\Pi + \sum_{i=1}^{N_C} \mu_i dn_i \quad (10)$$

For the adsorbed phase, the work term ΠdA is analogous to the mechanical work term PdV in a conventional vapor-liquid system. The spreading pressure is positive in physical adsorption, indicating that the system does work on the surroundings during the conceptual process of increasing the area of the adsorbate. There is no experimental technique to measure the spreading pressure directly. The concept of spreading pressure is necessary, however, and useful when dealing with adsorption systems. It is usually calculated based on some other measurable variables.

Based on Eq. (10), chemical potential, μ_i , is actually the partial molar Gibbs free energy of species i in a mixture:

$$\mu_i = \left[\frac{\partial G}{\partial n_i} \right]_{T, \pi, x_j \neq i} \equiv \hat{g}_i \quad (11)$$

Another useful concept in multi-component adsorption is the excess molar Gibbs energy which is defined as [7]

$$g^e \equiv g^{mix}(T, \Pi, x_1 \dots) - \sum_{i=1}^{N_C} x_i g_i^0(T, \Pi) = RT \sum_{i=1}^{N_C} x_i \ln \gamma_i \quad (12)$$

where, g^{mix} is the molar Gibbs free energy of the mixture with composition (x_1, x_2, \dots) at temperature T and spreading Π , and g_i^0 is the molar Gibbs free energy of pure i at the same temperature and spreading pressure, and γ_i is the activity coefficient.

$$n_i g^{mix}(T, \pi, x_1, \dots) = G^{mix} = \sum_{i=1}^{N_C} (n_i \hat{g}_i) = \sum_{i=1}^{N_C} (n_i \mu_i) \quad (13)$$

Based on Eq. (11), Eq. (12), and Eq. (13), the chemical potential of component i in the adsorbed phase is

$$\mu_i(T, \Pi, x_1 \dots) = g_i^0(T, \Pi) + RT \ln(\gamma_i x_i) \quad (14)$$

where,

$$g_i^0(T, \Pi) = g_i^0(T) + RT \ln f_i^0(\Pi) \quad (15)$$

In which, $g_i^0(T)$ is the molar Gibbs free energy of pure i at the perfect gas state and at a pressure of 1 *atm*.

Chemical potential for the adsorbed phase can be get by substituting Eq. (15) into Eq. (14):

$$\mu_i(T, \Pi, x_1, \dots) = g_i^0(T) + RT \ln f_i^0(\Pi) + RT \ln \gamma_i x_i \quad (16)$$

Chemical potential for the gas phase with the same reference state is

$$\mu_i(T, \Pi, y_1, \dots) = g_i^0(T) + RT \ln \hat{f}_i \quad (17)$$

where, \hat{f}_i is the fugacity of the gas phase:

$$\hat{f}_i = P y_i \hat{\varphi}_i \quad (18)$$

At adsorption equilibrium, chemical potential in the adsorbed phase equals chemical potential in the gas phase. Combining Eq. (16), Eq. (17), and Eq. (18), we get the equation of equilibrium for mixed-gas adsorption at constant T :

$$P y_i \hat{\varphi}_i = f_i^0(\Pi) x_i \gamma_i \quad (19)$$

In the above equations, P is the equilibrium pressure, y_i and x_i is the mole fraction of component i in the gaseous and adsorbed phase respectively; $\hat{\varphi}_i$ is the fugacity coefficient of component i in the gaseous phase, accounting for the nonideality of the gaseous phase; f_i^0 is the fugacity of the pure component in its standard state; and γ_i is the activity coefficient of component i accounting for the nonideality of the adsorbed phase. At low to moderate pressures, the gas phase and the adsorbed phase can be considered ideal. Equation (19) becomes

$$P y_i = P_i^0(\Pi) x_i \quad (20)$$

This is analogous to Raoult's law for vapor-liquid equilibrium.

The Potential Approach

In this theory, it is assumed that the adsorbate molecules surround the adsorbent surface at certain concentration gradient due to a potential field. This approach is not within the scope of interest of this study.

Adsorption Calculation

Adsorption of pure gases is usually measured in the lab. It has been shown that simple formula such as Langmuir equations represent pure adsorption isotherms very well [2]. Laboratory measurement and accurate numerical modeling for multi-component adsorption of gas on coal, however, are lacking in the literature. In this section, several algorithms for calculating multi-component adsorption were demonstrated. The methodologies were first tested on some experimental data from a paper in the literature [8]. Reasonable values for activity coefficients were obtained thereby giving confidence in the accuracy of the algorithms. Multi-component adsorption experiments were designed based on the algorithms in the next section.

Pure Adsorption Isotherms: The system under consideration is adsorption of CO₂/C₃H₈ binary mixtures of different composition on zeolite NaX. Parameters for pure gas adsorption isotherms were found first. As mentioned above, it is not a problem to model pure adsorption isotherms. The Langmuir equation, Eq. (6), and its modifications are the ones usually used. In the paper, the authors used the modified virial equations:

$$P = \frac{n}{H} \left[\frac{m}{m-n} \right] \exp(C_1 n + C_2 n^2 + C_3 n^3 + C_4 n^4) \quad (21)$$

where, n is the amount of adsorption in the unit of *moles/(kg · kPa)*; C_1, C_2, C_3, C_4 are constants; and H is the Henry's constant defined as [10]

$$H \equiv \lim_{P \rightarrow 0} \frac{n}{P} \quad (22)$$

In Eq. 21, the term $\left(\frac{m}{m-n}\right)$ enforce Langmuir behavior at high pressure, while the virial expansion terms modify the low-pressure adsorption. Therefore, the modified virial equation is also a modification of the Langmuir equation. The corresponding Langmuir constant B is

$$B = \frac{H}{m} \quad (23)$$

The pure adsorption isotherm given by the modified virial equations and the Langmuir equations are plotted in Fig. 1. Even though the modified virial adsorption and the Langmuir adsorption were constrained by the same maximum amount of adsorption m , the actual adsorption at low pressures are quite different. For the data under investigation, the authors used the modified virial equations for their pure adsorption isotherms. However, both the modified virial equation and the Langmuir equation were used in calculations of this report to demonstrate the significance of the accuracy of the pure adsorption isotherm in binary adsorption calculations. The pure adsorption constants for the modified virial equations and the Langmuir equations for the CO₂-C₃H₈-NaX system under investigation are given in Table 1.

Surface Potential: For a multi-component adsorption system, the mixture adsorption and the individual pure component adsorption is related by the following equation (taking binary adsorption as an example):

$$\psi_i^0 = \psi = \psi_j^0 \quad (24)$$

In the above equation, ψ for the mixture is a variable related to the *surface potential* of adsorption:

$$\psi = -\frac{\Phi}{RT} = \frac{A\Pi}{RT} \quad (25)$$

where, $\Phi = A\Pi$ is the surface potential. In the physical world, surface potential is the chemical potential of the solid adsorbent with the adsorbed “solution” relative to its pure state *in vacuo* at the same temperature [6]:

$$\Phi = (\mu - \mu_s) \quad (26)$$

In order to calculate ψ , Gibbs adsorption isotherms are employed [1]:

$$-Ad\Pi + \sum_{i=1}^{N_C} n_i d\mu_i = 0 \quad (\text{constant } T) \quad (27)$$

And the chemical potential is expressed as in the Lewis's definition of fugacity for any system [7]:

$$\mu_i - \mu_i^0 = RT \ln \frac{f_i}{f_i^0} \quad (28)$$

Combining Eq. (25), Eq. (27), and Eq. (28), the following equation describes ψ (reference state $\Pi = 0$ and $P = 0$):

$$\psi = \frac{A\Pi}{RT} = \sum_{i=1}^{N_C} \int_0^{f_i} \frac{n_i}{f_i} df \quad (29)$$

For pure component, Eq. (29) becomes

$$\psi_i^0 = \int_0^{f_i^0} \frac{n_i^0}{f_i^0} df \quad (30)$$

If we would use saturation pressure P_i^0 in place of f_i^0 at low to moderate pressures, Eq. (30) becomes

$$\psi_i^0 = \int_0^{P_i^0} \frac{n_i^0}{P_i^0} dP \quad (31)$$

Pure adsorption isotherms, such as Eq. (21), can then be used to calculate ψ_i^0 using Eq. (31):

$$\psi_i^0 = \frac{1}{2}C_{i1}n_i^{02} + \frac{2}{3}C_{i2}n_i^{03} + \frac{3}{4}C_{i3}n_i^{04} + \frac{4}{5}C_{i4}n_i^{05} - m_i \ln \left[1 - \frac{n_i^0}{m_i} \right] \quad (32)$$

Calculating ψ using Binary Adsorption Data

Based on Eq. (29), variable ψ is obtained from the experimental data of binary adsorption in the first four columns of Table 2. The integral is obtained numerically from the area below the curves in $\frac{n_i}{f_i} \sim f_i$ plots, Fig. 2 and Fig. 3. In the equation, n_i is experimentally measured: $n_i = n_i x_i$. Gas phase fugacity, f_i , is calculated using Eq. (18), where $\hat{\varphi}_i(P, T, \mathbf{y})$ is calculated based on Equation of State (EOS), such as Soave-Redlich-Kwong (SRK).

After calculating ψ , the value of ψ_1^0 and ψ_2^0 are known given the relationship in Eq. (24). ψ_i^0 is then used to calculate n_i^0 based on Eq. (32). Then, n_i^0 , P_i^0 are calculated based on Eq. (21). At the end, every term in Eq. (19) is now known except for γ_i , thus the activity coefficients are calculated. The results obtained by this method are

shown in Table 2, labeled as “Direct Calculation”. Note that we use P_i^0 instead of f_i^0 in Eq. (19) for simplicity. This is the case for all the calculations in this section.

For this calculation, it is essential to compute the integral in Eq. (29) accurately. In our calculation, we fitted curves to experimental data, fitted equations to the curves, and calculated the integral based on the equations, Fig. 2 and Fig. 3. The experimental data at very low pressure were lacking. We only knew that the curves would be constrained by the Henry’s constants at zero pressure. The actually shape of the curve may vary, which would give different values of ψ , and thus different values of the activity coefficients.

Three-Constant Model [8]

For a system of multi-component adsorption, the equilibrium properties (activity coefficients, excess loading, etc.) are all related to the excess Gibbs free energy. This algorithm is based on a three-constant model of the excess Gibbs free energy:

$$g^e = (A + BT)x_1x_2(1 - e^{-C\psi}) \quad (33)$$

where, A , B , and C are constants.

From Eq. (12), the activity coefficient is

$$RT \ln \gamma_i = \left[\frac{\partial (n_t g^e)}{\partial n_i} \right]_{T, \psi, n_j} \quad (34)$$

The combination of Eq. (33) and Eq. (34) gave an equation for activity coefficients:

$$RT \ln \gamma_i = A_o (1 - e^{-C\psi}) x_j^2 \quad (i \neq j) \quad (35)$$

where, $A_o = A + BT$.

The excess reciprocal loading can also be calculated based on the three-constant model:

$$(1/n)^e = \left[\frac{\partial (g^e/RT)}{\partial \psi} \right]_{T, x} = \frac{C}{RT} A_o x_1 x_2 e^{-C\psi} \quad (36)$$

In summary, for a binary system, we have the following. Adsorption isotherms for the individual pure components are

$$P_1^0 = \frac{n_1^0}{H_1} \left[\frac{m_1}{m_1 - n_1^0} \right] \exp \left(C_{11}n_1^0 + C_{12}n_1^0{}^2 + C_{13}n_1^0{}^3 + C_{14}n_1^0{}^4 \right) \quad (37)$$

$$P_2^0 = \frac{n_2^0}{H_2} \left[\frac{m_2}{m_2 - n_2^0} \right] \exp \left(C_{21}n_2^0 + C_{22}n_2^0{}^2 + C_{23}n_2^0{}^3 + C_{24}n_2^0{}^4 \right) \quad (38)$$

The condition of equal surface potential: $\psi_1^0 = \psi = \psi_2^0$, where,

$$\psi_1^0 = \frac{1}{2}C_{11}n_1^0{}^2 + \frac{2}{3}C_{12}n_1^0{}^3 + \frac{3}{4}C_{13}n_1^0{}^4 + \frac{4}{5}C_{14}n_1^0{}^5 - m_1 \ln \left[1 - \frac{n_1^0}{m_1} \right] \quad (39)$$

$$\psi_2^0 = \frac{1}{2}C_{21}n_2^{02} + \frac{2}{3}C_{22}n_2^{03} + \frac{3}{4}C_{23}n_2^{04} + \frac{4}{5}C_{24}n_2^{05} - m_2 \ln \left[1 - \frac{n_2^0}{m_2} \right] \quad (40)$$

The equations for activity coefficients become

$$RT \ln \gamma_1 = A_o (1 - e^{-C\psi}) x_2^2 \quad (41)$$

$$RT \ln \gamma_2 = A_o (1 - e^{-C\psi}) x_1^2 \quad (42)$$

The condition of equal chemical potentials are

$$Py_1 \hat{\phi}_1 = x_1 \gamma_1 P_1^0 \quad (43)$$

$$Py_2 \hat{\phi}_2 = x_2 \gamma_2 P_2^0 \quad (44)$$

And the excess loading, $(1/n)^e$, is

$$\frac{1}{n_t} - \left[\frac{x_1}{n_1^0} + \frac{x_2}{n_2^0} \right] = (1/n)^e = \frac{C}{RT} A_o x_1 x_2 e^{-C\psi} \quad (45)$$

There are 11 equations and 11 unknowns: A_o , C , P_1^0 , P_2^0 , n_1^0 , n_2^0 , ψ_1^0 , ψ_2^0 , ψ , γ_1 , γ_2 . All the unknowns are found by solving the equations together. The results of the calculation are shown in Table 2, labeled as ‘‘ABC-Virial’’.

If the Langmuir equations were used for pure adsorption, Eq. (39) and Eq. (40) become

$$\psi_1^0 = -m_1 \ln \left[1 - \frac{n_1^0}{m_1} \right] \quad (46)$$

$$\psi_2^0 = -m_2 \ln \left[1 - \frac{n_2^0}{m_2} \right] \quad (47)$$

The same eleven-equation system was solved and the results are also shown in Table 2, labeled as ‘‘ABC-Langmuir’’. The results are different from those based on the modified virial equations. Therefore, the accuracy of the pure adsorption isotherm also plays a role in getting correct results in binary adsorption calculation.

Based on the three sets of results obtained by the two algorithms in Table 2, the following conclusions were drawn:

1. Between the two algorithms, the ‘‘direct’’ method of calculating ψ based on experimental data is theoretically more rigorous. It is very hard, however, to get an accurate value of the integral in Eq. (29).
2. It is helpful to use some empirical models to facilitate the calculation. The ABC model for excess Gibbs free energy seems appropriate. Reasonable values for the activity coefficients were obtained based on this model.
3. Not only the algorithm of calculation, but the accuracy of the pure adsorption isotherms affect the accuracy of the binary adsorption calculation. It is essential to obtain accurate pure adsorption isotherms for the gases in the system.

Experiments

The initial interest of our research is to measure the permeability change of coal with the injection of different gases. A coal pack was made from ground coal packed tightly into a rubber sleeve then into a perforated aluminum sleeve. The sleeved coal pack was then put into a second aluminum sleeve. Confining pressure was inserted to the core by injecting high pressure gas into the second bigger aluminum sleeve. Gases of different composition from pure CO_2 , pure N_2 , and pure CH_4 , to CO_2/N_2 binary mixtures of various composition were injected into the coal pack, and adsorption equilibrium was reached at different pressure. The net confining pressure, which is the confining pressure minus the pore pressure, of the system was kept constant by adjusting the confining pressure according to the pore pressure. The permeability of the coal pack was measured at the end of each adsorption equilibrium. The permeability before and after adsorption were compared. Experimental results showed that the permeability of the coal pack decreased after adsorption as pore pressure increased. At the same pressure, the permeability decrease was greater with the increase of CO_2 in the injected gas as shown in Fig. 4. The details of the experimental setup and results are presented elsewhere [3].

It is believed that the permeability decrease of the coal pack is due to adsorption. Because the net confining pressure of the system was kept constant which eliminates the effect of pressure-induced stress on permeability. In order to investigate further the phenomenon, a new experimental setup was designed to measure the permeability change, the amount of adsorption, and the volumetric swelling of a coal core simultaneously, Fig. 5. Instead of a coal pack made from ground coal, coal plugs were drilled and assembled to form a composite core, Fig. 6. The core coated with silicon sealant was wrapped with heat-shrinkable tube, and then placed in the aluminum confined-pressure sleeve. The two ends of the core were connected to two piston accumulators whose pistons were controlled by pumps. High-precision syringe pumps were used because they can be set at constant flow rate or constant pressure modes. Injection gas was put in the piston accumulators. The pumps pushed the pistons and circulated the gas through the core. The gas portions of the piston accumulators and the core formed a closed volume where adsorption occurred, and the volume and pressure of the system were recorded. The total amount of adsorption can be calculated based on the initial and equilibrium volume and pressure of the closed system. The confined-pressure sleeve was also connected to a high-precision syringe pump which was running at constant pressure mode. The liquid volume change within the confining pressure annulus was recorded by the pump. This volume reflected the volume change of the core (swelling/shrinkage). After adsorption equilibrium, the permeability of the core was measured by pushing the gas through the core and recording the pressures at the two ends of the core by the pressure transducers. After finishing all these procedures, gas samples were taken from the system and analyzed by a gas chromatograph (GC). The free gas composition after adsorption was thereby known. The composition of the adsorbed phase was calculated based on the initial injection gas composition and the equilibrium free gas composition. In summary, the new setup enabled us to measure the total amount (in moles) of adsorption, the composition of

the adsorbed phase, the volume change of the core, together with the permeability of the core. As far as we know, this was the first time such simultaneous measurements were done.

The core was also scanned using Computed Tomography (CT). Figure 7 shows some CT images of a composite core at different conditions. The fractures in the core are clearly visible. Experiments of adsorption of CO₂/N₂ binary mixture of 12%/88% have been done on the core, and the data are still being processed.

Summary and Conclusions

Based on the results of the numerical calculation and experimental observations, the following conclusions were drawn:

1. Multi-component adsorption calculation is essential. Such calculations are not straightforward.
2. Based on thermodynamics and pure adsorption isotherms, it is possible to conduct multi-component calculation.
3. To implement the algorithms described in this paper, experiments of multi-component adsorption need to be conducted to collect the necessary data.
4. The accuracy of the multi-component adsorption calculation relies on the correctness of the algorithm and the accuracy in calculating each term, for instance the accuracy of the pure adsorption isotherm and the accuracy of getting the integral for ψ .
5. Experiments can be designed to measure adsorption, swelling, and permeability simultaneously.

Future Work

1. Experiments of permeability, swelling, and phase behavior of the adsorbed phase for different gas compositions at different pressures shall be finished.
2. Adsorption of N₂/CO₂ binary mixtures on coal will be modeled and the activity coefficients calculated based on the described algorithms.
3. The adsorption model would be merged with a permeability model.
4. The measured permeability and volumetric swelling would be used to compare against the model predictions.

Nomenclature

α	Sticking probability
β	Rate constant for desorption
γ	Activity coefficient
$\hat{\phi}$	Fugacity coefficient
κ	Boltzmann constant
μ	Chemical potential
Φ	Surface potential
Π	Spreading pressure
θ	Fractional coverage of adsorption
ϖ	Mass
A	Area
B	Langmuir constant
C	Constant
e	Excess
E_d	Activation energy of desorption
f	Fugacity
G	Gibbs free energy
g	Molar Gibbs energy
G^{mix}	Gibbs free energy of the mixture
H	Henry's constant
i, j	Component indices
m	Maximum
n	Number of moles
N_C	Number of components
P	Pressure
R	Rate (Universal gas constant)
S	Entropy
T	Temperature

U	Internal energy
V	Volume
v	Rate (frequency)
x_i	Mole fraction of component i in the adsorbed phase
y_i	Mole fraction of component i in the free gas (vapor) phase

References

- [1] Hill, T.L., 1949. Statistical Mechanics of Adsorption. V. Thermodynamics and Heat of Adsorption, *J. Chem. Phys.*, Vol. 17, 520, DOI:10.1063/1.1747314.
- [2] Jessen, K., G.Q. Tang, and A.R. Kavscek, 2008. Laboratory and Simulation Investigation of Enhanced Coalbed Methane Recovery by Gas Injection, Transport in Porous Media, DOI:10.1007/S11242-007-9165-9.
- [3] Lin, W., Tang, G.-Q., and Kavscek A.R., 2008. Sorption-Induced Permeability Change of Coal during Gas-Injection Processes, *Reservoir Evaluation & Engineering* August 2008, 792 - 802.
- [4] Mavor, M.J., Gunter, W.D., and Robinson, J.R., 2004 Alberta Multiwell Micro-Pilot Testing for CBM Properties, Enhanced Methane Recovery and CO₂ Storage Potential, paper SPE 90256, presented at the SPE Annual Technical Conference and Exhibition held in Houston, Texas, USA, September 26-29, 2004..
- [5] Myers, A.L. and Prausnitz, J.M., 1965. Thermodynamics of Mixed-Gas Adsorption, *A.I.Ch.E. Journal*, Vol. 11, 121-127.
- [6] Myers A.L., 2002 Thermodynamics of Adsorption in Porous Materials, *A.I.Ch.E. Journal*, Vol. 48, No. 1, 145 - 160.
- [7] Prausnitz, J.M., 1986. Molecular Thermodynamics of Fluid-Phase Equilibria, Prentice-Hall, Inc., Englewood Cliffs, New Jersey, 196 - 200.
- [8] Siperstein, F.R. and Myers A.L., 2001 Mixed-Gas Adsorption, *A.I.Ch.E. Journal*, Vol. 47, No. 5, 1141 - 1159.
- [9] Stevens, S.H. and Riemer, P., 1998 Enhanced Coalbed Methane Recovery Using CO₂ Injection: Worldwide Resource and CO₂ Sequestration Potential, paper SPE 48881, presented at the SPE International Conference and Exhibition held in Beijing, China, 2-6, November 1998..
- [10] Talu, O., Li, J., and Myers, A.L., 1995. Activity Coefficients of Adsorbed Mixtures, *Adsorption* Vol. 1, 103 - 112.
- [11] Yang, R.T., 1987. Gas Separation by Adsorption Processes, Butterworths Publishers, Johannesburg, South Africa, 26-51.

Table 1: Pure adsorption constants for CO₂ (1) and C₃H₈ on NaX at 20 °C.

Gas	Zeolite	H <i>mol/(kg · kPa)</i>	C ₁	C ₂	C ₃	C ₄	m <i>mol/kg</i>	Error %	Langmuir B <i>1/kPa</i>
CO ₂	NaX	27.253	1.2338	-0.1241	0.0038	0.0	6.4674	3.0	4.2139
C ₃ H ₈	NaX	2.3657	-0.5251	0.3367	-0.2419	0.0648	3.4288	1.3	0.6899

Table 2: Adsorption of binary mixtures of CO₂ (1) and C₃H₈ on NaX

Experimental Data					Fugacity Coefficients		Activity Coefficients and ψ								
							Direct Calculation			ABC-Viral			ABC-Langmuir		
P (kPa)	n_t (mol/kg)	x_1	y_1	$s_{1,2}$	$\hat{\phi}_1$	$\hat{\phi}_2$	γ_1	γ_2	ψ	γ_1	γ_2	ψ	γ_1	γ_2	ψ
3.59	3.214	0.922	0.913	1.126	0.9998	0.9995	0.3614	0.1258	11.7318	0.9924	0.3433	8.1291	0.9785	0.0480	3.9208
4.16	3.362	0.926	0.920	1.088	0.9998	0.9994	0.3720	0.1207	12.2310	0.9928	0.3217	8.7205	0.9798	0.0412	4.2295
4.99	3.606	0.862	0.854	1.068	0.9997	0.9993	0.3835	0.1165	12.8595	0.9734	0.3498	9.5955	0.9310	0.0615	4.3042
6.25	3.805	0.869	0.866	1.026	0.9997	0.9992	0.4005	0.1094	13.6819	0.9746	0.3216	10.5045	0.9343	0.0502	4.8042
8.23	4.030	0.818	0.804	1.096	0.9996	0.9989	0.4187	0.1120	14.6732	0.9483	0.3423	11.6145	0.8743	0.0662	5.0581
10.26	4.192	0.826	0.812	1.099	0.9995	0.9986	0.4346	0.1075	15.5449	0.9505	0.3188	12.4877	0.8794	0.0552	5.6225
14.35	4.376	0.786	0.741	1.284	0.9993	0.9980	0.4489	0.1141	16.8376	0.9220	0.3343	13.7576	0.8179	0.0664	6.1278
17.80	4.507	0.794	0.745	1.319	0.9991	0.9975	0.4622	0.1095	17.7692	0.9251	0.3146	14.6108	0.8239	0.0563	6.8415
26.14	4.638	0.764	0.659	1.675	0.9987	0.9962	0.4627	0.1167	19.3618	0.8986	0.3260	15.9153	0.7682	0.0631	7.7299
32.52	4.756	0.774	0.660	1.764	0.9984	0.9953	0.4704	0.1109	20.4096	0.9040	0.3060	16.8462	0.7789	0.0533	8.8117
44.82	4.828	0.753	0.584	2.172	0.9979	0.9933	0.4574	0.1121	21.8430	0.8830	0.3147	17.9623	0.7357	0.0577	10.1211

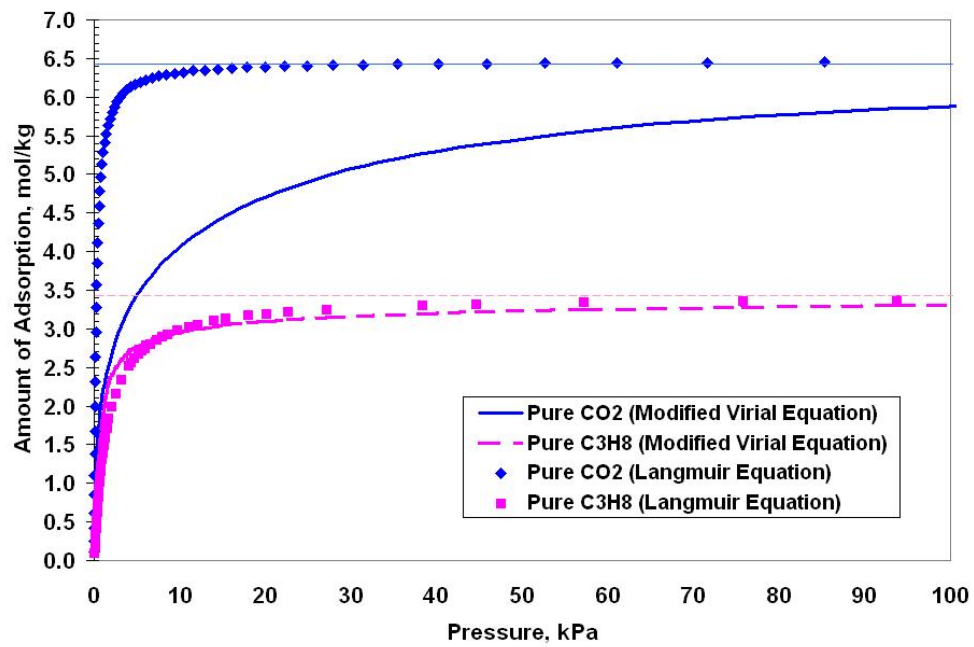


Figure 1: Adsorption of CO₂ (1) and C₃H₈ on NaX at 20 °C.

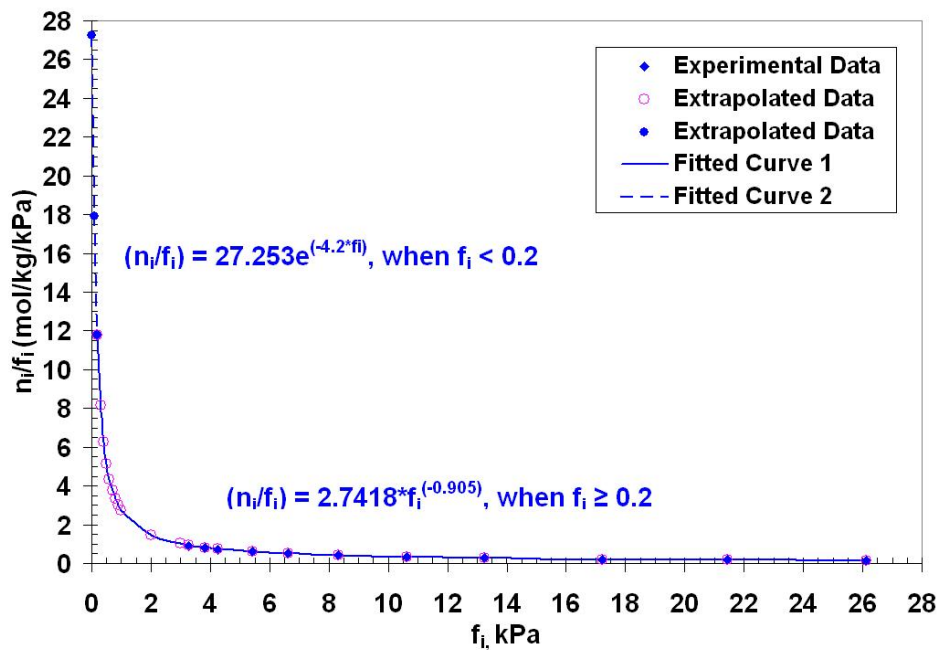


Figure 2: Adsorption of CO₂ (1) and C₃H₈ on NaX at 20 °C: f_i vs. n_i/f_i of CO₂.

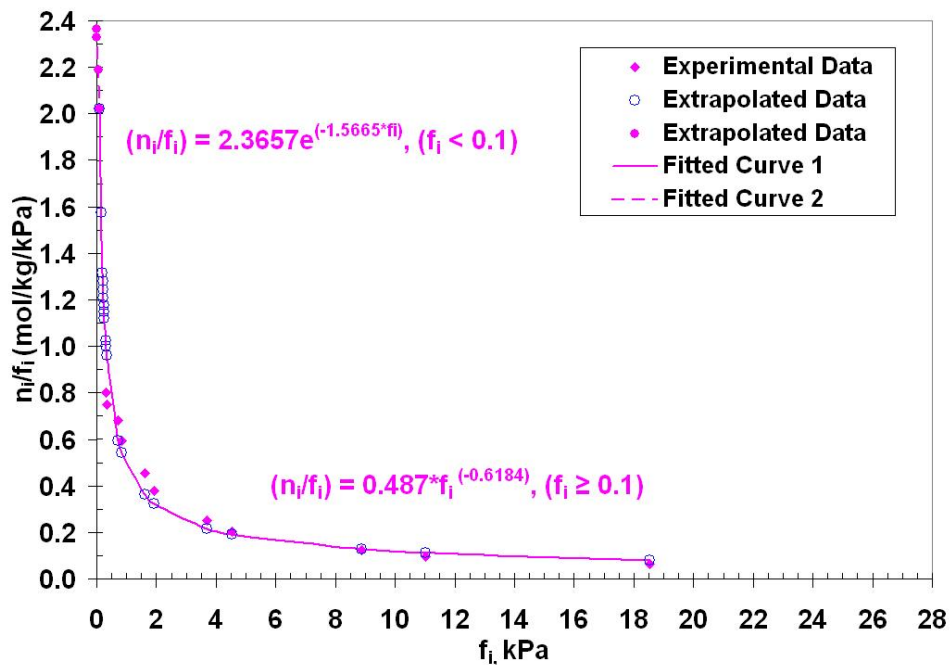


Figure 3: Adsorption of CO₂ (1) and C₃H₈ on NaX at 20 °C: f_i vs. n_i/f_i of C₃H₈.

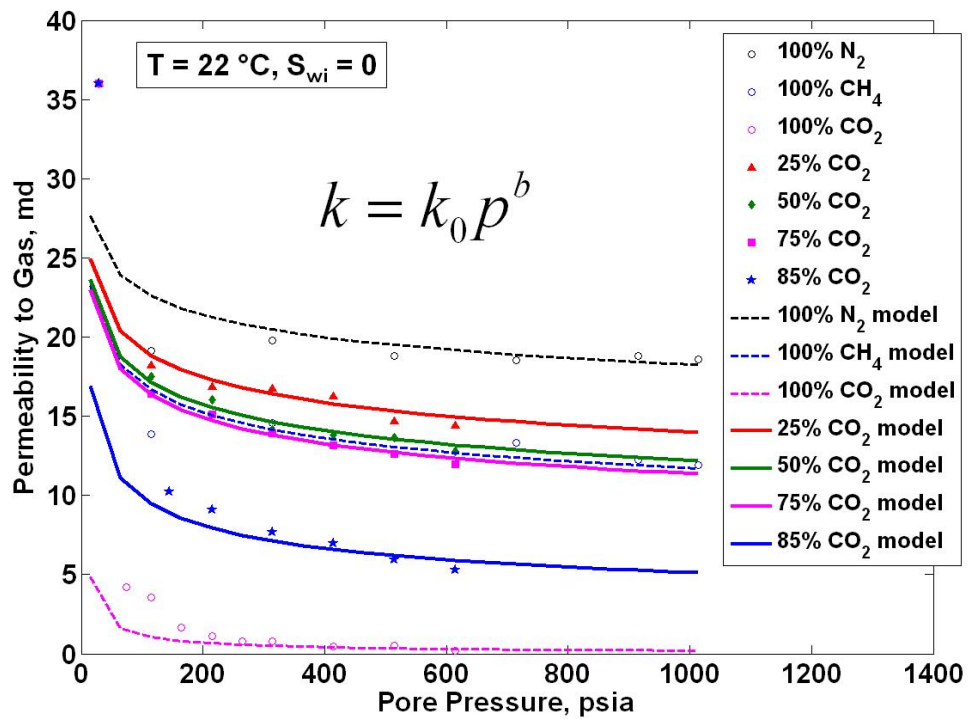


Figure 4: Permeability evolution with the injection of different gases.

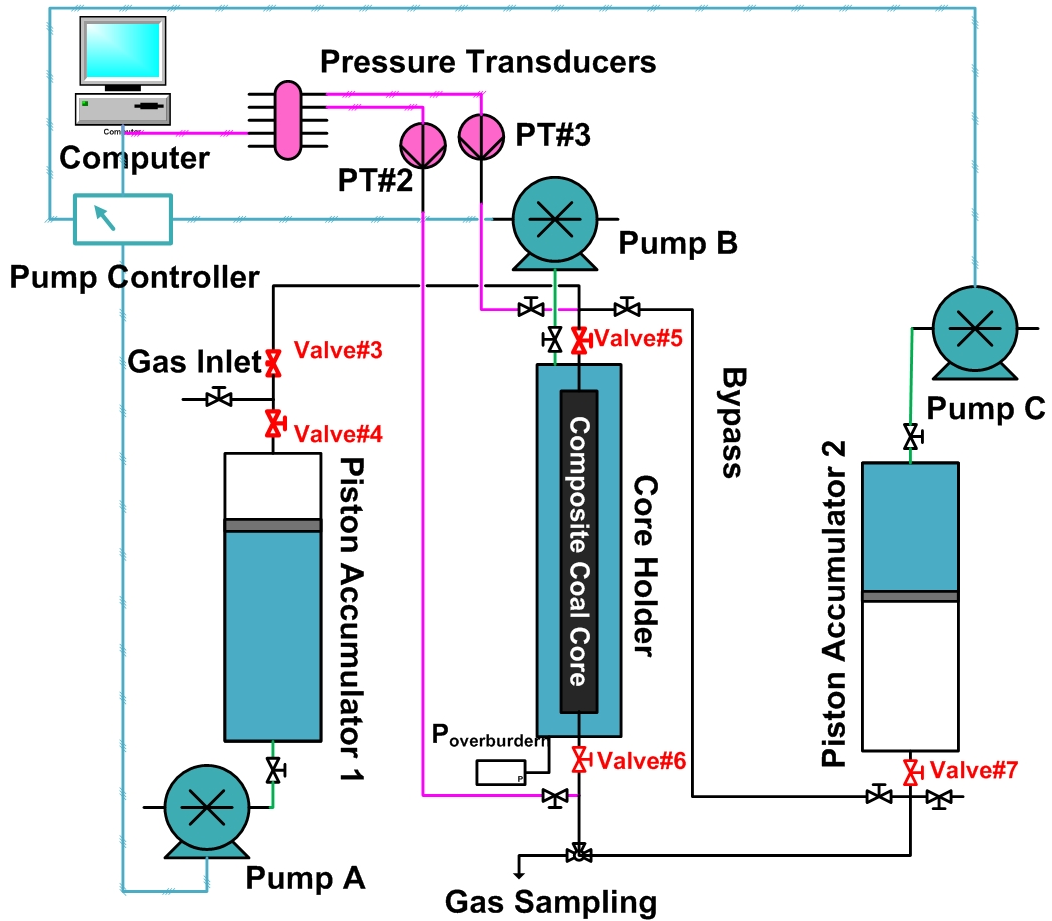


Figure 5: Schematic apparatus for simultaneous measurement of permeability, adsorption, and swelling.



(a) A piece of coal plug.



(b) Assembled coal plugs.



(c) Composite coal core.

Figure 6: The coal used in the experiments.

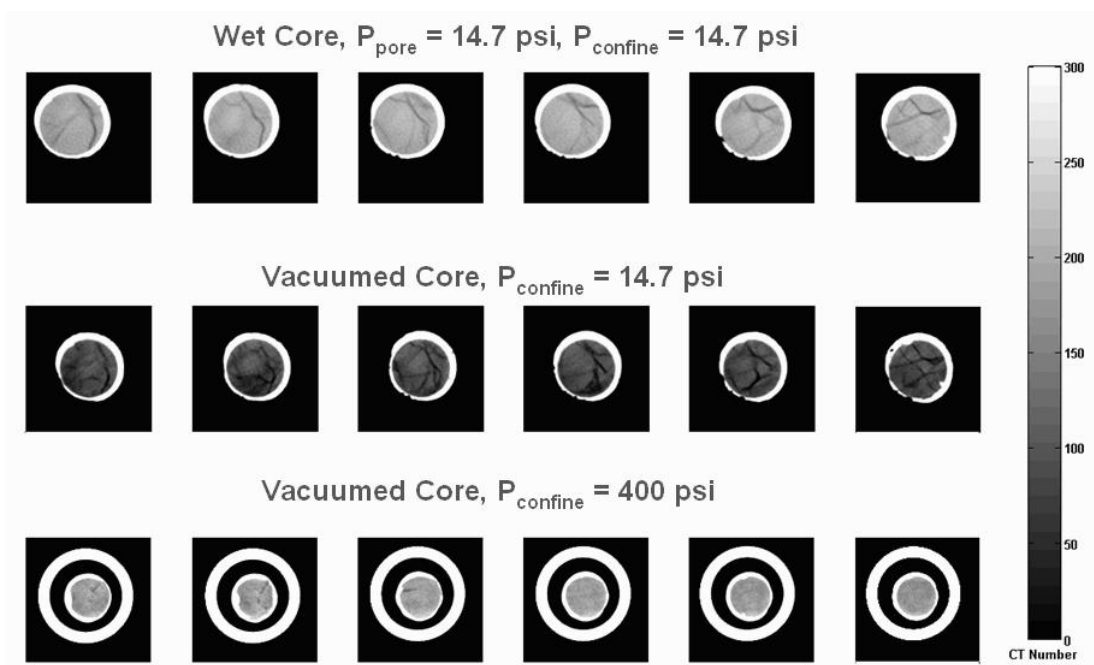


Figure 7: CT images of the composite core at different confining pressures.

Simulation Investigation of Multicomponent Sorption Modeling in ECBM Recovery Calculations

Introduction

With rapid industrialization and growth in world population, energy demand is on the rise. Fossil fuels are the conventional sources of energy and their widespread consumption has led to emission of vast amounts of greenhouse gas. One of the methods to reduce the level of carbon dioxide (CO_2) concentration in the atmosphere is by sequestering it in geologic formations such as coalbed seams, depleted oil reservoirs and saline aquifers¹. To be economically viable, geologic sequestration activities should be considered in conjunction with enhanced recovery of oil and natural gas.

Storage of CO_2 in coal seams is a potentially attractive carbon sequestration technology because it enhances methane (natural gas) production from coalbeds as well as has the potential to be carbon neutral and perhaps a carbon sink^{2,3}. In some cases, this can be cost effective as the additional CH_4 recovery from coal can either partially or completely offset the operational costs incurred.

Coal beds have large internal surface area and show a strong affinity towards methane (CH_4) and CO_2 . In coal bed methane (CBM) reservoirs, most of the CH_4 is present in an adsorbed state at liquid like density, within the micropores. Only a small amount of the gas is in a free phase. Primary recovery of this CBM involves dewatering the coalbeds, leading to reduced pressures. CH_4 then desorbs from the coal surfaces. Unfortunately, the primary recovery techniques recover less than half of the CBM in place⁴ and the costs of dewatering are significant. Injection of nitrogen (N_2) and CO_2 , so called as enhanced coal bed methane (ECBM) recovery is a means to improve the ultimate recovery. The gas injection serves to reduce the partial pressure of CH_4 , thereby leading to desorption from the coalbed but at the same time, maintains the coalbed reservoir pressure. In practice, ECBM gases can be N_2 and/or CO_2 . N_2 injection generally leads to a more rapid response whereas CO_2 injection leads to a more complete and better sweep. Moreover the coalbed surface shows a greater affinity towards CO_2 than CH_4 or N_2 . As a result, the CH_4 is readily desorbed from the coalbed in the presence of CO_2 as the injectant⁵.

Moving away from the big picture, there is a genuine lack of understanding of the mechanism of ECBM. This is partly because of the complicated structure of coalbed matrix. There are intricate networks of micro and macro pores, as well as the coupled adsorption-transport mechanisms that take place as CO_2 is injected. Broadly categorizing, the physical mechanisms that dominate CO_2 -ECBM recovery are multicomponent diffusion and adsorption. It is this interplay between the adsorption properties of coal surfaces and the advance of individual gas species that makes the theoretical and numerical modeling such a difficult task. Apart from this, the heterogeneity of the coalbed and sorption induced permeability changes are other factors that contribute to the complexity^{6,7}.

This lack of understanding motivated us to undertake a simultaneous experimental and numerical model validation study of the CO_2 -ECBM recovery process. There are several models that have been proposed for modeling multicomponent sorption on coal. The more popular ones are the extended Langmuir model⁸ and Ideal Adsorbate Solution (IAS) model⁹.

With this big picture in mind, the ensuing work is based on developing coupled adsorption-diffusion models for multicomponent systems. The modeling effort is complemented by a simultaneous experimental study of the CO₂- ECBM process. The experimental data ascertains the validity of the simulation effort and in many cases serve as the input data file for the simulation runs. The experimental study concentrates on the use of X-ray Computed Tomography (CT) for observing single phase fluid flow within coal. The basic principle underlying CT scanning is the differential attenuation of a beam of X-rays as they pass through layers of varying thickness and density. The CT scans generate cross-sectional images of the coalpack and thereby assist in transient front tracking and flow profiling that otherwise is practically undetectable. The CT scanning also determines the dynamic phase saturation. Xenon shall be injected into the coalpack as the tracer gas because it is dense and give good image resolution.

Technology development and application for CO₂- ECBM recovery is still at a nascent stage. The numerical simulation model is a useful tool in the development of CO₂ sequestration for ECBM recovery. The experimental study further aids in validating the simulation results. A complete description of the process is challenging because of the extreme complexity of the process. But nonetheless the CO₂- ECBM process is technically and commercially viable. CO₂ enhances the CBM production rates, increases the overall recovery and offers important possibilities for making further use of fossil fuels more compatible with climate change and mitigation policies¹⁰. The Weyburn and Sleipner projects have demonstrated the feasibility of large scale CO₂ injection projects^{4,10}.

Multicomponent Adsorption-Diffusion

There is lack of substantial research in the form of published literature, experimental study and numerical modeling of multicomponent transport phenomena for the following reasons.

- The physics behind the multicomponent diffusion phenomenon is quite complex whereas, the mathematical formulation required to solve numerically these highly non linear coupled PDE's makes the task look even more daunting.
- For non-ideal n_c component mixtures, there are (n_c-1) independent diffusion fluxes expressed by the generalized Fick's Law and $(n_c-1)^2$ diffusion coefficients^{11,12}. In the past, attempts to measure multicomponent diffusion coefficients have been limited and most of the correlations provide an "effective diffusivity" which does not work well for many non-ideal cases.
- The pore structure of coal is highly heterogeneous and complex, with the pore size varying from a few Angstroms to frequently over a micrometer in size. Consequently depending upon the pore size, different mechanisms for diffusion of an adsorbing gas tend to dominate.
- The non linear interplay between adsorption and diffusion makes the analytical solution of the governing equations almost impossible. In the absence of adsorption and assuming the "linearized theory of diffusion", one can solve for the unknown concentrations.
- As a direct consequence of the above mentioned difficulties and complexities involved, the mathematical formulation becomes an extremely challenging task.

The governing equations are described by a system of non-linear partial differential equations and appropriate numerical techniques need to be applied.

Numerical Modeling: Approach

To begin the development of the model for gas diffusion in a coal matrix, we decompose the problem into special cases and proceed by gradually adding to the complexity.

- **1D single component diffusion (no adsorption)**

Carbon-dioxide (CO₂) is taken and injected into a cylindrical coalpack and the resulting concentration profile is analyzed.

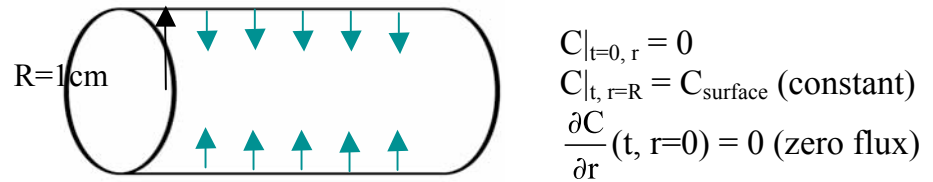


Figure 1: Single component radial diffusion inside a cylinder. Arrows indicate the direction of flux.

The diffusion equation in this case is:

$$\frac{\partial C}{\partial t} = \frac{D}{r} \frac{\partial(r \frac{\partial C}{\partial r})}{\partial r} \quad (1)$$

where D is the single component Fickian diffusion coefficient, C is the gas concentration and r the radial distance.

The above partial differential equation is solved numerically using a finite difference discretization technique. A fully implicit in time scheme is used. The resulting concentration profiles are matched with the analytical solution given by Crank¹³. Figure 2 gives the concentration at varying time scales as a function of grid numbers (radial distance).

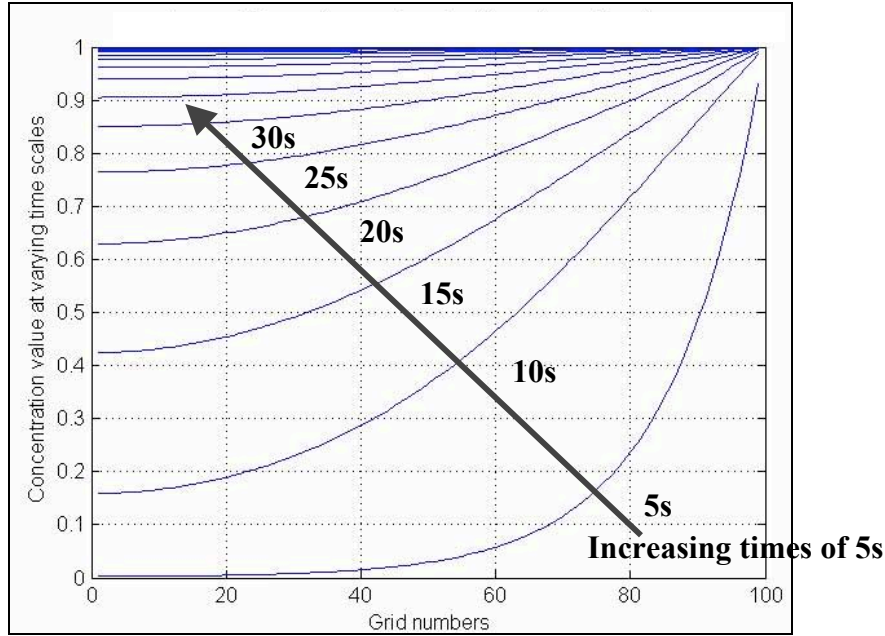


Figure 2: Concentration (mol/l) distributions at various times and radial distances for diffusion into a cylinder ($\Delta r=1\text{mm}$ and $\Delta t=0.1\text{s}$).

Once the simulation method is tested for the cylindrical case, the numerical formulation is tried in a spherical geometry. Diffusion is carried out in a sphere maintained at constant surface concentration condition, as shown in Figure 3.

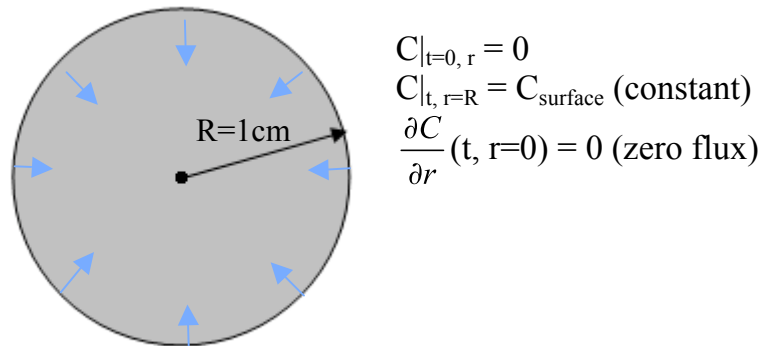


Figure 3: Single component radial diffusion inside a sphere. Arrows indicate the direction of flux.

The governing equation is:

$$\frac{\partial C}{\partial t} = \frac{D}{r^2} \frac{\partial(r^2 \frac{\partial C}{\partial r})}{\partial r} \quad (2)$$

Again the concentration profile generated numerically (Figure 4) is verified against the analytical solution given in Crank¹³.

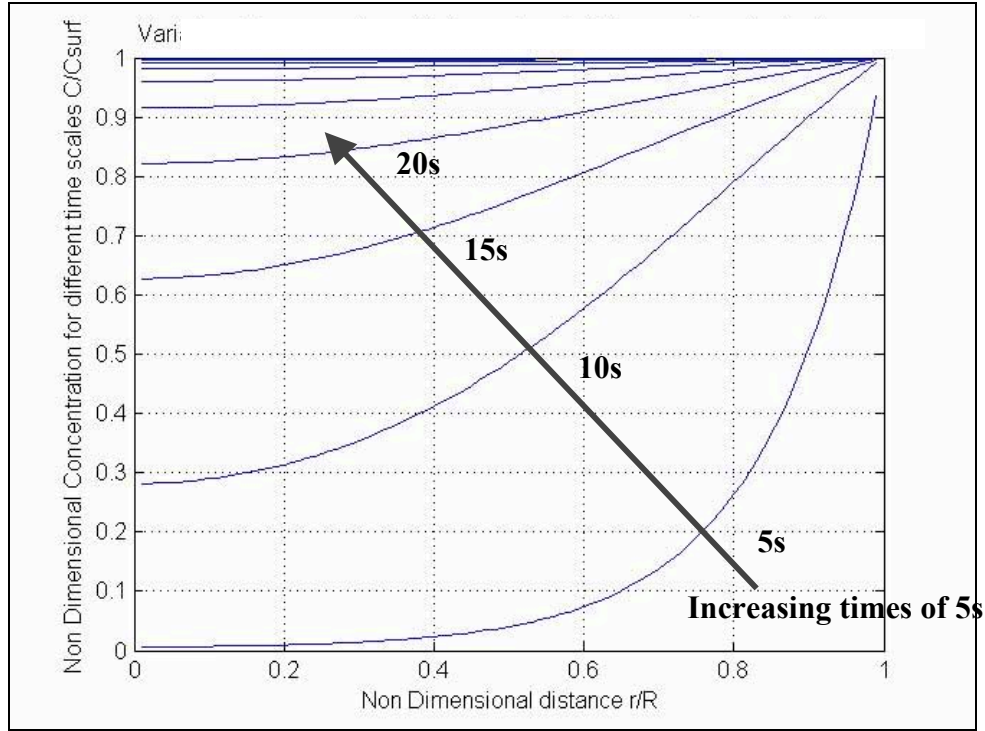


Figure 4: Concentration distributions at various times and radial distances for diffusion in a sphere ($\Delta r=1\text{mm}$ and $\Delta t=0.1\text{s}$).

- **Single component diffusion-adsorption using the extended Langmuir approach**

Once the diffusive transport model has been verified, adsorption phenomenon is introduced in the governing equations. The extended Langmuir approach^{14,15} and ideal adsorbate (IAS) theory (Myers and Prausnitz, 1965) are the most commonly used methods for prediction of mixed gas adsorption. Both the extended Langmuir model and IAS theory require pure component isotherm data for multicomponent predictions. The extended Langmuir approach due to its simplicity is the most common sorption model used in the simulation of ECBM recovery processes. This model predicts the adsorption of multicomponent gas mixtures solely from pure component data. The more general expression for the Extended Langmuir approach is:

$$a_i = \frac{\alpha_i \beta_i p_i}{1 + \sum_{j=1}^n \beta_j p_j} \quad (3)$$

where ρ_r is the density of the coalbed, ρ_i the molar density component i at standard conditions and V_{mi} and B_i the Langmuir constants for component i at a given temperature, $\alpha_i = \rho_i \rho_r V_{mi}$, $\beta_i = B_i$

Partial pressures of the component gases in the free-gas phase are determined using the following equation:

$$P_i = P y_i \quad (4)$$

The Langmuir parameters for pure component isotherms are used to predict component adsorbed volumes or concentrations for gas mixtures at any total gas pressure and free gas composition.

The governing equation for a single component simultaneous adsorption diffusion-adsorption phenomenon is:

$$\phi \frac{\partial C}{\partial t} + (1 - \phi) \frac{\partial a}{\partial t} + \frac{\partial J}{\partial x} = 0 \quad (5)$$

where C is the molar concentration of the free gas, a is the molar concentration of the adsorbed component, and J is the molar flux.

The above equation describes the transport phenomenon for a single component in a 1D system. The molar flux J is assumed to be solely due to diffusion with no advection. This is because the micro-pores inside the coal matrix offer a highly sinuous path for the gases to flow, thereby reducing the bulk velocity. From Ficks first law of diffusion, the expression for J is:

$$J = -D \frac{\partial C}{\partial x} \quad (6)$$

The adsorption behavior is represented by the extended Langmuir isotherm described by Eq. 3.

In our case the number of components (n_c) is 1 and moreover the Fickian diffusivity coefficient D is assumed to be a constant independent of concentration (linearized theory of diffusion). The governing equation takes the shape

$$\phi \frac{\partial C}{\partial t} + (1 - \phi) \frac{\partial a}{\partial t} = D\phi \frac{\partial^2 C}{\partial x^2} \quad (7)$$

For this simple case, CO_2 is injected into a 1D rectangular coalpack, with no initial injectant concentration. At the inlet the concentration is kept constant by a constant supply of CO_2 while at the other closed end, no flux condition is enforced. Finite difference scheme, explicit in space is used to discretize and numerically solve Eq. 7.

Figure 5 illustrates the development and penetration of concentration profile of CO_2 with time. The length of the core in this case is 10cm and the total time of simulation run is 200seconds. From Figure 5 one can visualize that the progress of CO_2 inside the core in presence of adsorption is quite slow.

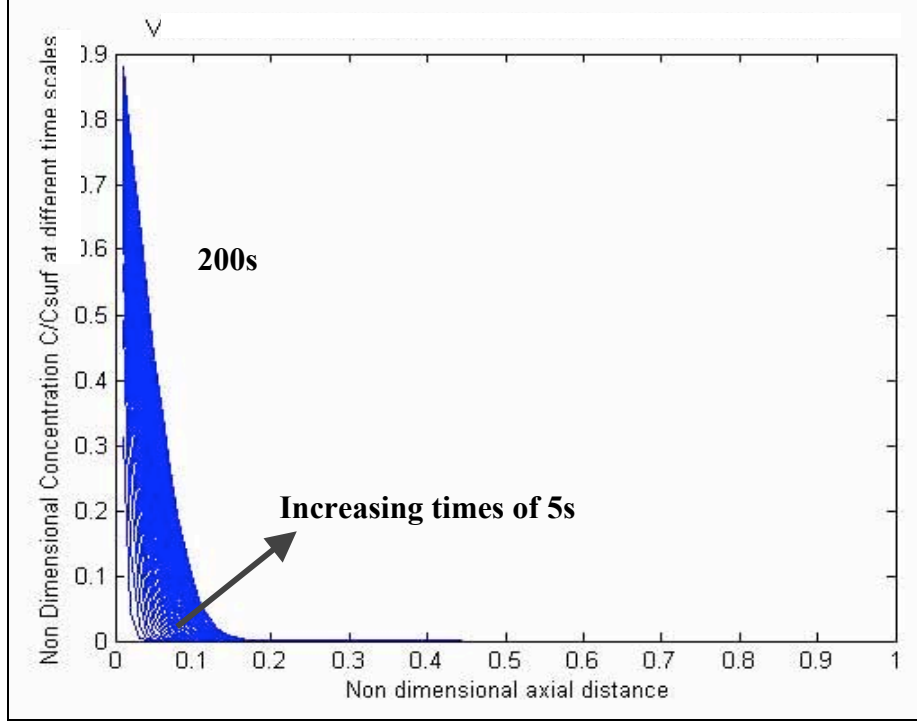


Figure 5: Concentration distribution for a single component undergoing simultaneous adsorption-diffusion phenomenon ($\Delta x=1\text{mm}$ and $\Delta t=0.1\text{s}$)

Binary adsorption-diffusion system

Once the numerical simulation for a single component undergoing simultaneous diffusion and adsorption was verified, a platform is set where one can now add to the complexity by increasing the number of components and trying out different adsorption-diffusion models. The next step was to model a 2 component adsorption-diffusion system such as CO_2 and CH_4 , wherein CO_2 is injected into a coal-pack from one end while CH_4 desorbs and diffuses out countercurrent to the flow of injectant. In the initial simulation runs, the Langmuir isotherm is used and later compared against the IAS model.

The governing equations in this case are

$$\phi \frac{\partial C_1}{\partial t} + (1 - \phi) \frac{\partial \left(\frac{\alpha_1 \beta_1 p_1}{1 + \beta_1 p_1 + \beta_2 p_2} \right)}{\partial t} = \phi D_{12} \frac{\partial^2 C_1}{\partial t^2} \quad (8)$$

$$\phi \frac{\partial C_2}{\partial t} - (1 - \phi) \frac{\partial \left(\frac{\alpha_2 \beta_2 p_2}{1 + \beta_1 p_1 + \beta_2 p_2} \right)}{\partial t} = \phi D_{21} \frac{\partial^2 C_2}{\partial t^2} \quad (9)$$

where C_1 and C_2 are the free gas concentration of CO_2 and CH_4 respectively, α and β are the Langmuir constants and D_{12}, D_{21} are Fickian binary diffusion coefficients. As the diffusion is equimolar and countercurrent, the diffusivities are equal in magnitude and

assumed to be constant. Initially the coalbed is saturated with CH₄ and CO₂ is injected from one end maintained at constant injectant concentration while a no flux boundary condition is enforced at the other end. Coal has greater affinity towards CO₂ and as a result it preferentially adsorbs into the coalbed while with decreasing partial pressure, CH₄ desorbs and is recovered as a free gas.

The gases are assumed to behave as ideal and as a result the partial pressure, p_i of component i in the free gas phase is

$$p_i = C_i RT \quad (10)$$

Eqs. 8 and 9 are coupled non-linear partial differential equations in C_1 and C_2 . Therefore, an iterative procedure is used to compute these values over each grid location and for each time step.

Figure 6 illustrates the development of the concentration profile of CO₂ and CH₄ with time. The length of the core in this case is 10cm and the total time of simulation run is 200seconds. Because of the countercurrent diffusion phenomena taking place, the concentration profiles for the two components are symmetric.

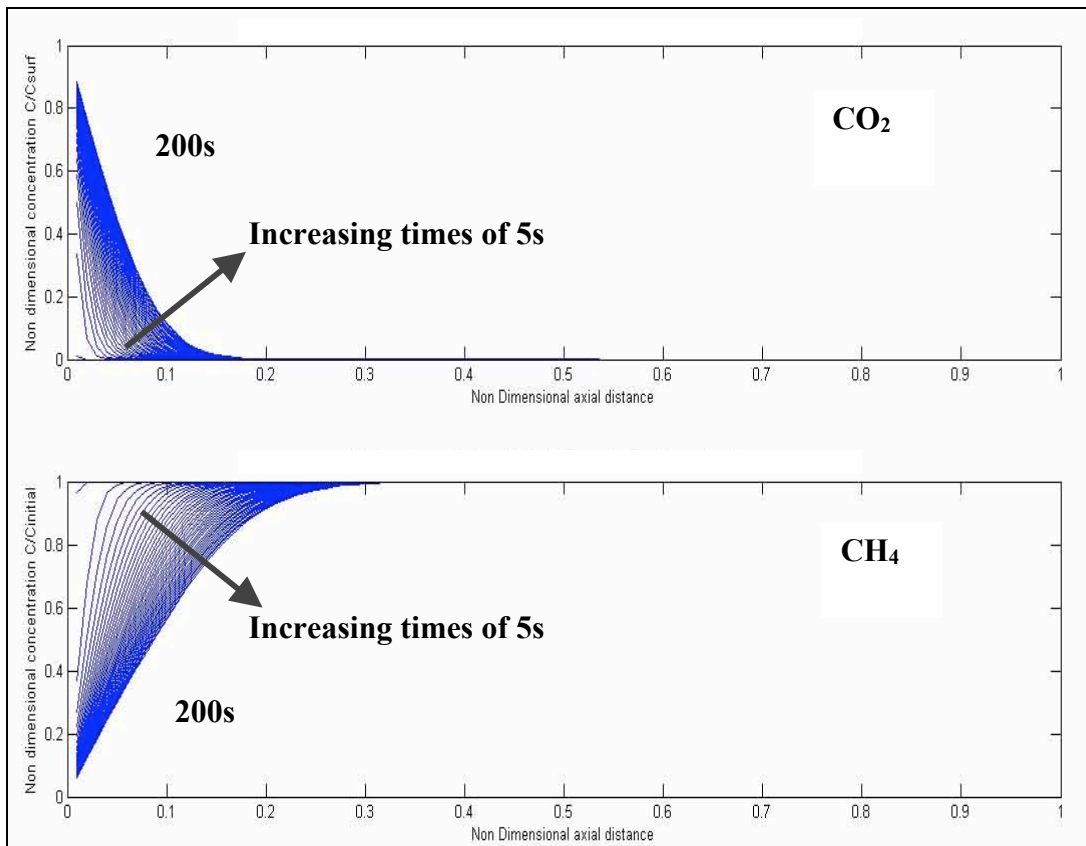


Figure 6: Concentration distribution for a binary system undergoing countercurrent adsorption-diffusion phenomenon ($\Delta x=1mm$ and $\Delta t=0.1s$).

Transport of multicomponent gases

In the multicomponent ($n_c > 2$) domain, it is the diffusion of gases that is the most intriguing part. Fick's law of diffusion is widely used to describe the coal bed gas diffusion process because of its simplicity. If used in its actual form, its validity is severely restricted and even misleading in many practical situations where the diffusion coefficients of the fluid species depend on composition. The Maxwell-Stefan (MS) diffusion formulation better applies to multicomponent fluid diffusion and deals rigorously with the interactions between multicomponent gas molecules.

In our case, the simplicity of the Fick diffusion expression has been retained but at the same time the MS approach has been incorporated to describe the transient multicomponent gas diffusion dynamics.

The expression of the molecular diffusion flux of an n_c multicomponent mixture is given by the generalized expression

$$\underline{\mathbf{J}} = - \underline{\mathbf{D}} \nabla \underline{\mathbf{C}} \quad (11)$$

where

$$\underline{\mathbf{J}} = \begin{pmatrix} J_1 \\ J_2 \\ \vdots \\ J_{n_c-1} \end{pmatrix}, \quad \underline{\mathbf{C}} = \begin{pmatrix} C_1 \\ C_2 \\ \vdots \\ C_{n_c-1} \end{pmatrix} \quad \text{and} \quad \underline{\mathbf{D}} = \begin{pmatrix} D_{1,1} & D_{1,2} & \dots & D_{1,n_c-1} \\ D_{2,1} & D_{2,2} & \dots & D_{2,n_c-1} \\ \vdots & \ddots & \ddots & \vdots \\ D_{n_c-1,1} & \dots & \dots & D_{n_c-1,n_c-1} \end{pmatrix}$$

Eq 11 in expanded form is

$$J_i = \sum_{j=1}^{n_c-1} D_{i,j} \nabla x_j, \quad i=1,2,\dots,n_c-1 \quad (12)$$

The diagonal entries $D_{i,i}$; $i=1,2,\dots,n_c-1$ are known as the main diffusion coefficients and the off diagonal entities $D_{i,j}$; $i,j=1,2,\dots,n_c-1$ ($i \neq j$) are known as the cross diffusion coefficients, which are generally non zero and not symmetric ($D_{i,j} \neq D_{j,i}$). Also the coefficients can take positive or negative values. The diffusion flux satisfies the constraint equation^{11,12}

$$\sum_{i=1}^{n_c} J_i = 0 \quad (13)$$

Thus, the diffusion flux for the n_c component is calculated using Eq 13.

Once the diffusion fluxes have been defined, the diffusion coefficients need to be estimated. Diffusion in micropores is strongly temperature and concentration dependent. It is here that the Maxwell-Stefan (MS) formulation is integrated with Ficks Law and the binary diffusivities \mathcal{D}_{ij} used to compute the Fickian diffusivities. For our ternary system, the elements of $\underline{\mathbf{D}}$ are given as

$$\begin{aligned}
D_{11} &= D_{13}(x_1 D_{23} + (1-x_1) D_{12})/S \\
D_{12} &= x_1 D_{23}(D_{13} D_{12})/S \\
D_{21} &= x_2 D_{13}(D_{23} - D_{12})/S \\
D_{22} &= D_{23}(x_2 D_{13} + (1-x_2) D_{12})/S
\end{aligned} \tag{14}$$

where

$$S = x_1 D_{23} + x_2 D_{13} + x_3 D_{12} \tag{15}$$

Note that the numerical values of D_{ij} depend on the particular choice of system numbering and do not have any physical significance to i - j interaction. In our case, component 1 is CO_2 , component 2 is N_2 and component 3 is CH_4 .

The diffusion and adsorption of gases takes place inside a linear 1 D geometry initially saturated with CH_4 . CO_2 and N_2 diffuses from one end while CH_4 diffuses countercurrent to the flow of injectant gases.

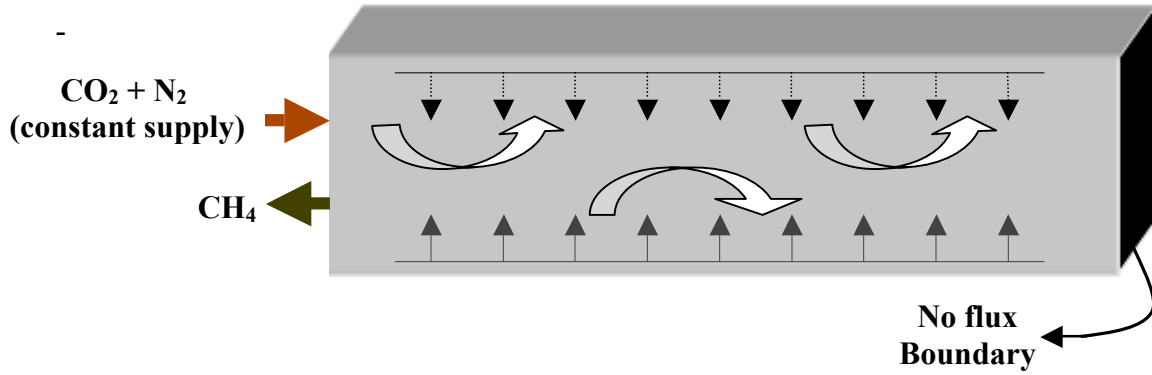


Figure 7: Schematic of a model coal matrix undergoing simultaneous adsorption-diffusion.

For the 3 component adsorption-diffusion problem, there are two species balance equation (Eqs. 16 and 17) and one overall mass balance relation (Eq. 18).

$$\phi \frac{\partial C_1}{\partial t} + (1-\phi) \frac{\partial}{\partial t} \left(\frac{\alpha_1' C_1}{1 + \beta_1' C_1 + \beta_2' C_2 + \beta_3' C_3} \right) = \phi \left(\frac{\partial}{\partial x} (D_{11} \frac{\partial C_1}{\partial x} + D_{12} \frac{\partial C_2}{\partial x}) \right) \tag{16}$$

$$\phi \frac{\partial C_2}{\partial t} + (1-\phi) \frac{\partial}{\partial t} \left(\frac{\alpha_2' C_2}{1 + \beta_1' C_1 + \beta_2' C_2 + \beta_3' C_3} \right) = \phi \left(\frac{\partial}{\partial x} (D_{21} \frac{\partial C_1}{\partial x} + D_{22} \frac{\partial C_2}{\partial x}) \right) \tag{17}$$

$$\phi \frac{\partial(C_1 + C_2 + C_3)}{\partial t} + (1 - \phi) \frac{\partial}{\partial t} \left(\frac{\alpha'_1 C_1 + \alpha'_2 C_2 + \alpha'_3 C_3}{1 + \beta'_1 C_1 + \beta'_2 C_2 + \beta'_3 C_3} \right) = 0 \quad (18)$$

Initially the concentration of CO₂ and N₂ (i.e. C₁ and C₂) is zero everywhere.

$$C_1(x, 0) = 0; \forall x, t = 0, \quad C_2(x, 0) = 0; \forall x, t = 0$$

The coal matrix is initially saturated with CH₄ (C₃)

$$C_3(x, 0) = C_{\text{initial}}; \forall x, t = 0 \quad (19a)$$

Constant supply of injectants (CO₂ and N₂) is maintained at the inlet while no flux boundary condition is enforced at x=L.

$$\begin{aligned} C_j(0, t) &= C_{j,\text{inlet}}; x = 0, \forall t > 0, j = 1, 2, \\ C_3(0, t) &= 0; x = 0, \forall t > 0 \\ \frac{\partial C_j}{\partial x}(L, t) &= 0; x = L, \forall t > 0, j = 1, 2, 3 \end{aligned} \quad (19b)$$

The differential equations describing the model are non-linear and solved numerically. The continuum equations were solved in the x-coordinate using the finite difference approximation. This leads to a set of coupled discretized equations that were solved for different spatial locations integrated in time using the non-linear form of Newton Raphson iteration technique. Based upon the time level of spatial discretization, the following are the numerical solution techniques used:

- Explicit (For LM adsorption isotherm)
- Semi-Implicit (For LM adsorption isotherm)
- Fully Implicit (For both IAS and LM adsorption isotherm)
 - Untuned numerical model
 - Tuned numerical model

Explicit solution method

In this solution method, the spatial discretization of the differential equations is done for variables at previous time step. Thus it allows the explicit determination of $C_{1,i}^{n+1}$, $C_{2,i}^{n+1}$, $C_{3,i}^{n+1}$ from known values at previous time level ($C_{1,i}^n$, $C_{2,i}^n$, $C_{3,i}^n$). But, in this case these discretized equations are coupled and Newton Raphson iteration technique is used to solve for C₁, C₂ and C₃ concentration profile. The extended langmuir model has been used to describe the adsorption mechanism for the ternary gas mixture.

The explicit discretization solution technique is conditionally stable and enforces a restriction on the size of the time step. For small time step values it is guaranteed to converge, but then this comes at the price of computational cost.

The numerical code takes porosity, Langmuir isotherm constants and MS diffusivities as the input and then implicitly calculates the Fickian diffusivities. In the past, attempts to measure multicomponent diffusion coefficients have been limited. Most correlation for

multicomponent diffusion coefficients are mainly based on data for binary diffusion coefficients¹⁶⁻²¹. But almost all these correlations neglect the cross diffusion coefficients at non-ideal conditions and assume effective diffusivity. So in the absence of adequate data, arbitrary binary diffusivity values were taken as input and the simulation performed. It was observed that for some input values, the concentration of CH₄ turned out to be negative for some grid locations and at arbitrary time scales. Most presumably this is due to physical inconsistency introduced into the model rather than any logical discrepancy.

The following concentration profiles have been generated using a grid size (Δx) of 1mm and a time-step size (Δt) of 0.1s. The binary diffusivities used in this case are $D_{13}=0.0123 \text{ mm}^2/\text{s}$; $D_{12}=0.0134 \text{ mm}^2/\text{s}$; $D_{23}=0.011 \text{ mm}^2/\text{s}$

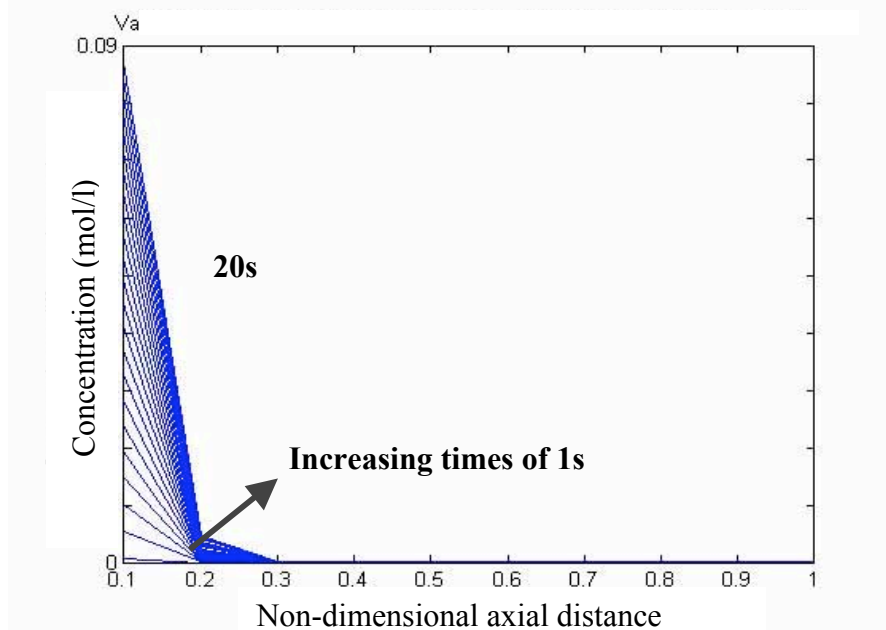


Figure 8: CO₂ concentration distribution as a function of space and time

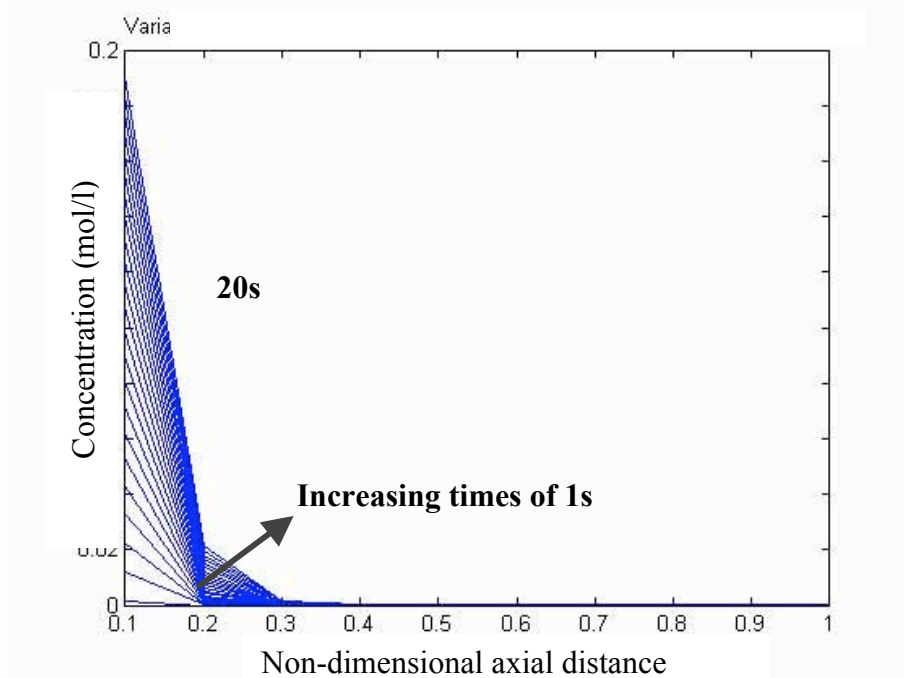


Figure 9: N_2 concentration distribution as a function of space and time

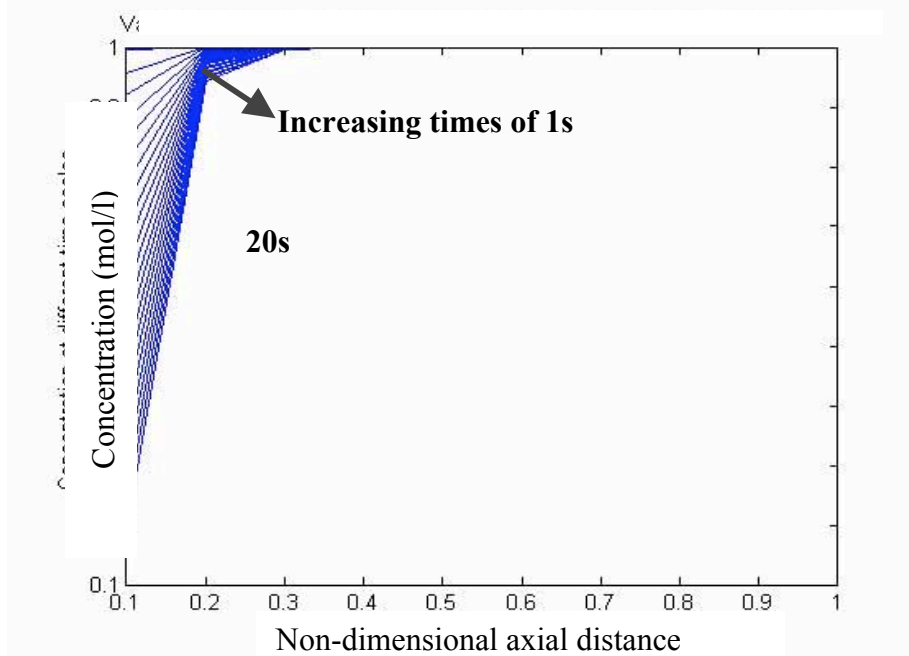


Figure 10: CH_4 concentration distribution as a function of space and time

Semi-Implicit solution method

In this solution technique, everything except the adsorption term has been treated in a fully implicit manner. The non-linear adsorption term (modeled using LM model) is treated in a semi-implicit fashion. Equation 20 shows the semi-implicit treatment of the adsorption term for C_1 component.

$$\frac{\partial a_1}{\partial t} = \frac{\partial a_1}{\partial C_1} \frac{\partial C_1}{\partial t} \approx \frac{\partial a_1}{\partial C_1} \bigg|_n \left(\frac{C_{1,i}^{n+1} - C_{1,i}^n}{\Delta t} \right)$$

(20)

Though the above treatment is intended to reduce the numerical complexity of the problem, the implicit treatment of the flux terms with respect to time makes the overall simulation task undeniably more challenging than the previous case. The semi-implicit discretization approach improves upon the stability and convergence of the numerical scheme and reduces the time step constraint significantly.

The following concentration profiles have been generated using a grid size (Δx) of 1mm and a time-step size (Δt) of 0.5s. The MS diffusivities used in this case are $D_{13}=0.02 \text{ mm}^2/\text{s}$; $D_{12}=0.03 \text{ mm}^2/\text{s}$; $D_{23}=0.01 \text{ mm}^2/\text{s}$. From Figures 11, 12 and 13 one finds that the semi-implicit solution technique results in much smoother concentration profiles for a larger time step than for the explicit solution method.

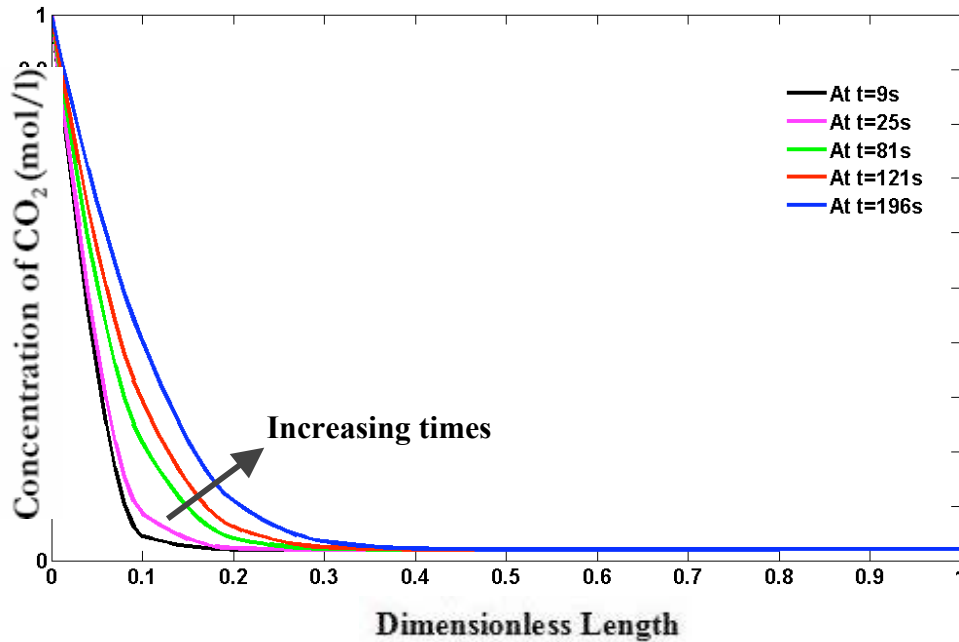


Figure 11: CO_2 concentration distribution as a function of space and time, semi-implicit method

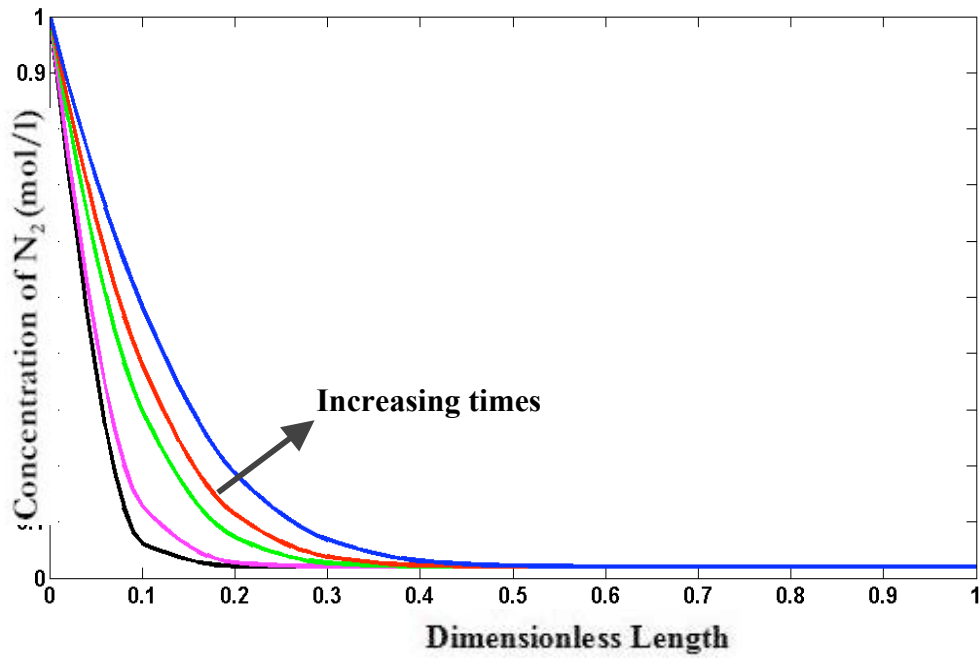
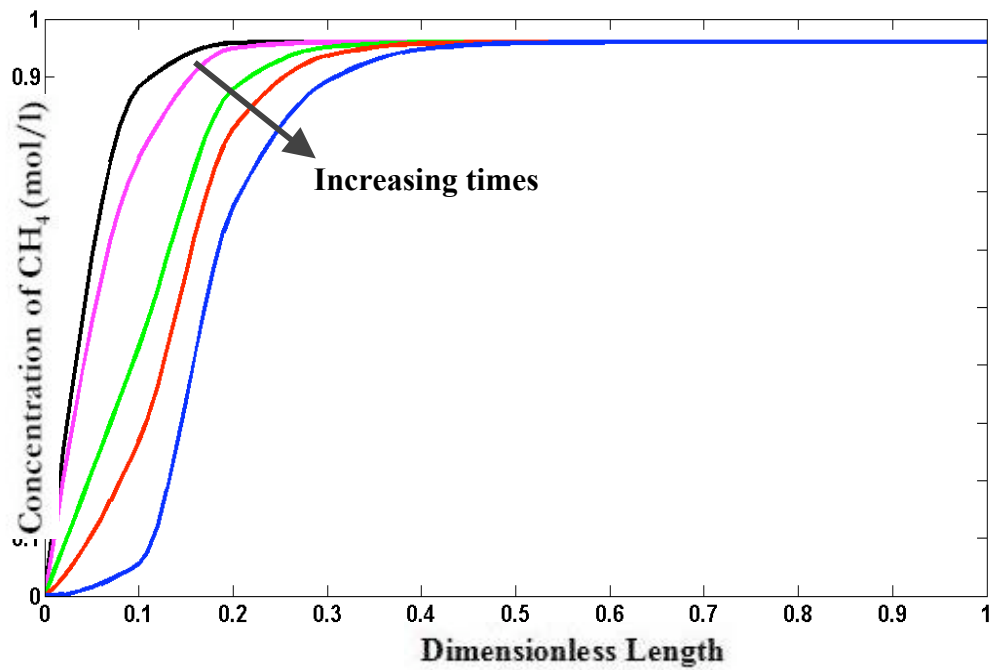


Figure 12: N_2 concentration distribution as a function of space and time, semi-implicit method



*Figure 13: CH_4 concentration distribution as a function of space and time, semi-implicit method
Fully Implicit solution method*

Here it is assumed that, at time t , C_i suddenly changes from C_i^n to C_i^{n+1} and stays at this value during the whole time interval (backward in time extrapolation). The unknown C_i^{n+1} is now implicitly related to unknowns of the neighbor grid points. The set of equations for all the grid points forms a tridiagonal system of equations that needs to be solved at each time step.

For the ternary adsorption-diffusion transport problem, there are 3 primary variables (C_1 , C_2 and C_3). Just like the semi-implicit solution technique, the fully implicit discretization scheme introduces 6 additional variables in the nonlinear residual equations (Eq. 21, 22). In the preceding examples of the residuals equations, the Extended LM model has been used to represent the adsorption term. Eq. 21 is the residual equation (R_{1i}) obtained upon discretizing the species balance PDE (Eq. 16). The structure of the residual equation (R_{2i}) for the other species balance equation (Eq. 17) is the same as R_{1i} , but with C_{2i} as the primary variable. The residual equation (R_{3i}) for the overall mass balance (Eq. 18) is shown in Eq. 22.

$$\phi \left(\frac{C_{1,i}^{n+1} - C_{1,i}^n}{\Delta t} \right) + \frac{(1-\phi)}{\Delta t} \left\{ \frac{\alpha'_1 C_{1,i}^{n+1}}{1 + \beta'_1 C_{1,i}^{n+1} + \beta'_2 C_{2,i}^{n+1} + \beta'_3 C_{3,i}^{n+1}} - \frac{\alpha'_1 C_{1,i}^n}{1 + \beta'_1 C_{1,i}^n + \beta'_2 C_{2,i}^n + \beta'_3 C_{3,i}^n} \right\} - \frac{\phi}{\Delta x^2} \left\{ \frac{D_{23} (C_{1,i+1}^{n+1} - C_{1,i}^{n+1}) \{ C_{1,i+1}^{n+1} (D_{23} - D_{12}) + (C_{1,i+1}^{n+1} + C_{2,i+1}^{n+1} + C_{3,i+1}^{n+1}) D_{12} \}}{(C_{1,i+1}^{n+1} D_{23} + C_{2,i+1}^{n+1} D_{13} + C_{3,i+1}^{n+1} D_{12})} - \frac{D_{13} (C_{1,i}^{n+1} - C_{1,i-1}^{n+1}) \{ C_{1,i}^{n+1} (D_{23} - D_{12}) + (C_{1,i}^{n+1} + C_{2,i}^{n+1} + C_{3,i}^{n+1}) D_{12} \}}{(C_{1,i}^{n+1} D_{23} + C_{2,i}^{n+1} D_{13} + C_{3,i}^{n+1} D_{12})} + \frac{D_{23} (D_{13} - D_{12}) C_{1,i+1}^{n+1} (C_{2,i+1}^{n+1} - C_{2,i}^{n+1})}{(C_{1,i+1}^{n+1} D_{23} + C_{2,i+1}^{n+1} D_{13} + C_{3,i+1}^{n+1} D_{12})} - \frac{D_{23} (D_{13} - D_{12}) C_{1,i}^{n+1} (C_{2,i}^{n+1} - C_{2,i-1}^{n+1})}{(C_{1,i}^{n+1} D_{23} + C_{2,i}^{n+1} D_{13} + C_{3,i}^{n+1} D_{12})} \right\} = 0 \quad (21)$$

$$\phi \left\{ \frac{(C_{1,i}^{n+1} + C_{2,i}^{n+1} + C_{3,i}^{n+1}) - (C_{1,i}^n + C_{2,i}^n + C_{3,i}^n)}{\Delta t} \right\} - \frac{(1-\phi)}{\Delta t} \left\{ \frac{\alpha'_1 C_{1,i}^{n+1} + \alpha'_2 C_{2,i}^{n+1} + \alpha'_3 C_{3,i}^{n+1}}{1 + \beta'_1 C_{1,i}^{n+1} + \beta'_2 C_{2,i}^{n+1} + \beta'_3 C_{3,i}^{n+1}} - \frac{\alpha'_1 C_{1,i}^n + \alpha'_2 C_{2,i}^n + \alpha'_3 C_{3,i}^n}{1 + \beta'_1 C_{1,i}^n + \beta'_2 C_{2,i}^n + \beta'_3 C_{3,i}^n} \right\} = 0 \quad (22)$$

The Jacobian (\underline{J}) is a 3×3 block tri-diagonal matrix. Equation 23 shows the i^{th} row of 3×3 blocks in the \underline{J} matrix. All the Jacobian terms are derived by analytical differentiations of the residual equations.

$$\underline{J}_i = \begin{bmatrix} \left(\frac{\partial R_{1i}}{\partial C_{1,i-1}^{n+1}} & \frac{\partial R_{1i}}{\partial C_{2,i-1}^{n+1}} & \frac{\partial R_{1i}}{\partial C_{3,i-1}^{n+1}} \right) & \left(\frac{\partial R_{1i}}{\partial C_{1,i}^{n+1}} & \frac{\partial R_{1i}}{\partial C_{2,i}^{n+1}} & \frac{\partial R_{1i}}{\partial C_{3,i}^{n+1}} \right) & \left(\frac{\partial R_{1i}}{\partial C_{1,i+1}^{n+1}} & \frac{\partial R_{1i}}{\partial C_{2,i+1}^{n+1}} & \frac{\partial R_{1i}}{\partial C_{3,i+1}^{n+1}} \right) \\ \left(\frac{\partial R_{2i}}{\partial C_{1,i-1}^{n+1}} & \frac{\partial R_{2i}}{\partial C_{2,i-1}^{n+1}} & \frac{\partial R_{2i}}{\partial C_{3,i-1}^{n+1}} \right) & \left(\frac{\partial R_{2i}}{\partial C_{1,i}^{n+1}} & \frac{\partial R_{2i}}{\partial C_{2,i}^{n+1}} & \frac{\partial R_{2i}}{\partial C_{3,i}^{n+1}} \right) & \left(\frac{\partial R_{2i}}{\partial C_{1,i+1}^{n+1}} & \frac{\partial R_{2i}}{\partial C_{2,i+1}^{n+1}} & \frac{\partial R_{2i}}{\partial C_{3,i+1}^{n+1}} \right) \\ \left(\frac{\partial R_{3i}}{\partial C_{1,i-1}^{n+1}} & \frac{\partial R_{3i}}{\partial C_{2,i-1}^{n+1}} & \frac{\partial R_{3i}}{\partial C_{3,i-1}^{n+1}} \right) & \left(\frac{\partial R_{3i}}{\partial C_{1,i}^{n+1}} & \frac{\partial R_{3i}}{\partial C_{2,i}^{n+1}} & \frac{\partial R_{3i}}{\partial C_{3,i}^{n+1}} \right) & \left(\frac{\partial R_{3i}}{\partial C_{1,i+1}^{n+1}} & \frac{\partial R_{3i}}{\partial C_{2,i+1}^{n+1}} & \frac{\partial R_{3i}}{\partial C_{3,i+1}^{n+1}} \right) \end{bmatrix} \quad (23)$$

Extended Langmuir Adsorption Model (ELM)

Figures 14, 15, 16 illustrate the concentration profiles for CO₂, N₂ and CH₄ generated using a grid size (Δx) of 1mm and a time-step size (Δt) of 0.1s. The MS diffusivities used in this case are $D_{13}=0.2 \text{ mm}^2/\text{s}$; $D_{12}=0.3 \text{ mm}^2/\text{s}$; $D_{23}=0.1 \text{ mm}^2/\text{s}$.

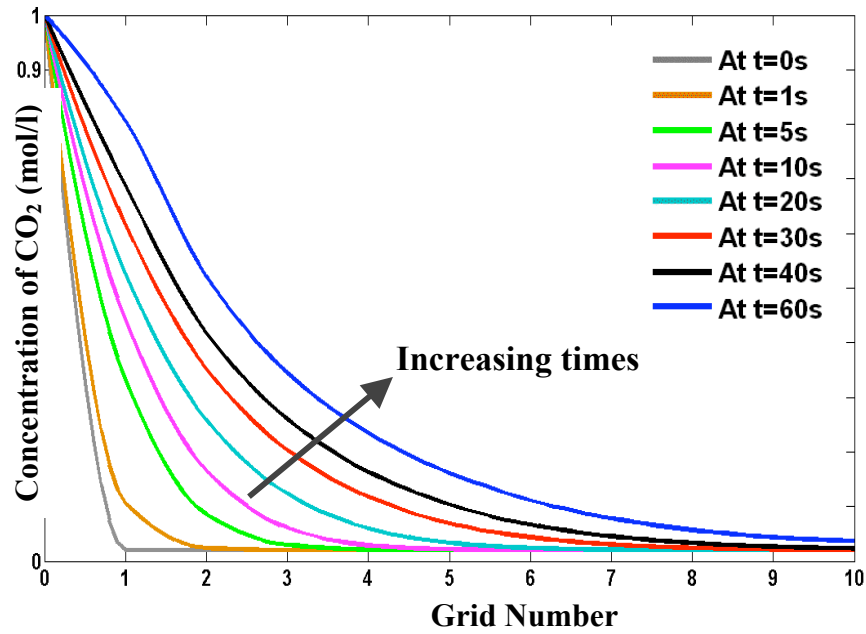


Figure 14: CO₂ concentration distribution as a function of space and time, ELM

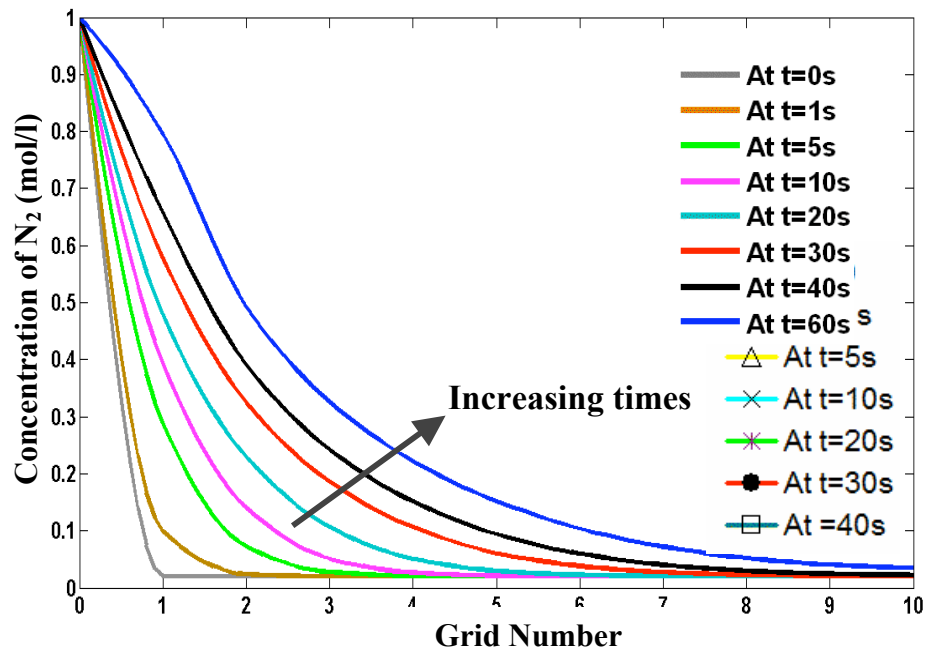


Figure 15: N₂ concentration distribution as a function of space and time, ELM

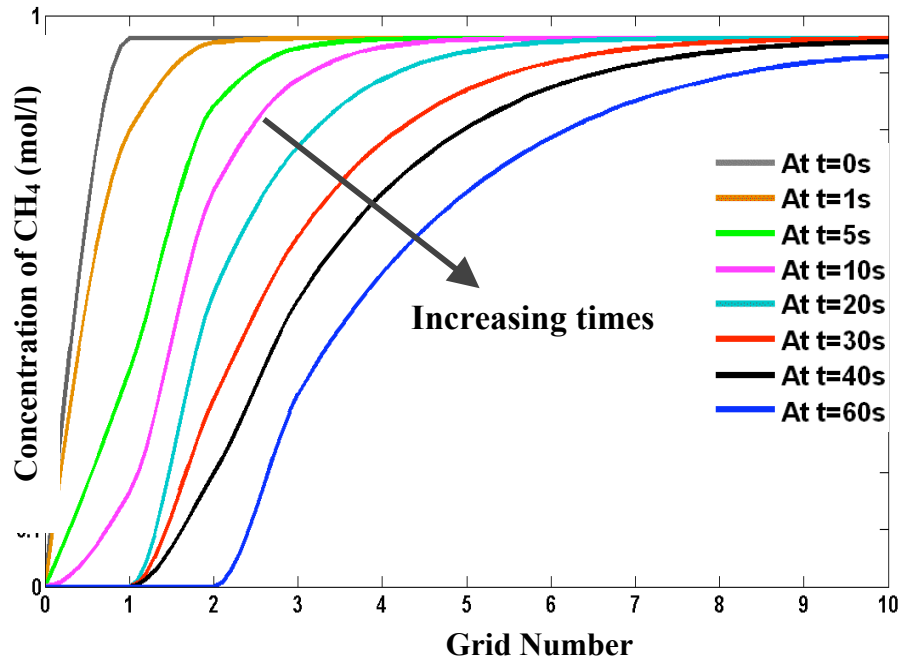


Figure 16: CH₄ concentration distribution as a function of space and time, ELM

Unlike many of the simulation models that assume the linearized theory of diffusion, the Fickian diffusivities in our case are computed rigorously from MS diffusivities and composition (Eq.14, 15). Figures 17, 18, 19, 20 illustrate the variation of diffusivity parameters with time. All diffusivities are in units of mm^2/s . For some cases, this variation is quite significant and has an important bearing on the gas adsorption-diffusion dynamics. For instance, D_{21} varies by a factor of about 10 in Fig. 19.

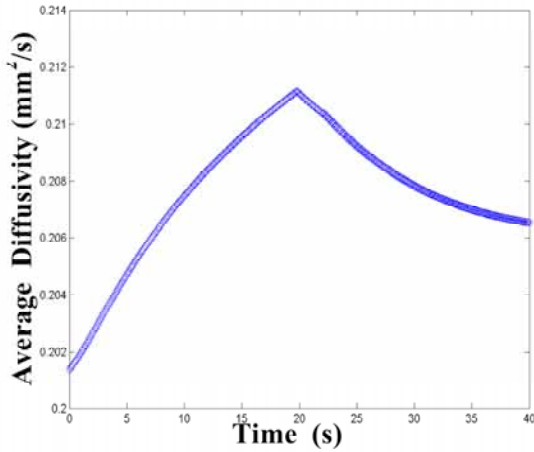


Figure 17: Variation of D_{11} with time

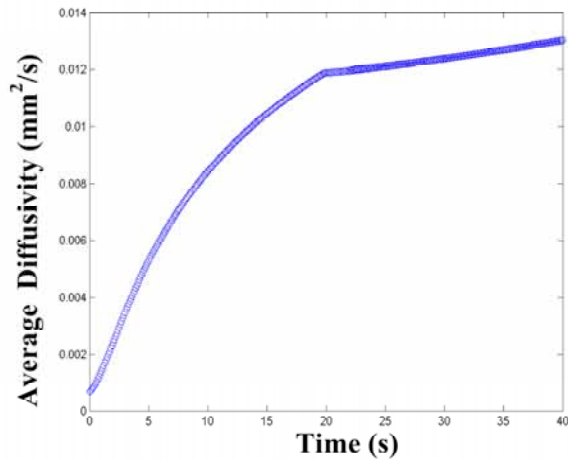


Figure 18: Variation of D_{12} with time

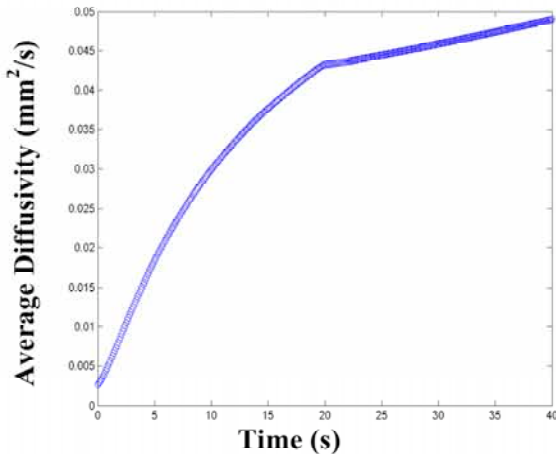


Figure 19: Variation of D_{21} with time

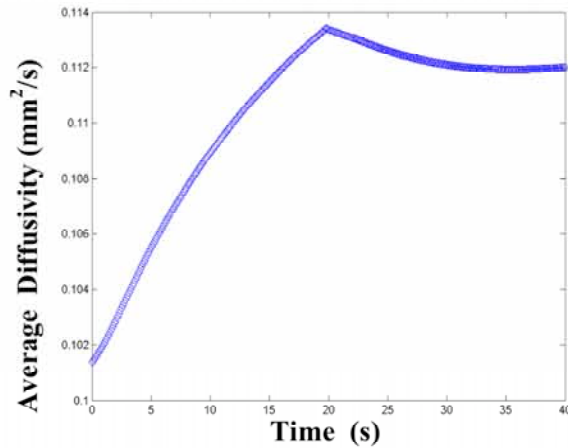


Figure 20: Variation of D_{22} with time

- *Ideal Adsorbate Solution (IAS) Model*

The extended Langmuir adsorption model has been used throughout the simulation study so far. Although fairly accurate for 2 component system^{5,22}, it would be interesting to

compare it against the *IAS model*⁹. The separation factor or selectivity ratio, for a binary gas adsorption system is defined as¹⁴

$$\alpha_{ij} = \frac{(x/y)_i}{(x/y)_j} \quad (24)$$

For the extended Langmuir isotherm, the separation factor is the ratio of adsorption equilibrium constants for the pure component isotherms¹⁴ and is therefore independent of the concentration and total pressure (Figure 21).

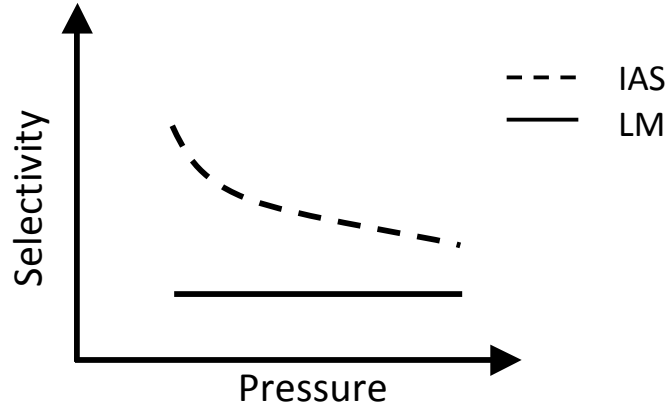


Figure 21: Selectivity to concentration or total pressure (Jessen et al., 2007)

The assumption, however of a constant separation factor is not necessarily accurate for all systems¹⁴. An increasing selectivity for the most strongly adsorbed component with decreasing concentration of that component is generally observed (Myers, 1968). Moreover from literature survey it has been found that the Extended Langmuir model is inadequate to describe the behavior of ternary CH₄/CO₂/N₂ displacements. A sorption model more sophisticated than the extended langmuir model is needed to represent the dynamics of multicomponent systems²². We use IAS model and compare the predicted behavior against the extended langmuir model.

The IAS model assumes that the gas phase behaves as an ideal gas and that the adsorbate phase behaves as an ideal mixture. Thus, the gas phase and adsorbed phase are related by the expression

$$y_i p = x_i p_i^{\circ}(\pi) \quad (25)$$

where $p_i^{\circ}(\pi)$ is the hypothetical spreading pressure of the pure component that gives the same spreading pressure on the surface (Eq. 26, for n_c components).

$$\psi = \frac{A\pi}{R_g T} = \int_0^{p_1^{\circ}} \frac{C_{\mu 1}}{P_1} dp_1 = \int_0^{p_2^{\circ}} \frac{C_{\mu 2}}{P_2} dp_2 = \dots = \int_0^{p_{n_c}^{\circ}} \frac{C_{\mu n_c}}{P_{n_c}} dp_{n_c} \quad (26)$$

The mole fractions in the gaseous and adsorbate phase satisfy the constraint relationship

$$\sum x_i = 1 \quad \sum y_i = 1 \quad (27)$$

The gas phase composition (y_i) is related to the total pressure (P) by the gas law (Eq. 28).

$$y_i P = Z C_i R T \quad (28)$$

In our case, we assume that the pressure is low and the Ideal Gas Law ($Z=1$) holds. Once the mole fractions in the adsorbed phase (x_i) and the hypothetical pressure of the pure component (P_i^0) that gives the same spreading pressure as that of the mixture (Π), the total amount adsorbed are calculated from the equation:

$$\frac{1}{C_{\mu T}} = \sum_{i=1}^{n_C} \frac{x_i}{C_{\mu i}^0} \quad (29)$$

where, $C_{\mu i}^0$ is the adsorbed amount (mol/l) of pure component j at the hypothetical pressure P_i^0 , that is

$$C_{\mu i}^0 = f^0(P_i^0) \quad (30)$$

Knowing the total amount adsorbed ($C_{\mu T}$), the amount adsorbed contributed by the component “ i ” is given by:

$$C_{\mu i} = x_i C_{\mu T} \quad (31)$$

For the case of adsorption-diffusion for an n_C component mixture modeled using IAS, the unknowns are:

1. n_C values of mole fractions in the adsorbed phase (X_i)
2. n_C values of mole fractions in the adsorbed phase (Y_i)
3. Spreading pressure Π
4. n_C values of the hypothetical pressure of the pure component, P_i^0
5. $C_{\mu T}$

The introduction of additional variable P_i^0 makes the IAS model more complicated because now unlike the extended langmuir model, the adsorbate composition (x_i) cannot be expressed directly in terms of the gaseous phase composition (Eq. 25). An iterative procedure has to be invoked in order to solve for the case when the IAS model is incorporated. With this big picture in mind, the adsorption-diffusion problem for the ternary case is divided into two parts.

Part 1:

The first part deals with formulating the algorithm to compute the adsorbate composition (x_i) given the pressure and gas phase composition (Figure 22). It is based on the procedure outlined by Do²³ and Jessen et al.²²

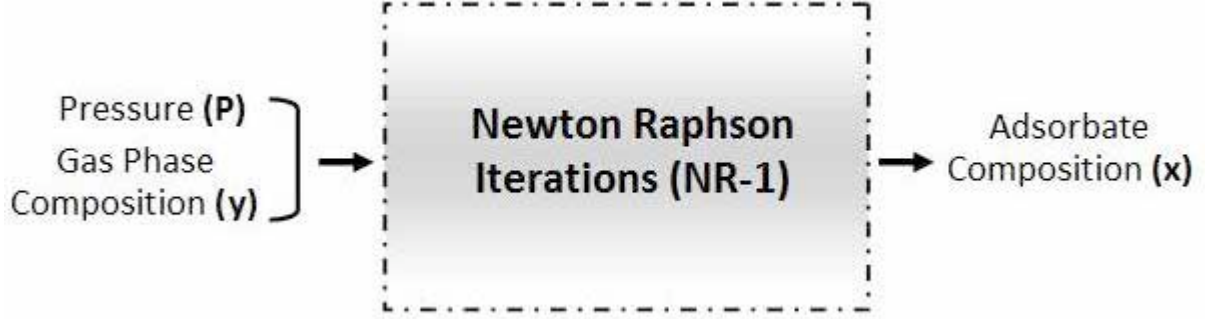


Figure 22: Figure stating the objective of the algorithm developed in part-1

It invokes Newton-Raphson iterations to solve the non-linear residual. The algorithm is referenced as NR-1 and is used in the later stages to solve the adsorption-diffusion transport problem, as follows.

Step 1: Estimate the reduced spreading pressure as the molar average of the following integral:

$$\psi = \frac{A\pi}{R_g T} = \sum_{j=1}^N y_j \int_0^P \frac{C_{uj}}{P_j} dp_j \quad (32)$$

The right hand side of the integral can be evaluated because all variables (y , P , and the single component isotherm equations) are known. If the pure component isotherm can be approximated by a Langmuir equation, then the initial estimate of the spreading pressure can be taken as:

$$\psi = C_{\mu s} \ln\left(1 + \sum_{i=1}^N b_i P_i\right) \quad (33)$$

where, $C_{\mu s}$ is taken as the average of the maximum adsorbed concentration of all species

Step 2: Using the estimated reduced spreading pressure from step 1, evaluate the pure component pressure P_i^0 that gives that reduced pressure using Eq. 26, and then evaluate the amount adsorbed for the single component from the single component isotherm at that hypothetical pressure P_i^0 . In order to solve the integral in Eq. 26 analytically, the pure gas adsorption isotherm has to be decided upon. When the single component isotherm takes the form of the Langmuir isotherm (Eq. 3), the spreading pressure (Ψ) for the pure component isotherm of Langmuir form is related to P_i^0 as:

$$\psi = \alpha_i \ln(1 + b_i P_i^0) \quad (34)$$

Hence, the pure component pressure (P_i^0) estimate can be obtained explicitly from the above equation as:

$$P_i^o = \frac{\exp(\psi / \alpha_i) - 1}{b_i} \quad (35)$$

Step 3: Use Eq. 25, 27 to form the residual and solve for Ψ using Newton-Raphson iterations.

$$F(\psi) = \sum x_i - 1 = \sum_{i=1}^N \frac{Py_i}{P_i^o(\psi)} - 1 = 0 \quad (36)$$

The residual (Eq. 36) is a function of only the spreading pressure (Ψ) as the hypothetical pressure (P_i^o) is a function of the spreading pressure. The iteration formula for the reduced spreading pressure is

$$\psi^{k+1} = \psi^k - \frac{F(\psi^{(k)})}{F'(\psi^{(k)})} \quad (37)$$

$$F'(\psi^{(k)}) = \left[-\sum_{j=1}^N \frac{Py_j}{[P_j^o(\psi)]^2} \frac{dP_j^o(\psi)}{d\psi} \right] = \left[-\sum_{j=1}^N \frac{Py_j}{[P_j^o(\psi)] C_{ij}^o} \right]_{\psi=\psi^{(k)}} \quad (38)$$

Step 4: Using the converged value of Ψ , compute the pure component pressure (P_i^o) using Eq. 35 and then the adsorbate composition (x_i) using Eq. 25.

Part 2:

This part solves the ternary adsorption-diffusion transport problem using the IAS model. Unlike the previous case (part 1), the pressure and gas phase composition is not known a priori. This makes the numerical solution strategy rather complicated and consequently, an iterative procedure has been developed to solve the transport problem. Figure 23 is a flowchart of the solution algorithm.

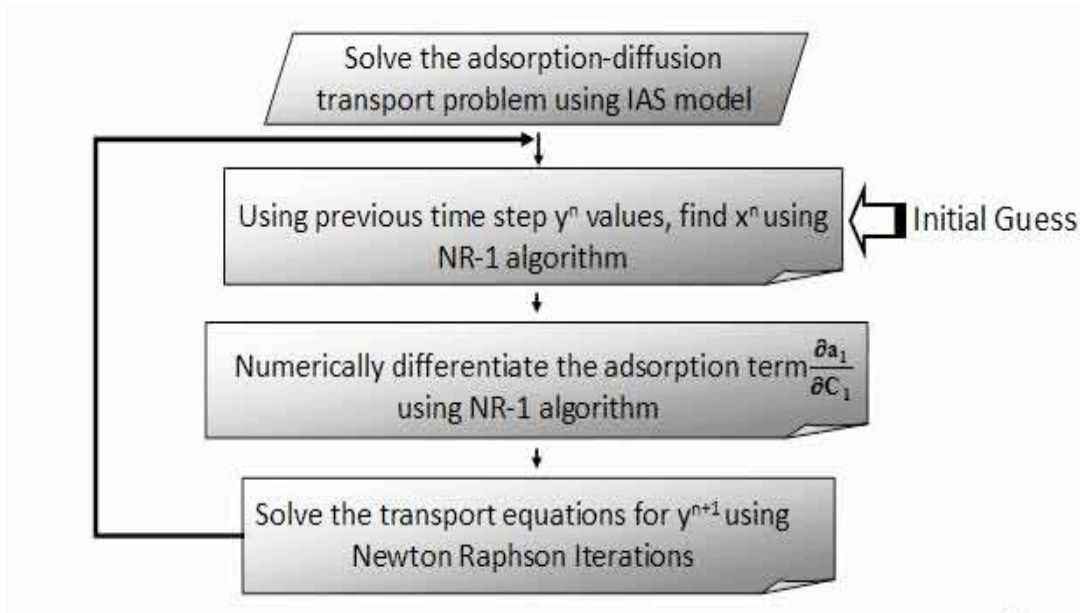


Figure 23: Flowchart of the solution strategy for the ternary adsorption-diffusion case using the IAS adsorption model

From the above flowchart, the NR-1 algorithm developed in Part-1 is invoked two times within each Newton-Raphson iteration. The following is the detailed description of the steps illustrated in the above flowchart.

Step 1: Using the previous time step gas phase composition (y^n), find the adsorbate composition (x^n) using the NR iterative procedure (NR-1) already developed. This y^n and x^n serve as the initial guess for the next NR iteration (referenced as NR-2) to solve for y^{n+1} and x^{n+1} .

Step 2: Using the chain rule of differentiation, express the adsorption term as

$$\frac{\partial a_1}{\partial t} = \frac{\partial a_1}{\partial C_1} \frac{\partial C_1}{\partial t} \approx \frac{\partial a_1}{\partial C_1} \left(\frac{C_{1,i}^{n+1} - C_{1,i}^n}{\Delta t} \right) \quad (39)$$

where, a_1 is the amount adsorbed for component 1 (CO_2) and the same being true for a_2 . The above derivative is computed numerically and NR-1 function is called to do so before the transport equations are solved.

Step 3: Once the initial guess values of x_i and y_i are known and the derivative of adsorption terms with respect to time numerically evaluated, solve the discrete form of the transport equations using Newton-Raphson iterations (NR-2).

Step 4: Once the gas phase compositions (y_i^{n+1}) converge, evaluate the adsorbate mole fraction (x_i^{n+1}) by doing a final NR-1 iterative flash.

Step 5: This completes the computation for a particular time step, after which we move over to the next time step and repeat steps 1-4.

The following figures compare the concentration profiles of CO₂, N₂ and CH₄ generated using the IAS and Extended Langmuir adsorption models.

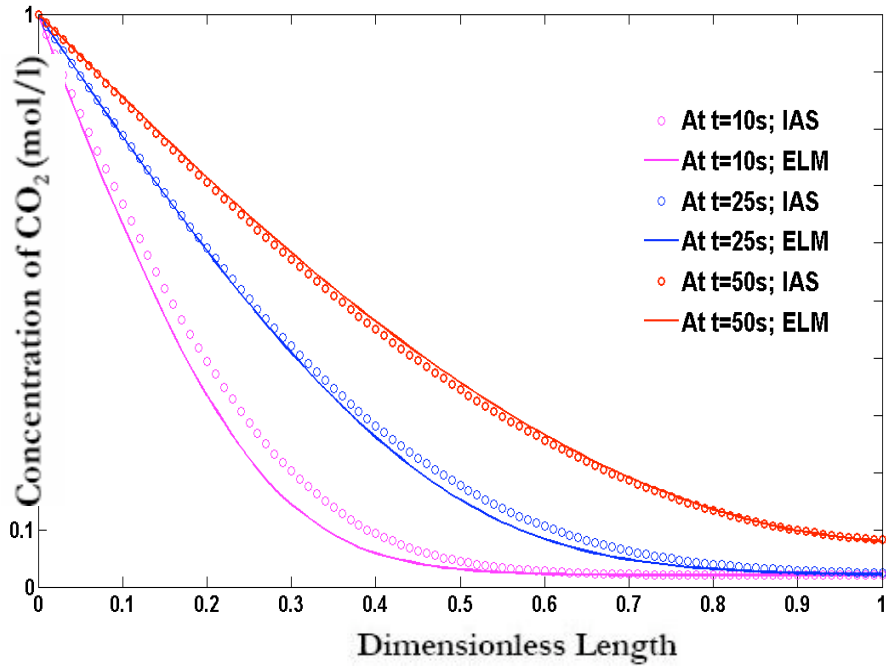


Figure 24: Comparison of concentration profile for CO₂

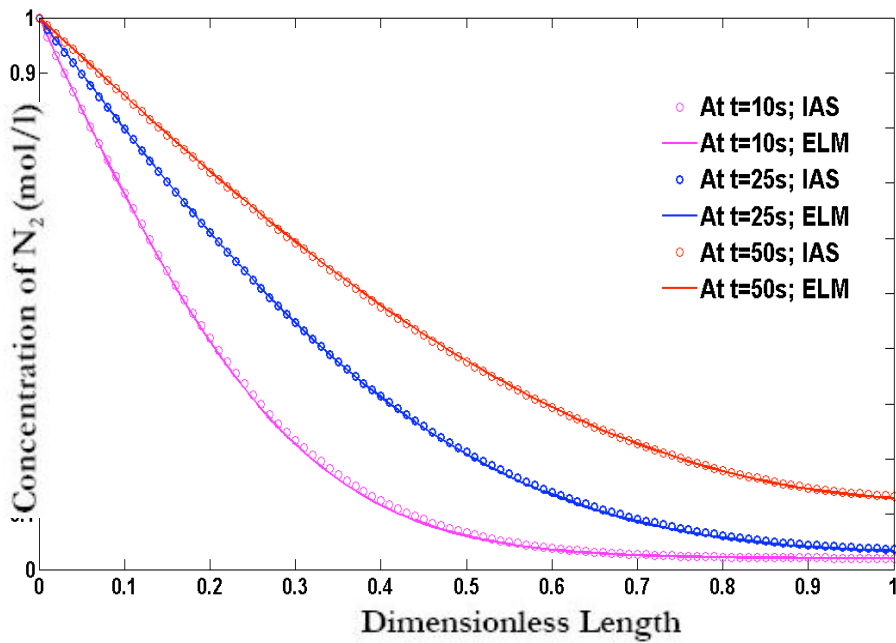


Figure 25: Comparison of concentration profile for N₂

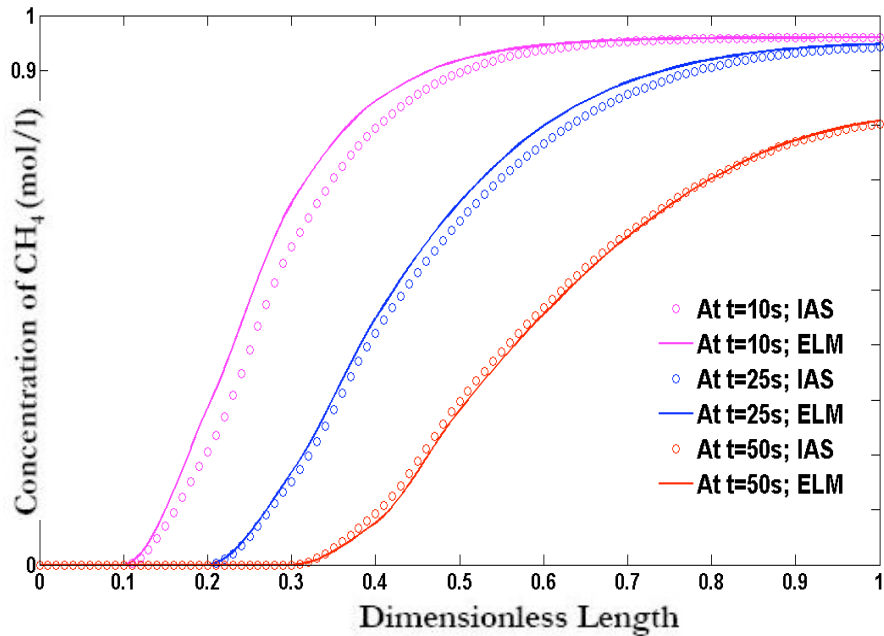


Figure 26: Comparison of concentration profile for CH_4

From the above graphs, one observe substantial mismatch in prediction during the early transient phase of adsorption-diffusion. Apparently, the IAS model is more sensitive to dynamic changes in concentration and pressure.

Sensitivity study

It is interesting to probe further into the fully implicit numerical solution technique. This is achieved by perturbing the simulation model and analyzing the impact on the simulation output.

The first part of the sensitivity study deals with the MS diffusivity input values. It was observed that for some high diffusivity values, the concentration of CH_4 goes negative (unphysical solution). In order to circumvent this issue, the numerical model was modified based on the following two approaches:

Shoe-Horn Technique

The following is the shoe-horn tuning procedure. For each NR iteration, if the NR update results in a negative C_i^{n+1} , then the update is approximated in an exponential fashion.

- Calculate ΔC and C^{n+1} using NR iteration
- Check if $(C_i^{n+1} < 0)$ for any i

$$C^{n+1} = C^n \exp(\Delta C / C^n)$$

else

$$C^{n+1} = C^n + \Delta C$$

Penalty Factor Technique

The following is the penalty factor technique. This is a commonly used simulation strategy involving Newton-raphson iterative solver. Like in the previous case, if the NR update results in a negative concentration, the penalty factor technique sets that value to

some positive value. This serves as the new guess to the NR solver for the next set of iterations.

- Calculate ΔC and C^{n+1} using NR iteration
- Check if the update results in $C_i^{n+1} < 0$, then set it equal to some positive value
- This serves as the new guess for the NR solver
- Continue iterating and updating the C values

Figure 27 illustrates the impact of tuning based on the above two approach on the CH₄ concentration profile and compares it against the untuned model. The MS diffusivity input values are: $D_{13}=D_{12}=D_{23}=0.1$ mm²/s. The results in Figs. 24 to 26 were obtained using the Shoe-Horn approach.

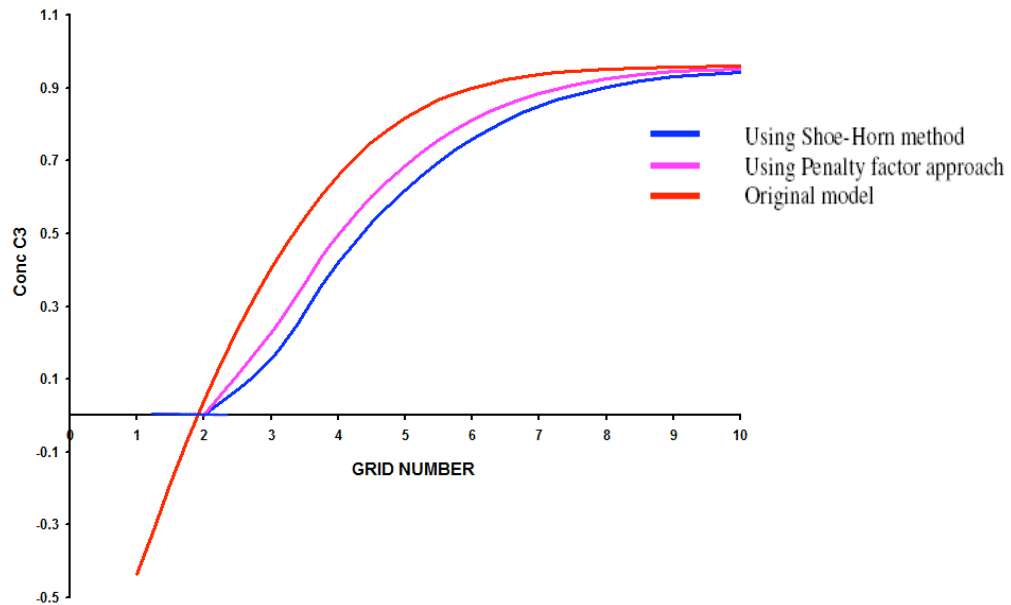


Figure 27: Effect of tuning on the CH₄ concentration profile at 39.9s using the LM adsorption model ($\Delta x = 1\text{mm}$, $\Delta t = 0.1\text{s}$)

The final part of the sensitivity study deals with the impact of time step size on the simulation convergence. Figure 28 shows the CH₄ concentration profile after 20s using MS diffusivities: $D_{13}=0.09$ mm²/s; $D_{12}=0.08$ mm²/s; $D_{23}=0.07$ mm²/s.

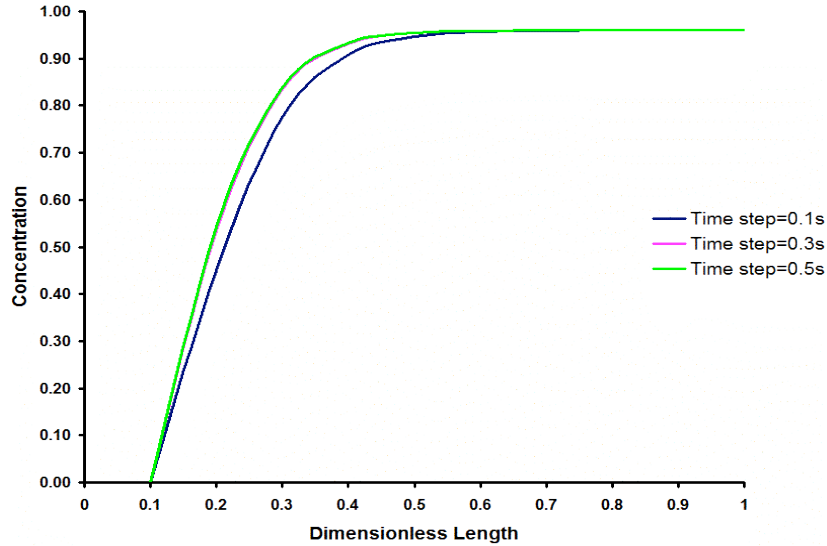


Figure 28: Time step size sensitivity on the CH_4 concentration profile.

The discrete form of the transport equations involves a first order approximation in the time discretization part. This means that for smaller time step sizes, the truncation error would decrease thus resulting in more accurate concentration profiles. This is illustrated by the above graph. For larger time step sizes (0.3s and 0.5s), the concentration profiles exactly overlap but as the time step size is made smaller (0.1s), the truncation errors associated with time discretization reduce and the solution converges to the exact solution. However, convergence is guaranteed for large time step sizes and this goes to show that the fully implicit solution method developed is unconditionally stable.

Experimental study of multiphase fluid flow in coal using CT scan

The objective of the experiments is to obtain transient diffusion results for flow through bulk coal to ground truth some aspects of the modeling effort. The experimental study concentrates on the use of X-ray Computed Tomography (CT) for observing single and multiphase fluid flow in porous medium interior. The basic principle underlying CT scanning is the differential attenuation of a beam of X-rays as it passes through layers of varying thickness and density difference²⁴ (Akin and Kavscek, 2003). The CT scans generate cross-sectional images of the coalpack and thereby assist in transient front tracking and flow profiling which otherwise is practically undetectable by standard practices. The CT scanning would also determine the dynamic two/three phase saturations. Xenon was injected into the coalpack as the tracer gas because it is strong X-ray absorber and gives good image resolution.

Figure 29 shows the CT image of the experimental setup. The coal holder has 3 separate pieces of coal on top of each other, the gap between the three mimicking cleats and fractures in coal. High pressure (70 psia) N_2 serves as the confining pressure while xenon gas is exposed to the base of the core at a pressure of 15 psia. The coal holder top is kept sealed, thereby enforcing a no flow/flux boundary condition.

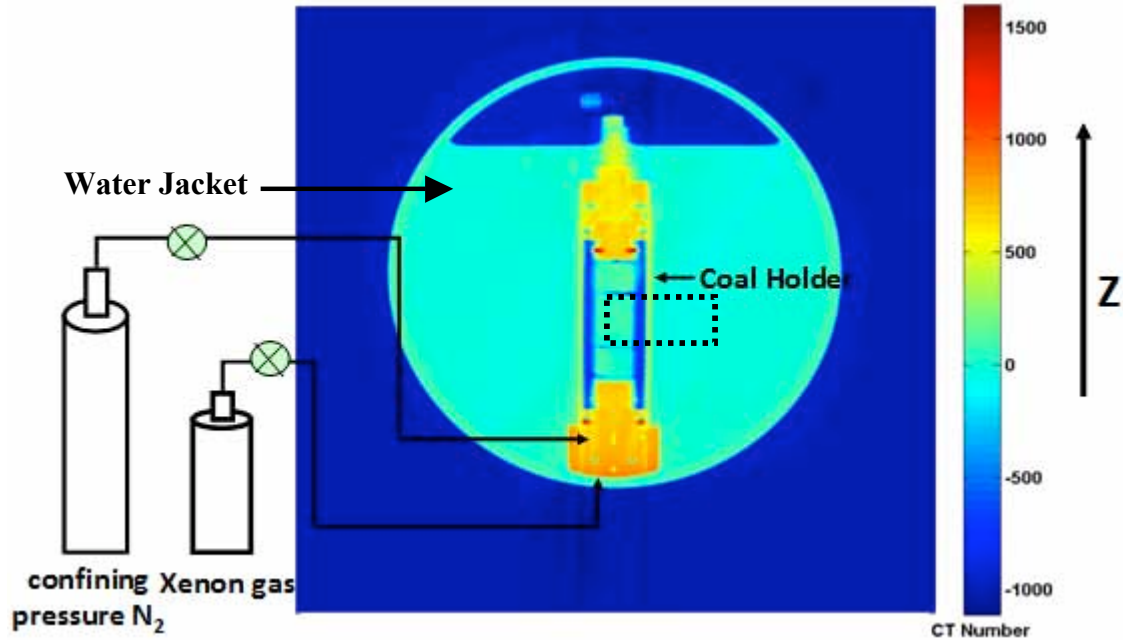


Figure 29: CT scan image of the experimental setup. Dashed box illustrates the portion of core shown in detail in Figs. 30-33.

With time, xenon gas diffuses into the coal matrix and as a result its concentration in the coal matrix increases with time. The idea of the experimental study is to capture this dynamic flow profile of Xenon involving diffusion and advection in coal via CT scan images. An increase in CT numbers with time implies a proportional increase in the Xenon concentration in coal. Figures 30, 31, 32 and 33 are CT scans for the middle coal piece at different time instances.

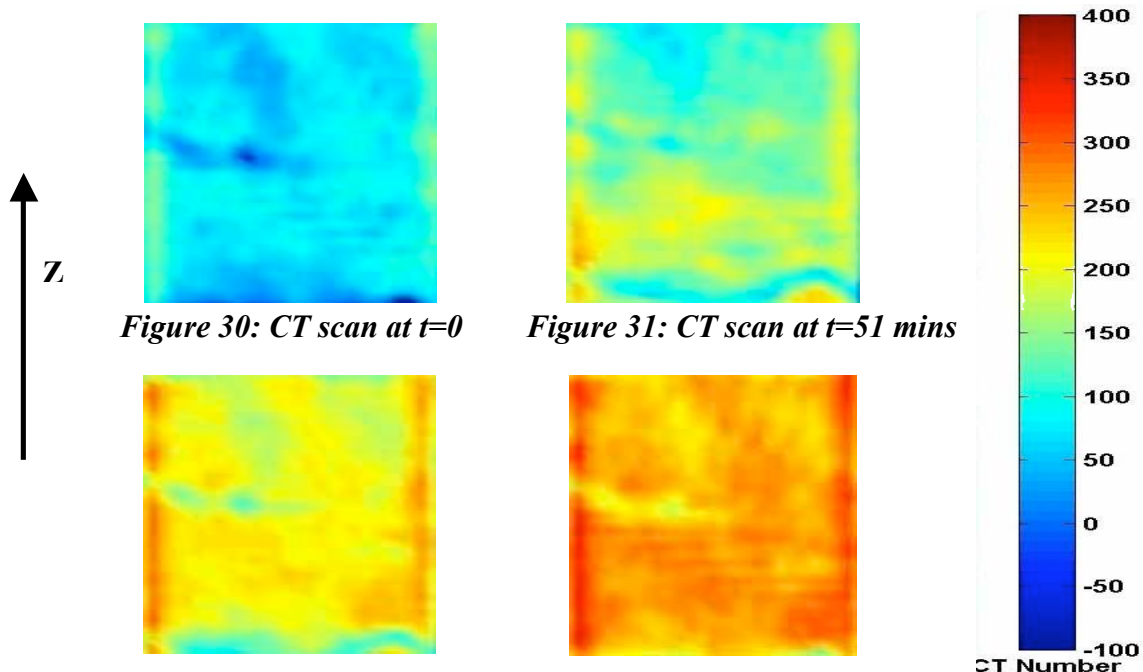


Figure 32: CT scan at $t=8\text{hrs}33\text{mins}$ Figure 33: CT scan at $t=44$ hrs

The concentration of xenon inside coal is directly proportional to the increase in CT number; as a result the variation of CT number along the length of coal at different time instances is representative of the xenon concentration profile as a function of time. The CT numbers along the horizontal plane were averaged to come up with a single average CT number. Figure 34 shows the CT number variation with time along the length of coal.

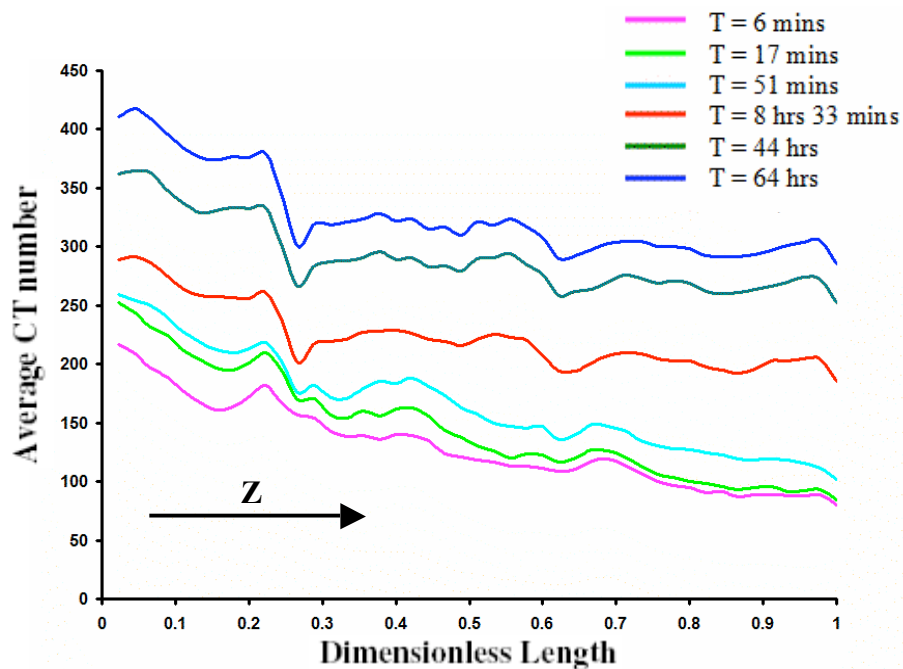


Figure 34: CT number variation along the length of coal with time

Conclusion

In order to model successfully and realistically multicomponent diffusion, it is almost essential to incorporate the MS approach to incorporate concentration dependent diffusivities. Application of the linearized theory leads to significant deviation. This is because there is a strong dependence of diffusivity on the concentration in a langmuirian sorbed phase (Figures 17, 18, 19, 20).

From simulation study, it is observed that there is significant mismatch in concentration prediction during the early transient phase. The IAS model seems to be more sensitive to initial dynamic changes in pressure and composition.

The fully implicit scheme is more robust and accurate than the explicit and semi-implicit numerical schemes. It is found to work fine for a wide range of MS diffusivity values and is unconditionally stable (no time step constraint). Care is needed during updates to concentration to avoid spurious solutions. The shoe-horn technique (exponential limiter) and penalty factor approach both gave acceptable results.

Future work

- Continue validating the present simulation model so as to make it more robust.
- Incorporate parameters such as tortuosity, pore geometry etc so as to make the problem more realistic.
- Mathematically formulate the different mechanisms for adsorption of a gas in the macropores. They are molecular diffusion (molecule-molecule collisions dominate), Knudsen diffusion (molecule-wall collisions dominate) and surface diffusion (transport through physically adsorbed layer).
- Continue with the experimental study of the CO₂- ECBM process using X-ray Computed Tomography (CT) scan.

References

1. IPCC Special Report, 2005
2. Wong, S., Gunter, W.D., and Mavor, M.J.: "Economics of CO₂ Sequestration in Coalbed Methane Reservoirs", SPE 59785, presented at the 2000 SPE/CERI Gas Technology Symposium held in Calgary, Alberta Canada, 3-5 April 2000.
3. Harris, J. GCEP Report 2008
4. Stevens, S.H., Spector, D., and Reimer, P.: "Enhanced Coalbed Methane Recovery Using CO₂ Injection: Worldwide Resources and CO₂ Sequestration Potential", SPE 48881, presented at the 1998 SPE International Conference and Exhibition held in Beijing, China, 2-6 November 1998.
5. Tang, G.-Q., Jessen, K, and Kovscek, A.R.: "Laboratory and Simulation Investigation of Enhanced Coalbed Methane Recovery by Gas Injection", SPE 95947, presented at the 2005 SPE Annual Technical Conference and Exhibition held in Dallas, TX U.S.A., 8-12 October 2005.
6. Shi, J.Q., and Durucan, S.: "A bidisperse pore diffusion model for methane displacement desorption in coal by CO₂ injection", Fuel, Vol 82,1219-1229 (2003).

7. Lin, W., Tang, G.-Q., and Kavscek, A.R.: "Sorptions-Induced Permeability Change of Coal During Gas-Injection Processes", SPE 109855, presented at the 2007 SPE Annual Technical Conference and Exhibition held in Anaheim, CA U.S.A., 1-14 November 2007.
8. Markham, E.C., and Benton, A.F.: "The adsorption of gas mixtures by silica", *J. Amer. Chem. Soc.* 53, 497-507 (1931).
9. Myers, A.L., and Prausnitz, J.M.: "Thermodynamics of Mixed-Gas Adsorption", *AIChE Jr.* 11, 121-127 (1965).
10. Sengul, M.: "CO₂ Sequestration – A safe Transition Technology", SPE 98617, presented at the SPE International Conference on Health, Safety, and Environment in Oil and Gas Exploration and Production held in Abu Dhabi, U.A.E., 2-4 April 2006.
11. Cussler,
12. Taylor, R. and Krishna, R.: "Multicomponent Mass Transfer", Wiley Series in Chemical Engineering, U.S.A (1993).
13. Crank, J.: "The Mathematics of Diffusion", Oxford University Press, Oxford U.K. (1958).
14. Ruthven, D.M.: "Principles of Adsorption and Adsorption Processes", Wiley, New York (1984).
15. Yang, R.T.: "Gas Separation by Adsorption Processes", Butterworth, London (1987).
16. Mather, G and Thodos, G.: "The self diffusivity of substances in the gaseous and liquid states", *AIChE J.* 11, 613 (1965).
17. Dawson, R., Khoury, F., Kobayashi, R.: "Self Diffusion Measurements in Methane by Pulsed Nuclear Magnetic Resonance", *AIChE J.* 16, 725 (1970).
18. Takahashi, S.: "Preparation of generalized chart for the diffusion coefficients of gases at high pressures", *J. Chem. Eng. Jpn* 7, 417 (1974).
19. Sigmund, P.: "Prediction of molecular diffusion at reservoir conditions. Part 1- Measurements and prediction of binary dense gas diffusion coefficients", *J. of Canadian Petro. Tech.* 48 (1976a).
20. Sigmund, P.: "Prediction of molecular diffusion at reservoir conditions. Part 2- Estimating the effect of molecular diffusion and convective mixing in multicomponent systems", *J. of Canadian Petro. Tech.* 53 (1976b).
21. Riazi, M.R., and Whitson, C.H.: "Estimating Diffusion Coefficients of Dense Fluids", *Ind. Eng. Chem. Res.* 32, 3081 (1993).
22. Jessen, K., Lin, W., and Kavscek, A.R.: "Multicomponent Sorption Modeling in ECBM Displacement Calculations", SPE 110258, presented at the 2007 SPE Annual Technical Conference and Exhibition held in Anaheim, CA U.S.A., 11-14 November 2007.
23. Do, D.D.: "Adsorption Analysis: Equilibria and Kinetics-Vol. 2", Imperial College Press. (1998).
24. Akin, S., and Kavscek, A.R.: "Computed tomography in petroleum engineering research", Geological Society, London, Special Publications (2003) 23-38.

Characterization of a Coalbed Fire Near Durango, CO: Fieldwork, Numerical Simulation Modeling, and Analysis

Introduction

Uncontrolled subsurface fires in coalbeds can account for significant releases of CO₂ to the atmosphere. One of the world's largest active coalbed fires has been documented in Wuda, China [1], where the estimated annual loss of coal is around 200,000 tons, equivalent to a yearly emission of ~1.5Mt of CO₂ [2]. In addition to the problem of CO₂ emissions, gases released into the atmosphere from these fires are often toxic. Furthermore, the loss of coal volume in the subsurface can lead to significant surface subsidence and fissures, resulting in damages to near-surface or surface infrastructures. Coalbed fires are burning in many locations in China, Indonesia, India, and the United States [3]. They can be started naturally by forest fires that burn near an outcrop, by lightning strikes, by human activities, or by spontaneous exothermic reactions of pyrites [4]. Forest fires in Indonesia in 1997 and 1998 ignited hundreds of coal fires at outcrops [5]. In the U.S., a subsurface fire near Centralia, Pennsylvania, was started in May of 1962 when the local government decided to burn an unregulated trash dump in an abandoned strip mine to reduce trash volume and control rodents. The fire ignited an anthracite outcrop, eventually connected to and spread through underground tunnels, and has been burning since. Fissures created by the coal fire emit hot gases, some of which are toxic. A combination of subsidence and emissions from fissures has caused the town of Centralia to be abandoned [4, 6].

In the United States, there are two types of coalbed fires. The first type of coalbed fires are located in abandoned coalmines and are sometimes referred to as “abandoned underground mine fires” [7]. The fire draws air from the surface through high permeability mine tunnels and shafts to support the combustion. Natural coalbed fires also occur. These fires are believed to start when an outcrop ignites, and the resulting combustion front subsequently burns into the formation away from the outcrop. In natural fires, O₂ inlet and exhaust gas outlets are not as well defined as those in coalmine fires. Fissures are created when ash and void areas that result from coal combustion collapse under the overburden pressure. Fissures probably function both as inlets and outlets that allow the exchanges of gases between the surface and the coal seam.

Most abandoned underground mine fires stay close to old mine tunnels, but they can sometimes burn away from the old mining network and burn into the formation [6]. Once the fire burns into the formation, surface features similar to that of natural coalbed fires are observed. In the United States, almost 100 abandoned underground mine fires across 10 states were documented by the Department of Interior in 1988. The costs to control or extinguish these fires were estimated to cost around \$741 million at the time [7]. Since natural coalbed fires do not fall under the category of Abandoned Mine Land (AML), they are less well documented and thus the total number of underground fires in the U.S. is expected to be greater. A cost effective way to control these fires would be beneficial.

Various researchers have studied coalbed fires, and their research can be largely divided into the following topics: Development of automated remote sensing methods for early detection [8,9], collection of both surface and subsurface field data [6,7,10,11], numerical models of coalbed fires [12,13], and impact of coalbed fires on policies and regulations [14,15]. In this research project, we focus on the collection of field data and their application to numerical simulations of processes that influence propagation of the fire. The coalbed fire site where the field data is gathered is located just outside of Durango, CO, in the San Juan Basin. The particular fire examined in this study, called the North Coalbed Fire, to distinguish it from other active fires in the region, was discovered in 1998 on the Southern Ute Indian Reservation when sets of fissures that are orthogonal to each other—similar to those observed at other coal fires around the world—appeared at the surface [16]. Anecdotal evidence provided by local Southern Ute Tribe members [17] suggests that the fire may have been smoldering for decades prior to the reported date of discovery. The fire continues to burn today.

Research Objectives

The primary objective of this research project is to design an inert gas injection system to extinguish or control the North Coalbed Fire. To design such a system, it is necessary to understand the approximate combustion front location as well as the rate of combustion with respect to the locations of potential O₂ inlet fissures and exhaust outlet fissures. Currently available analysis do not provide sufficient insight into the relationship between the surface expressions and the subsurface combustion that would enable us to choose appropriate injection locations. The surface above any given coalbed fire is likely to be fractured, and some of these fractures emit hot combustion gases. While these fissures indicate the existence of combustion in the subsurface, it is hard to determine the location and/or the profile of the combustion front by surface expressions alone. Measurable surface anomalies such as fissure locations and apertures must be related to subsurface activity, and it is this relationship that we strive to define through this research project.

At any given coalbed fire site around the world, surface variables such as surface topography, fissure orientations, fissure lengths and fissure apertures are relatively straightforward to measure and quantify using tools such as a pack-mounted GPS machine. However, subsurface variables are harder to constrain. Many surface irregularities and subsurface voids created by combustion processes pose challenges to traditional subsurface imaging techniques. In addition, boreholes often cannot be drilled through the hottest regions over the fire, and thus it may be hard to achieve a high density of boreholes that is necessary to construct representative subsurface geologic models. Due to these uncertainties in the subsurface, it is presently impossible to relate surface expressions precisely to subsurface activities. While a precise relationship may be unattainable, it may be possible to define an approximate first order relationship that relates the surface to the subsurface. Such a relationship would allow us to design better injection schemes to control this fire in particular and if successful, could have wider application.

We have examined the first order relationship between the surface and the subsurface through assembly of: a solid understanding of the local geology, both at the basin scale

and at the coalbed fire scale (600 x 200 m), various field data for both the surface and the subsurface, and numerical modeling of the subsurface behavior. In this report, each of these topics, and its contribution to the primary objective of this research is discussed.

The local geology of the San Juan Basin near the North Coalbed Fire will be presented first. In 2008, much effort concentrated on building an understanding of the geology in the neighborhood of the North Coalbed Fire. Knowledge of the geology enables us to constrain more accurately both the boundary and initial conditions in our numerical simulations. Second, field data collected at the North Coalbed Fire site are briefly described. These include surface topography, fissures (types, orientations, apertures, temperatures and lengths), well logs, driller's logs, subsurface temperature, gas composition, subsurface images using seismic and GPR, and regions of snowmelt over the coalbed fire. Near the North Coalbed Fire, there is also an outcrop containing a fossilized coalbed fire, and data were collected there as well. At this outcrop, there is evidence of coal combustion, subsequent subsidence and a set of fissures that seems to have widened as a result of the collapse. The field data collected were pieced together to build intuitions about the propagation of the coalbed fire, as well as to provide data to test our simulation results. To conclude the field data section, future field campaigns using magnetometers will be discussed.

Finally, numerical simulations of the coalbed fire are described. Four different numerical simulations are proposed, one of which—a simple boundary element method (BEM) subsidence model—has been explored in detail. The first two simulations consider the structural aspects of coalbed fires. The overall objective of the subsidence simulations is to relate subsurface subsidence to fissure locations and apertures at the surface. In the BEM model we explored whether coal combustion followed by subsurface subsidence can produce fissures with systematic patterns at the surface. In the second simulation, a finite element model (FEM) will be used to explore cases when assumptions made in the BEM simulations such as homogeneity and flat topography are relaxed. The FEM simulations can also show that different subsidence kinematics can give rise to different types of fissures at the surface. At the coalbed fire, there are four distinct types of fissures. These are termed gaping, buckled / molehill, plateau / offset, and narrow fissures. Each of these types of fissures has unique features that are not shared by other fissure types. Images of fissures and their attributes are discussed below. Differences between the four types of fissures result in different boundary conditions and may have varying impacts on the subsurface combustion activity.

In the last two simulations, the combustion aspects of coalbed fires will be explored. The subsidence simulations tell us where the fissures will be created when a subsidence event occurs, while the combustion simulations tell us how fast and how much of the coal will be consumed given those boundary conditions. In the context of ultimately designing an inert gas injection scheme, the subsidence models can aid in determining the locations of the injection points, while the combustion models will constrain the amount of inert gases necessary to deprive the combustion zone of O₂.

In the first combustion simulation, a simple chimney model is used to represent the overall behavior of coalbed fires. Field observations, along with previous literatures, show that it is plausible that some fissures act as O₂ inlets while others act as vents to emit combustion gases. We hypothesize that there exists a length scale between the inlet fissure(s) and vent fissure(s) beyond which combustion is not sustainable. Knowing the length scales between the fissures will constrain the rate of energy release that can be sustained by such a chimney. This can then be converted to obtain the rate of coal combustion. This chimney model cannot provide us with a combustion profile or subsurface flow characteristics. Thus in the second combustion simulation, we will use a commercial simulator to explore the relationships between reaction and subsurface flow. Such numerical simulations will lead to both a rate of coal conversion estimate and a combustion profile. There are challenges due to the heterogeneous nature of coal combustion kinetics. This will be discussed in more detail in subsequent sections of this report. The two combustion models, though varying in approach, should provide similar relationships between the variables that control the combustion process on a first order basis.

The report concludes by presenting a conceptual diagram, showing how a combustion front may be propagating at the North Coalbed Fire. Preliminary suggestions for the location of inert gas injection sites as well as questions that will be tackled this year are presented in the conclusion.

Geology – San Juan Basin and the North Coalbed Fire

The San Juan Basin is an asymmetric, coal bearing basin that covers approximately 16,800 – 19,400 square kilometers, stretching approximately 145km west-east and 160km north-south [18,19]. It is located near the Four Corners, and spans across northwest New Mexico and southwest Colorado (Figure 1). The region affected by the coalbed fire is located near the coal outcrop along the Hogback, and is circumscribed by the dotted box. In this region, the local topography slopes between 5 and 9 degrees to the southeast, and the coal layer dips 6 to 15 degrees in the same direction [20]. Both the surface topography and the coal seam flatten towards the southeast in the direction of the Central Basin.

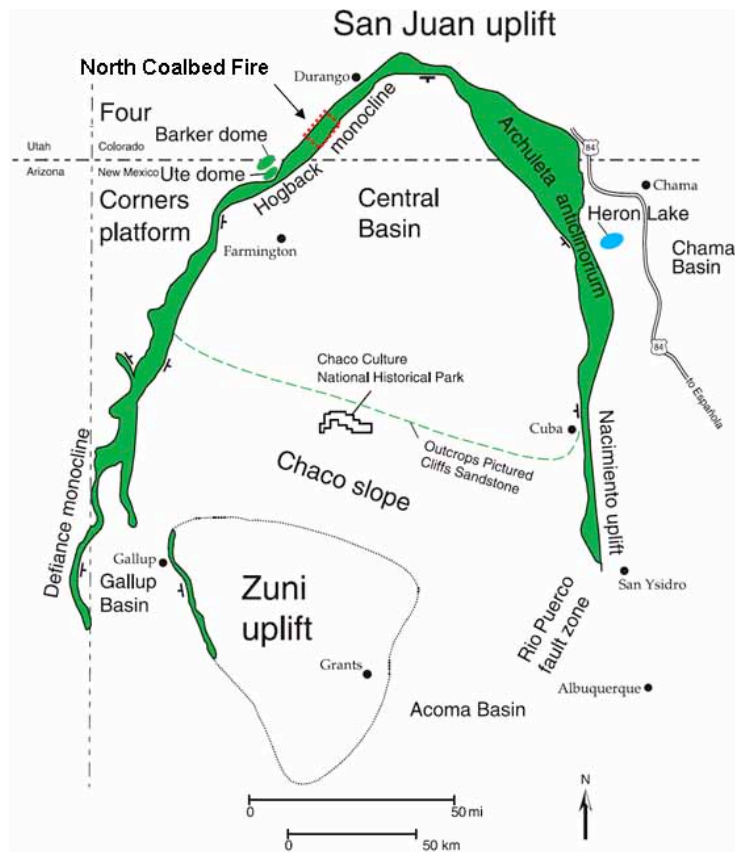


Figure 1: San Juan Basin and its characteristic geologic features. The North Coalbed Fire location is highlighted in the box in the northwestern corner of the basin along the Hogback Monocline. The green area denotes outcrops of Pictured Cliffs sandstone. Figure reproduced from Lorenz and Cooper, 2003 [20].

The North coalbed fire is contained between latitude $N37^{\circ}01'57''$ and $N37^{\circ}02'24''$ and longitude $W108^{\circ}06'36''$ and $W108^{\circ}06'18''$, and has an aerial extent of approximately 600 m x 200m. Using a USGS geological survey map, a cross-section map over the North Coalbed Fire was created (Figure 2). The cross-section line is roughly perpendicular to the strike of the Hogback monocline. This cross-section shows that the Fruitland Formation crops out along the Hogback Monocline limb. To the northwest of the Hogback, only a basement formation called the Lewis Shale is observed. The continuous and low permeability Kirtland Shale Formation, which is absent over the North Coalbed Fire, caps the Fruitland Formation to the southeast.

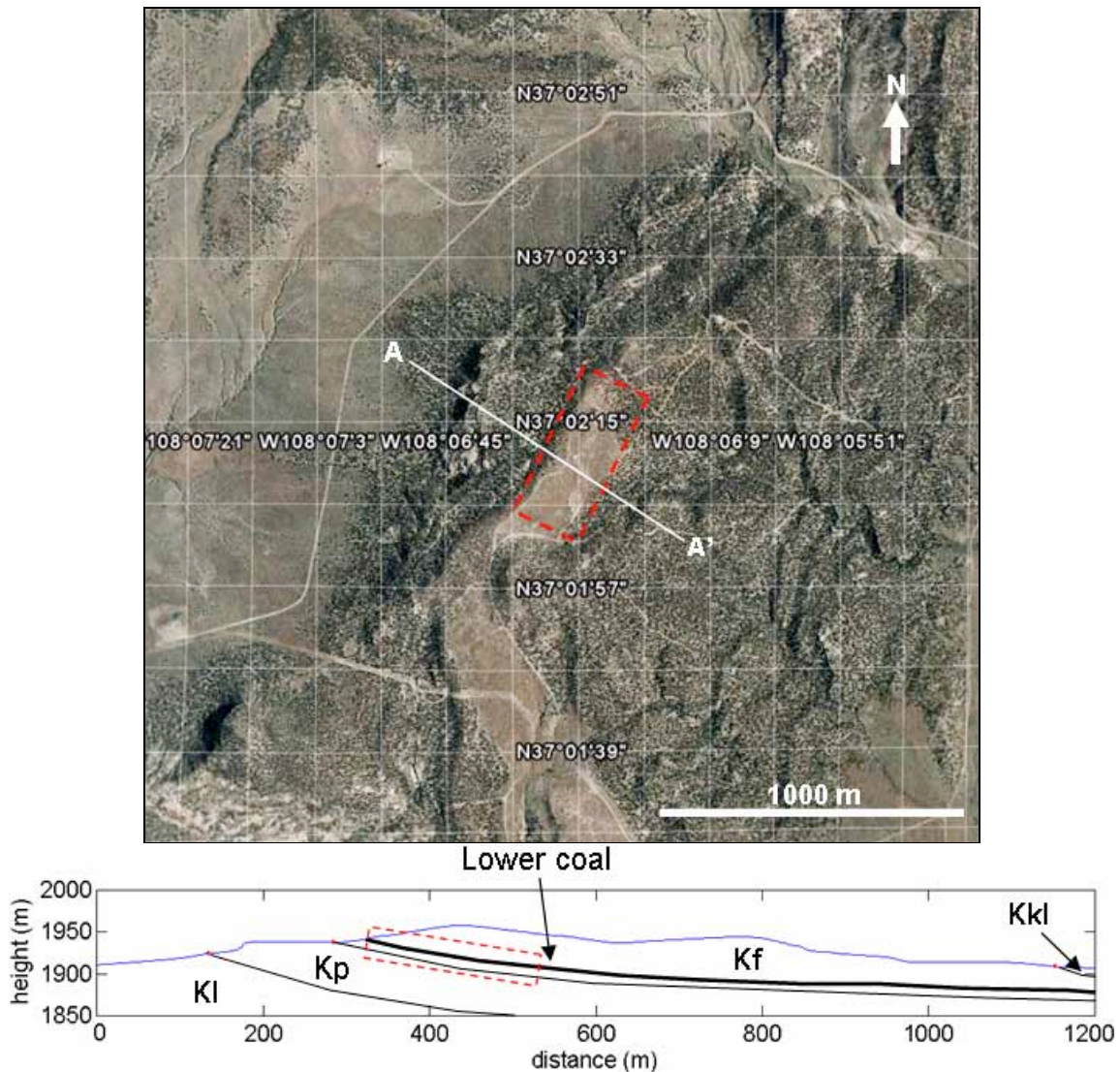


Figure 2: a) A satellite image over the North Coalbed Fire. The red dotted box outlines the region affected by the underlying fire. A cross-section line A-A' is used in Figure 3b. Satellite image is provided by Googlemaps. b) Cross section A-A' showing surface topography and representative subsurface stratigraphy in the vicinity of the North Coalbed Fire. The coalbed fire is located near the coal outcrop inside of the red dotted box. Kf = Fruitland Formation, Kp = Pictured Cliffs Sandstone, Kk1 = Kirtland Shale.

Many fissures are exposed on the surface overlying the North Coalbed Fire. The fissures are distinguished from regional joint sets in the same strata because fissures typically have widths on a decimeter scale, whereas joints have apertures less than 0.5 cm [21]. Some of these fissures emit high temperature combustion gases, indicative of the active fire below, while others are at ambient temperature. Orientations of the fissures are systematic, and they often form orthogonal patterns at the surface. The directions and the lengths of 165 fissures are represented on a rose diagram in Figure 3a. Lengths of fissures have been made dimensionless with respect to the longest fissure in the field, which is 75m. The diagram shows that there are three main fissure directions over the North Coalbed Fire and that the longest and most frequently occurring fissures, F1, have

azimuths approximately in the N50E direction. The next most prominent set, F2, strikes in the N35W direction, roughly perpendicular to the first set. The third set, F3, is directed towards the North, and these have similar lengths to the N35W set. The fissures frequently occur together in approximately orthogonal pairs, including members of the N50E and N35W sets.

The azimuths of the fissures are compared with observations of joint orientations reported in Condon, 1988. Condon measured 1,600 joints and coal cleats at 37 different outcrop locations on the Southern Ute Indian Reservation. Of the 37 measurement stations, 8 of them are located along the Hogback Monocline and are spaced approximately 2km apart. Most of his measurements are fractures found in formations of the Upper Cretaceous, the majority of which are in the Kirtland Shale, Fruitland Formation and the Pictured Cliffs Sandstone. Four dominant joint sets, labeled J1 through J4, are presented, and their stereonet projections are reproduced in Figure 3b. A comparison of Figures 3a and 3b shows that F1 corresponds to J3, F2 to J4, and F3 to J2 based on similarities between the fissure orientations and joint orientations. Typically, the joints occur in pairs—a J1-J2 pair and a J3-J4 pair—much like the fissures F1 and F2 that form orthogonal pairs above the North Coalbed Fire. Condon classifies the J1~J4 joints as extension joints, due to the lack of features such as slickenside striations that would suggest lateral shear movement and the presence of plumose structures, arrest lines, and twist hackle features that indicate extension joints [21].

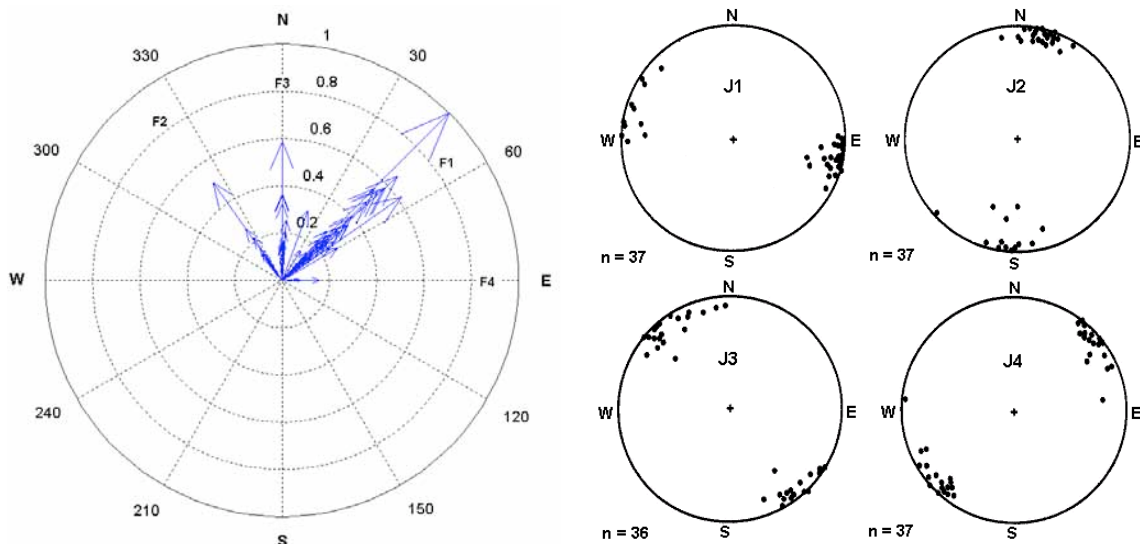


Figure 3: (a) A rose diagram showing the orientation and the lengths of the fissures found above the North Coalbed Fire. The characteristic length scale is ~100m, and (b) Four stereonet projections of J1~J4 reproduced from Condon, 1988 [21].

Field Data

Various field data have been collected over the past year at the North Coalbed Fire. In 2008, many surface and subsurface data were recollected or updated to observe temporal changes. Below is a list of data that we have collected, the methodology of collection, and a brief description for each.

Surface field data

Surface topography – This was collected by using a pack-mounted GPS (Trimble ProXH) by walking around and over the North Coalbed Fire. The GPS points are accurate to better than 1m, with most better than 0.5m. We now have enough point density to recreate the surface contour using appropriate interpolation methods.

Fissures (types, lengths, orientations, apertures, temperatures) – Over the North Coalbed Fire, there are four different types of fissures that have been documented. These are termed gaping, plateau/offset, buckled/molehill, and narrow fissures. Gaping fissures are fissures that are wider than 0.5 meters in width at the surface with only slight rotation of the floating rocks at the surface. These fissures are predominantly found in the upfield regions closest to the outcrop, where the surface gradient is around 8°. Plateau or offset fissures have similar surface apertures as the gaping fissures, but one side of the fissure has fallen, while the other side does not show significant displacement or rotation. Sometimes the drop on one side can expose a scarp surface, and offsets can be as great as 2 meters. The buckled or the molehill fissures are fissures where surface layers of sedimentary rock are rotated to form an apex. At molehill fissures with visible fractures at the surface, combustion gases with temperatures as high as 290°C (550°F) have been recorded. Finally, narrow fissures, which are the most abundant fissures over the coalbed fire, are fissures that are only about 0.05 meters in width. They are approximately an order of magnitude narrower than the gaping fissures. There are no appreciable rotations of the surface sedimentary layers near the narrow fissures. These fissures are found in the most downfield regions over the North Coalbed Fire, where the surface is flatter.

The lengths of the fissures were collected using a pack-mounted GPS, the orientations with a Brunston compass, the apertures with a tape measure, and the temperature using a Raytek Raynger 3i series that can measure temperatures up to 1000 °C. These fissure measurements have shown that there is a systematic pattern in orientations, which can be explained by the fact that fractures that existed in the area prior to the coalbed fire open to form fissures when subsidence occurs.

Goodson and Associates, Inc.—who were contracted by the Southern Ute Indian Tribe—used a foam grouting material to fill the fissures that were thermally active in 2000 and 2001. They were unable to locate and seal off all of the fissures, and furthermore, some of the fissures that they located were not sealed completely. Field observations suggest that they mainly grouted the narrow fissures over the North Coalbed Fire. The locations of their grouting activities were mapped using the GPS unit.

Surface subsidence – The surface subsidence was measured using a Contour LaserRange Finder. A laser beam was focused on a reflector cube, which was moved along a predetermined line over the North Coalbed Fire. This resulted in a surface cross-section along this line, clearly depicting the surface subsidence.

Surface temperature data using an IR camera – The Southern Ute Indian Tribe contracted with outside parties to measure surface temperatures. The surface temperatures were measured using an IR camera. This data shows that most of the high

temperatures escape through fissures, and that thermal transfer through conduction in rocks is small in comparison.

Snowmelt data – Two sets of snowmelt data were collected 3 days and 10 days after a snowstorm in January 2009. After a snowstorm, snow over the hottest regions of the North Coalbed Fire melted immediately, while snow over the currently cold and inactive regions stayed. Fissures that were in the snow-covered regions and are very wide may be locations from where O₂ is being drawn to sustain the subsurface combustion.

Subsurface field data

Stratigraphic map using core data, well-log data, driller's log data – The wellbore data, along with well-logs, driller's logs and core data was used construct a stratigraphic map and a coalseam contour in the subsurface. Results show that some regions of the coalseam have burned, while others show coal that is unaffected. Using a tabular deposition assumption, we can use this to calculate the total amount of coal that is available for combustion at the North Coalbed Fire.

Thermocouple data – There are thermocouples in boreholes that were drilled in 2000, 2001, and 2007. Temperature measurements from these thermocouples show a rough fire propagation direction and rate at the North Coalbed Fire.

Gas composition data – Evacuated stainless steel chambers were used to collect gases at a number of boreholes over the coalbed fire. The gas compositions show a clear distinction between gases coming from unburned coal regions, currently active combustion regions and formerly burned but now cooled region. In native coalseams, the gas compositions are mostly CH₄ and CO₂. In combustion regions the gas compositions contain CO₂, CO, CH₄, H₂, N₂, and in cool regions, the gas compositions are equivalent to that of air.

Subsurface imaging (seismic, GPR) – Subsurface imaging using seismic and ground penetrating radar (GPR) techniques have been employed at the North Coalbed Fire. A sledgehammer was used as the acoustic source for the shallow seismic measurements. The objective of the imaging exercise was to distinguish between regions that remain unburned and regions affected by the coalbed fire. Analysis of the data collected is underway.

Outcrop data – At the outcrop just north of the North Coalbed Fire, there is an outcrop that shows a fossilized coalbed fire. This outcrop contains ash, subsidence, unburned coal and fissures at the surface. These features were mapped using the Contour LaserRange Finder. This data was used to define both initial and boundary conditions in subsidence simulations.

Results from field observation

Figures created from the field data are presented below. First, in Figure 5, pictures of the four different types of fissures are shown. Figure 5a is an example of a gaping fissure that is large enough for a 6ft adult to stand inside. Figure 5b shows a molehill/buckling

type fissure with surface sediment layers tilting in opposite directions around the fissure. Figure 5c is the plateau fissure with an offset of about 1 meter, and Figure 5d shows a narrow fissure that is currently emitting hot exhaust gases. The conceptual drawings in Figures 6 (a) through (d) correspond to Figures 5 (a) through (d), respectively. Figures 7 through 13 show different combinations of both the surface and the subsurface data that were collected over the North Coalbed Fire. The data were organized in a graphical user interface to allow a user to simultaneously visualize multiple sets of different field data. This image-rendering tool was created to gain further insight into the workings of the North Coalbed Fire and to help generate new questions that can be explored in this project.

Figure 7 is a contour map of the surface over the North Coalbed Fire. Mapped fissures, locations of boreholes that were drilled in 2007 and the locations of thermocouples that were drilled in 2001 and 2000 are superposed onto the contour plot. All features were mapped with the portable GPS device. The left edge of the contour plot roughly coincides with the Fruitland Formation outcrop. The figure shows that the majority of the fissures are approximately parallel to the strike of the formation.

Figure 8 is a plot of the fissures over the North Coalbed Fire distinguished by its type. The four types of fissures discussed above are represented by different colors. In addition, the directions of the tilt of the surface sedimentary layers are indicated. Figure 9 is a figure that zooms in on one portion of the field, showing clearly both the magnitude and the orientations of the surface sedimentary layer rotation.

Figure 10 is a contour map of the subsurface coal seam, which was created using a combination of data from well-logs, drillers' logs and cores obtained at the North Coalbed Fire. The points used to create the interpolated surface are also plotted (boreholes and thermocouples). The figure indicates that the coal surface does not necessarily correspond to the contour map of the surface. There appears to be a raised hill in the contour towards the northern end of the coalbed fire field. Such a steep rise in subsurface elevation may become a preferential pathway for rising hot gases, which in turn may result in the propagation of the fire in that direction. The coal surface is approximately 20 meters below surface.

Figure 11 shows the thermocouple measurements made in 2001 by Goodson and Associates Inc. The thermocouples are stationary and measures temperatures at a fixed depth of approximately 15~20m (the depths vary, and are not well documented). In 2001, the fire was active towards the downfield portion of the site, about 100 meters away from the outcrop. The fissure map that overlay the temperature measurements show that fissures that fall in this active region were grouted in 2001.

Figure 12 shows the temperature distribution over the North Coalbed Fire in 2008. Temperatures have been collected approximately every year since 2001. This is the latest temperature data collected in October of 2008. Comparison to Figure 11 shows that the high temperature region has migrated upfield towards the outcrop. Comparison of this figure to Figure 10 suggests that the combustion front may have propagated along the

greatest elevation gradient along the coalbed surface. The green line indicates the boundary between snow-melted regions and snow-covered regions a week after a snowstorm in January, 2009. The areas enclosed by the green lines are locations where the snow is melted. The region of high temperatures corresponds well with the snowmelt region.

Figure 13 shows the different gas chromatography measurements obtained over the North Coalbed Fire. Gas samples were collected at the boreholes drilled in 2007 (blue triangles). The figure is combined with the snowmelt region (January, 2009) and the fissure distribution at the surface. The red fissures indicate fissures with a thermal signature, while the blue fissures indicate fissures with ambient temperatures. The gas chromatography measurements show that there are clear differences between native gas compositions found downfield ($\sim 50/50$ CH₄/CO₂) where we know the coal is unburned, gas compositions found at boreholes outside of the snowmelt (\sim air composition) where we believe that the coal once burned and has now ceased and at boreholes found inside of the snowmelt (a mix of CO₂, CO, H₂, CH₄, N₂), where coal combustion is likely occurring today. Thermally active fissures are mostly contained within the snowmelt regions, while other fissures remain covered in snow.

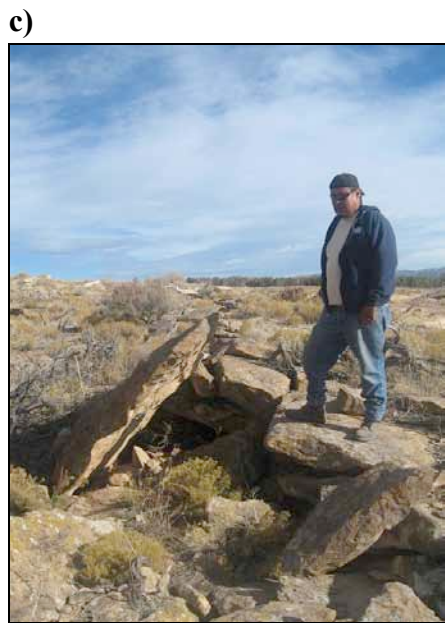
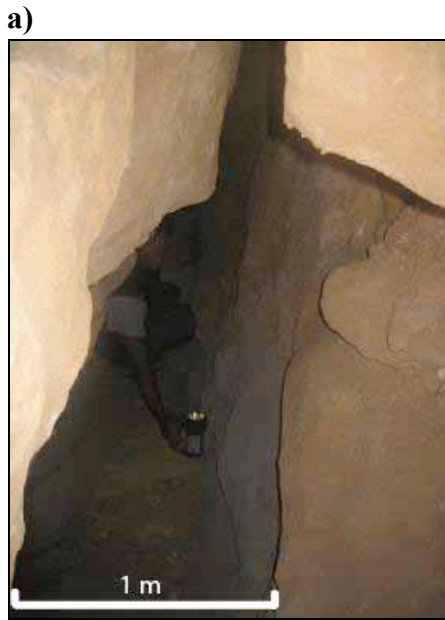


Figure 5: a) a gaping fissure with a 6ft adult inside, b) a plateau/offset fissure that shows surface sediment layers that are displaced only on one side, c) a buckle/molehill fissure with the sediment layers forming an apex, and d) a narrow fissure on an even surface emitting hot combustion gases.

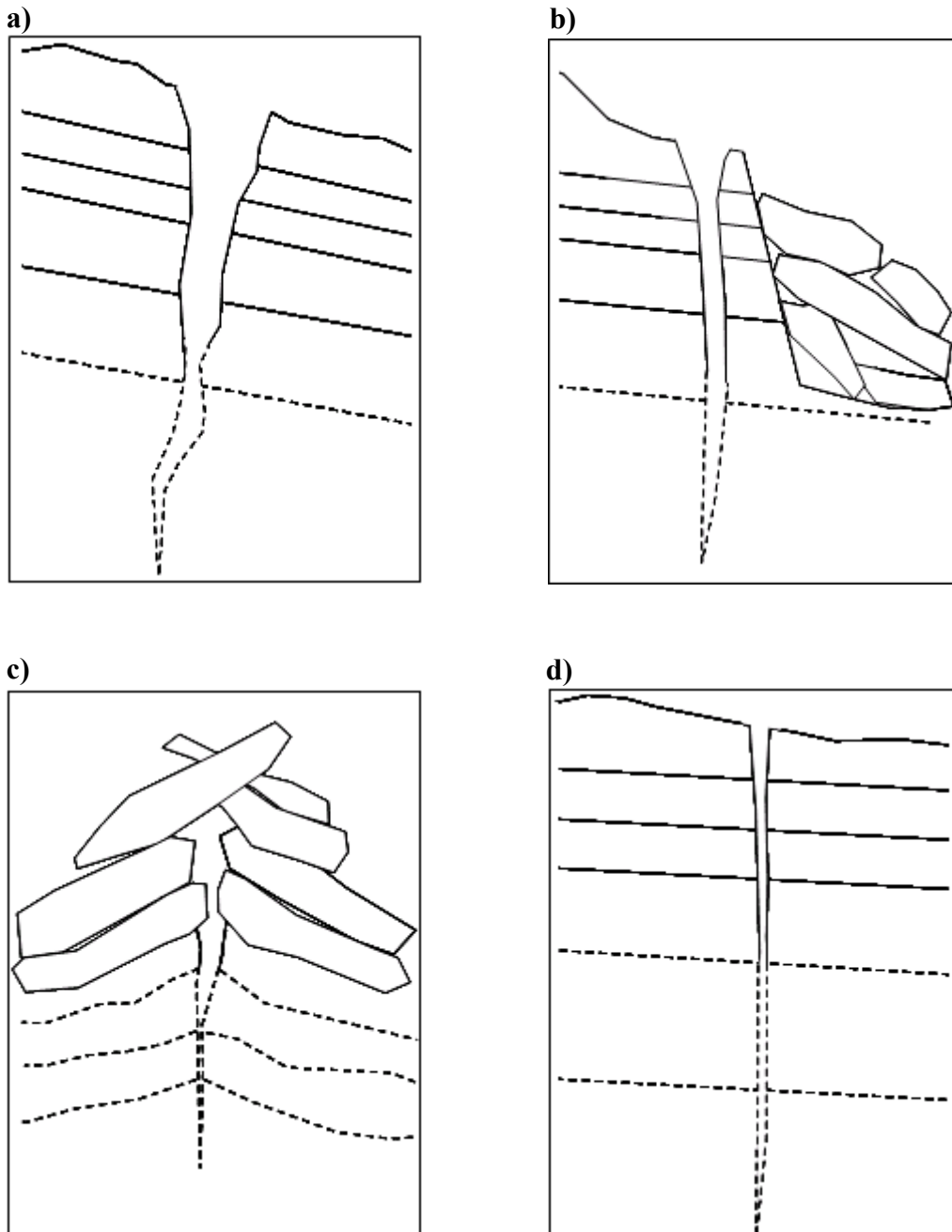


Figure 6: A conceptual drawing of each of the four fissures. Solid lines indicate observed features, while dotted lines are educated guesses of the subsurface configuration beneath each type of fissure. a) a gaping fissure, b) a plateau/offset fissure, c) a buckle/molehill fissure, and d) a narrow fissure on an even surface.

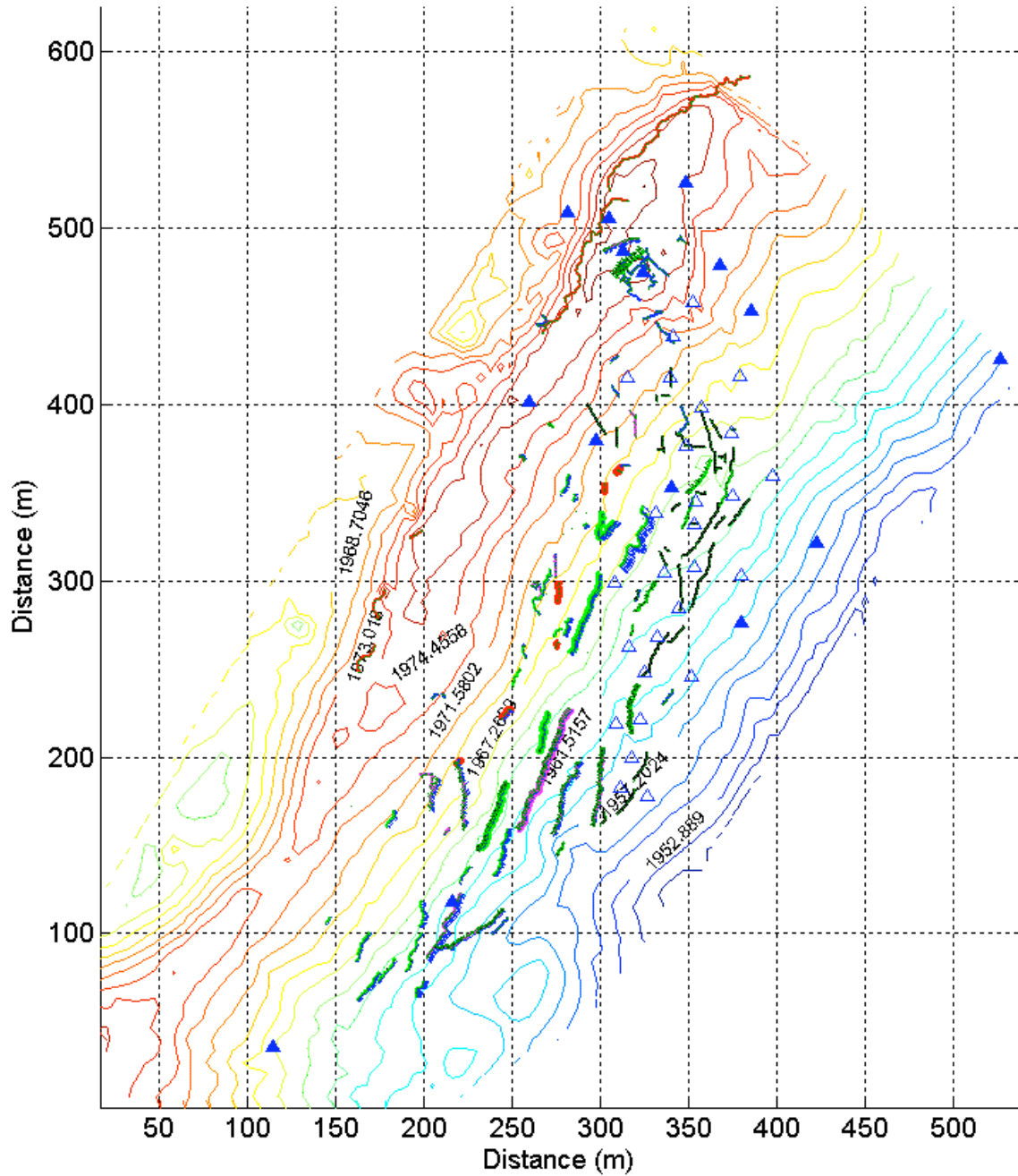


Figure 7: Contour map of the area created by the portable GPS-unit, Trimble Pro-XH, overlain by boreholes (solid triangles, drilled in 2007), thermocouples (open triangles, drilled in 2000 and 2001) and mapped fissure locations. The contour elevations are in meters. The left edge of the contour map coincides approximately with the location of the Fruitland Formation outcrop. The narrow red lines—towards the top and left edge of the contour line—denotes red clinkers (thermally altered rocks) that are found at the top of the Fruitland outcrop.

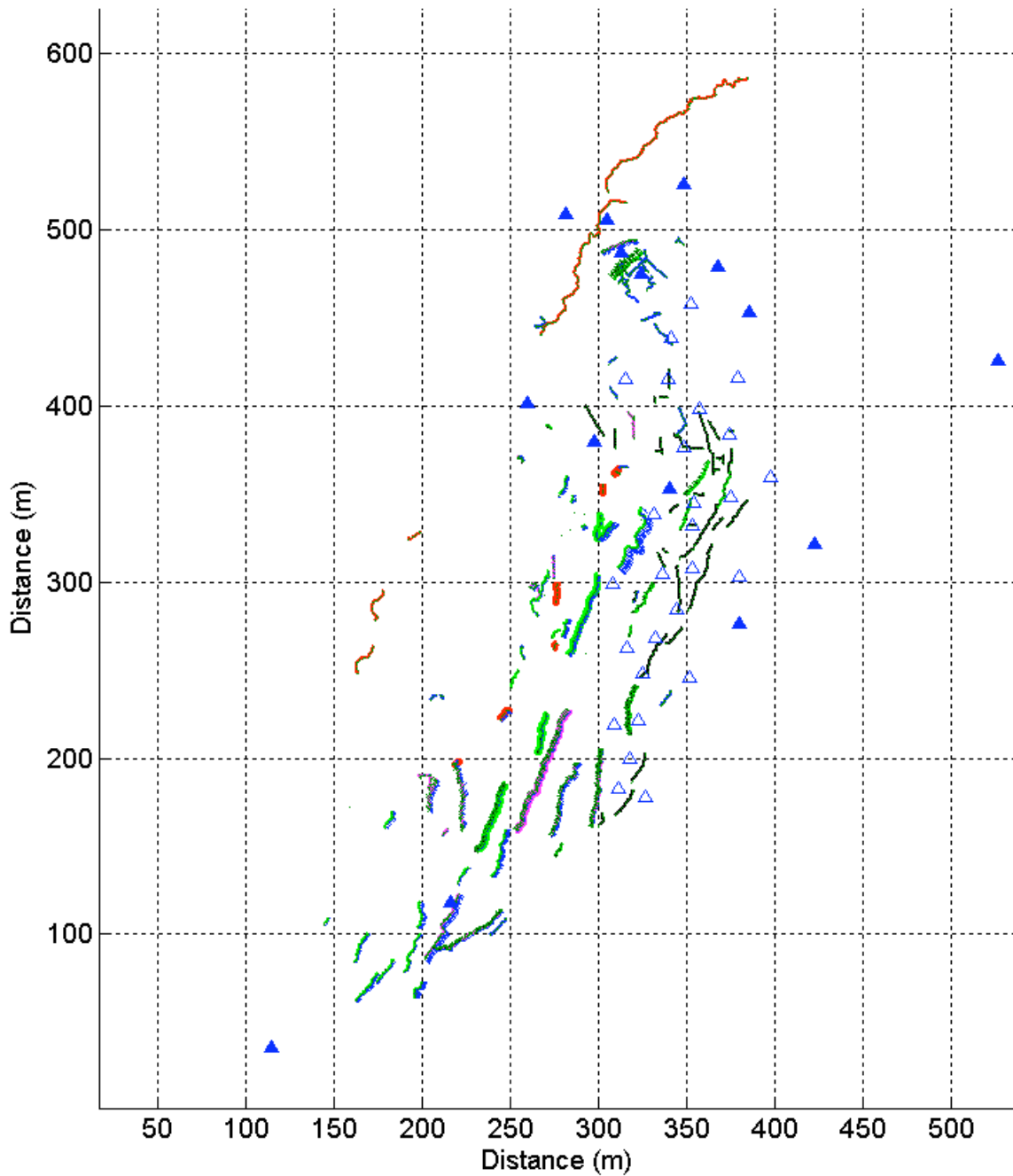


Figure 8: Mapped fissures over the North Coalbed Fire. Fissures that are represented as thick lines indicate fissures that have surface apertures greater than 0.3 meters. Different types of surface expressions are distinguished by color. Red thick lines are gaping fissures, magenta lines are molehill/buckling type fissures, green lines are plateau fissures, and the blue lines are narrow fissures. Black lines are narrow fissures that were grouted by Goodson and Associates Inc. in 2000 and 2001. Narrow red lines near the outcrop (left edge) are red rocks and ash deposits found at the Fruitland outcrop.

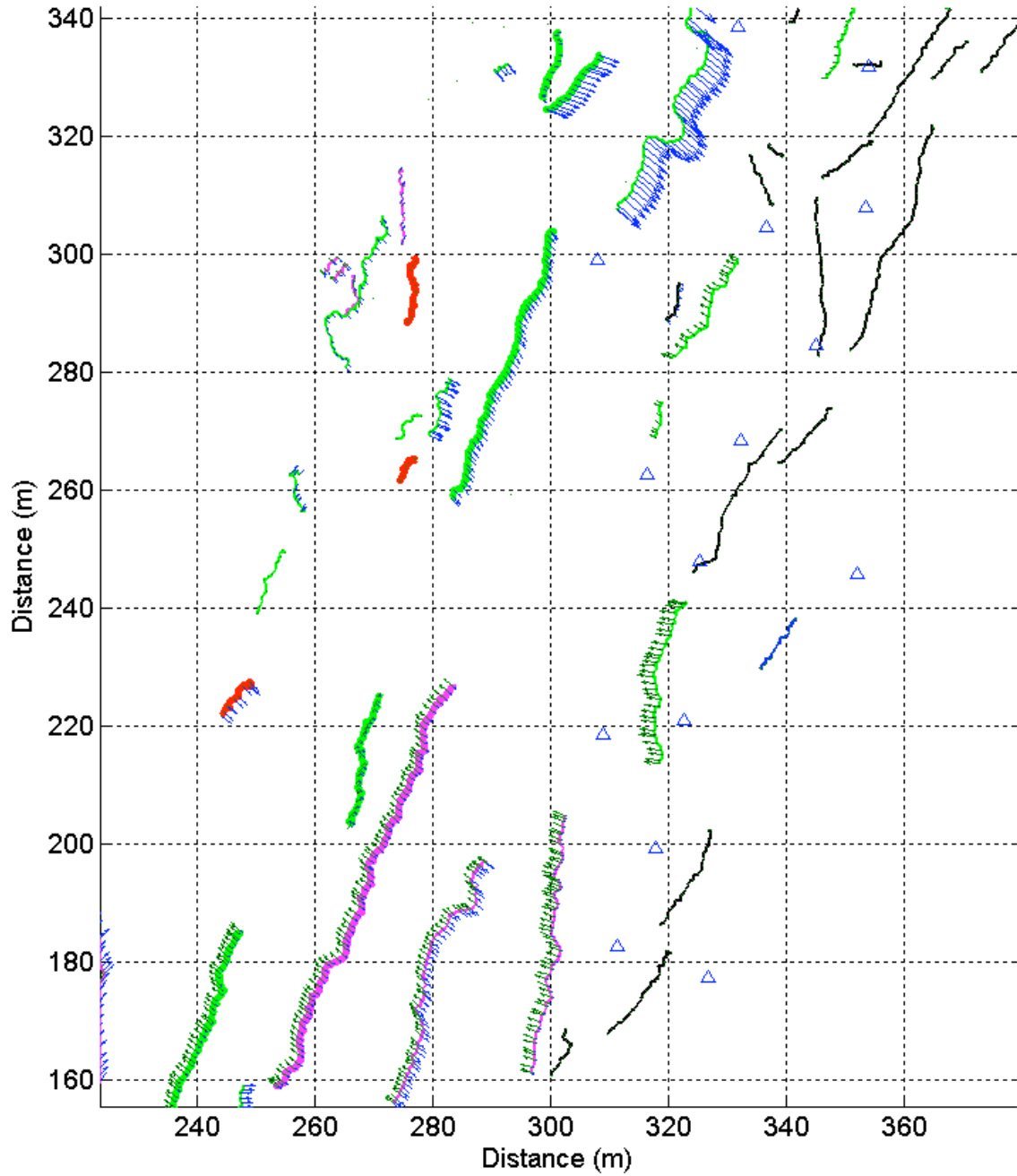


Figure 9: A close up of a portion of the field from Figure 8. The arrows denote the dip direction of the surface sediment layers. The magnitudes of the arrows are proportional to the angle of the dip observed at the edges of the fissures. Blue arrows indicate a dip in the downfield direction away from the outcrop, while the green arrows indicate a dip in the upfield direction.

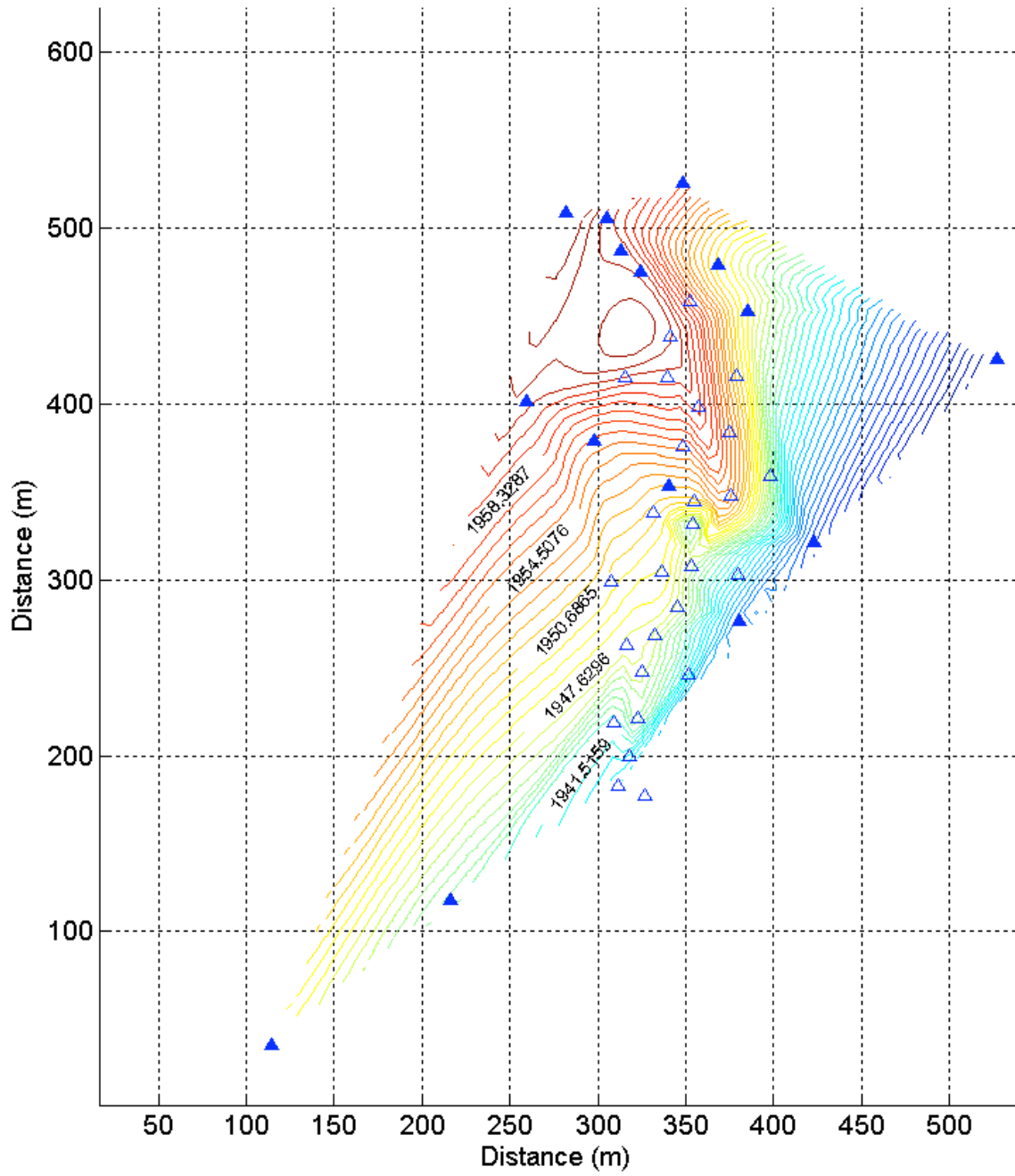


Figure 10: A figure showing the coal contour map in the subsurface, overlain by boreholes (solid triangles) and thermocouples (white triangles) in the area. Contour labels are in meters.

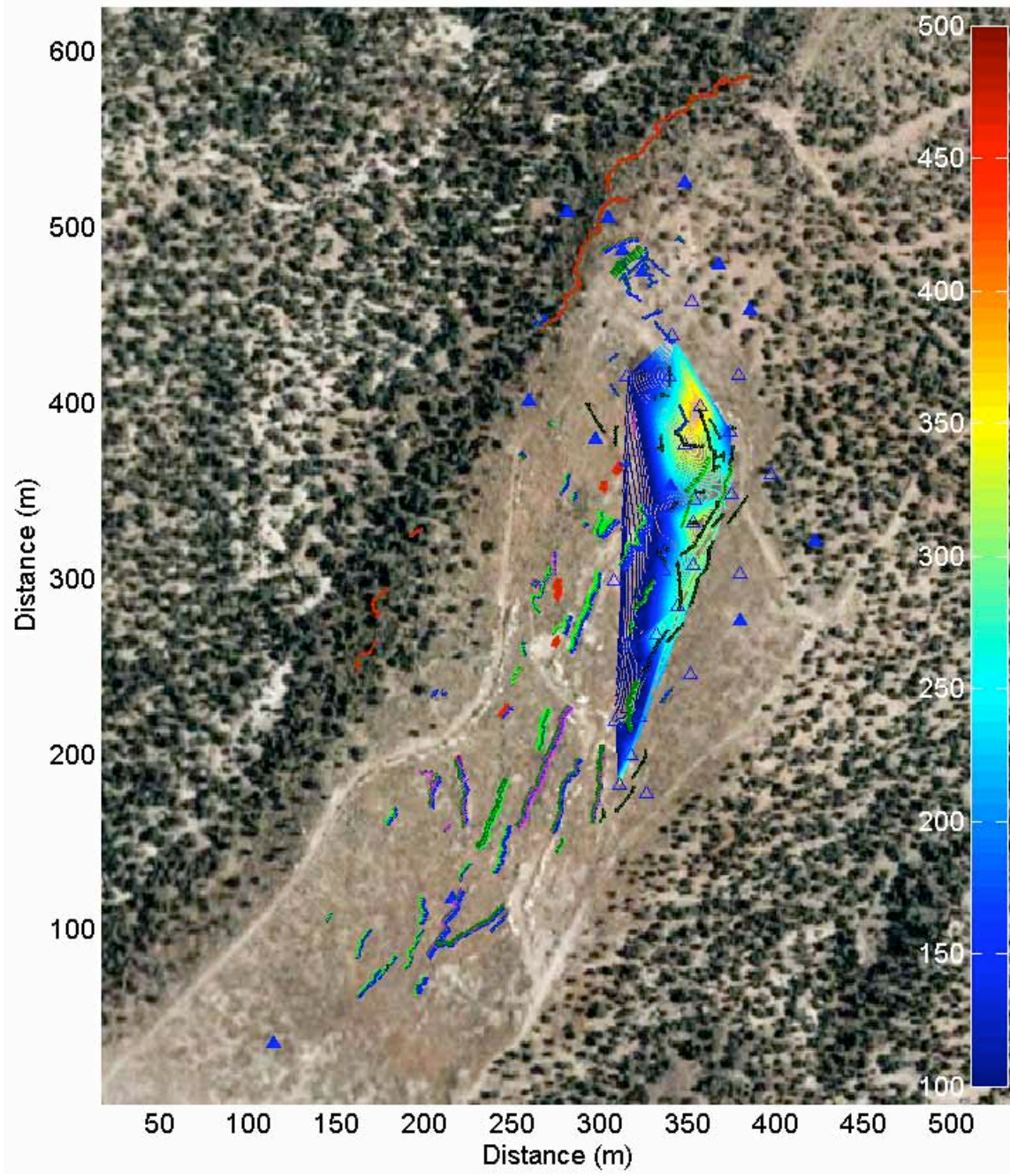


Figure 11: A satellite image of the area overlain by mapped fissures and thermocouple temperatures measured in 2001. Locations of boreholes (solid triangles) and thermocouples (white triangles) are also shown. Temperatures are in Celsius.

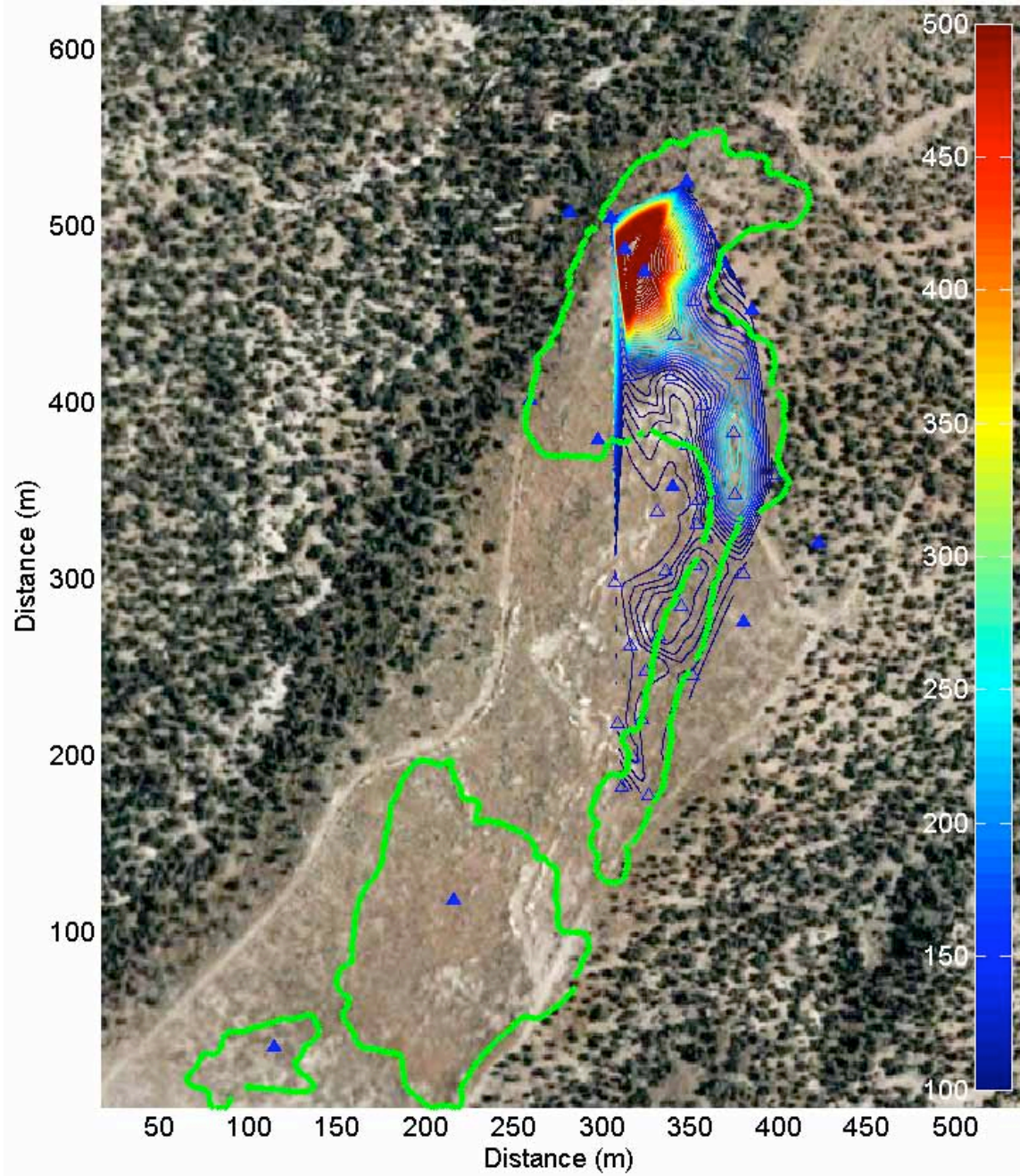


Figure 12: Figure shows the boundaries of the melted snow area (areas inside of the green lines) on top of a set of thermocouple measurements made in October of 2008. Locations of boreholes (solid triangles) and thermocouples (white triangles) are also shown. Temperatures are in Celsius.

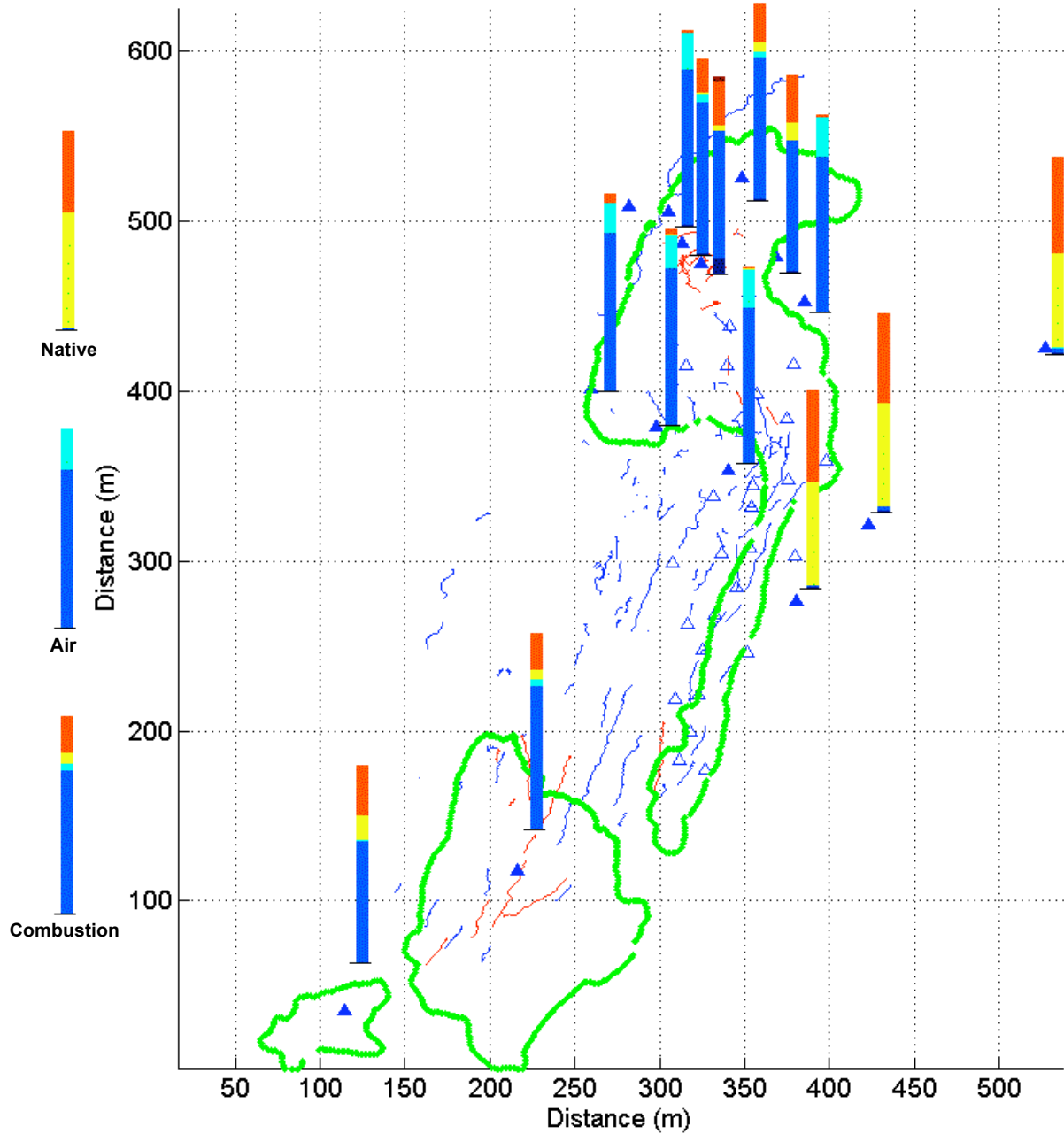


Figure 13: Gas composition distribution over the North Coalbed Fire. Fissures that are red indicate thermally active fissures, while the blue fissures indicate fissures that are at ambient temperatures. Snowmelt boundaries, boreholes (solid triangles), and thermocouples (white triangles) are also shown.

Interpretation of the field data

The field data collected provide various insights that are necessary for the characterization of this coalbed fire. Some caution must be exercised when using these data to draw conclusions about the fire. First, while we believe that we have documented most of the fissures that are uncovered over the North Coalbed Fire, there may be more fissures that are buried under the topsoil that remain unmapped. If these covered fissures lie in regions where the coal is no longer burning, it would be hard to uncover these even with the use of a thermal camera. Second, there is some limitation as to how the gas composition data may be used. When coal burns, it produces char, combustion gases, liquid tar and steam. When the gases are collected in the evacuated canister, we fail to collect the tar. Furthermore, during the gas analysis using gas chromatography, the water vapor is not separated. Thus the measured gas compositions are not representative of the atomic population of coal and air that resulted in the combustion. We cannot draw any quantitative conclusions about the in-situ state of the coal prior to combustion from the gas composition data. Gas composition measurements can be used to delineate regions that are unburned, currently burning, and previously burned as gas composition measurements from each of these regions have distinct gas composition signatures. Finally, a thermocouple temperature that is measured at any given point is at a fixed depth. While stationary temperature points may help in constructing a general propagation pathway of the combustion front, it cannot be used as a reliable data set for history matching in combustion simulations due to the low density of data.

Subsidence Modeling

Subsidence can occur when a burned coalseam loses its structural integrity and collapses under the weight of the overburden. Understanding the formation of fissures is important, as they appear to foreshadow the direction of the combustion front propagation and may play a key role in sustaining the underground fire. The hypothesis is that pre-existing joints with systematic patterns in the strata overlying the North Coalbed Fire widen to form fissures when the underground coalseam burns and then compacts as its structural integrity is lost. Previous literature has suggested or described relationships between surface deformation and subsurface subsidence, but no work has established useful first order functional relationships between variables that govern fissure widening and subsurface subsidence in a coalbed fire. In this study, a simple BEM model was formulated to simulate the collapse of the coalseam and the opening of pre-existing vertical fractures. The variables considered in this simulation were: E (Mpa), the Young's modulus, σ_{zz} (Mpa), the normal compressive stress defined along the horizontal elements to simulate the downward pressure due to the overburden, fd (m), the height of the vertical fracture, fl (m), the distance between the vertical fracture and the edge of the horizontal collapse, d (m), the depth, and a (m), the horizontal length of the collapse.

Results showed that the aperture of the fissures at the surface depends strongly on where the vertical fracture is located with respect to the subsurface subsidence. Sensitivity analyses that were performed also showed that relationships among the governing variables could be used to estimate the location and the magnitude of subsidence based on the fissure widths measured at the surface. The model was tested using a dataset obtained from a near by outcrop that showed evidences of subsidence in a

combusted coalseam and an opening of a vertical fracture above. Many assumptions, such as homogeneity, using a reduced elastic modulus to represent rocks instead of explicitly modeling the cracks, and flat topography, were made in this numerical simulation, and thus there is some discrepancy between the model results and measured values. A result from the study is presented in Figure 14.

In Figure 14a, a 12m horizontal line of elements that is located 10m below the surface is deformed by applying a uniform compressive stress of 0.25MPa, which is exerted by the weight of the overlying rock. The elastic modulus of the overburden is 10MPa, and a maximum compaction of 1.5m is induced at the horizontal elements. Figure 12 depicts the distribution of the horizontal component of normal stress, σ_{xx} , in response to the inward directed displacement discontinuity on the horizontal elements. The sign of σ_{xx} at the surface is indicated by the words tension (+) and compression (-). The blue solid line along the bottom of the figure indicates the horizontal elements subject to subsurface subsidence. We suggest that this inward directed relative motion is similar to what would occur as compaction of the coalseam developed during burning. Directly above the elements at the surface σ_{xx} is compressive. The greatest concentrations of surface tensile stresses emanate diagonally upward from the ends of the line of collapse.

A modification to the first simulation investigates the effects of the collapse on traction free vertical joints. The setting and the parameter values are the same as the first simulation (cf. Figure 14a), except vertical elements are introduced to simulate the joint. The vertical elements are placed at $x = -12\text{m}$, where tensile stresses found in the first case (cf. Figure 14a). Figure 14b shows the model geometry and the resulting normal horizontal stress (σ_{xx}) distributions when a horizontal collapse occurs near the vertical fracture. A comparison of Figures 14a and 14b shows that if a vertical joint exists off to the side of the compaction zone, σ_{xx} relaxes and becomes less tensile as the joint opens. Publication of detailed results is in progress (International Journal of Rock Mechanics).

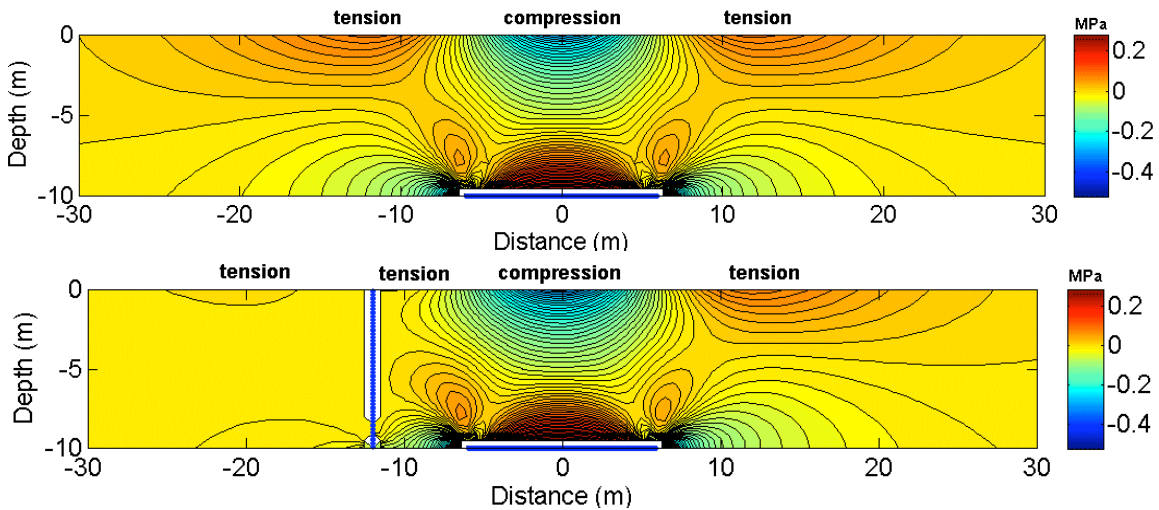


Figure 14: a (above): Subsidence along horizontal elements (blue solid line, bottom center) and resulting stress distributions in the domain. Tensile stresses emanate diagonally upwards from the edge of the

horizontal elements. Colorbar in MPa. b (below) A vertical joint located to the left of the collapsed region. Tensile stresses near the vertical joint are relaxed due to the traction free elements.

Currently, we are running similar subsidence simulations using a finite element method (FEM) algorithm provided by COMSOL. This method allows us to relax some of the previously mentioned assumptions associated with the BEM model. One of the major assumptions in the BEM model was the homogeneity of rocks above the coal layer. In the FEM simulations, each distinctive lithology is assigned an independent elastic modulus. In addition, each of the preexisting joints in the overburden may be explicitly modeled rather than assigning a reduced homogeneous and isotropic elastic modulus to the crack bearing rock. The first objective of running the subsidence simulations using the FEM algorithm is to compare these results with the relationships that were obtained from the BEM simulations. The same outcrop that was used to define the initial and boundary conditions in the BEM approach is used to define the model in the FEM simulation. Preliminary results show that removing assumptions of homogeneity and surface topography does not significantly change the variable relationships obtained from the BEM cases. The effects of explicitly modeling the cracks instead of assigning the rock a reduced elastic modulus are currently being investigated.

The second objective of the FEM simulations is to explore the different kinematics that would give rise to the four different types of fissures above the North Coalbed Fire. Different combustion profiles and thus different subsidence activities near pre-existing fractures will most likely result in variations in surface expressions. Exploring the subsurface kinematics may also help us understand the propagation path of the combustion front. To explore the occurrences of the four types of fissures at the surface, a model is defined as follows: In a domain, one pre-existing crack will be considered. A combustion profile—modeled as a void space—will be defined as the initial condition. The overburden will be allowed to collapse into this combusted area, and the resulting surface expressions will be analyzed. Sensitivities to variables such as proximity of the pre-existing fracture to the combustion front, depth and the length of collapse, the length of pre-existing fractures, and the overburden rock stiffness will be explored.

Combustion Modeling

Subsurface geology characterization fixes the amount of coal that is available for combustion. Using appropriate combustion simulation models, we will attempt to understand the rate at which this available resource is consumed given a set of boundary conditions obtained from the subsidence simulations. The objectives of combustion modeling are to determine: a) the rate of coal consumption by mass, b) the flux of air required to sustain a given rate of coal combustion, c) the effects of different types of fissures on combustion front profiles, and d) the length scale between the O₂ inlet and exhaust gas outlet fissures beyond which combustion is not sustainable.

In general, coal combustion can be characterized by devolatilization followed by a set of heterogeneous reactions between char and gases that are produced during pyrolysis. The kinetics that control char gasification with steam, CO₂, and H₂ and kinetics that control char combustion with O₂ or air are well documented [22]. To capture coal combustion adequately over a wide temperature and pressure ranges, introduction of radicals and hundreds of elementary kinetics into our simulation model are necessary.

Field scale length scales can be as $O(10^9)$ greater than length scales for which the elementary kinetics are derived; thus grid block resolutions necessary to resolve accurately the reactions may be beyond practical limits of computational efforts.

There are two different approaches that can be applied to overcome this computational problem. The first is to set up simple mass and energy balance systems to determine the rate of energy production that can be sustained for a given geometry. The second is to use simplified global equations to represent the reactions while still capturing the aspects of flow through porous media. In the first method, the combustion zone is likened to a chimney that has been built to sustain a specific rate of energy production. If chimneys are poorly designed, it cannot sustain a fire. At the North Coalbed Fire, the chimney dimensions are predetermined by the subsidence activities and the depth to the coal seam. Since a fire is currently active at the field, nature has created a functional chimney. It must then be possible to obtain a first order estimation of the rate of energy production that is sustainable given such dimensions. Given the rate of energy production, it is possible to calculate the rate of coal consumption. We are currently in the initial stages of calculating estimates using this approach. This approach, however, does not give rise to any insight involving flow dependent attributes such as combustion profiles.

The second approach that may be employed to model subsurface coal combustion is to use a set of global reactions that represent the coal combustion. Global reactions can represent coal combustion by either, a) using a set of frequency factors and activation energies to determine the rate of the reactions or b) assuming a high surface reactivity rate and thus diffusion limited combustion. Both of these methods are discussed below.

The first method of assumes a set of reactions that only involve a stable set of species (i.e. no radicals) that represent coal combustion. One can then define a set of frequency factors and activation energies associated with each reaction. Such values are readily available from literature [22, 23]. The limitation of such an approach is that these fitted frequency factors and activation energies are strongly temperature and pressure dependent. Once the temperatures and pressures in the simulation fall outside of the ranges for which the kinetics values were measured, the values are may not be valid. Furthermore, these values can vary significantly ($O(10^3)$) between different coals, even if they are within the same rank or type. Because rates of reaction are highly dependent on activation energies, a wide range in these values will impact the results significantly.

The second approach to coal combustion kinetics is to assume again, a set of reactions containing only stable species and assume a high rate of chemical reactions such that as soon as the a gas molecules (O_2 , CO_2 , H_2 , etc) reach the surface of the char, they are consumed. Thus the coal is consumed only at the outer edges. Under this assumption, neither frequency factors nor activation energies are necessary. Instead, the rate of reaction is controlled only by the rate of diffusion of these molecules to the surface of the char. Such an assumption is typically valid for coals with high temperature, high pressure, and a high density of active carbon sites, large particle diameters and low porosity [22]. At the North Coalbed Fire, large particle diameters and

low porosity are observed or documented, while high temperatures and high pressures by coal combustion standards (2000K, >>1 atm) are not observed. Finally, the number of active carbon sites has not been measured.

In both of these approaches, we will be modeling the combustion using only stable species. Because a propagation of a combustion front is governed by the presence of radical species, it is not possible to draw any conclusions about the relative amounts of stable species that result from the simulations. Typically, in numerical simulations of coal combustion such as those used to model Underground Coal Gasification processes, reaction parameter values are altered to fit experimental gas concentration or temperature data. As previously discussed, neither the GC data collected nor the underground temperature data provide enough information for such a history matching procedure. Since there are significantly more numerical parameters compared to the number of data points we have to match, a unique set of solutions cannot be expected. However, the results from these simulations can be used to understand the approximate, first-order dependency of coal combustion profiles on variables such as reaction rate, flow velocity, permeability, porosity, and the distance between O₂ inlets and exhaust gas outlets. In addition, in the modeling approach where the reaction is diffusion limited, (due to a high surface reactivity), an upper limit of the rate at which coal can be consumed can be obtained. Knowing the upper limit of the rate of combustion will be useful in designing fire-extinguishing strategies.

Conceptual Model

Figure 15 is a conceptual model of how the propagation of the combustion front at the North Coalbed Fire can lead to opening of fissures at the surface. The figure illustrates the local geology and geometry as well as some of the findings from the numerical investigations. In the figure, the lithology above the coalbed fire is characterized as either shales or sandstones. At the site, shales are often softer than the sandstones. In this conceptual model, the coalseam is transformed into a layer of ash as the thin combustion front propagates through the lower coal. The overlying strata collapse and a pre-existing joint opens up to form a surface fissure. The underlying Pictured Cliffs sandstone remains intact. Opened fissures above the fire may act as conduits that connect the surface and the coalseam. These fissures allow combustion gases to escape from the combustion zone, and enable fresh oxygen to reach the coalseam in order to keep the combustion alive. It is likely that combustion fronts do not propagate uniformly from the outcrop into the formation, as evidenced by the different types of fissures observed at the surface. This conceptual diagram will be edited accordingly as we gain further understanding of difference subsurface kinematics that give rise to the unique surface expressions over the North Coalbed Fire.

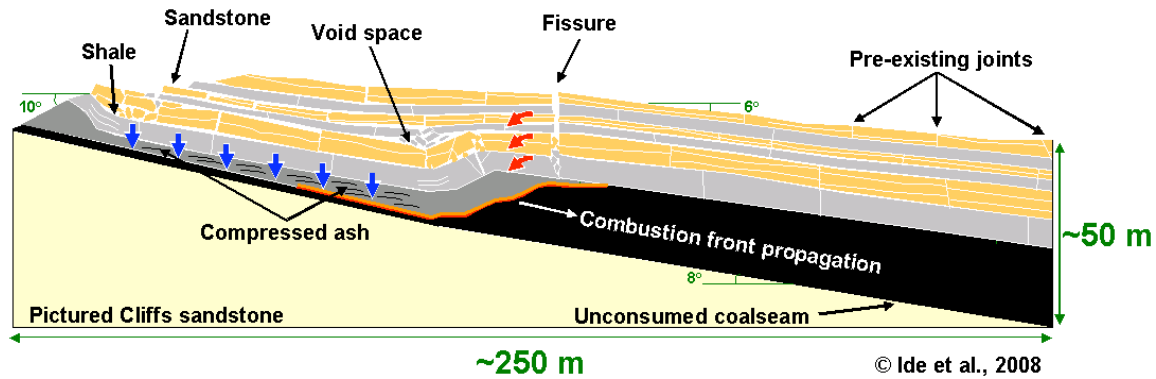


Figure 15: Figure showing the conceptual model of how a combustion front may propagate from the outcrop into the formation. Evidences such as thermally altered sandstones suggest that coal combustion took place near the outcrop. This conceptual model may only be one of many different ways in which a coalbed fire can propagate through the North Coalbed Fire site.

Future Plans

Future plans for this project include a field survey using a magnetometer, which measures the magnetic potential of the ground below the device. A contour plot of the magnetic potential can be constructed by collecting a large number of data points over the North Coalbed Fire. This contour map may be useful in understanding the history of the combustion propagation of the coalbed fire at the site. The fissures at the surface would not affect the magnetometer readings.

As discussed above, FEM subsidence modeling is currently underway to investigate the influences of variables such as heterogeneity on the results that we have obtained from the BEM subsidence modeling. Combustion simulations will be carried out in detail, starting with a simple energy and mass balance model (the ‘chimney model’) as described in the text. More complex combustion simulations will be considered to understand subsurface flow and combustion interaction.

Finally, combining our results from the simulations and field data, we hope to propose a method of introducing an inert gas into the subsurface through appropriate injection points above the coalbed fire. First order relationships that are obtained from running the subsidence and combustion simulations will determine both the location and the rate of inert gas necessary, respectively, to deprive the combustion zone of O_2 .

Acknowledgements

The authors of this paper would like to acknowledge: Bill Flint of the Southern Ute Indian Tribe for facilitating fieldwork details and his help in securing funding, the Southern Ute Indian Tribe for their gracious hospitality, allowing us to access their land and their continued support, Jonathan Begay, Kyle Siesser and Ashley Neckowitz for their help in the field, Nigel Crook, Seth Haines and Sjoerd de Ridder for their subsurface imaging expertise and analysis and GCEP and its contributors for their funding to make this research possible.

References

- [1] Dai, S., Ren, D., Tang, Y., Shao, L., and Li, S., Distribution, isotopic variation, and origin of sulfur in coals in Wuda Coalfield, Inner Mongolia, China, *International Journal of Coal Geology*, 2002:57:237-250.

- [2] Kuenzer, C., Voigt, S., and Morth, D., Investigating land cover changes in two Chinese coal mining environment using partial unmixing, **Gottinger Geographische Abhandlungen**, 2005:113:31-37.
- [3] Stracher, G., Taylor, T., Coal fires burning around the world: thermodynamic recipe for environmental catastrophe, **International Journal of Coal Geology**, 2004:59:7-17.
- [4] DeKok, D., Unseen danger: a tragedy of people, government and the Centralia Mine fire, **Philadelphia, PA: University of Pennsylvania Press**, 1986.
- [5] Brown, K., Subterranean Coal Fires Spark Disaster, **Science**, 2003:299:1177.
- [6] GAI Consultants, Inc., Engineering Analysis and Evaluation of the Centralia Mine Fire, 2 vols. Springfield: U.S. Department of Commerce, National Technical Information Service, 1983.
- [7] Kim, A., and Chaiken, R., Fires in abandoned coal mines and waste banks. Washington: United States Department of the Interior, Bureau of Mines, Information Circular 9352, 1993.
- [8] Prakash, A. and Gupta, R.P., Land-use mapping and change detection in a coal mining area: a case study in the Jharia coalfield, India. *International Journal of Remote Sensing*, 1998:19:391-410.
- [9] Kuenzer et al., Detecting unknown coal fires: synergy of automated coal fire risk area delineation and improved thermal anomaly extraction, *International Journal of Remote Sensing*, 2007:28:4561-4583.
- [10] Wessling et al., Numerical modeling for analyzing thermal surface anomalies induced by underground coal fires, *International Journal of Coal Geology*, 2008:74:175-184.
- [11] Kuenzer et al., Uncontrolled coal fires and their environmental impacts: Investigating two arid mining regions in north-central China, *Applied Geography*, 2007:27:42-62.
- [12] Huang, J., Bruining, J. and Wolf, K., Modeling of gas flow and temperature fields in underground coal fires, **Fire Safety Journal**, 2001:36:477-489.
- [13] Wessling, S., The investigation of underground coal fires: Towards a numerical approach for thermally, hydraulically, and chemically coupled processes, Ph.D. Thesis at **Westfälische Wilhelms-University**. Muenster: Germany, 2007.
- [14] McCurdy, K., Congressional response to coal fires: Illustrating transitions in the policy process. In: *Geology of coal fires: Case studies from around the world*, G. Stracher, ed. The Geological Society of America, 2007, pp. 97-115.
- [15] Kuenzer, C., Clean development mechanism: CDM – a booming market in China, *BusinessForum China*, 2007:3:54-56.
- [16] Williamson, R., Putting out the fire down below, **Denver Rocky Mountain News**, January, 1999.
- [17] Ide, T., Personal Communications with the Southern Ute Indian Tribe, 2007.
- [18] Kelso, B. S., and Wicks, D. E., A geologic analysis of the Fruitland Formation Coal and coal-bed methane resources of the San Juan Basin, Southwestern Colorado and Northwestern New Mexico, In: *Geology and coal-bed methane resources of the northern San Juan Basin, Colorado and New Mexico*, J. Fassett, ed. Denver: **Rocky Mountain Association of Geologists**, 1988, pp 69-79.

- [19] Fassett, J., Geology and coal resources of the upper cretaceous Fruitland formation, San Juan Basin, New Mexico and Colorado, Chapter Q, **U.S. Geological Survey, Professional Paper 1625B**, 2000.
- [20] Lorenz, J. C. and Cooper, S. P., Tectonic setting and characteristics of natural fractures in Mesaverde and Dakota reservoirs of the San Juan Basin, **New Mexico Geology**, 2003:25:3-14.
- [21] Condon, S. M., Joint patterns on the Northwest side of the San Juan Basin (Southern Ute Indian Reservation), Southwest Colorado. In: Geology and coal-bed methane resources of the northern San Juan Basin, Colorado and New Mexico, J. Fassett, ed. Denver: **Rocky Mountain Association of Geologists**, 1988, pp 61-68.
- [22] Larendeau, N. M., Heterogeneous kinetics of coal char gasification and combustion, *Prog. Energy Combust. Sci*, 1978:4:221-270.
- [23] Thorsness, C.B., Grens, E.A., and Sherwood, A., A one-deimensional model for in situ coal gasification. Livermore: Lawrence Livermore Laboratory, UCRL-52523, 1978.

Seismic Detection of CO₂ Leakage in Monitoring Wellbores

Introduction

A demonstration CO₂ sequestration project was carried out in Otsego County in the northern part of the Michigan Basin (Figure 1). This project is part of the Midwest Region Carbon Sequestration Partnership (MRCSP, www.mrcsp.org), funded by the Department of Energy/National Energy Technology (DOE/NETL) and several co-sponsors. Potential target formations for sequestration in the frame of MRCSP projects include several Paleozoic reservoirs, and in particular, Upper Silurian to Middle Devonian strata. The objectives of the demonstration project at this site were to evaluate the injectivity, storage capacity and overall suitability of the Bass Island Dolomite (BILD), a saline aquifer at 1050 m depth as a potential repository for CO₂ separated from natural gas produced from the Antrim shale. As will be shown, this demonstration experiment also provided the opportunity to test the possibility of leakage up pre-existing wellbores near the injection well. Given the very large number of pre-existing wells in depleted oil and gas reservoirs that might be considered for long term storage of CO₂, it is important to have a suite of monitoring strategies in place to assure that migration is not occurring through the caprock, along sub-vertical faults or fracture zones or along pre-existing oil and gas wells that may have been improperly plugged or whose cements may have been incomplete or corroded (Celia et al., 2004; Duguid et al., 2004).

A total of 10,241 metric tonnes of supercritical CO₂ were injected through a vertical well that was perforated at the depth of the target formation. The CO₂ for this project was separated from natural gas produced from the Antrim Shale at six centralized gas-processing plants in Otsego and adjacent counties. These plants produce ~1.2 million metric tons of CO₂ per year. A preliminary fluid flow simulation (Chiaramonte et al., 2007) indicates that the BILD formation as a whole has the potential to allow storage of about 50% of the Antrim Shale CO₂. The CO₂ is delivered to the test site through a pipeline that has been utilized for CO₂-EOR projects at approximately 1670 meters depth in the area.

Figure 2d shows a generalized stratigraphic column in the target area obtained from borehole logs and cores. The test interval for the demonstration project comprises the Bass Island Dolomite (BILD) and the Bois Blanc formations at 1050 m. The BILD formation is a porous dolostone at the top of the Silurian Bass Islands group which is found throughout the Michigan Basin at an average thickness of 15 m (Figure 1). Its local thickness is 22 m and no major structural complexities are reported. Porosity in the BILD formation averages 15% but ranges from less than 5% to more than 25%. The average permeability is less than 13 mD. Barnes *et al.* (*in press*) present a geologic interpretation based on cores from the BILD injection that was drilled in 2006. The authors suggest that the target unit was deposited in a restricted marine, possibly tidal flat, environment with periodic and possibly protracted, subaerial exposure surfaces that resulted in repeated karsted intervals. They indicated that mineralized natural fractures are common. The Bois Blanc Formation is overlying the BILD formation and described as a cherty carbonate strata of 78 m thickness. Although it could locally be considered as a seal due to the

apparent lack of suitable injectivity potential, it has been mentioned in other parts of the Michigan basin as another potential storage target. At the injection site, the BILD formation is considered as primary storage interval. The primary caprock is the Amherstburg-Lucas Formation (see Figure 2d), a dense limestone with very low porosity and permeability. Like the BILD formation, it has a laterally uniform thickness of ~80 m. Porosity values are mostly less than 5%. Permeability measurements showed very low permeability, mostly less than 1 mD. The unit was described from cores as a fossiliferous, dense, skeletal wackestone to mud-rich packstone unit that shows good potential as an effective caprock (Barnes *et al.*, *in press*).

One pre-existing production well and one recompleted, previously abandoned well were used to deploy a downhole seismic network (Figures 2 and 3). Another well close to the western monitoring well and deviated to the north has been used for EOR-related CO₂ injection for the previous 2.5 years into the Coral Reef reservoir that is located below the BILD formation at 1670 m depth (Figure 2). Due to the limited capacity of the CO₂ pipelines in the area, the injection into the Coral Reef had to be interrupted to carry out the injection into the BILD formation.

Figure 4 summarizes the injection flow rates into the BILD formation and the associated downhole pressure within BILD. It also shows the daily rate of the detected microseismic activity and the fluid flow rates into the Coral Reef for the same time period. The BILD injection started on Feb 8, 2008 (Julian day 39), injecting at ~7 million cubic feet per day (Mmcf/d) for about two days. During that time no remarkable increase of the downhole pressure at the injection well was observed. After a five-day shut-in phase (days 41-46) a short-term injection at maximum flow rate of up to 20 mmcf/d was performed on day 46. The main injection into the BILD formation started on day 49 and resulted in a pressure maximum of 8.5 MPa. After a drop in pressure during continued injection throughout day 74 a slow but systematic increase in pressure is observed reaching a plateau at ~7.5 MPa. Upon completion of the BILD injection pressure slowly decreased.

Prior to the demonstration project in the BILD formation, injection into the deeper Coral Reef reservoir had gone on for 2.5 years (non-continuously) and was stopped on day 39 after injecting at rates as high as 12 mmcf/d (Core Energy, pers. comm.). After a one-day break (day 41) injection into the Coral Reef continued at a high level until day 50. In Fig. 4, it should be noted that only 1 day averages of the Coral Reef injection rate are available. After effective termination of the BILD injection on day 67 the Coral Reef injection was resumed. The temporal evolution of the microseismicity is discussed in the following section.

Downhole Passive Seismic Monitoring (PSM) of the CO₂ injection

One principal monitoring objective of the Michigan Basin demonstration project was to evaluate whether the CO₂ injection into the BILD formation was accompanied by induced microseismicity. At the same time, this experiment was seen as a generic study investigating the potential role of downhole PSM in the framework of CCS in similar formations in this region. Pressure increases associated with CO₂ injections into deep formations will reduce effective normal stresses and may thereby induce slip on pre-existing faults, leading to induced microseismicity in conjunction with permeability

enhancements. PSM aims at monitoring such induced microseismic activity in the target formation at low-magnitude detection threshold. PSM is a well-established technique and is frequently applied during hydraulic fracturing operations in the hydrocarbon industry or during permeability enhancements in geothermal reservoirs (e.g. Rutledge et al., 1994; Shapiro, 2008). Microseismic data are also crucial in other rock engineering applications, such as mining activity, excavation stability in nuclear waste repositories or geotechnical stability studies (e.g. review by Bohnhoff et al., 2009).

The great majority of induced microearthquakes are usually of extremely small magnitude and thus cannot be detected at hypocentral distances greater than a few hundred meters (e.g. at the surface). Changes in the number of microearthquakes can be correlated with changes in the fluid-injection rates and pressure perturbations. Microseismic activity usually starts close to the injection point where pressure increases are largest. The hypocentral cloud then migrates away from that initial location following preferred orientations predefined by the local stress-field orientation or local fault structure (see Shapiro, 2008 for examples). Because there is the need is for passive seismic monitoring with as low a magnitude detection threshold as practical, PSM is usually carried out with seismometers in monitoring wells within several hundred meters of the injection well. Microseismic monitoring was selected for this project because there are two accessible wells for monitoring near the injector well, at only 150 and 550 m lateral distance from the injector well, respectively (Figure 3). A downhole seismometer array consisting of eight, three-component sensors was deployed in each well. Both arrays have an overall aperture of 105 m with equidistant sensor spacing of 15 m (Figure 3). Array 1 was deployed in the vertical eastern monitoring well at 550 m lateral distance to the injection point. Array 2 was deployed in the western monitoring well that is vertical down to 530 m. Below that it deviates 11° towards WNW (Figure 3). Both monitoring wells were drilled in the 1970s as vertical production wells extending all the way down into the Coral Reef reservoir. The deviated section of the western monitoring well was completed recently, and extends down to 1200 m. The original vertical section of this well below 530 m was plugged and abandoned (we refer to this later in the text).

Both seismic arrays were deployed slightly above BILD at ~900-1000 m true vertical depth and both monitoring wells were sealed above the BILD formation by a packer (Figures 2 and 3). This exceptionally good network geometry allowed to monitor potentially induced microseismic activity within the BILD formation down to magnitudes as low as -3.0 (Engineering Seismology Group, pers. comm.). The PSM field campaign and pre-processing of the seismic recordings was conducted by Engineering Seismology Group, Kingston/CA (www.esg.ca). A total of seven calibration shots were fired inside the BILD injector well on day 24, directly after the seismic arrays were deployed but several weeks before the BILD injection commenced. Shots were fired at two distinct depth levels in order to record incoming seismic waves at two different incidence angles. The recordings of the shots served to ensure the functionality of the seismic arrays and recording system, to determine the orientation of the sensors at depth from the polarization of the P-waves and to calibrate the velocity model. The signal-to-noise ratios obtained from the shots was adequate to allow us to reliably determine the azimuth and incidence angles of the incoming rays and determine the orientation of the sensors. A waveform example showing the vertical components of all 16 sensors of one of the calibration shots is shown in Figure 5a. A measure of the hypocenter location accuracy,

the shots were located with an uncertainty of less than 20 m. Clear P and P-to-S converted phase onsets were identified for each of the shots on both arrays. To check the consistency of the picked phases and determine the P- to S-wave velocity, (v_p/v_s) for the area between the wells we plotted Wadati diagrams (Wadati, 1933). Therein, the differential travel time between P and S wave (T_s-T_p) at either sensor is plotted against T_p . Assuming a constant v_p/v_s ratio for the various travel paths of the seismic waves, the data of all sensors should fall on a line. Thus, the quality of the line fit is a measure of the consistency of the data set. Figure 5b shows the Wadati diagram for the recordings of all seven shots demonstrating the high consistency of the data set. The obtained average v_p/v_s ratio is 1.84 for the volume sampled by the elastic waves which is in good agreement with 1.90 as obtained from sonic logs along the wells at the relevant depth interval.

Seismic monitoring was carried out between days 23 and 70 continuously recording at a 4 kHz sampling rate. During that time period a total of 817 “triggers” were observed on the seismic arrays. 770 of the events were detected only at array 1 in the eastern monitoring well while only 39 events were detected at array 2 in the western monitoring well. Only eight events were recorded at both arrays of which seven were the calibration shots. The difference in number of detections cannot be explained by a difference of the overall noise conditions in the two monitoring wells as indicated from analysis of background noise levels at each particular sensor. Some sensors (sensor 5 of array 1; sensors 9 and 11 of array 2) did show a substantial higher noise level than others and were excluded from any further data processing in the following.

Data processing and spatiotemporal occurrence of microseismicity

Each of the 817 detected events was inspected individually to separate ‘seismic events’ from ‘non-seismic’ detections such as spikes, electronic noise or non-seismic signals of unknown origin. Thereafter, a total of 225 events were classified as ‘microseismic events’ and considered for further evaluation. 201 out of the 225 microseismic events were detected only at array 1 while 23 were detected only at array 2. Only a single microseismic event was seen on both sensor arrays. Interestingly, the vast majority of the 225 seismic events occurred during the first days of the monitoring period and the seismicity rate decays to almost zero before the shallow injection into the BILD formation was even started. This was completely unexpected as fluid-injection induced microseismicity is expected to start only after the onset of injection.

Onset times of the different seismic phases were picked manually in the seismograms. Several distinctly different frequency characteristics of the P waves were observed in the seismic recordings. Figure 6 gives an overview on the most common types of waveform characteristics. A large number of events contain prominent secondary phases that appear to be S phases. However, the v_p/v_s ratios calculated from the apparent S-P differential travel times would correspond to nonphysical values for Poisson’s ratio for geologic formations. Nor do the apparent S-P times agree with the values determined from analysis of the calibration shots (1.84) and sonic logs (1.90). Most importantly, the inversion of the P and apparent S onset times did not converge towards reliable hypocenters. Determining the phase velocities across the sensor arrays of the first and secondary arrival times we obtained values of typically 4.8 ± 0.2 km/s (P waves) and 1.5

+/- 0.1 km/s (secondary waves), respectively. While these values reflect compressional wave velocities of the surrounding rock formation (P waves), the secondary phases are not S waves but appear to be tube waves. Tube waves are waves propagating along a well with the speed of the borehole fluid. Tube waves are a well-known phenomenon in borehole seismology (e.g. White, 1983; Paillin & Cheng, 1991) with early observations dating back to the 1950s (Summers and Broding, 1952; Vogel, 1952). Tube waves are generated in a variety of ways, one of which is when an incoming elastic wave passes a discontinuity (i.e. a density contrast). The density contrast may be represented by the well itself, a strong impedance contrast in the formation surrounding the well, a change in casing size or a body inside the well. Once generated, tube waves propagate in both directions along the well with little energy loss. This is exactly what we observe along both of the two seismic arrays. In our case, the arrays themselves probably represent the requisite density contrast (steel versus fluid) inside the well needed to generate tube waves. These tube waves then propagate to either side along the arrays and, in some cases, are even back-reflected at the end of the array (Figure 6b).

The vast majority of the 225 events identified as induced seismic signals, therefore, do not appear to represent shear failure on reactivated fault patches due to increased fluid pressure near the injection well as one would expect in fluid injection experiments. This is especially important with respect to the unusual location of the hypocenters discussed below. Only one event (on day 56) appears to be an expected injection-induced microseismic event associated with shear slip on a pre-existing fault. Using the hypocentral location techniques described below, this event was found to be located between the two sensor arrays (it was the only event, other than the calibration shots, detected on both arrays). As shown in Fig. 3, it is located ~100m above and some ~250 m to the southeast of the injection point.

A number of sensors exhibited a ringing signal after the P onsets. Such a signal may either be caused by reverberating casing that is not properly bonded to the formation by cement, or by bad coupling of the sensor to the casing. Regardless of the exact origin of these reverberations, we performed a frequency analysis for each of the events at each sensor to exclude the ringing signals by digital filtering of the affected traces. We removed 60 Hz noise in the same manner. After noise removal, we classified the events with different waveform characteristics into the following subgroups: 1. Events with P wave frequencies of ~500 Hz (see Figure 5 a-c); 2. Events with P wave frequencies of ~100-150 Hz (see Figure 5d-f); 3. Events with precursory phases (see Figure 5 c+e); 4. Swarm-type events (see Figure 5f) and furthermore a total number of 5 events (4 of which are extremely weak in amplitude) exhibit secondary phase that might be associated with S-waves. Furthermore, we observe one event-triplet, i.e. three events with highly similar waveforms occurring within a few seconds.

Hypocenters were determined by applying a least-square inversion to the P wave arrival times at the individual sensors of the arrays. A homogeneous velocity model with $v_p=4.8$ km/s was used and the position of the sensor with the earliest arrival time was used as the starting location for the inversion. As we are inverting only P wave arrival times (but no shear-wave arrival times) we do not have information on sensor-specific source distances. Particle motion analysis for the individual three-component recordings did not result in stable azimuth determinations for the events. Therefore, the actual inversion is performed in 2D and the obtained hypocenters contain information about

depth and lateral distance to the array, but there is no information about the azimuthal position. As a consequence, we project the hypocenter locations onto an EW-trending depth section in Figure 3 for illustration purposes only. We obtained a total of 94 stable hypocenter locations. All of the events were found to be located in the direct vicinity of one of the arrays with a maximum lateral distance of 35 meters (Figure 3). The majority of events occurred near the shallower portion of the arrays. In addition, a total of 40 events produced clear P onsets on the sensors but occurred above or below the arrays (e.g. Figure 5 a+b), not permitting us to determine their exact source location. Because of their extremely small magnitude and rapid decay of amplitude with distance, these events appear to have occurred in very close vicinity to the arrays and are indicated by the circles in Figure 3. With the average picking accuracy for the P onset times of 0.25 msec we estimate the precision of the hypocenters to be in the range of 5 meters for the events near the arrays. No microseismic events were found to have occurred at the depth of the BILD formation. The eastern monitoring well (201 events) that extend down into the Coral Reef shows a much higher seismicity rate than the western well (23) that extends to just slightly below the BILD.

Discussion

It is widely recognized that events detected during passive seismic monitoring of fluid-injection operations result from slip on pre-existing faults, sometimes revealing a network of intersecting fractures (e.g. Rutledge et al., 1994; Baisch & Harjes, 2003, Shapiro, 2008). Even during hydraulic fracturing operations, the hydrofrac acts as a source of fluid pressure that stimulates slip on the pre-existing fracture and fault network, but is not itself the origin of the great majority of the seismic events. Hypocenters typically cluster into well-defined small-scale geometrical patterns (e.g. Philips et al., 2002) and the enhanced use of such data sets has made significant progress in recent years applying location collapsing methods (Jones & Stewart, 1997) as well as relative relocation techniques (Waldhauser & Ellsworth, 2000).

In the case of the CO₂ injection into the BILD formation, we did not expect to create a hydraulic fracture because the injection pressure did not exceed the least principal stress at depth. Instead we expected to determine if shear slip on pre-existing faults and fractures within the storage formation was induced by the increased pore-fluid pressure. Prior to the BILD injection, a packer was installed in the western monitoring well below the sensor array to prevent potential upward flow of CO₂ inside the well from the BILD formation. No such packer was needed in the second well, because it was not perforated in the BILD formation.

As mentioned above, the observed microseismic events occurred before the injection into the BILD formation started (Figure 4). Hence, the observed microseismic events cannot be related to the BILD injection, both in terms of its spatial and temporal distribution. In contrast, the temporal occurrence of the induced microseismicity has a clear correlation with the EOR-related injection of supercritical CO₂ into the Coral Reef at 1670 m depth (Figure 4). As described above, the deeper injection was going on for about 2.5 years and was interrupted to carry out the BILD injection. It is likely, therefore, that the observed microseismicity reflects leaking CO₂ that rises from the Coral Reef along gaps in the cement annulus of each of the monitoring wells during injection into the

Coral Reef. Several other observations in Figure 4 further support this argument. First, the microseismic events stop when the deep injection is stopped after day 50. Second, microseismic events with the same characteristics as during the early phases of deep injection again occur on day 69 when the deep injection resumes.

Highest microseismicity rates are observed when flow rates of the deep injection reached maximum values of ~11 mmcf/d on day 38 (Figure 4) then declined after the Coral Reef injection was stopped. Microseismic activity again appeared during the Reef injection on days 42-50 but then decreased to zero during the entire major phase of the BILD injection (day 50-67). It is interesting that not a single seismic event was observed within the BILD formation. One possible explanation for this observation is that a hydraulic communication between the Coral Reef and BILD formations exists along old wellbores. Such a communication may have released shear stress on pre-existing faults and fractures in the BILD formation during the Coral Reef injection, sometime during the last several years.

The CO₂ is injected under high pressure as a supercritical fluid resulting in a complex multiphase fluid system within the Coral Reef reservoir. Fluid properties such as density, enthalpy and viscosity are essential for describing non-isothermal flow in porous media and they might severely change depending on the actual pressure conditions and on the exact resulting fluid composition. Buoyancy due to gravitational forces plays an important role when CO₂ is injected into the subsurface because of its low density with respect to formation brines. CO₂ is also known to have larger compressibility than water, so that modest pressure reductions can cause a large volumetric expansion. Up flow of leaking CO₂ from the deep reservoir towards the surface would result in decreasing pressure and temperature conditions eventually resulting in the CO₂ changing from a supercritical fluid to a gaseous phase. This process is accompanied by volume expansion and reduction in average fluid density.

The downhole pressure at the Michigan test site at the depth of BILD is essentially hydrostatic. Temperature measurements from more than 100 sites throughout the Michigan Basin indicate an average thermal gradient of 2.9 °C / 100 m (Gardner & Bray, 1984). Using the downhole pressure and thermal gradients as boundary conditions we calculated the density versus depth relation for pure CO₂ according to the Peng-Robinson Equation of State (PREOS) (Kovscek, pers. comm.). The resulting graph indicates a systematic decrease of CO₂ density with decreasing depth (Figure 7, left). Moreover, the density gradient with depth has a pronounced maximum between 850 m and 950 m (Figure 7, right). This is exactly the depth interval covered by the seismic arrays and the depth, where we observed microseismic activity as discussed above. We conclude that the detected microseismic events most likely represent the volume increase (degassing) of the CO₂ that is leaking up around the two monitoring wells. This also helps explain the extremely small size and the unusual characteristics of the seismic waveforms acquired by the two downhole seismic arrays (Figure 6). While the density changes reach their overall maximum at 850-950 m the curve suggests that degassing of CO₂ while migrating towards the surface might also occur slightly above and below this depth, but at a lower activity level. This would suggest that a small number of microseismic events of the same type as observed along the sensor arrays occurred off the arrays but remained undetected due to their small magnitude size.

The actual physical mechanism responsible for the leakage is not fully understood. For simplification, we assume that a multi-phase system of CO₂, formation water and oil exists in the Coral Reef formation. Assuming that these phases do not interact over the time scale of injection due to buoyancy effects, the CO₂ will likely accumulate at the reservoir/cap rock interface (Figure 8). There, the significantly lower permeability of the overburden would be expected to prevent the CO₂ from rising and acts as a seal unless a through-going permeable fault or a leaky wellbore were present. As described above, the Coral Reef injection on day 69 instantaneously induced microseismicity close to the eastern monitoring well. It appears, therefore, that flow along the pre-existing wellbores result in rapid vertical pressure communication between the two formations. A confirmation of the potential migration from Coral Reef along well bores and assessment of physical mechanisms for the migration can only made through additional characterization of wellbore and cement integrity in the Coral Reef well.

Conclusions

As illustrated in Figure 9, it seems clear that the unusual (i.e., non-shear) microseismic events detected near the two monitoring arrays is due to the EOR-related injection into the Coral Reef formation and leakage of CO₂ along the outside of the well casings. The instant occurrence of microseismicity ~700 m above the depth of injection following the resumption of the Coral Reef injection further demonstrate vertical hydraulic communication between the two formations due to leakage along the well casings.

The fact that 90% of the detected events were observed at the eastern monitoring well and only few events were detected at the western monitoring well probably reflects the relative amount of leakage along the two wells, but requires further investigation. As both seismic arrays had essentially equal noise levels, it does not appear to be a detection phenomenon.

The single shear microseismic event that was detected during BILD injection and the complete absence of microseismic events in the BILD formation both raise a number of interesting questions. For example, it is not known if the shear event occurred along a pre-existing fault connected to the BILD formation or if the absence of microseismic events within the BILD result from the fact that the pressure change within the formation during injection was inadequate to initiate slip on pre-existing faults. However, pressure changes in the BILD over the past ~2.5 years associated with the Coral Reef injection may have caused slip on faults and effectively *de-stressed* the BILD formation.

It was indeed fortuitous that the placement of the seismic arrays was exactly at the depth where the density of the supercritical CO₂ changes abruptly as it changes from being in a critical state to a gas. This said one could use knowledge of pressure and temperature at depth to deploy seismic arrays at the depth of the CO₂ phase change in order to use passive microseismic monitoring to detect leakage along pre-existing wellbores.

Acknowledgements

We thank Core Energy for permission to use the wells for the experiment and for providing extensive logistical support. We also thank Engineering Seismology Group,

Kingston/CA for conducting the seismic field campaign. We thank Jerry Harris for fruitful discussions.

References

- Baisch, S. and Harjes, H.P., A model for fluid-injection-induced seismicity at the KTB, Germany. *Geophys. J. Int.*, 152, 160-170, 2003.
- Barnes, D.A., Wahr, A., Harrison, W.B. III, Grammer, G.M., and Gupta, N., Geological Carbon Sequestration Potential in Devonian Saline Aquifers of the Michigan Basin, AAPG/EMD/DEG Special Publication on Geological Sequestration of CO₂, in press.
- Bohnhoff, M., Dresen, G., Ellsworth, W.L., Ito, H., Passive Seismic Monitoring of Natural and Induced Earthquakes: Case Studies, Future Directions and Socio-Economic Relevance. ILP special volume: *Frontiers in Geosciences*, Springer, in press.
- Celia, M., Bachu, S., Nordbotton, J.M., Gasda, S.E., Dahle, H.K., Quantitative Estimation of CO₂ Leakage from Geological Storage: Analytical Models, Numerical Models, and Data Needs. Paper 228, 7th Int. Conf. on Greenhouse Gas Control Technologies, Vancouver, Canada, Sept 5-9, 2004.
- Chiaromonte, L., Zoback, M.D., Gerst, J., Gupta, N. Can Controlled Induced Microseismicity be used to Enhance Permeability in Geological CO₂ Sequestration Targets?, 6th Ann. Conf. on Carbon Capture and Sequestration, 2007.
- Duguid, A., Radonjic, M., Bruant, R., Mandecki, T., Scherer, G., Celia, M., The effect of CO₂ Sequestration on Oil Well Cements, paper 123, 7th Int. Conf. on Greenhouse Gas Control Technologies, Vancouver, Canada, Sept 5-9, 2004.
- Gardner, W.C. and Bray, E.E., Oils and Source Rocks of Niagaran Reefs (Silurian) in the Michigan Basin, in J.G. Palacas, ed., *Petroleum geochemistry and source rock potential of carbonate rocks: AAPG Studies in Geology* 18, p.33-44, 1984.
- Jones, R.H., and Stewart, R.C., A method for determining significant structures in a cloud of earthquakes. *J. Geophys. Res.*, 102(B4), 8245-8254, 1997.
- Paillet, F.L., Cheng, C.H., *Acoustic Waves in Boreholes*, ISBN 0-8493-8890-2, CRC Press Inc., Boca Raton, Florida, 1991.
- Phillips et al., 2002. Phillips WS Rutledge JT House LS Fehler MMC (2002) Induced Microearthquake Patterns in Hydrocarbon and Geothermal Reservoirs: Six Case Studies. *PAGEOPH* 159:345-369
- Rutledge, J.T., Phillips, W.S., Roff, A., Albright, J.N., Hamilton-Smith, T., Jones, S., Kimmich, K. Subsurface fracture mapping using microearthquakes detected during primary oil production, Clinton County, Kentucky, paper SPE 28384, Soc. of Petro. Eng. Ann. Tech. Conf., 1994.
- Shapiro, S.A. *Microseismicity: A tool for reservoir characterization*. Education Tour Series CIS, EAGE, ISBN 978-90-73781-70-2, The Netherlands, 2008.
- Summers, G.C., Broding, R.A., Continuous velocity logging, *Geophysics*, 17, 598-614, 1952.
- Vogel, C.B. A seismic velocity logging method, *Geophysics*, 17, 586-597, 1952.
- Wadati, K. On the travel time of earthquake waves II, *Geophys. Mag.*, 7, 101-111, 1933.

Waldhauser, F., Ellsworth, W.L. A Double-Difference Earthquake Location Algorithm: Method and Applications to the Northern Hayward Fault, California. *Bull. Seismol. Soc. Am.*, doi:10.1785/0120000006, 2000.

White, J.E. *Underground Sound: Application of Seismic Waves, Methods in Geochemistry and Geophysics*, 18, Elsevier Amsterdam-Oxford-New York, 1983.

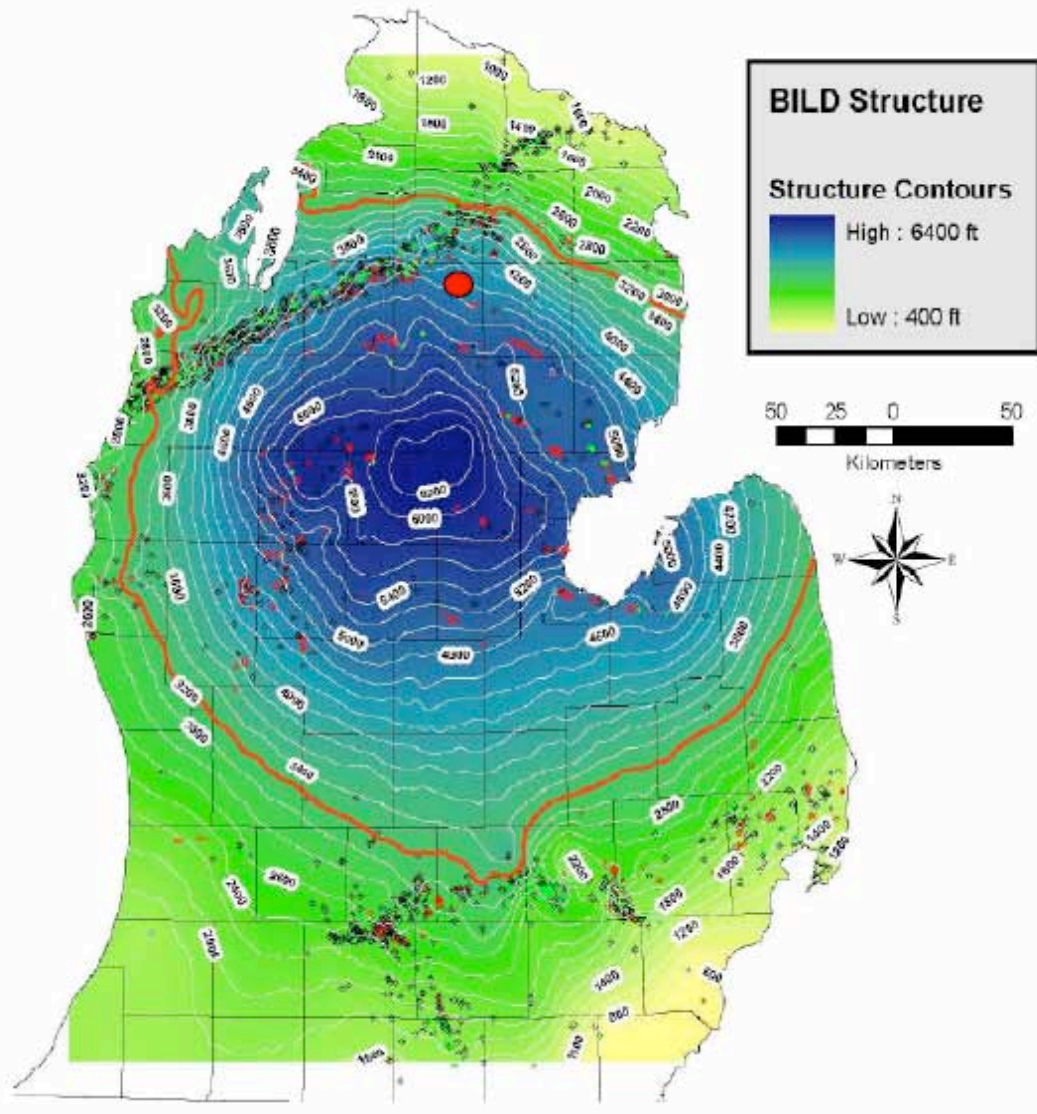
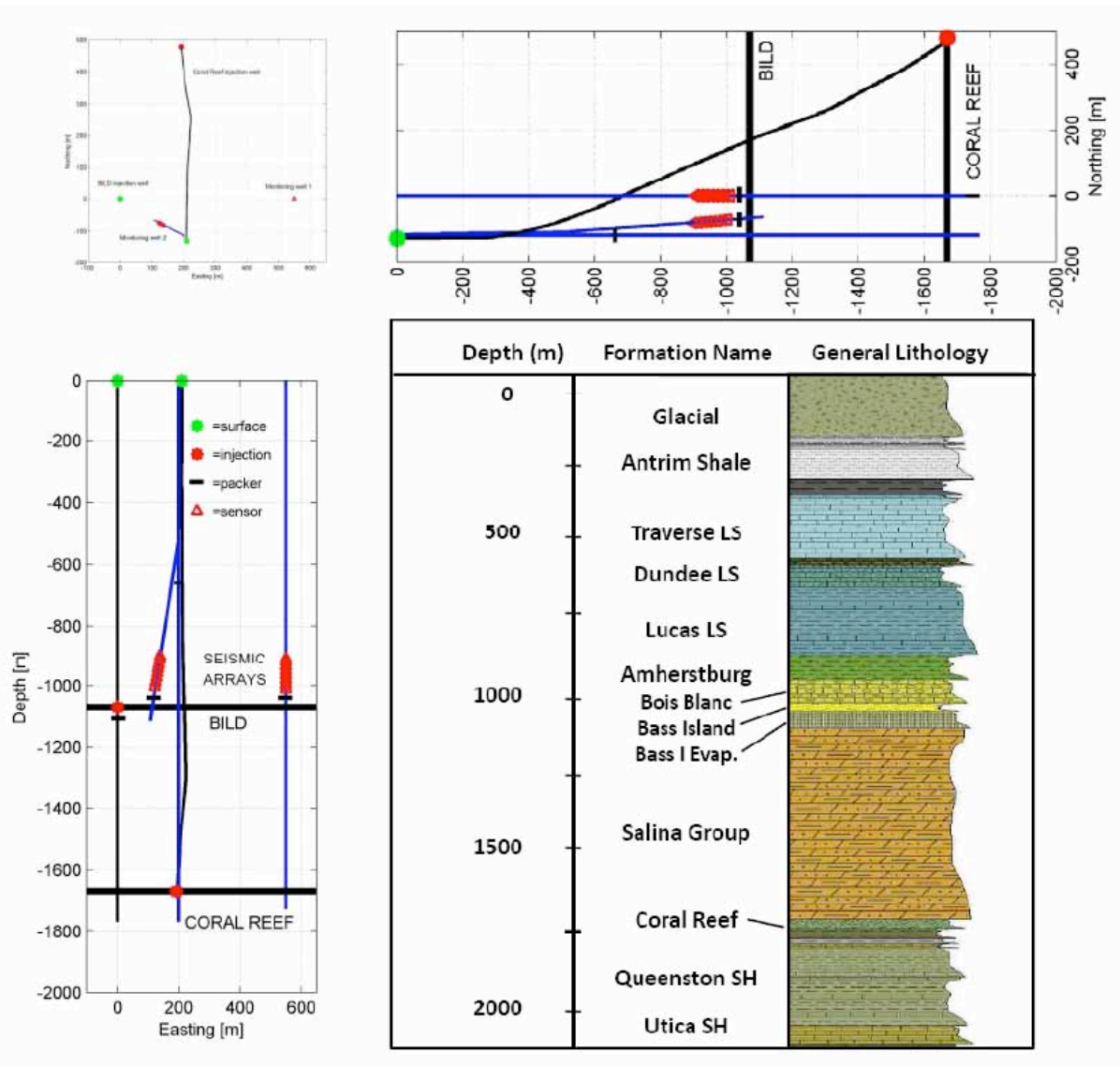


Figure 1: Depth of the Bass Island Dolomite (BILD) formation throughout the Michigan Basin. The red circle represents the location of the test site, where the combined CO₂ sequestration and downhole Passive Seismic Monitoring (PSM) experiment was carried out. The average thickness of the BILD layer throughout the Michigan Basin is 15 m and its local thickness at the injection site is 22 m. While regional changes of the depth of the BILD layer are considerable no major local variations in its depth (1050 m) are reported.



Figures 2: a)-c): Geometry of the wells involved in the combined CO₂ injection and Passive Seismic Monitoring (PSM) campaign at the Michigan test site. Injection wells are plotted black while monitoring wells are plotted in blue. Two seismic sub-arrays of eight three-component sensors each were deployed in two monitoring wells at 150 and 550 m lateral distance to the BILD injector, respectively. The aperture of either array is 105 and the sensors (indicated by the red triangles) have a 15 m equidistant spacing. The eastern monitoring well is vertical while the western monitoring well consists of an older abandoned vertical part and a new part that is deviated towards the WNW (see text for details). The Coral Reef injection well is located close to the western monitor well and deviated towards the north. The green circle represents the surface location of either injection well whereas the red circle represents the injection point at depth. Black circles represent packers. The geometry of the wells is shown in map view (a), and as depth section from the east (b) and the south (c). Target formations for the shallow (BILD) and deep (Coral Reef) injections are indicated by the bold black lines. 2d): Stratigraphic column of the well used for CO₂ injection into the Bass Island Dolomite (BILD) at 1050 m depth and the overlying Bois Blanc Formation. The Amherstburg-Lucas formation was expected to act a seal against CO₂ leakage. LS= limestone. The Coral Reef was used for EOR-related CO₂ injection and is located at 1670 m depth.

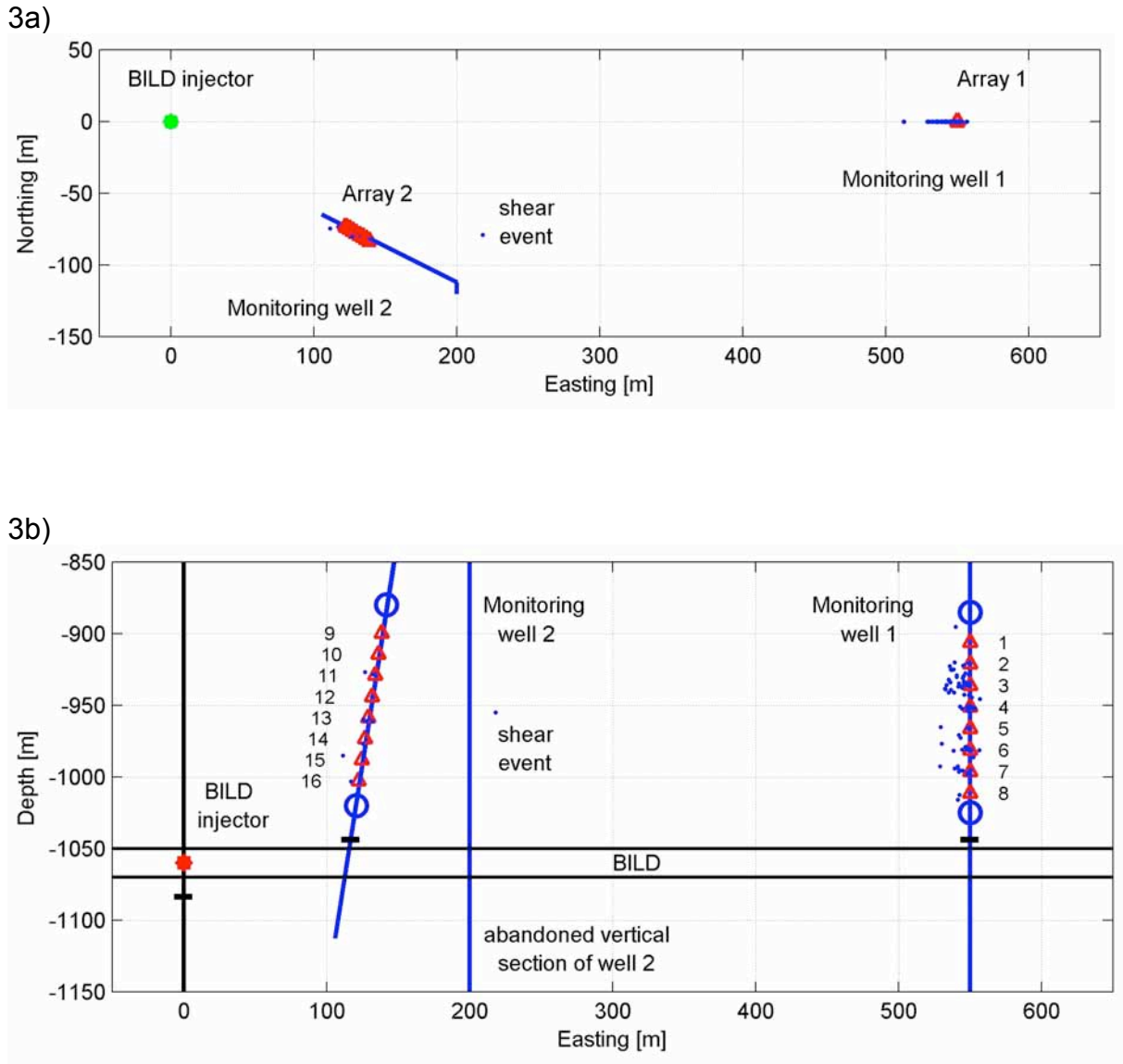


Figure 3: Blow-up of Figure 2 focusing on the downhole seismic network and the BILD injection well (the Coral Reef injection well is not shown). a) shows the map view and b) is a depth section seen from the south. Symbols are as in Figure 2. Blue dots represent hypocenters of the induced microseismicity. Blue circles represent a smaller number of events that could not be located precisely but that are known to be located close to either end of the sub-array (see text for details). The only event seen on both sensor arrays was also the only shear event and is indicated in a) and b).

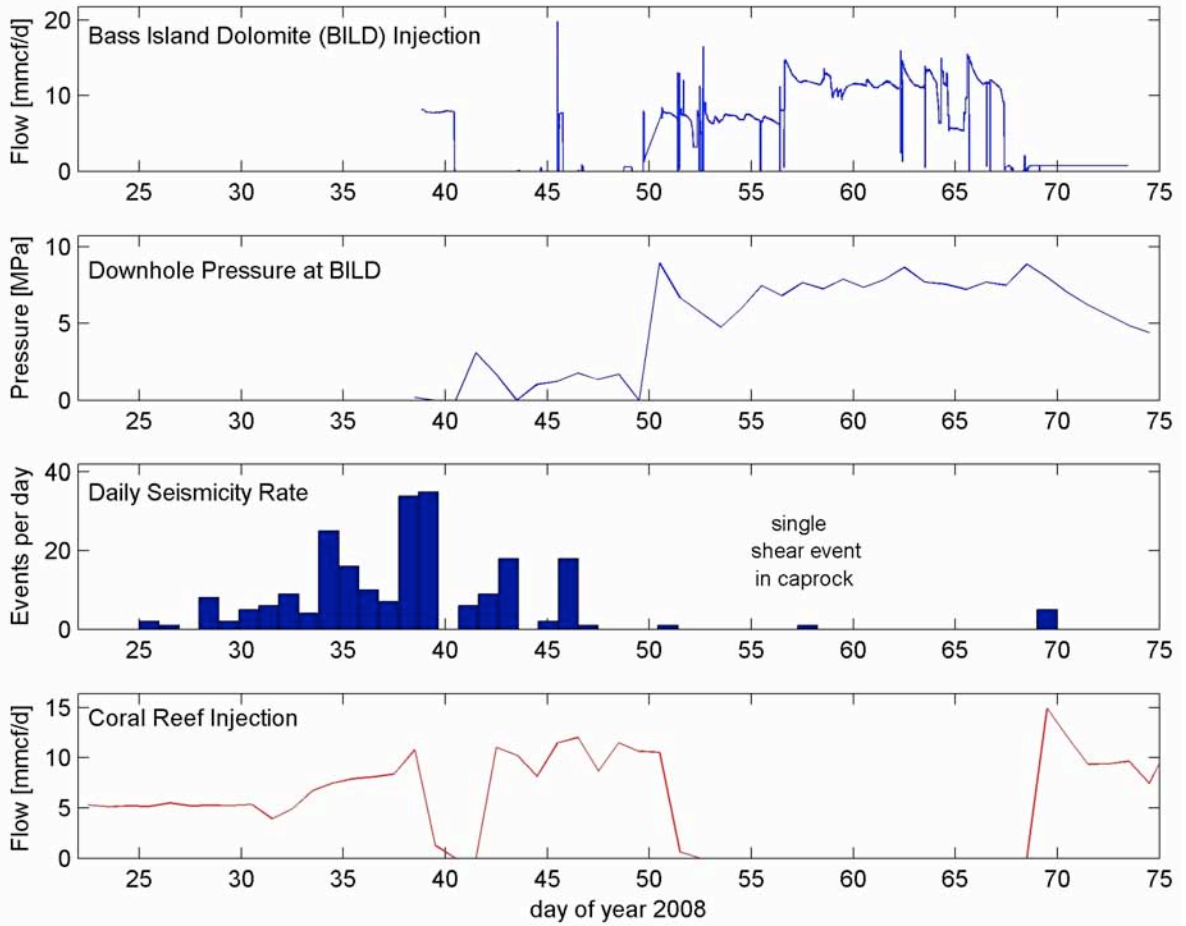
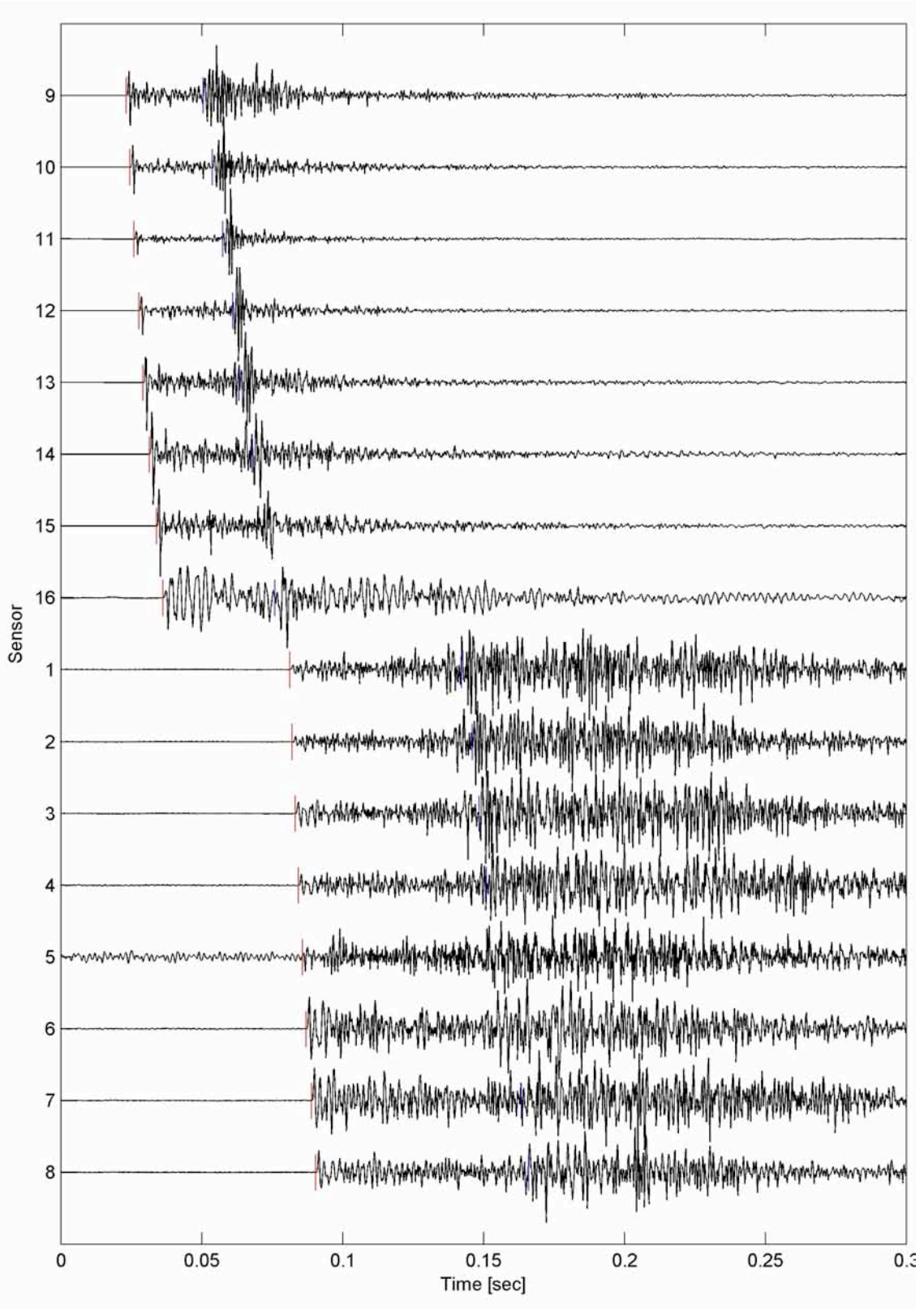
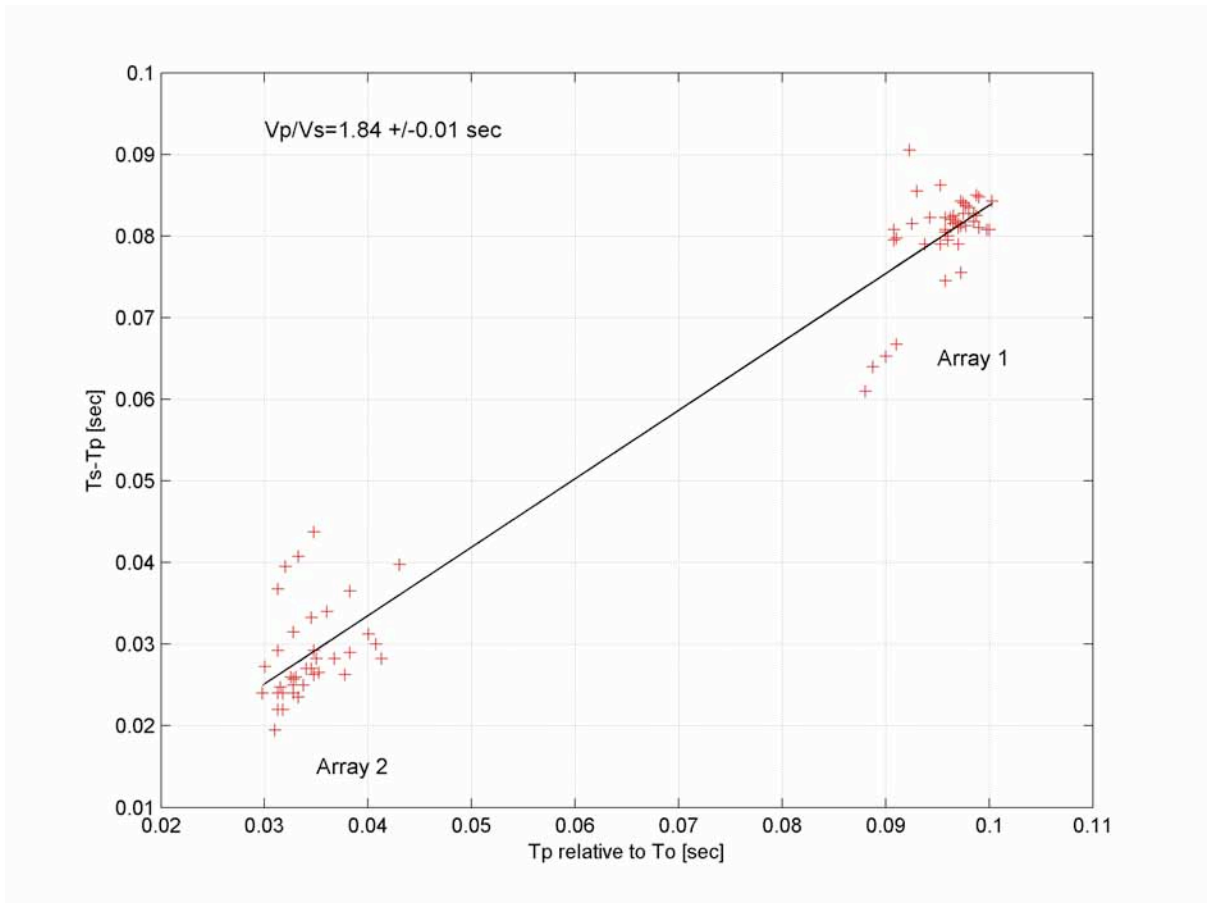


Figure 4: Hydraulic and seismicity data from the Michigan Basin Injection Experiment. From top to bottom the diagrams show flow rates of the injection into the BILD formation at 1050 m depth, downhole pressure in the BILD formation (measured in the BILD injection well), daily seismicity rate as detected by the downhole seismic network and flow rates of the deeper EOR-related injection into the Coral Reef reservoir at 1670 m depth. The time scale is uniform for all four diagrams in days of year in 2008.

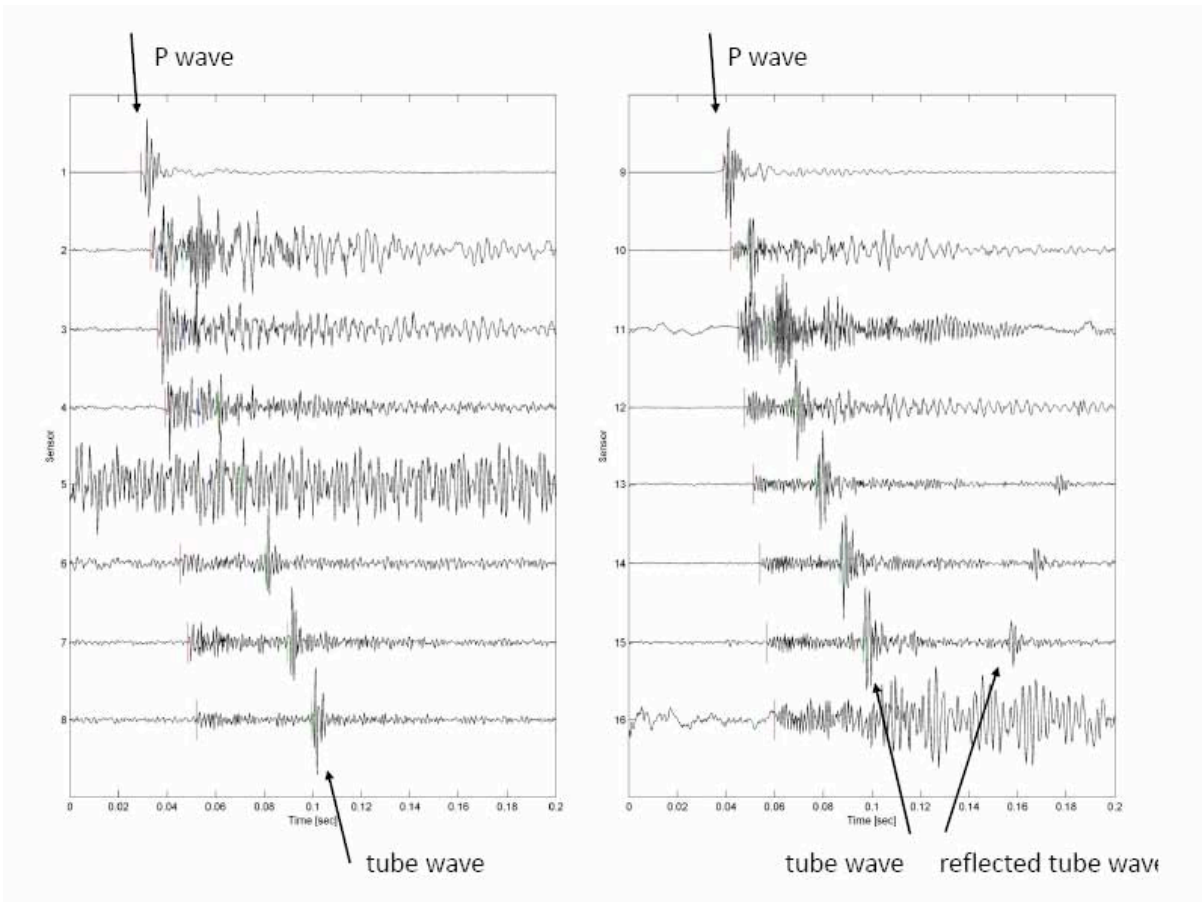


(a)



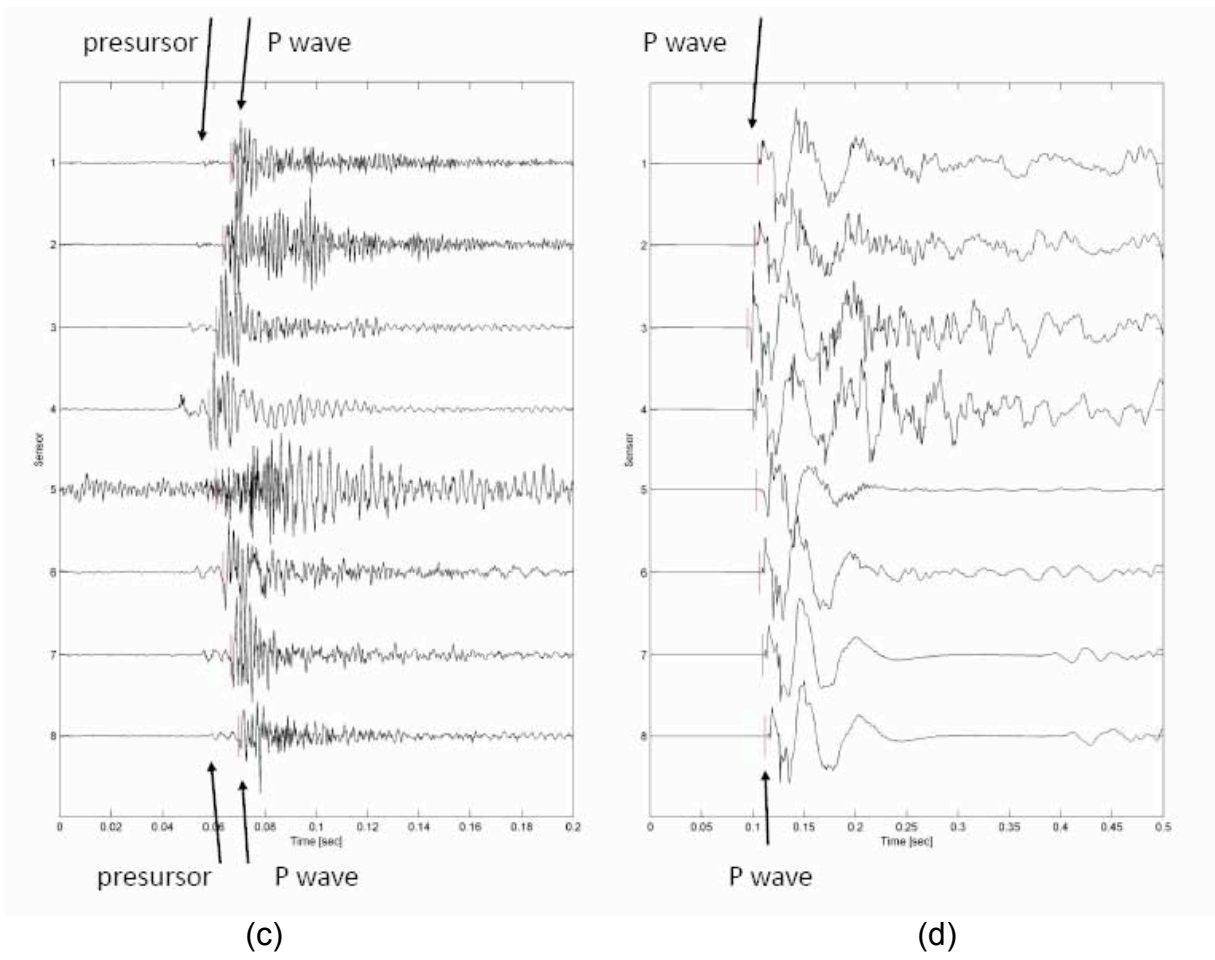
(b)

Figure 5: a) Waveform example from a calibration shot conducted in the BILD injector at 797 m depth on the 24th January 2008, i.e. after deployment of the downhole seismic array and prior to the start of the BILD injection. Plotted are the vertical components of the 16 sensors from both sensor sub-arrays (see Figure 3 for sensor location). Array 1: sensors 1-8, array 2: sensors 9-16. Clear P and P-to-S converted phases are obtained at both sensor arrays. b) Wadati diagram (Wadati, 1933) for the seven calibration shots. Plotted are the differential travel times between P and S wave ($T_s - T_p$) at each of the 16 sensors with T_p . Assuming a constant v_p/v_s ratio, the data of all sensors should fall on a line. Thus, the quality of the line fit is a measure of the consistency of the data set. The obtained average v_p/v_s ratio is 1.84 for the volume sampled by the elastic waves which is in good correlation with the results of 1.90 obtained from sonic logs along the wells at the relevant depth interval.



(a)

(b)



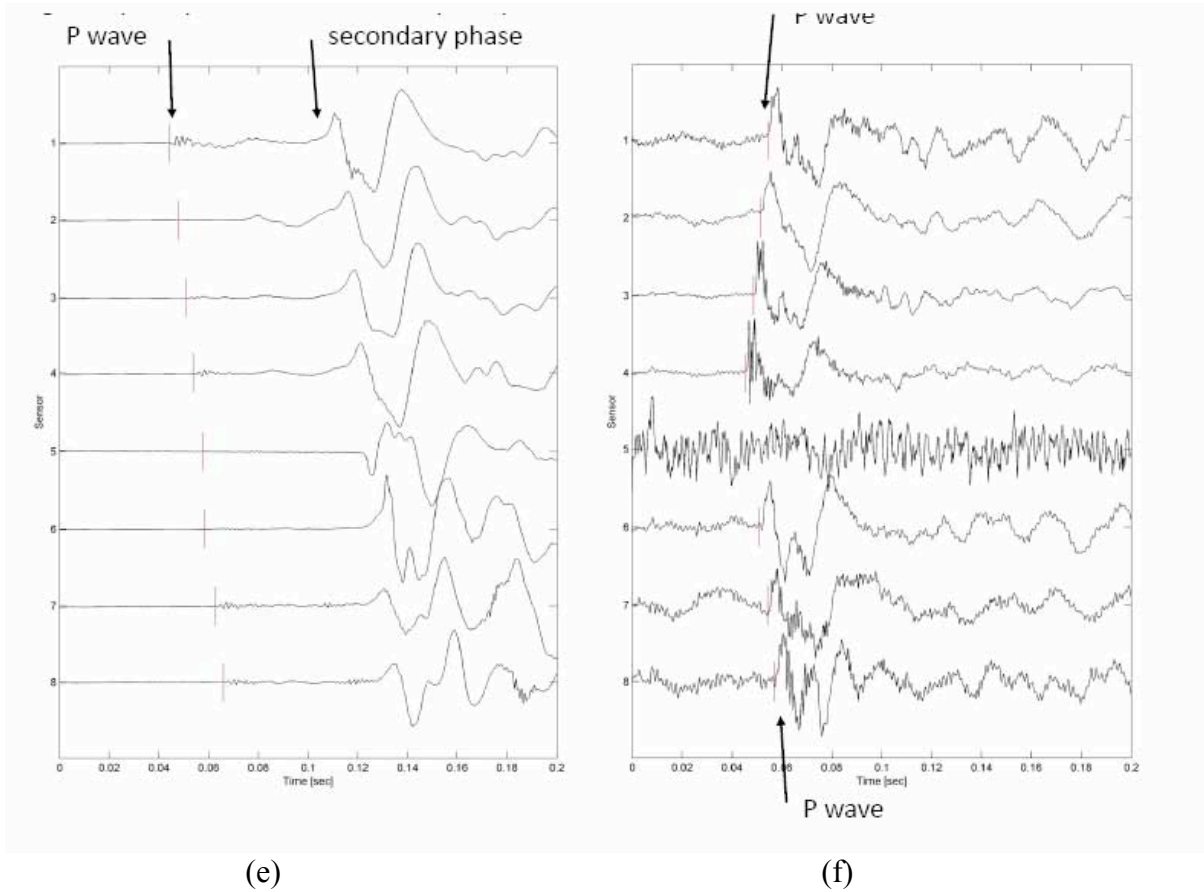


Figure 6: Examples for the different waveform characteristics obtained from the induced microseismic events. For each event the vertical components of the eight sensors from the relevant seismic array are plotted (array 1: sensors 1-8, array 2: sensors 9-16; see Figure 3 for location of sensors). a) Event with a high-frequency P wave (~500 Hz) and clear tube waves that are generated at the upper end of the sensor array when the P wave enters the monitoring well. The source is located slightly above the array. b) Event with high-frequency P wave (~500 Hz) similar to the events in a) but with a reflected tube wave propagating back upward the array. The source is located slightly above the array. c) Event with a high-frequency P wave (~500Hz) and a precursor phase prior to the P wave and at a constant delay time at all sensors. The source is located close to the array near sensor 4. d) Event with a 'low-frequency' P wave (~150Hz). The source is located close to the array near sensor 3. e) Event with a weak first arrival followed by a strong main arrival of 'low frequency' (~100Hz). The source is located near the upper end of the sensor array. f) Weak event with a 'low-frequency' first arrival (~100 Hz). The source is located near the array close to sensor 4.

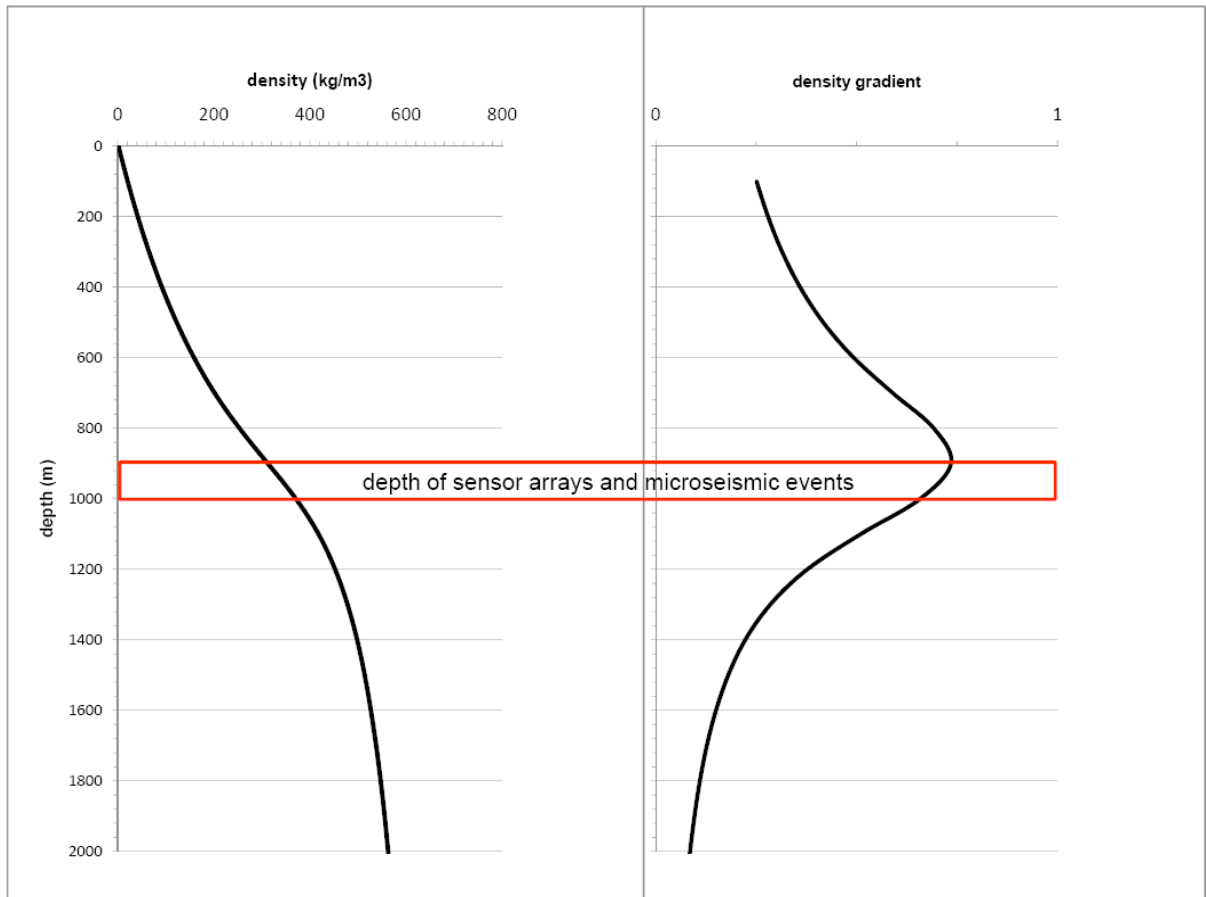


Figure 7: Density versus depth (left) and density gradient (right) for pure CO₂ calculated according to the Peng-Robinson Equation of State (PREOS) (Kovscek, pers. comm.). For the calculation we assumed hydrostatic pressure at the Michigan test site and a regional thermal gradient of 2.9 °C/100 m (Gardner & Bray, 1984). A systematically decreasing CO₂ density is observed with decreasing depth. The largest density gradient is observed at ~850-950 m depth, i.e. exactly where the sensor arrays were placed and where we observed microseismic activity. This supports the conclusion that the microseismic events reflect volume changes (degassing) of the CO₂ while rising towards the surface. See text for details.

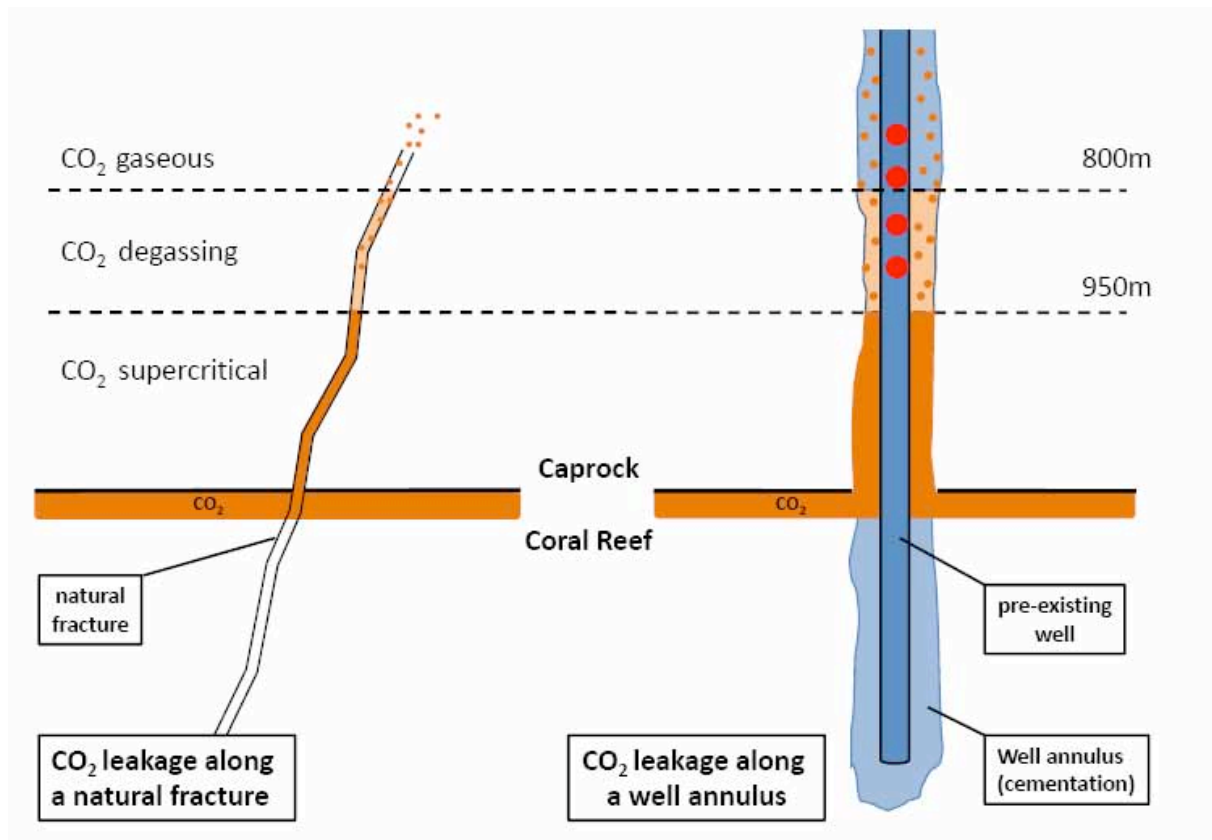


Figure 8: Sketch of potential CO₂ leakage into the caprock. Leakage may occur along a natural fault or fracture (a) or along a pre-existing vertical well penetrating the reservoir (b). Increased pore-fluid pressure during injection permits upward migration of the supercritical CO₂ once a critical overpressure is reached in the reservoir. The CO₂ then rises along the most permeable pathway (in our case the annulus of the monitoring wells). The observed induced microseismicity occurs along the monitoring wells at the depth of the sensor array and correlated with the depth section where the largest volume change of the CO₂ is expected (see Figure 7).

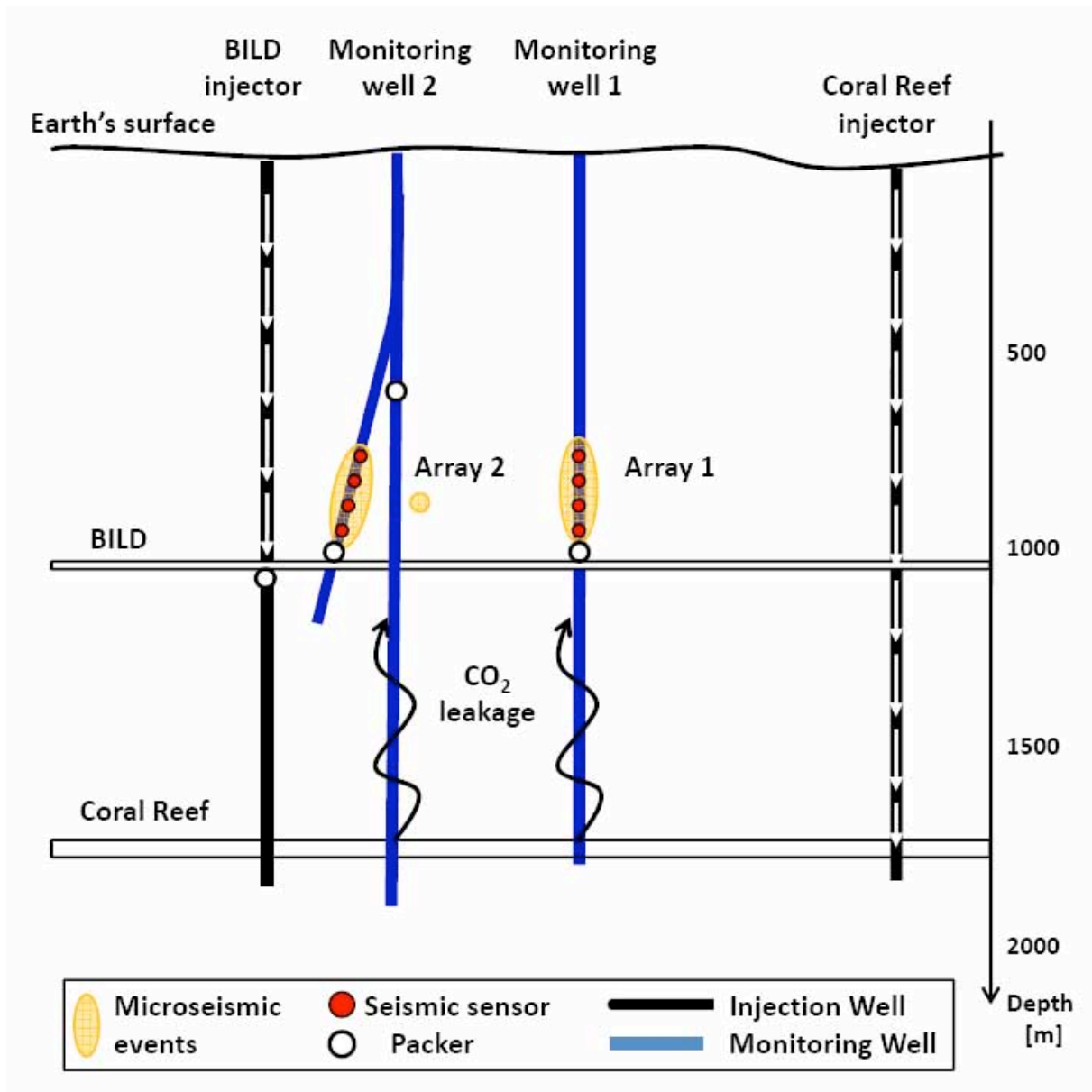


Figure 9: Conceptual model for the observed CO₂ leakage from the Coral Reef reservoir along the annulus of the two monitoring wells as discussed in the text.

Subsurface Monitoring of CO₂ Storage in Coal

True 4-D Seismic Subsurface Monitoring

Traditional 4-D seismic subsurface monitoring uses multiple 3-D seismic snapshots to capture temporal changes of the reservoir. The snapshots are repeatedly acquired at time intervals of several months to years. In our approach, reservoir time or “slow” time is the independent fourth dimension. We propose to sample slow time quasi continuously, thus the name True 4-D. The traditional approach suffers from serious temporal aliasing. More importantly, while sensitive to reservoir changes due to CO₂ it may fail to detect a dangerous leak in a geological storage site for months of years because of inadequate temporal sampling. Figure 1 illustrates the traditional snapshot approach. It can be seen that we have difficulty to identify a small leak (circled) from a single snap shot, especially in the present of noise. However, if we have quasi-continuous data in the temporal axis as shown in Figure 2, the leak or other temporal changes can be easily identified with the help of the true time axis. As shown in Figure 3, we expect quasi-continuous monitoring to detect the leak sooner.

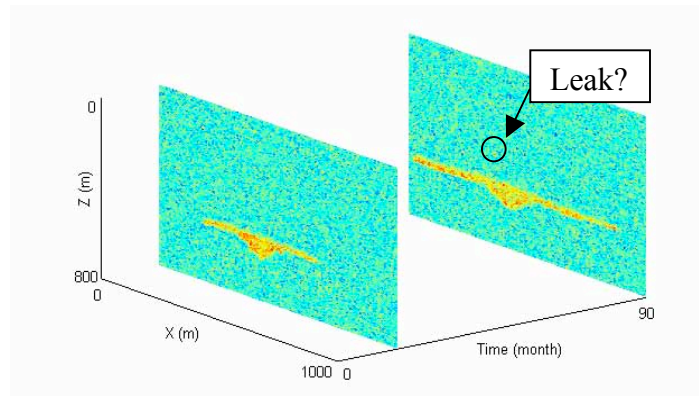


Figure 1: Traditional monitoring uses a large temporal sampling interval. The images are 2-D seismic profiles corresponding to two discrete observation times. It is difficult to identify a leak (circled) from these two images.

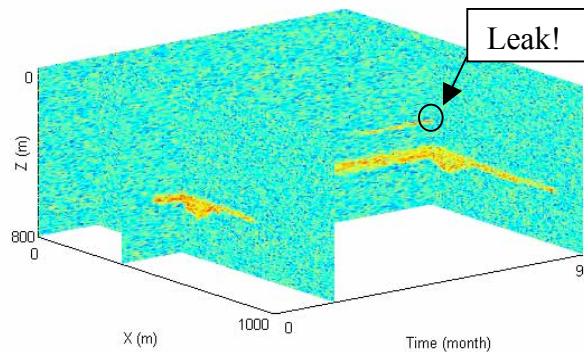


Figure 2: Monitoring with a small (True 4-D or quasi-continuous) temporal sampling interval. When we have a large of number of time-lapse images, we can better separate signal from noise, in this case the small leak from spatially noisy image.

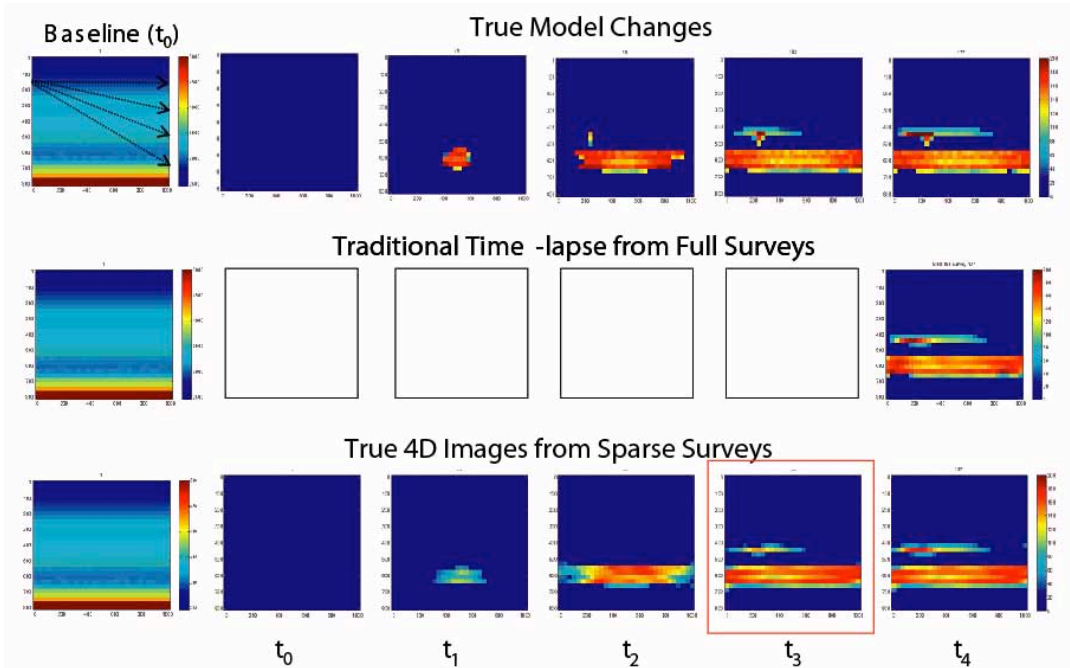


Figure 3: Quasi-continuous monitoring can detect a leak earlier as indicated at time t_3 .

In this report we describe a series of synthetic tests to investigate the feasibility of True 4-D. True 4-D approach can overcome the temporal aliasing problem and help interpret subtle temporal changes. However, the cost of true 4-D monitoring will be prohibitively high if we just simply reduce the time interval between surveys and repeatedly collect complete data as done in the traditional approach. We assume the running costs of True 4-D should be comparable to the traditional approach, though spread over time and with some higher startup expense for embedded instrumentation. To accomplish this, we trade spatial resolution for temporal resolution, use embedded data acquisition systems, dynamic imaging, and/or sparse data evolution algorithms to implement True 4-D monitoring.

In following subsections, a comprehensive synthetic study of True 4-D seismic monitoring is reported. We construct a 3-D coalbed model, run a flow simulator to simulate CO₂ storage, and use simulated seismic depth imaging and finite difference seismic modeling to study the various data acquisition and processing strategies that have the potential of making True 4-D practical. In a separate section, sparse data evolution technique is discussed.

Flow Simulation of CO₂ Storage in a Coalbed

An illustrative geological model for a 3-D coalbed was built with GOCAD based on the work of Ross (2007). The model, consisting of three layers (coal, shale and sand), is shown in Figure 4. The model is imported into flow simulator GEM (www.emgroup.com) for the simulation for CO₂ injection and storage. The simulated flow models are output in time steps of weeks and months for 8 years.

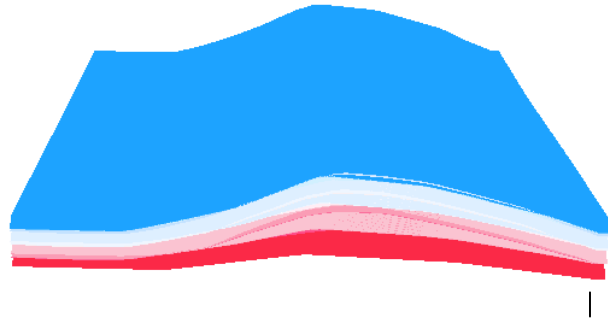


Figure 4: The coalbed model used in this monitoring study. The size of the model is about 1000 x 900 x 50 (m³), and the depth is about 500 m. From top to bottom, the three layers are sand, shale, and coal. Here, the overlying shale serves as reservoir seal. We put a low permeability hole in this shale layer to simulate a leakage into the overburden.

Initially the model is water saturated. We assume injection begins on January 1, 2008. As CO₂ is injected into the coalbed, a volume becomes gas saturated. Figure 5 shows the gas saturation in the coal layer at four different times. The shale layer above the coal normally maintains a seal that keeps the injected CO₂ within the coal. To mimic a possible leakage, we place a high permeability channel in the shale. Figure 6 shows the gas saturation at two times as leaking through the seal begins and spreads in the top sand layer.

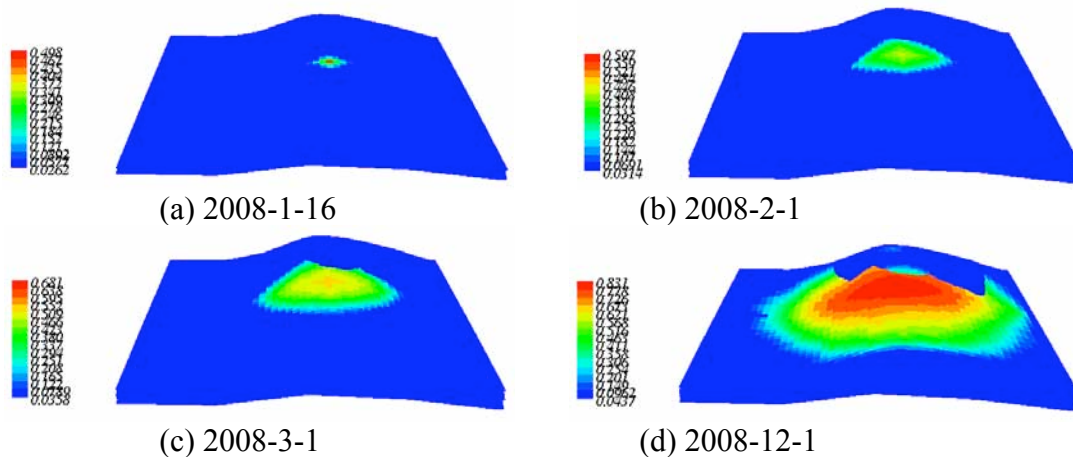


Figure 5: Gas saturation changes within coalbed. The objective of subsurface monitoring is to track the gas front and detect possible leakage into the overburden.

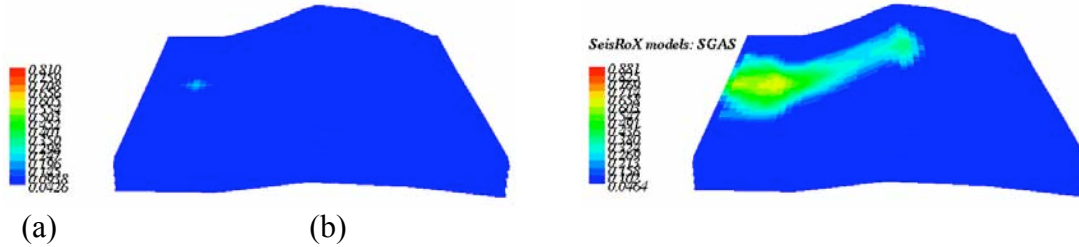


Figure 6: CO₂ leaking occurs through a high permeability channel and spreading in the sand layer above: (a) 9-1-1009. CO₂ leaks begins; (b) 10-1-2010. Leak spreads in overburden sand.

Simulated Seismic Depth Imaging

The time-lapse flow models (including porosity, permeability, water saturation, gas/CO₂ saturation and pore pressure) are imported into simulated seismic depth imaging software SeisRox (www.norsar.com) for the monitoring study. Simulated seismic depth imaging convolves the reflectivity model with illumination vectors. This method of simulating depth migration is preferred over 1-D wavelet convolution because it includes the effects of acquisition geometry, 3-D illumination, ray paths, anisotropy and lateral resolution in complex models (Lecomte & Kaschwich, 2008). With SeisRox we can convert flow snapshots into seismic velocity snapshots and compute simulated 3-D depth images without the compute intensive shot simulation and migration steps. Figure 7 shows the initial velocity model, converted from the initial flow model. Figure 8 shows the velocity changes about one year later, 10-1-2009. The traditional approach is to calculate 3-D seismic data using the finite difference method, and then perform depth imaging. It may take days to get forward modeling and migration imaging done for a single 3-D model. Now we have more than one hundred time-lapse models, and it is impossible to do this in the conventional way. The simulated seismic depth imaging, however, is very fast. It takes a few hours to computer hundreds of 3-D depth images. In order to compute the seismic images, 1-D overburden layers are added to the top o the reservoir. Next we will use simulated depth imaging to demonstrate the concepts of true 4-D monitoring and study the strategies for true 4-D monitoring.

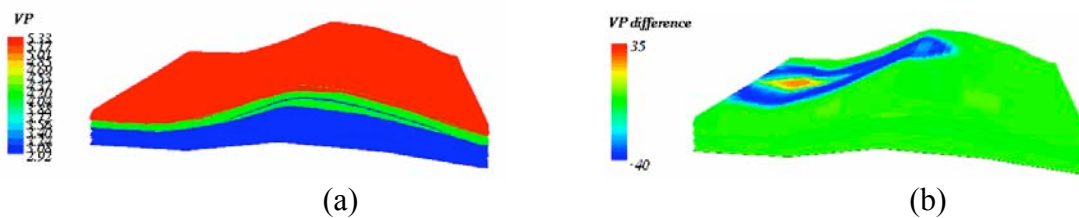


Figure 7: Velocity models converted from flow models. The velocity change shown in (b) is the difference between the initial model and the model approximately one year later.

The Case of Full 3-D Surveys

When a site is first selected as a potential candidate for CO₂ storage, a detailed site characterization must be performed. The first baseline characterization must include a full coverage 3-D survey with state-of-the-art-technology. Figure 8 shows the traditional data acquisition geometry, with the model and imaging target used in our simulation. Figure 9 is the depth image differences between given times and the initial time.

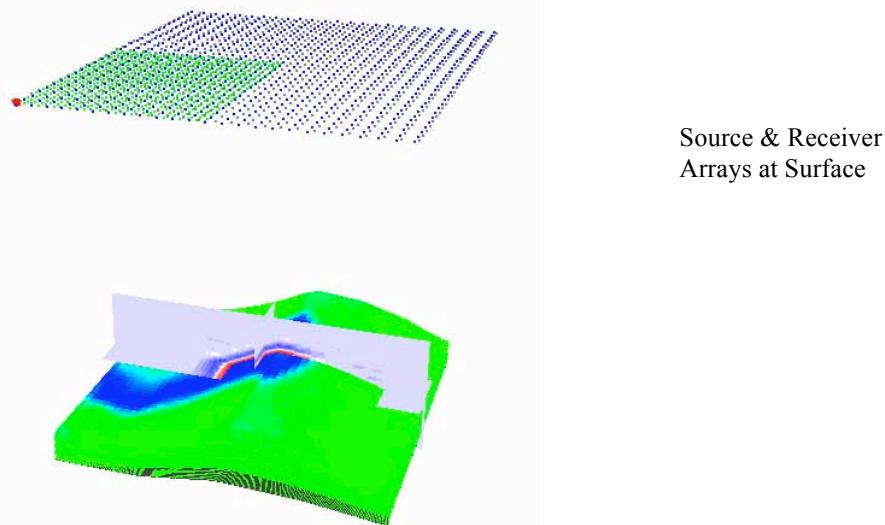


Figure 8: A full 3-D data acquisition geometry. Green dots are the mid-points corresponding to the source (red dot). Blue dots indicate receiver locations. Gray dots are source arrays. Three planes in the model show slices through the depth images at the target area.

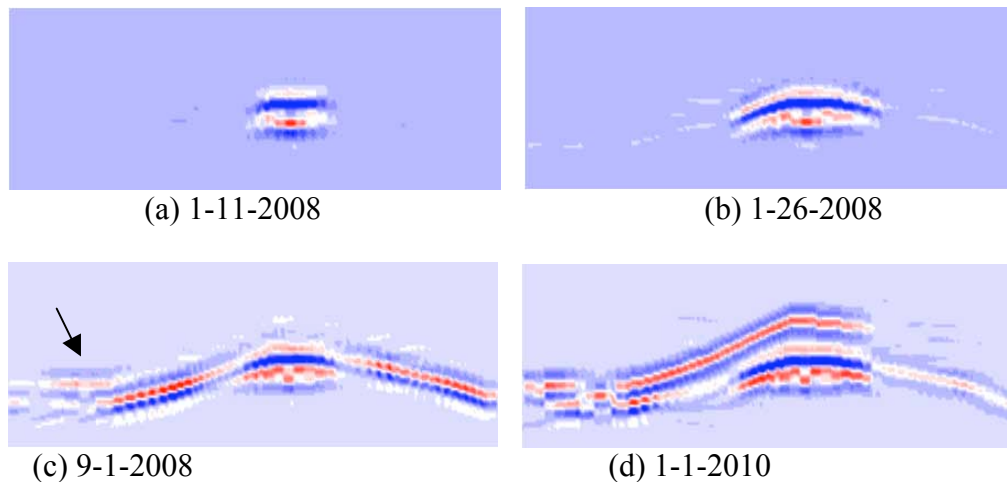


Figure 9: Depth image differences at four different times. The subsurface image at a given time is subtracted from the image corresponding to the baseline model. The leak starts around 9-1-2008.

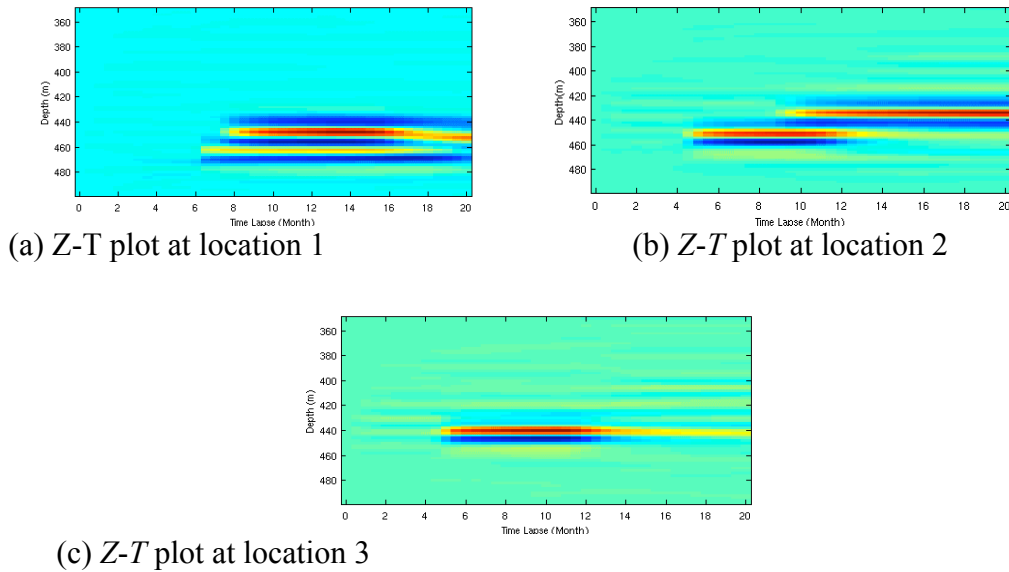


Figure 10: 2-D visualization of continuous monitoring data. A profile at a specified surface location is displayed versus time. The resulting plot is a depth vs. time-lapse display.

Quasi-continuous monitoring creates a huge volume of data, e.g., Data (X, Y, Z, T) . We can visualize subsets of the True 4-D dataset in many different ways. A particularly revealing 2-D image is to select a (X, Y) surface location and display the (Z, T) plane as shown in Figure 10. There are two features in Figures 10a and 10b. The upper one is the leakage of CO_2 in the sand layer and lower one is CO_2 storage in the coal. Since these two images come from different (X, Y) locations, we can see the CO_2 reaches the locations them at different times. The two events begin at location 1 at almost the same time. This is because location 1 is very close to the leaking channel. Location 3 is far away from the leaking channel, and only one event appears. The example in Figure 10 tells us that a small change in subsurface conditions has a very good chance to be seen with the help of the new temporal axis.

The Case of Sparse 3-D Surveys

The acquisition of a full 3-D seismic survey is very expensive and requires a long period of time. It is impractical to do True 4-D monitoring with regular full surveys. We now present another extreme case of 3-D acquisition geometry as shown in Figure 11, which consists of a source array and a receiver array. This simple cross array geometry generates a true 3-D image albeit at single fold (Harris et al. 2006; Walton 1972). However, it may not produce adequate signal-to-noise because of its low fold. We here

use simulated depth imaging as an idealized seismic migration to see how it works. Figure 12 is the depth difference image obtained from cross array geometry. Clearly, the migration artifacts are severe, though the effects of CO₂ injection can also be seen.

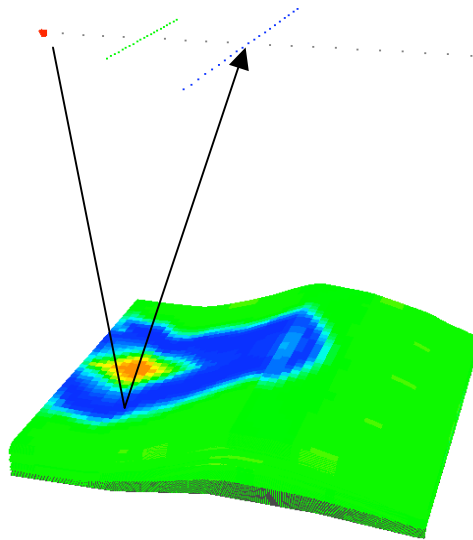


Figure 11: Cross array acquisition geometry that has a source array (gray dots) and receiver array (blue dots). The green dots show the mid-points for the given source (red square).

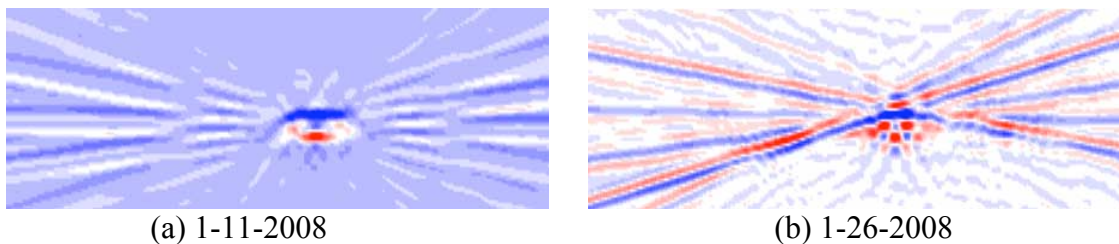


Figure 12: Depth difference images (relative to baseline). It can be seen that the imaging artifacts are dominant.

Embedded Source and Receiver and Pre-stack Data Approach

We have discussed the two extreme cases (full survey and the sparse cross-array survey) in the previous subsections. The cost and quality are the main problems for continuous monitoring. It seems we need to choose a proper trade-off between them. The migration-based imaging approach usually requires dense data acquisition geometry that is quite difficult if we want to carry out continuous monitoring. This motivates us to use pre-stack data directly.

We propose to embed sources and receivers (Figure 13a) near the surface and continuously collect the data, say every week. Then the recorded trace can be display in a plot of seismic time (fast) and reservoir time (slow). To test this idea, we use the finite difference method and the time-lapse velocity models to compute the seismic data. The computed seismic traces are displayed in Figure 13b. The attribute is amplitude difference. The horizontal axis shows the time when the data is collected. The travel-time and amplitude of the seismic reflection change slightly as CO₂ injection continues.

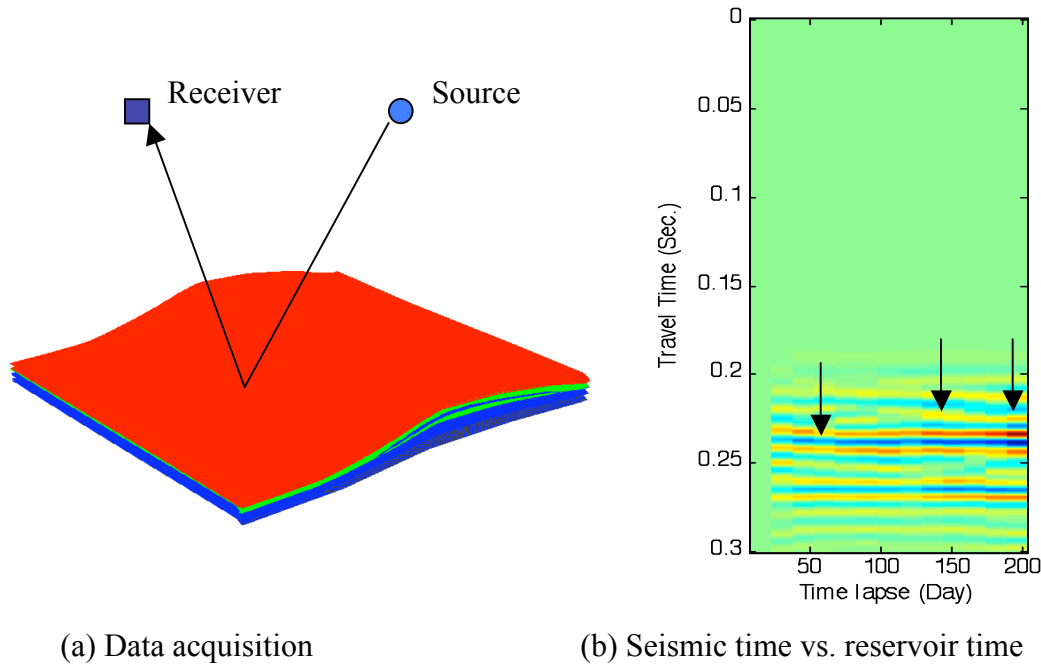


Figure 13: Embedded sources and receivers for continuous operation and the corresponding time image reflect the subsurface changes.

Dynamic Inversion for Quantitative Interpretation

Although we can see the changes in the raw seismic data, it will be very helpful if we perform seismic inversion and transform the amplitude vs. time data into acoustic impedance or other elastic properties of subsurface vs. depth. The True 4-D seismic monitoring is a typical dynamic process. The dynamic inversion approaches introduced by Quan & Harris (2008) and Jin et al. (2008) are especially suitable for our continuous data. We are currently working on the dynamic inversion for the data shown in Figure 13b. After the dynamic inversion finished, we will have a (Z - T) image with the elastic attributes.

In addition to the methods discussed in this section, we are also working on another method for quasi-continuous seismic monitoring which will be presented in the next section.

An Approach to Quasi-continuous Time-lapse Seismic Monitoring using Data Evolution of Sparse Data Recording

We take the advantage of small changes in the seismic property of a geological reservoir that are expected to occur in a small time interval. The goal of this approach is to obtain high temporal and spatial resolution in reconstructed, time-lapse geophysical images using comparable resources that would have provided high spatial but low temporal resolution images with conventional approaches. This is done by acquiring spatially sparse data at small time intervals. In this case, a spatially sparse dataset refers to that dataset which is a small fraction (as little as 5%) of what would be acquired to reconstruct a high spatial resolution tomographic image of the subsurface. The high spatial resolution obtained by the proposed approach occurs because unrecorded data are predicted from future and past data. With high temporal and spatial resolution, early detection of important reservoir changes is more likely to occur.

Introduction

Geophysical imaging has played a large part in subsurface monitoring projects, especially in petroleum reservoir monitoring projects (e.g., Harris et al., 1995; Rickett and Lumley, 2001). This is primarily due to the kind of seismic changes that occur in the reservoir rock properties (Wynn, 2003). In addition, seismic data analysis is a well developed and understood subject (Yilmaz, 1987; Yilmaz, 2001). Seismic signals are able to penetrate deep into the earth and can be used in virtually any geologic setting (Wynn, 2003). The use of seismic tomography in time-lapse monitoring takes advantage of the changes in a seismic property of the reservoir rock during the time interval under consideration. For example, a reservoir velocity model can be quantitatively reconstructed from either seismic reflection or transmission traveltimes using tomography.

Consider a time-lapse seismic monitoring study designed to last for several decades as might be the case in whole-life monitoring of a petroleum reservoir or for a CO₂ storage site. The conventional approach is to acquire a large amount of seismic data such that a high spatial resolution image of the subsurface can be obtained each time a dataset is acquired. The time intervals between successive data acquisition campaigns are often so large that there are large changes in the successive seismic data acquired. The time intervals are usually of the order of years (e.g., Mathisen et al., 1995; Landrø et al., 1999; Arts et al., 2004). Such a strategy works very well for some time-lapse projects but for other applications such as monitoring CO₂ storage, the late identification of a reservoir leak by a year could have dire consequences. In other words, some time-lapse monitoring strategies are more effective when the changes in successive time-lapse datasets are small. In such cases, temporal resolution is as important as spatial resolution, and sometimes, more important.

If resources are to be kept comparable, two scenarios are possible – acquiring data such that the monitoring provides either high spatial resolution and low temporal resolution images, or low spatial resolution and high temporal resolution. In the second scenario, low spatial resolution results because a small amount of data is acquired each time, and

high temporal resolution results because data are acquired more frequently. The traditional approach to inverting sparse data is to reduce the number of model parameters solved. Because only a fraction of the data that will normally be used to get a high resolution image is used, the resulting seismic image has a lower spatial resolution. We propose to estimate unrecorded data (Harris et al., 2004; 2007; 2008), and then reconstruct geophysical models without reducing the number of model parameters solved, thereby maintaining the high spatial resolution.

Although the idea posed here is somewhat similar to the recently developed concept of compressive sampling (Candès and Romberg, 2007) in the sense that sparse data are acquired and used in estimating unrecorded data, we deal here with datasets that are even sparser than what would be acquired as compressive sampling. Also, we take advantage of the large portion of the data space available in the dense baseline data.

Theory

Let the dense time-lapse data be composed of a recorded sparse part and an unrecorded part. i.e.

$$\mathbf{d}_d = \mathbf{S}\mathbf{d}_d + (\mathbf{I} - \mathbf{S})\mathbf{d}_d \quad (1)$$

$$\mathbf{d}_d = \mathbf{d}_s + \mathbf{d}_u \quad (2)$$

where \mathbf{S} is the data sampling operator that selects which data are recorded from the “dense” dataset \mathbf{d}_d , and \mathbf{d}_s and \mathbf{d}_u are “sparse” and “unrecorded” datasets respectively. From (1) and (2), we see that

$$\mathbf{d}_s = \mathbf{S}\mathbf{d}_d, \quad \mathbf{d}_u = (\mathbf{I} - \mathbf{S})\mathbf{d}_d \quad (3)$$

In this notation, each vector \mathbf{d} contains all previously measured and some future measured data. Our goal is to find an estimate $\tilde{\mathbf{d}}_u$ for the unrecorded dataset from the measured data \mathbf{d}_s . The fitting goal for estimating finding $\tilde{\mathbf{d}}_u$ is

$$\mathbf{A}\mathbf{d}_d \approx \mathbf{0} \quad (4)$$

subject to the constraint

$$\mathbf{d}_s = \mathbf{S}\tilde{\mathbf{d}}_d \quad (5)$$

where in (4) the operator \mathbf{A} is the model constraint or estimation operator. Substitution of (2) into (4) gives

$$\mathbf{A}\mathbf{d}_s + \mathbf{A}\tilde{\mathbf{d}}_u \approx \mathbf{0} \quad (6)$$

The estimated unrecorded data, $\tilde{\mathbf{d}}_u$ is then obtained using (6), and minimizing the objective function

$$\Phi = \left\| \mathbf{A}\tilde{\mathbf{d}}_u + \mathbf{A}\mathbf{d}_s \right\|^2 \quad (7)$$

Time-lapse Field Monitoring Example

The field data example presented here are crosswell data from the McElroy field in West Texas. The datasets were acquired to monitor velocity changes in the reservoir in response to CO₂ injection (Harris et al., 1995; Lazaratos and Marion, 1997) between 1993 and 1995. The wells are over 3000ft deep and are separated by approximately 600ft. Figure 14 shows common-shot gathers data from the surveys. First arrival seismic traveltimes were picked from the data. The largest traveltimes differences occur at the depths corresponding to the location of the reservoir between 2750 and 3150 ft. Using these traveltimes, velocity models were reconstructed using the tomography code, FAST (Zelt and Barton, 1998). Figure 15 shows the reconstructed velocity models and the difference between them when the complete dataset in both cases are used. The most obvious difference in the velocity models is the significant drop in the p-wave velocity between 1993 and 1995, resulting from the injection of CO₂ into the reservoir.

Having a time interval of two years between the baseline image and the monitor image is satisfactory for some monitoring projects. However, if potentially dangerous consequences could occur from an abnormality in the reservoir, it will be necessary to monitor the reservoir with a finer sampling in time. Also, if resources necessary for data acquisition are limited, a more efficient time-lapse monitoring strategy is needed. This, scenario illustrates the need for a quasi-continuous monitoring strategy using sparse data.

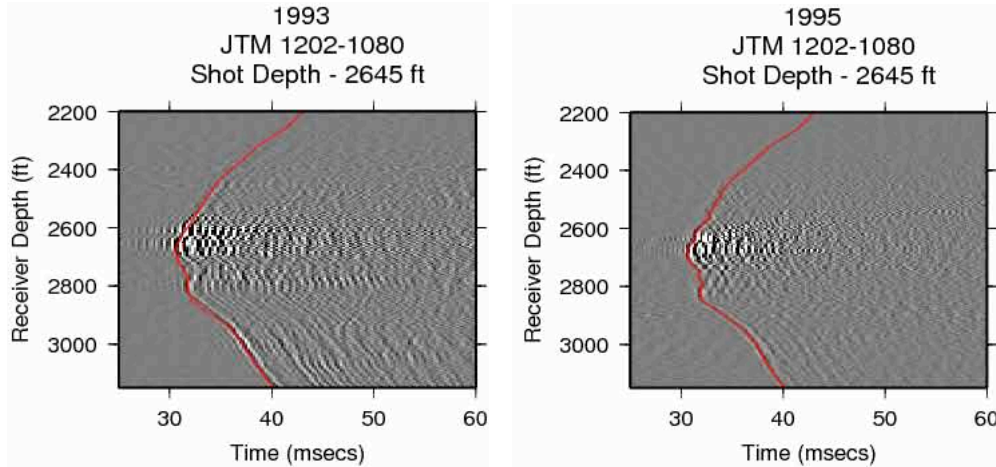


Figure 24: Common-source gathers from the 1993 and the 1995 surveys at the McElroy field in West Texas. The red lines indicated first arrivals.

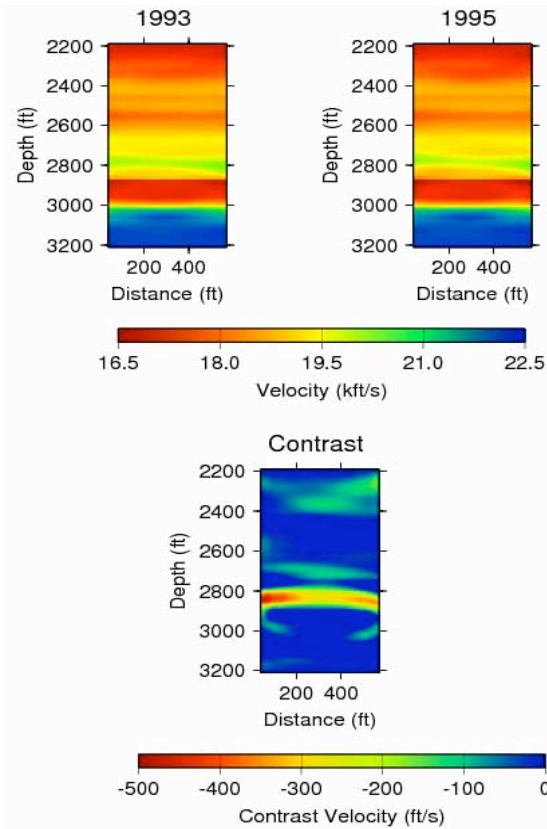


Figure 15: Reconstructed velocity models from the baseline (1993) and monitor (1995) surveys, and the difference between both models.

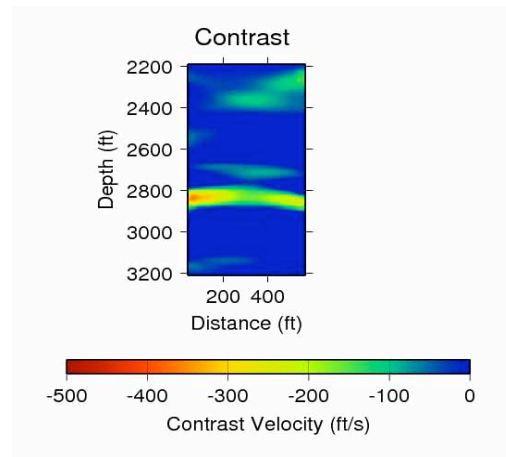


Figure 16: Reconstructed contrast model from the decimated 1995 field dataset.

To test the efficiency of the approach presented in this paper on field data, we used the complete dataset from the 1993 survey and 1% of the dataset from the 1995 survey to estimate the discarded data from the 1995 dataset. Here, the \mathbf{A} operator in equation (7) was the first order derivative. The velocity models were then reconstructed from the estimated data. Figure 16 shows the resulting contrast model. We obtained a good comparison between the true contrast model and the contrast model from the reconstructed dataset.

Time-lapse Synthetic Monitoring Example

In order to test this approach of quasi-continuous monitoring, we created a series of 70 two-dimensional P -wave velocity models from the baseline model reconstructed using the 1993 dataset, and a set of simulated fluid flow models converted to velocity models. The conversion was done using a Gassmann fluid substitution model. These models are intended to simulate CO_2 injection into the reservoir over a period of 32 months. We included a fracture in the model which allowed injected CO_2 to flow out of the reservoir.

Leakage occurred after the injected CO₂ reached the fracture zone approximately 10 months after the start of injection.

Using the finite differencing eikonal solver scheme given by Hole and Zelt (1995), we calculated dense first arrival seismic traveltimes recorded in a crosswell data acquisition geometry for all 70 synthetic velocity models. Gaussian noise with a standard deviation that we consider to be the picking error of the field data was then added to the synthetic dataset. To simulate sparse data, we reduced the data size to 10%, 5%, 2%, and 1% of the original size for a given dataset in time. The reduction was done such that the total data volume in each sampling scenario was constant. From these sparse synthesized datasets, we estimated the dense datasets using the methods described in the previous section, and then reconstructed the corresponding velocity models using traveltime tomography.

In estimating missing data, we used zeroth, first and second order derivative operators as the **A** operator in equation (7). We then used the resulting dataset to reconstruct the synthetic velocity models. We present the results of the reconstructed velocity models by their root mean square (rms) errors with respect to the known synthetic models (Figure 17). In this case, we use the rms errors measured in the regions of the model where changes are known to occur. The rms error curves of the estimated datasets show a consistent pattern. This implies that we can maintain an approximately equal level of misfit in our estimated datasets and reconstructed velocity models if we reduce data size and sample the data space more frequently in time. From the plots, we see that the rms error reduces with time, indicating the impact of additional data on data estimation. What is not captured by the rms error plots is that using only 1% data measured every two weeks, the leaked CO₂ was detected soon after it occurred. With the conventional strategy such a leak might not be discovered for years.

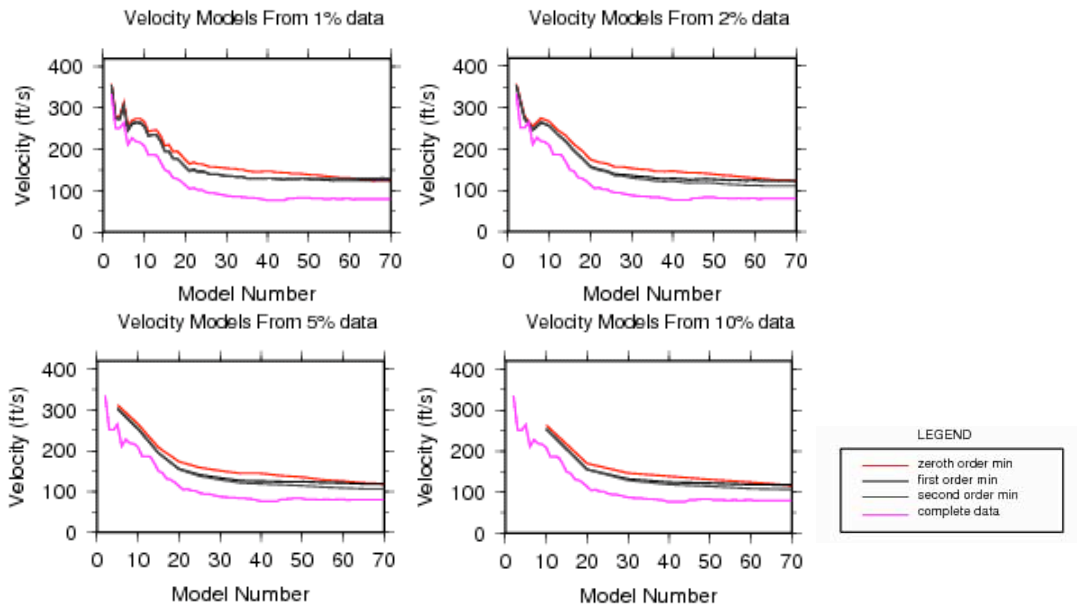


Figure 17: RMS error plots of the reconstructed velocity models using the estimated datasets.

Summary – True 4D and Data Evolution

We have presented monitoring methodologies for True 4-D seismic monitoring of CO₂ storage. First, we simulated surface acquisition scenarios of full and sparse surface arrays with simulated depth migration. Then we showed how data evolution can be used to fill in missing data before processing. Data evolution proved quite effective for both synthetic and field datasets. In the synthetic example, the CO₂ leak which occurred in the synthetic reservoir was detected early. Even though we assumed crosswell seismic acquisition geometry, data evolution can be applied to data acquired using any kind of data acquisition geometry. We intend to continue research in the area of time-lapse seismic monitoring with sparse seismic data using full seismic traces. Future work will involve the development of techniques that will take advantage of time dependent data covariance in time-lapse data. The most challenging aspect of data evolution is deciding on the optimal data size that produces the desired results, and the optimal time-lapse survey design. The benefit of data evolution is the ability to sample the data space more frequently in time with much less data without significantly losing spatial resolution in reconstructed velocity models. Also temporal resolution is increased with increased temporal sampling.

Estimating the Attenuation of Porous Rock with Changing Pressure and Saturation using Differential Acoustic Resonance Spectroscopy (DARS)

The objective of this work is to measure the acoustic compressibility and attenuation of coal under varying pressure and saturation. This laboratory measurement can provide useful information for seismic subsurface monitoring in CO₂ saturated coals. The previous DARS I system does not have pressure capability.

DAR II Construction

The first generation of DARS, called DARS I, measures the acoustic compressibility and attenuation at atmosphere pressure and conditions of full saturation. A cross section of DARS I is shown in Figure 1 and its signal path is shown in Figure 2. The SR850 lock-in amplifier generates the signal that is sent to the BNC3090 power amplifier that drives the PZT source. The PZT source excites the sound waves in the fluid, e.g., silicone oil. The hydrophone detects the signal and sends it to a B&K2635 charge amplifier, which amplifies the signal and returns it to the SR850 lock-in amplifier for phase locked measurement of the amplitude versus frequency.

DARS II is designed to have independent control on pore pressure and saturation and confining pressure. The design for DARS II is to take the DARS I set up and place it into a pressure vessel. A picture of the DARS II system is shown in Figure 3. DARS II has a high-capacity pressure pump connected to the pressure vessel. Inside the pressure vessel is an aluminum cavity which is ~18 inches in length with a piezoelectric disc source located at the bottom of the pressure vessel and a hydrophone receiver located at the top of the cavity for signal generation and detection.

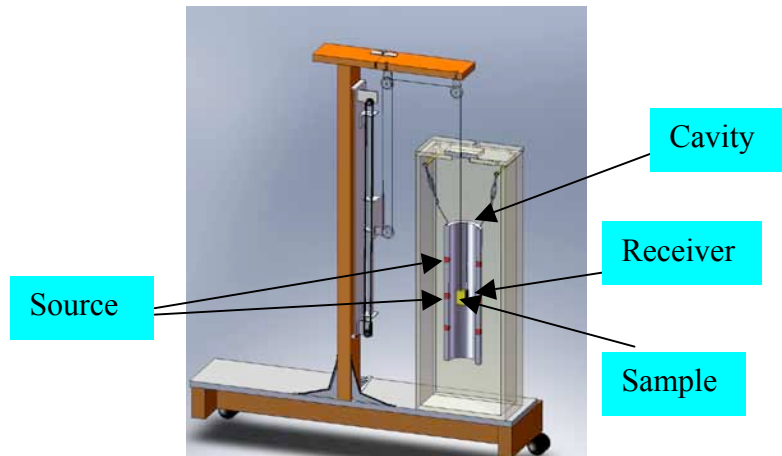


Figure 18: DARS I Cross Section

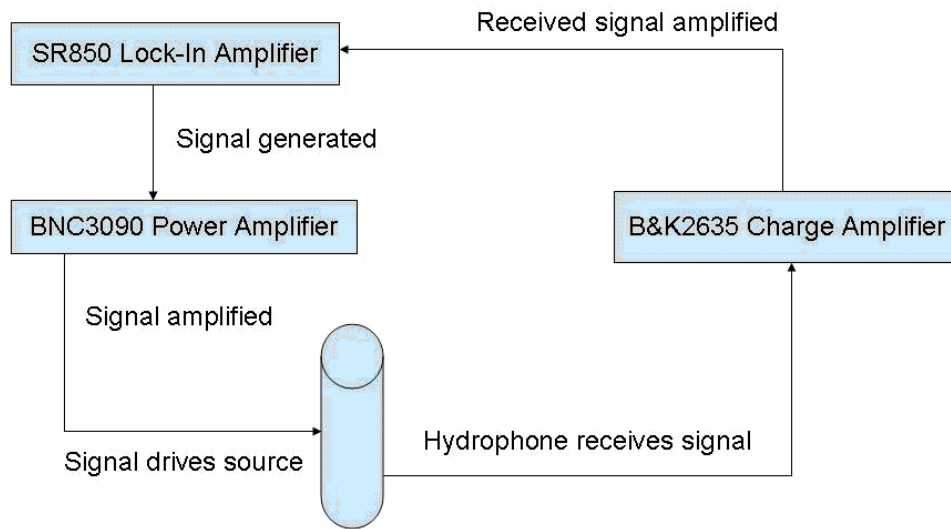


Figure 19: Signal path of DAR I

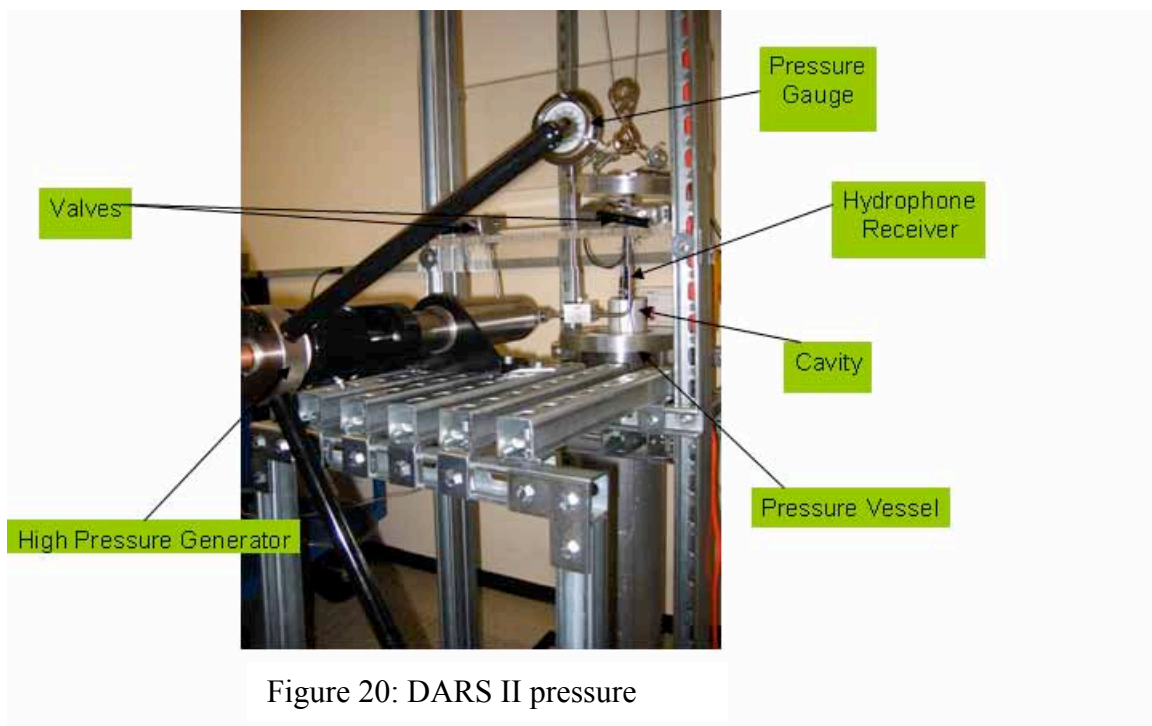


Figure 20: DAR S II pressure

The system Q for DAR S II is about 240 at atmosphere pressure. This is reduced from

DARS I, whose Q is about 300. The resonant frequency of the DARS I system is about 1080 Hz, whereas for DARS II the resonant frequency is about 750 Hz. The cavity has been increased in length by about 2 1/2 inches and thus the decrease in resonant frequency. The drop in Q from DARS I to DARS II was not expected. From Figure 5, one can see that the drop in Q is due changes in both resonance frequency and linewidth. More measurements and analysis will be performed to better understand this change in Q .

Preliminary measurements were made using the DARS II system at different pressures. First the pressure vessel is filled with silicone oil. The system is vacuumed for about 5 minutes, then measurements were taken at 0, 50, 100, 150 and 200 psi, respectively. The results are shown in Figures 4-5.

Two accomplishments in DARS II development have been made. One accomplishment is determining the best source and receiver configuration for the DARS II pressure conditions. The second accomplishment is placing pressure on the DARS II system and taking measurements with the empty system. All the confining pressure component components work as they should, however, we must fix some leaks in order to go to higher confining pressures. We plan to conduct set of samples measurements under various pressures. Also, the pore pressure portion of DARS II needs to be added; parts for the latter have been designed and some ordered.

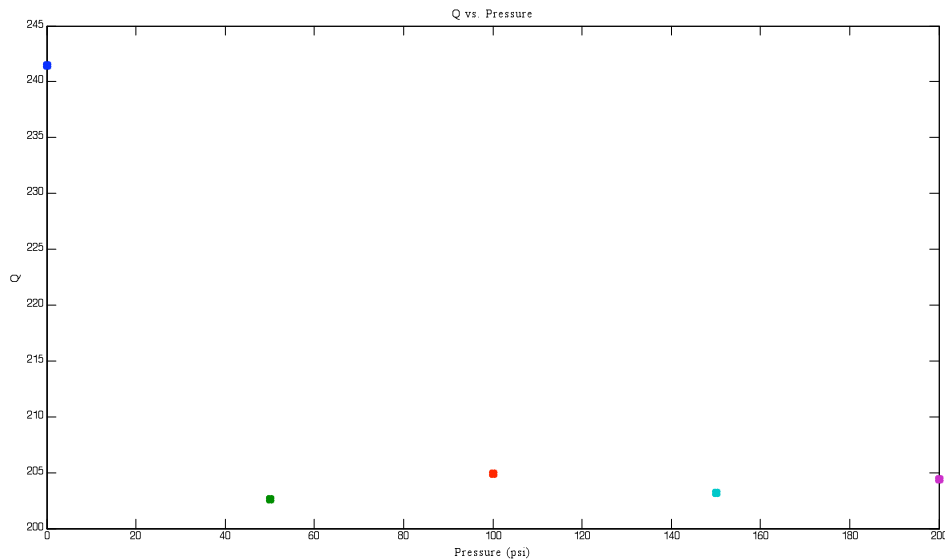


Figure 21: DARS II Q vs. Pressure.

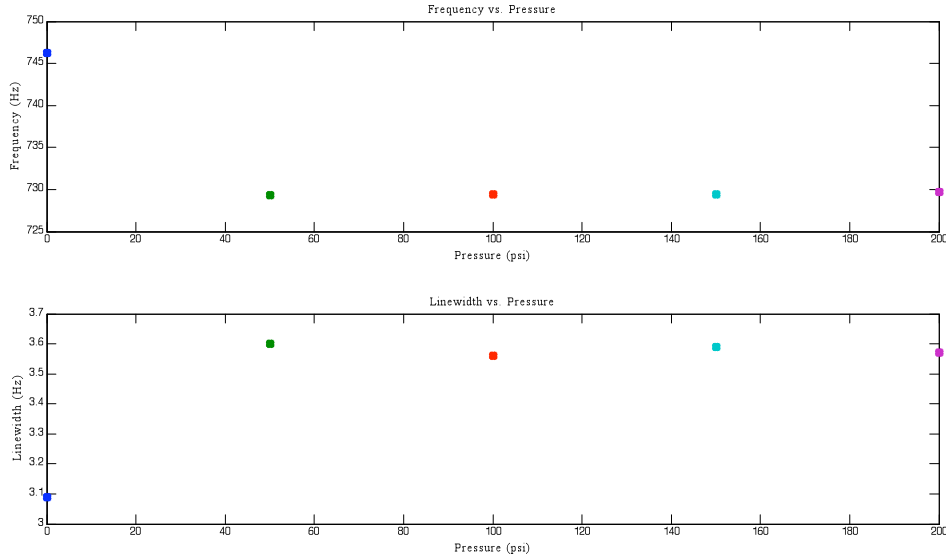


Figure 22: DARS II Resonant Frequency and Linewidth vs. Pressure.

DARS Numerical Simulation

A numerical simulation can help us to design DARS system. It also helps to understand and process DARS data. Previously we carried out DARS eigenvalue analysis to model its resonance frequencies. In order to simulate DARS in a more realistic way, we now use a finite difference simulator (COMSOL) to run the time harmonic modeling of DARS and apply this simulation for attenuation estimation of rock samples.

According to the exact size of experimental DARS I, we build a 3-D numerical model and perform the time harmonic analysis. The time-harmonic equation is the inhomogeneous Helmholtz equation in the frequency domain

$$\nabla \cdot \left(-\frac{1}{\rho_0} (\nabla p - q) \right) - \frac{\omega^2}{\rho_0 c_s^2} p = S$$

where $p = p(\mathbf{x}, \omega)$ is pressure and S is source. When damping exists, ρ_0 and c_s become complex quantities. In our model, a point source located at the point r_0 generates a pressure wave on the cavity wall. This point source is monopole and can be described by

$$S = i\omega S_0 \delta(r - r_0)$$

In this numerical simulation, the key step is to choose the size of mesh grid. We use Finite-element code to generate the mesh by specifying a maximum element size of $L/6$, where $L = c/f$ is the free-space wavelength of the sound waves at the resonant frequency 1086 Hz for the empty cavity.

Attenuation is classically implemented with complex velocities. In the damping settings, we can choose frequency-independent Q or frequency-dependent Q . If we define the complex velocity by $c=c_0*(1-i*1/2Q)$, it means frequency independent Q model (Toksöz and Johnston, 1981). We can also choose dependent-frequency attenuation that is specified by the absorption coefficient $\alpha = \pi f / cQ$. Figure 6 gives an example of simulated resonance curve. The resonance frequency is the same as the lab data, but the system Q value (1646) is much higher than the lab data. We need more work to understand this problem.

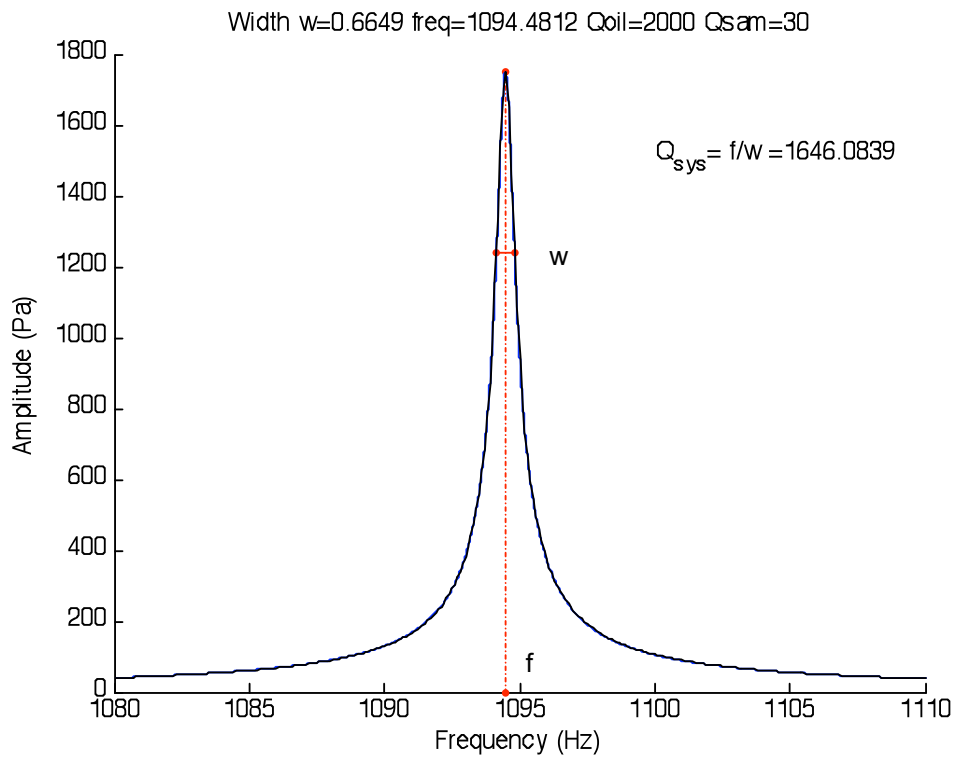


Figure 23: Simulated resonance curve. The cavity has a rock sample ($Q=30$) in it.

A Finite Element Algorithm for 3D Transient Electromagnetic Modeling

Seismic is probably the most powerful geophysical tool for subsurface monitoring. However, the electromagnetic (EM) method is also useful for subsurface monitoring, especially for a relatively shallow target like coalbed. The EM forward modeling is the first step for applying the EM method to surface monitoring.

We here present a 3-D finite-element time-domain (FETD) algorithm for the simulation of electromagnetic (EM) diffusion phenomena. The algorithm simulates transient electric fields and time derivatives of the magnetic fields for a general anisotropic earth. In order to compute transient fields, the electric field wave equation is transformed into a system of ordinary differential equations (ODE) via a Galerkin method with Dirichlet boundary conditions. To ensure both numerical stability and an efficient time step size, the system of ODE is discretized in time using the implicit backward Euler scheme. The resultant FETD matrix-vector equation is solved using a sparse direct solver with a fill-in reducing algorithm. When advancing the solution in time, the algorithm adjusts the time step by examining if or not a current step size can be doubled without affecting the accuracy of the solution. Instead of directly solving another FETD matrix-vector equation for transient magnetic fields, Faraday's law is employed to compute time-derivatives of magnetic fields only at receiver positions. The accuracy and efficiency of the FETD algorithm are demonstrated using time-domain controlled source EM (TD-CSEM) simulations.

Introduction

Transient electromagnetic (TEM) methods are used in both near-surface and deep exploration geophysics. Since interpretation of TEM data in complex geological environments increasingly resort to forward/inverse modeling, the numerical simulation of TEM fields is of particular interest. Among the variety of numerical simulation techniques, finite-difference time-domain (FDTD) algorithms have become the most popular for TEM simulations (Wang and Hohmann, 1993; Commer and Newman, 2004). Their popularity is due to the fact that they are relatively simple to implement, efficient, and can provide accurate solutions to a wide range of TEM simulations.

However, the FDTD method also has well known drawbacks. From a modeling point of view, its biggest weakness is that large complex geological structures (e.g. bathymetry), which do not conform to rectangular grids, need to be captured by stair-step approximations. The stair-step approximation might seem to adequately model significantly-irregular topography using a series of very small grids in parallel computing environments. However, such a stair-step modeling approach can introduce errors into numerical modeling results especially when sources and receivers are placed on the complex surface described by the fine stair steps. Furthermore, the stair-step modeling approach can introduce unnecessarily small grid spacing in the computational domain, resulting in inefficiently small time steps when the Du Fort-Frankel method is used.

We present herein a 3-D FETD algorithm as an alternative to FDTD for diffusive EM simulation in complex geological environments. In contrast to finite difference (FD) methods, finite element (FE) algorithms are based on a geometry-conforming unstructured mesh which allows precise representations of complex geological structures in computationally economic and elegant ways. The price paid is the development cost of the finite-element simulation code.

Theory and Method

In a given computational domain v , the full electric field wave equation is given as

$$\nabla \times \left[\frac{1}{\mu} \nabla \times \mathbf{e}(\mathbf{r}, t) \right] + \frac{\partial^2 \mathbf{e}(\mathbf{r}, t)}{\partial t^2} + \frac{\partial \mathbf{e}(\mathbf{r}, t)}{\partial t} = -\frac{\partial \mathbf{j}_s(\mathbf{r}, t)}{\partial t}, \quad (8)$$

where $\mathbf{e}(\mathbf{r}, t)$ is the electric field at time t at position $\mathbf{r} \in V$, μ , $\boldsymbol{\varepsilon}$, $\boldsymbol{\sigma}$ and $\mathbf{j}_s(\mathbf{r}, t)$ are magnetic permeability, a 3x3 dielectric permittivity tensor and a 3x3 electric conductivity tensor, and an electric current source term, respectively.

First, a residual vector for eqn. (8) is defined as

$$\begin{aligned} \mathbf{p}(\mathbf{r}, t) \equiv & \nabla \times \left[\frac{1}{\mu} \nabla \times \mathbf{e}(\mathbf{r}, t) \right] + \frac{\partial^2 \mathbf{e}(\mathbf{r}, t)}{\partial t^2} \\ & + \boldsymbol{\sigma} \frac{\partial \mathbf{e}(\mathbf{r}, t)}{\partial t} + \frac{\partial \mathbf{j}_s(\mathbf{r}, t)}{\partial t}. \end{aligned} \quad (9)$$

The residual vector must be zero everywhere within V in order to satisfy eqn. (8). However, from a numerical point of view, it is practical to discretize the computational domain into a number of finite elements. Then, the residual vector for each element is forced to be zero in a weighted-integral sense (Jin, 2002):

$$\int \int \int_{v^e} \mathbf{f}_i^e(\mathbf{r}) \cdot \mathbf{p}^e(\mathbf{r}, t) dV = 0 \quad (10)$$

where the superscript e denotes the e^{th} tetrahedral element, $\mathbf{n}_i^e(\mathbf{r})$ with i varying from 1 to n is a set of weighting functions, and v^e is the volume of the e^{th} tetrahedral element.

If the set of $\mathbf{n}_i^e(\mathbf{r})$ functions used in eqn. (10) is also chosen as the set of basis functions for the electric field, the electric field is expanded as

$$\mathbf{e}^e(\mathbf{r}, t) = \sum_{j=1}^n \mathbf{e}_j^e(\mathbf{r}, t) = \sum_{j=1}^n u_j^e(t) \mathbf{n}_j^e(\mathbf{r}) \quad (11)$$

where $u_j^e(t)$ is an amplitude of the electric field on the j^{th} edge of the e^{th} element and needs to be determined using the FETD method. In this study, edge-based Whitney

functions (Whitney, 1957) are chosen as the basis functions as well as weight functions for eqns. (10) and (11).

Substituting eqn. (11) into eqn. (10) and dropping the displacement current term yield the following system of 1st-order ODEs:

$$\mathbf{B}^e \frac{d\mathbf{u}^e(t)}{dt} + \mathbf{C}^e \mathbf{u}^e(t) + \mathbf{s}^e = 0 \quad (12)$$

where

$$(i,j) \text{ element of } \mathbf{B}^e = \iiint_{V^e} \mathbf{n}^e \mathbf{n}_i^e(\mathbf{r}) \cdot \mathbf{n}_j^e(\mathbf{r}) dV ; \quad (13)$$

$$(i,j) \text{ element of } \mathbf{C}^e = \iint_{\partial V^e} \mathbf{n}_i^e(\mathbf{r}) \cdot \nabla \times \mathbf{n}_j^e(\mathbf{r}) dV ; \quad (14)$$

$$i \text{ element of } \mathbf{s}^e = \iint_{\partial V^e} \mathbf{f}_i^e(\mathbf{r}) \cdot \frac{\partial \mathbf{j}_s(\mathbf{r},t)}{\partial t} dV ; \quad (15)$$

$$\mathbf{u}^e = [u_1^e \quad u_2^e \quad \dots \quad u_n^e], \quad (16)$$

and n is the number of the basis functions for the e^{th} tetrahedron.

The system of ODEs is considered local because it results from each individual tetrahedral element. Using connectivity information about finite elements and applying Dirichlet boundary conditions to the boundaries of the computational domain \mathbf{V} , the local systems of diffusion equations from individual elements are assembled into a single global system of diffusion equations:

$$\mathbf{B} \frac{d\mathbf{u}(t)}{dt} + \mathbf{C} \mathbf{u}(t) + \mathbf{s} = 0 \quad (17)$$

Using an implicit 2nd-order backward Euler scheme, eqn. (17) is discretized in time into

$$\mathbf{D} \mathbf{u}^{n+2} = (3\mathbf{B} + 2\Delta t \mathbf{C}) \mathbf{u}^{n+2} = \mathbf{B}(4\mathbf{u}^{n+1} - \mathbf{u}^n) - 2\Delta t \mathbf{s}^{n+2}, \quad (18)$$

where $\mathbf{u}(t) = \mathbf{u}(n\Delta t) = \mathbf{u}^n$, and Δt is the time step size.

The most expensive part in the FE computation is advancing the solution in time. Our primary choice of the numerical solver for eqn. (18) is a direct solver. Matrix \mathbf{D} is explicitly factorized into the product of lower and upper triangular matrices \mathbf{L} and \mathbf{U} . Because Matrix \mathbf{D} is a function of Δt in eqn. (18), the factorization is performed only when Δt is changed. Before the factorization starts, matrix \mathbf{D} is re-ordered to minimize fill-in in the resulting triangular matrices. Finally, forward and backward substitution completes the solution process at a given time. When models are too large for the memory of a given computer, we use an iterative solver. In this case, the solution at the previous time step is used as the initial guess at the current time step. A preconditioner also needs to be re-constructed only when Δt is changed.

EM diffusion simulations require a very small Δt in early time to resolve the broad frequency spectrum of the induced TEM fields. However, because the high frequency component of the TEM field is more rapidly attenuated in time, one can take increasingly larger time steps and thus advance the solution quickly without affecting the accuracy. Therefore, our FETD algorithm tries to double Δt every m time steps, where m is an input parameter. If an earth model is conductive, a smaller m is chosen; if an earth model is rather resistive, a larger m needs to be chosen. When the FETD algorithm attempts to switch a time step size from Δt to $2\Delta t$, the electric fields are computed using both time steps. If the difference between the two solutions is smaller than a specified tolerance, $2\Delta t$ is accepted as a new time step. If the tolerance criterion is not satisfied, the FETD algorithm rejects $2\Delta t$ and continues using the current Δt . However, the byproduct matrices (e.g. the triangular matrices or preconditioner) for $2\Delta t$ are stored for future uses after another m time steps. For brevity, we call this approach the adaptive time step doubling method.

In order to advance eqn. (18), the initial electric fields must be provided. When an earth model is excited using a step-on or Gaussian source waveform, the initial fields are set to zero. However, when a step-off source waveform is employed, the initial DC electric fields need to be calculated via the Poisson equation. Therefore, we also solve the Poisson equation using the FE method. The FE method is based on secondary potential approach since it provides more accurate solutions near sinks and sources (Li and Spitzer, 2002). Once the electric potentials are determined at every FE node in the computational domain, the electric fields along the edges of the elements can be directly calculated using the gradients of the potentials.

After the transient electric fields are calculated in the computational domain using the FETD algorithm, the magnetic fields are determined exploiting the fact that most magnetic receivers do not measure amplitude of magnetic fields, but rather the time derivative of magnetic fields (Commer and Newman, 2004). The time derivatives can be easily determined via Faraday's law by directly applying the curl operator to the basis function in eqn. (11). In this way, we compute the time derivatives of magnetic fields only at receiver positions and avoid having to solve another matrix-vector equation for the transient magnetic field diffusion.

Time-Domain CSEM Simulation Examples

To demonstrate the accuracy and performance of our FETD algorithm, a serial implementation named FETDEM3D is written in MATLAB, from where several external routines are called. The MATLAB portion of FETDEM3D mainly includes FE pre-processing tasks, whereas the external routines are responsible for main FE computations. The FETD modeling was carried out on Sun V40z with 4 Opteron dual-core CPUs with 32 GB memory running Red Hat Linux. The results are compared with the 1D analytical or the 3D FDTD solution of Commer and Newman (2004). Although our FETD algorithm can simultaneously handle multiple arbitrarily-configured electric dipoles with various source waveforms over anisotropic media, single step-off electric dipole

responses over isotropic media are considered in this section for comparison and verification purposes.

The first example is a simple marine TD-CSEM model. The model consists of a 0.7 Ohm-m resistive homogeneous seafloor and a 400 m deep, 0.3 Ohm-m resistive seawater column. To ensure numerical stability, the resistivity of the air is set to 10,000 Ohm-m. A 250 m long, x-oriented electric dipole is placed 50 m above the seafloor. Its ramp-off time is set to $1e-2$ (seconds). Three EM receivers are placed on the seafloor at $x=2, 4$ and 6 km source-receiver offsets. The model is discretized into 108,540 tetrahedral elements, generating 125,883 unknowns. The FETD solutions are plotted in Figure 24, showing excellent agreement with the analytical solutions.

Figure 25 summarizes the performance of the adaptive time step doubling method for the seafloor model above. Without the method, it took 16.2 hours with 50,000 time steps to complete the simulation. In contrast, when the doubling method was employed, the simulation was completed in 36 minutes with 1,393 time-steps. The time step doubling procedures were performed 8 times.

The next example is a 3-D resistive gas reservoir model shown in Figure 26a. The inline TD-CSEM responses over the gas reservoir are simulated using both 3-D FDTD and FETD algorithms. A 250 m long electric dipole whose ramp-off time is set to $1E-4$ seconds is placed at the center of the model. The 3-D FDTD solutions for the model were imported from Um (2005). The FETD algorithm discretizes the model into 114,116 tetrahedral elements, generating 131,741 unknowns. It took 53 minutes to complete the FETD simulation with a total of 1,559 time steps when the adaptive time step doubling method is employed. The solutions from both the FETD and FDTD methods are plotted together in Figures 26b and 26c. The curves for each receiver position agree well with each other at most times except at very early times where slight differences in the electric fields are observed because the employed FD grid does not handle high frequency EM signals very well.

The final example is a gently dipping (4 degrees) two-dimensional (2D) seafloor with and without a 3-D hydrocarbon reservoir illustrated in Figure 27a. In order to elucidate the effects of the slope on the marine TD-CSEM method, a flat seafloor model with and without the same hydrocarbon reservoir is also simulated. The flat seafloor model has a uniform 400 m thick seawater column. The dipping and flat seafloor models are discretized into 165,528 tetrahedral elements with 191,780 unknowns and 127,046 tetrahedral elements with 146,871 unknowns, respectively. The simulations were completed in 65 and 41 minutes, respectively. The inline electric field responses at 4 km source-receiver offset are plotted in Figures 27b and 27c. The differences observed in Figure 27 can be thought of as the combination of the following factors: 1) the airwave effect varies as the thickness of the seawater column above the receiver changes due to the bathymetry; 2) the receiver coordinate is tilted towards the slope; 3) the receiver on the slope measures stronger galvanic effects than that on the flat seafloor because of its shorter distance from the hydrocarbon reservoir. In short, a gently-dipping simple seafloor structure can cause significant effects on the TD-CSEM measurements and, as demonstrated above, seafloor bathymetry needs to be modeled with special care.

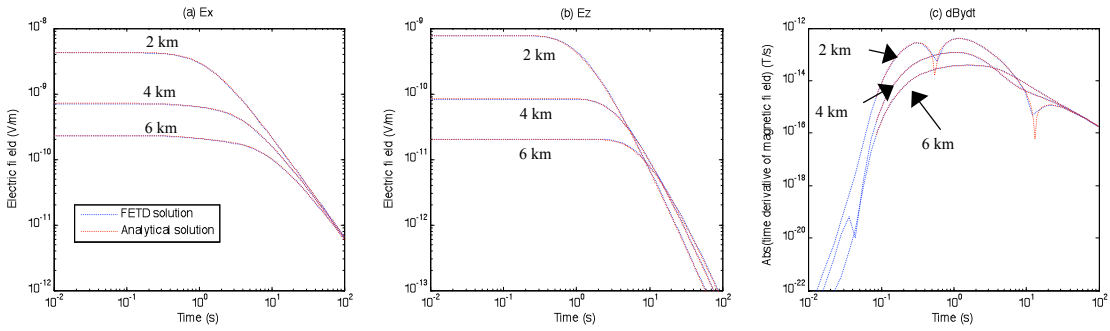


Figure 24: In-line TD-CSEM responses at 2, 4 and 6 km source-receiver offsets over the homogeneous seafloor model.

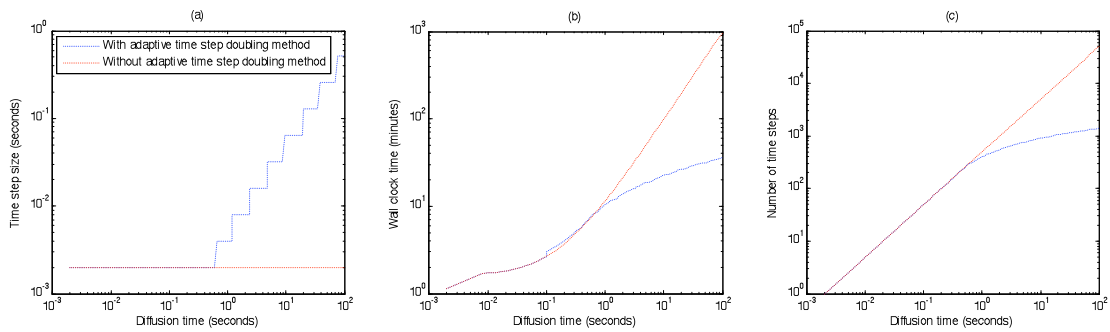


Figure 25: Comparison of computational efficiency with and without the time step doubling method.

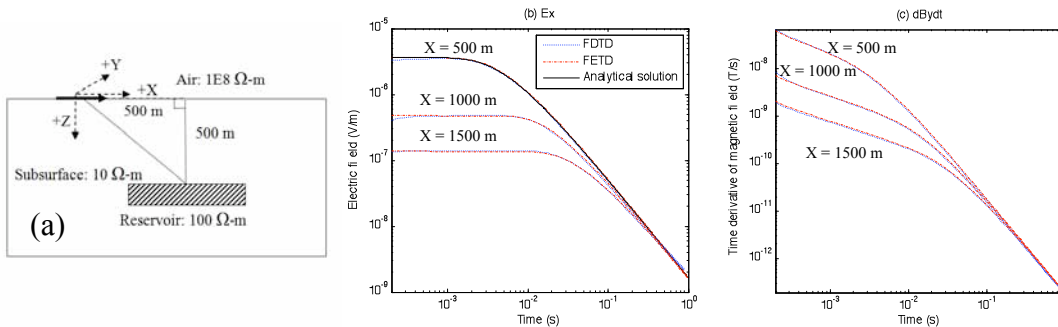


Figure 26. (a) The 3-D gas reservoir model. (b) Ex fields from FETD and FDTD. (c) dBydt fields from FETD and FDTD.

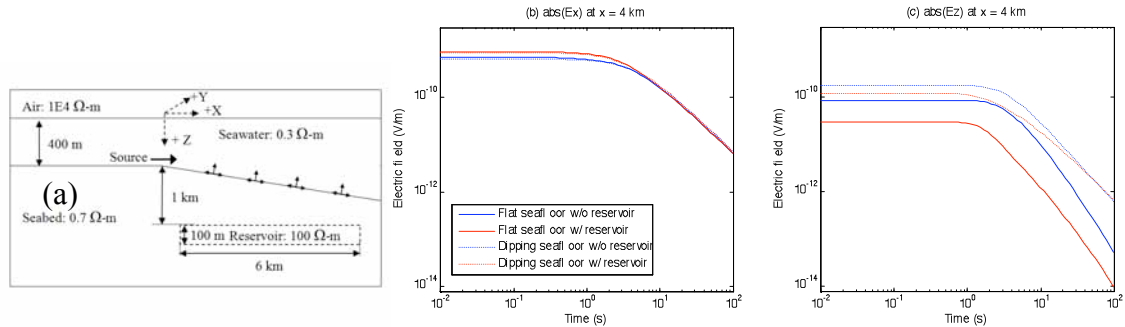


Figure 27. (a) The 2D seafloor model with and without the 3D reservoir. (b) E_x fields. (c) E_z fields. The size of the 3D reservoir is 6 (km)-by-6 (km)-by 0.1 (km) in the x-, y- and z- directions, respectively. Its axis base point is (1 km, -3 m, 1500 m).

Summary – Electromagnetic Simulations

We have presented an efficient 3-D FETD algorithm to simulate diffusive electromagnetic phenomena. The algorithm is especially useful for modeling complex topography and reservoir geometry. The FETD algorithm uses an implicit backward Euler scheme to retain numerical stability with a larger time step size that helps accelerate FETD solution processes especially in late time. The inherent high-computational efforts associated with solving the resultant FETD matrix-vector equation at every time step are mitigated by re-factorizing the FETD matrix only when a time step size is changed. By adaptively doubling the time step at intervals, the FETD algorithm trades off the computational cost of re-factorizing the FETD matrix for the faster advance in FETD solutions. The adaptive time step doubling method plays an important role in speeding up the FETD computation especially in a marine TD-CSEM simulation where an EM diffusion process occurs slowly until very late time due to the high electrical conductivities.

Future Work

True 4-D is a new concept for seismic subsurface monitoring. There are many researches must be done before applying it for real world. We will run more examples for embedded acquisition system using the finite difference method and apply the dynamic inversion to the simulated pre-stack data. For the data evolution work, we will apply our method to surface reflection data. We also plan to use the EM modeling algorithm to run surface and borehole monitoring scenarios.

References

Arts, R., Eiken, O., Chadwick, A., Zweigel, P., van der Meer, L., Zinszner, B., 2004, Monitoring of CO₂ injected at Sleipner using time-lapse seismic data: *Energy*, **29**, 1383–1392.

Candès, E., and Romberg, J., 2007, Sparsity and incoherence in compressive sampling: *Inverse Problems* **23**, 969–985

Commer, M., and G. Newman, 2004, A parallel finite-difference approach for 3D transient electromagnetic modeling with galvanic sources: *Geophysics*, **69**, 1192-1202.

Harris, J. M., Y. Quan, C. Xu, and J. Urban, 2006, Seismic Monitoring of CO₂ Sequestration: GCEP Annual Report.

Harris, J. M., Nolen-Hoeksema, R. C., Langan, R. T., Van Schaack, M., Lazaratos, S. K., Rector III, J. W., 1995, High resolution crosswell imaging of a west Texas carbonate reservoir: Part 1-Project summary and interpretation: *Geophysics*, **60**, 667-681.

Harris, J. M., Zoback, M. D., Kovscek, A. R., Orr, F. M. Jr, 2004, Geologic Storage of CO₂, *in* Global Climate and Energy Project 2008 Technical Report, section 2.5.3.

Harris, J. M., Zoback, M. D., Kovscek, A. R., Orr, F. M. Jr, 2007, Geologic Storage of CO₂, *in* Global Climate and Energy Project 2008 Technical Report, section 2.5.3.

Harris, J. M., Zoback, M. D., Kovscek, A. R., Orr, F. M. Jr, 2008, Geologic Storage of CO₂, *in* Global Climate and Energy Project 2008 Technical Report, section 2.5.3.

Hole, J. A., and Zelt, B. C., 1995, 3-D finite-difference reflection traveltimes: *Geophysical Journal International*, **121**, 427-43

Lazaratos, S. K., and Marion, B. P., 1997, Crosswell seismic imaging of reservoir changes caused by CO₂ injection: *The Leading Edge*, **16**, 1300-1306.

- Landrø, M., Solheim, O. A., Hilde, E., Ekren, B. O., Strønen, L. K., 1999, The Gullfaks 4D seismic study: [Petroleum Geoscience](#), **5**, 213-226.
- Lecomte, I., and T. Kaschwich, 2008, Closer to real earth in reservoir characterization: a 3D isotropic/anisotropic PSDM simulator: SEG Expanded Abstracts.
- Li, Y. and K. Spitzer, 2002, Three-dimensional DC resistivity forward modeling using finite elements in comparison with finite-difference solutions: *Geophysical Journal International*, 151, 924-934.
- Mathisen, M. E., Vasiliou, A. A., Cunningham, P., Shaw, J., Justice, J. H., Guinzy, N. J., 1995, Time-lapse crosswell seismic tomogram interpretation: Implications for heavy oil reservoir characterization, thermal recovery process monitoring, and tomographic imaging technology: *Geophysics*, **60**, 631-650.
- Jin, J., 2002, *The finite element method in electromagnetics*, 2nd edition: John Wiley and Sons.
- Jin, L., M.K. Sen, and P.L. Stoffa, 2008, One-dimensional prestack seismic waveform inversion Using Ensemble Kalman Filter: SEG Expanded Abstracts.
- Quan, Y. and J.M. Harris, 2008, Stochastic Seismic Inversion using both Waveform and Traveltime Data and Its Application to Time-lapse Monitoring: SEG Expanded Abstracts.
- Rickett, J. E., and Lumley, D. E., 2001, Cross-equalization data processing for time-lapse seismic reservoir monitoring: A case study from the Gulf of Mexico: *Geophysics*, **66**, 1015–1025.
- Ross, H. E, 2007, Carbon dioxide sequestration and enhanced coalbed methane recovery in unmineable coalbeds of the powder river basin, Wyoming: PhD Thesis, Stanford University.
- Toksöz and Johnston, 1981, Seismic wave attenuation: SEG Expanded Abstracts
- Um, E. S., 2005, On the physics of galvanic source electromagnetic geophysical methods for terrestrial and marine exploration: M.S. thesis, University of Wisconsin-Madison.
- Walton, G. G, 1972, Three-dimensional seismic method: *Geophysics*, 37, 417–430.
- Wang, T., and G. W. Hohmann, 1993, A finite-difference, time-domain solution for three-dimensional electromagnetic modeling: *Geophysics*, 58, 797-809.
- Whitney, H., 1957, *Geometric integration theory*: Princeton University Press.

Wynn, D., 2003, Survey of geophysical monitoring methods for monitoring CO2 sequestration in aquifers. M.S. Thesis, Department of Geophysics, Stanford University.

Yilmaz, O., 1987, Seismic Data Processing, S. M. Doherty: Society of Exploration Geophysicists, Tulsa.

Yilmaz, O., 2001, Seismic Data Analysis: Processing, Inversion, and Interpretation of Seismic: Society of Exploration Geophysicists, Tulsa.

Zelt, C. A., and Barton, P. J., 1998, 3D seismic refraction tomography: A comparison of two methods applied to data from the Faeroe Basin: JGR, **103**, 7187-7210.

Acknowledgements

The authors JMH, YQ, JR-M and YA are grateful to GCEP for support of their work on this project. TZ and EU thank the SGFs and the SES for their fellowship support.

Publications

1. Arogunmati, A. and J. M. Harris, 2009, An approach for quasi-continuous time-lapse seismic monitoring from sparse data: Expanded Abstract submitted to the 2009 SEG Annual Meeting, Houston.
2. Chaturvedi, T, J.M. Schembre, and A. R. Kovscek, " Spontaneous Imbibition and Wettability Characteristics of Powder River Basin Coal,". *International Journal of Coal Geology* 77(1-2), 34-42 (2009). doi:10.1016/j.coal.2008.08.002
3. Ide, T., Pollard, D., and Orr, F.M., Fissure Formation and Subsurface Subsidence in a Coalbed Fire. *International Journal of Rock Mechanics*. (Revised and resubmitted, 2009).
4. Jessen, K., Tang, G.-Q. and A. R. Kovscek, "Laboratory and Simulation Investigation of Enhanced Coalbed Methane Recovery by Gas Injection," *Transport in Porous Media*, 73(2) 141-159 (2008). DOI: 10.1007/s11242-007-9165-9.
5. Lin, W., G.-Q. Tang, and A. R. Kovscek, "Sorptions-Induced Permeability Change of Coal During Gas-Injection Processes," *SPE Reservoir Engineering and Evaluation*, 11(4), 792-802 (2008).
6. Lucier, A. and M. D. Zoback, "Assessing economic feasibility of regional deep saline aquifer CO₂ injection and sequestration: A geomechanics-based workflow applied to the Rose Run Sandstone in Eastern Ohio, USA." *International Journal of Greenhouse Gas Controls*, (2008).
7. Ross, H., E., M. D. Zoback, et al., "CO₂ sequestration and enhanced coalbed methane recovery in unmineable coalbeds of the Powder River Basin, Wyoming: Reservoir characterization and fluid flow simulations," *International Journal of Greenhouse Gas Controls*, (2008).
8. Um, E. and J. M. Harris, 2009, A finite element algorithm for 3D transient electromagnetic modeling: Expanded Abstract submitted to the 2009 SEG Annual Meeting, Houston.

Contacts

Jerry M. Harris: harris@stanford.edu
Anthony R. Kovscek: kovscek@stanford.edu
Franklin M. Orr, Jr.: fmorr@stanford.edu
Mark D. Zoback: zoback@stanford.edu
Marco Bohnhoff: marcob@stanford.edu
Laura Chiramonte: chiarlau@gmail.com
J. Gerst: Gerstj@battelle.org
Neeraj Gupta: gupta@battelle.org
Paul Hagin: phagin@Stanford.edu
David Pollard: dpollard@stanford.edu
Reginald Mitchell: remitch@stanford.edu
Youli Quan: quany@stanford.edu
Jolene Robin-McCaskill: jmrobin@stanford.edu
John P. Vermilyen: vermylen@stanford.edu
Abhishek Dutta: adutta@stanford.edu
Taku Ide: idetaku@stanford.edu
Wenjuan Lin: wenjuanl@stanford.edu
Evan Um: eum@stanford.edu